論文 / 著書情報
Article / Book Information

題目(和文)	南インド・ダルワール超層群のテクトニクス及び後期太古代の古環境学的研究
Title(English)	Tectonic and paleo-environmental study of the late Archean Dharwar Supergroup, Southern India
著者(和文)	三島郁
Author(English)	Kaoru Mishima
出典(和文)	学位:博士(理学), 学位授与機関:東京工業大学, 報告番号:甲第10415号, 授与年月日:2017年3月26日, 学位の種別:課程博士, 審査員:上野 雄一郎,綱川 秀夫,中島 淳一,中本 泰史,太田 健二,SATISH KUMAR MADHUSOODHAN
Citation(English)	Degree:Doctor (Science), Conferring organization: Tokyo Institute of Technology, Report number:甲第10415号, Conferred date:2017/3/26, Degree Type:Course doctor, Examiner:,,,,,
学位種別(和文)	博士論文
Type(English)	Doctoral Thesis

Tectonic and paleo-environmental study of the late Archean Dharwar Supergroup, Southern India

Kaoru Mishima

Department of Earth and Planetary Sciences,
Tokyo Institute of Technology

Doctor Thesis, 2017

Abstract

Earth’s tectonic and climatic systems may have changed fundamentally before the Great Oxidation Event (GOE) at about 2.3 Ga. Sulfur Mass Independent Fractionation (S-MIF) has demonstrated that Earth’s atmosphere was virtually oxygen-free before the GOE. During 3.0 to 2.4 Ga, the change in $\Delta^{33}S$ and $\Delta^{36}S$ signals may reflect the perturbation of atmospheric chemistry, though the mechanisms of the change are uncertain. The S-MIF signiture possibly reflect many factors, including paleogeography, atmospheric composition, tectonics, and microbial activity. However, global trend of S-MIF signature has not yet established. Here, we reported the sulfur isotopic study of Archean volcano-sedimentary sequences of Dharwar Supergroup, occured in the Chitradurga Schist Belt (CSB), Southern India together with Onverwacht Suite, Barberton Greenstone Belt, South Africa. New systematic field mapping and zircon U-Pb dating allows us to reconstruct detailed lithostratigraphy of the Dharwar Supergroup. The lower unit consists of post-3.0 Ga basal conglomerate, stromatolitic carbonate, siliciclastics with diamictite, chert/BIF, pillowed basalt and pyroclastic sediment in ascending order. Especially, the diamictite layer in the lower unit show dropstone structure, suggesting glaciation in the late Archean. The upper unit consists of 2.6-2.5 Ga conglomerate, heavily carbonated basalt, BIF and silici-clastic sequence in ascending order. This Dharwar sequence preserve the Archean rifting and collisional tectonics. Sulfides in the stromatolitic carbonates show enriched $\delta^{34}S$ values (+19‰) with negative $\Delta^{33}S$, suggesting microbial reduction in the carbonate platform. Considering the microbial processes, the original $\Delta^{36}S/\Delta^{33}S$ is estimated as −1.5 in the lower unit. On the other hand, the upper unit show the $\Delta^{36}S/\Delta^{33}S$ slope of −0.9. This change in $\Delta^{36}S/\Delta^{33}S$ ratio is roughly consistent with those recorded in the other late Archean sequences from Kaapvaal and Pilbara Cratons, suggesting the $\Delta^{36}S/\Delta^{33}S$ ratio records global signal, probably reflecting the change in atmospheric chemistry and climate during the late Archean period.

Contents

Chapter 5 Multiple sulfur isotope geochemistry of the Onverwacht Suite, South Africa

Chapter 6 Synthesis

Chapter 1

Introduction and overview

Introduction and overview

The late Archean (3.0-2.5 Ga) is one of the most specific eras in the Earth's history. Several geological evidences indicate rapid crustal growth, climate changes such as glaciation, and evolution of oxygenic photosynthesis in this period (Condie et al., 2009; Young et al., 1998, 2009; Brocks et al., 2003, 2005; Canfield, 2005; Rasmussen et al., 2008). Dramatic change of Earth's surface environment may have been related with mantle activities at the late Archean (e.g. Condie et al., 2009). Moreover, major changes of C, N, S, and Fe isotopic compositions are recorded in the late Archean sediments, and have been interpreted as a result of the environmental changes and their aftermath on biological activity (e.g. Hayes et al., 2001; Altabet et al., 1992; Beaumont et al., 1999; Crosby et al., 2007; Coplen et al., 2002; Kung et al., 1979; Bekker et al., 2004; Canfield et al., 2000, 2006; Johnson et al., 2005, 2008; Thomazo et al., 2009; Yoshiya et al., 2012). On the other hand, the disappearance of sulfur mass-independent fractionation (S-MIF; $\Delta^{33}S$) record in the sedimentary rocks after 2.32 Ga was associated with a rise of atmospheric oxygen, termed Great Oxidation Event (GOE; Holland, 2002, 2006; Farquhar et al., 2000; Kasting et al., 2002). S-MIF is known to be produced by SO_2 photolysis in a low oxygen atmosphere based on previous photochemical experiments (Farquhar et al., 2001; Ono et al., 2013; Endo et al., 2016). Thus, the existence of the S-MIF in the Archean sedimentary rock is strong evidence of the Archean oxygen free atmosphere.

While the presence of large Archean S-MIF is widely accepted as indicating a reducing atmosphere (Farquhar et al., 2007; Johnston, 2011), the magnitude and sign of S-MIF is still less understood. The Archean $\Delta^{33}S$ record exhibits clear changes in the magnitude of MIF over time: minimum $\Delta^{33}S$ at around 2.9 Ga, subsequent large $\Delta^{33}S$ variations culminating at 2.5 Ga, followed by its sudden drop in the Paleoproterozoic. The change in $\Delta^{33}S$ signature may possibly reflect a fluctuation in oxygen levels (Ono et al., 2006a), the presence of large volcanic eruptions (Ohmoto et al., 2006), speciation of volcanic gasses (SO_2/H_2S ratio; Kump and Barley, 2007; Halevy et al., 2010) and/or other changes in atmospheric chemistry (Farquhar et al., 2007; Domagal-Goldman et al., 2008; Thomazo et al., 2009; Zerkle et al., 2012; Claire et al., 2014). In addition, the atmospheric $\Delta^{33}S$ value can be diluted by mixing it with mass-dependent sulfur compounds (Ono et

al., 2003, Penniston-Dorland et al., 2008, Guy et al., 2012). So far, it has been difficult to decouple the $\Delta^{33}S$ variations caused by atmospheric processes from other subsequent reactions in the several processes (biology, photolysis, mixing, open system, etc.) before sedimentation (Halevy et al., 2013).

Recently the quadruple sulfur isotope ratio ($\Delta^{36}S/\Delta^{33}S$) attracts interests, because it could potentially reflect the change in atmospheric composition before the GOE (Kaufman et al., 2007; Farquhar et al., 2007; Zerkle et al., 2012). Unlike the $\Delta^{33}S$ record, the $\Delta^{36}S/\Delta^{33}S$ ratio is not diluted by the later mass-dependent effect or mixing with it with mass-dependent sulfur compounds. However, the information about the late Archean quadruple sulfur isotope records has come mainly from Kaapvaal Craton (South Africa) and Pilbara Craton (Western Australia). Several paleomagnetic and lithostratigraphic studies suggested that the Pilbara and the Kaapvaal Craton might have been part of the single continent called Vaalbara during the late Archean (e.g. Cheney et al., 1996). Therefore, it is possible that the S-MIF signals in previous works may reflect local changes such as non-atmospheric reactions may be implicated in some sulfur MIF (e.g., Watanabe et al., 2009) and may not necessarily catch global events. In order to distinguish the local and global signatures, it is necessary to check the S-MIF signals in other late Archean sections.

In order to identify the global characteristics of S-MIF signature in the Archean rocks, I selected the two areas for this research: 3.0-2.5 Ga Chitradurga Schist Belt, Western Dharwar Craton, Southern India, and 3.5-3.4 Ga Onverwacht Suite, Barberton Greenstone Belt, South Africa. The Chitradurga Schist Belt is occupied by the continuous volcano-sedimentary rocks, but these rocks suffered from severe deformations and an intense metamorphism up to the amphibolite facies (Raase et al., 1986; Hokada et al., 2013). The Onverwacht Suite is occupied by weakly metamorphosed supracrustal rocks (Furnes et al., 2011, 2012; de Wit et al., 2011; 2016).

Reassessment of lithology in the Dharwar Supergroup, Southern India

Following the above brief overview, the second chapter of this thesis introduces geological, geochemical, geochronological, and petrological studies of the Chitradurga Schist Belt, Western Dharwar Craton, Southern India. Many previous studies described

lithology and deformation structures, and provided tectonics history of the Chitradruga Schist Belt (e.g. Chadwick et al., 1981, 1989; Seshadri et al., 1981; Jayananda et al., 2006; 2013; Chardon et al., 2011). However, the intense deformations and severe alteration observed in this belt make stratigraphical study complicated, and led to many interpretations of the stratigraphy of the Dharwar Supergroup (e.g. Naqvi, 1973; Naqvi and Rogers, 1987; Seshadri et al., 1981; Chadwick et al., 1981). Due to the paucity of primary structures and lack of systematic study, the precise stratigraphic succession of Dharwar Supergroup is still unresolved and debatable. In contrast with the conventional regional geological study of Chitradurga Schist Belt, it is necessary to systematically integrate individual lithologies at each section. As discussed in Chapter 2, our new field mapping and detrital zircon U-Pb dating allows us to reconstruct a detailed lithostratigraphy of the Dharwar Supergroup. A synthesis of new and existing data reveals that an unconformity separate the rocks of the Chitradurga Schist Belt into two units with different geological histories. We argue here that the status of the traditional classification such as Bababudan Group, Vanivilas Formation, Ingaldhal Formation and Hiriyur Formation of the Dharwar Supergroup should be integrated into the two unit. The lower unit consists of basal conglomerate, stromatolitic carbonate, silici-clastics with conglomerate (known as Talya Conglomerate), chert/BIFs, and thick pillowed basalt in ascending order, indicating a rift margin environment at ~2.8-2.7 Ga. The upper unit unconformably overlies the pillow lava, and consists of conglomerate/sandstone, basaltic lava, BIFs and silici-clastic sequences with some mafic volcanic layers. Especially, age frequency in the upper unit (Hiriyur Formation) shows a peak around 2.54 Ga, suggesting that young granite intrusive rocks occurred in the hinterland. In the Chitradurga Schist Belt between 2.8 and 2.5 Ga tectonic processes appear to have operated similar to those within modern plate boundaries.

The third chapter of this thesis raises the possibility of glacial deposits in the Dharwar Supergroup. 2.8-2.7 Ga diamictites with dropstones in the basal Chitradurga Group in the supracrustal belts on the Dharwar Craton, proposed as glaciogenic by several workers (Srikantia, 1992; Ojakangas et al., 2014). However, the evidence of glacial deposit is very suspicious and inadequate. In this chapter, we provide evidence for the existence of floating glacier ice in the depositional basin. The new physical evidence

support a glacial interpretation of the 2.8-2.7 Ga Sadarahalli diamictite which occurs at the middle of Dharwar Supergroup. This evidence of 2.8-2.7 Ga glaciation, together with the 2.9-2.8 Ga Pongola glaciation (Young et al., 1998), indicate the climate cooling era at 2.9-2.7 Ga. This consistent with the presumed ‘‘faint young sun’’ suggested for Archean times would have resulted in cold climatic conditions (Sagan and Mullen, 1972; Kasting, 1993).

Late Archean geological record of atmospheric chemistry

The Chapter 4 presents the sulfur isotopic data obtained from the 3.0-2.5 Ga Dharwar Supergorup, Southern India. As discussed Chapter 4, the results in this study suggest that the $\Delta^{36}S/\Delta^{33}S$ gradient seems to have changed globally; from –1.5 to –0.9 at ~2.7 Ga. The global nature of the trend strongly supports the theory that the $\Delta^{36}S/\Delta^{33}S$ slope reflects the change in atmospheric composition through the late Archean. This result contradict that non-atmospheric reactions may be implicated in some sulfur MIF (e.g., Watanabe et al. 2009). Furthermore, our results strengthen the use of S-MIF signal to trace the change of atmospheric composition before the Great Oxidation Event. The change in $\Delta^{36}S/\Delta^{33}S$ ratio may have another clue to monitor volcanic activity and its influence on reducing gases contents in ancient atmosphere (see Chapter 5). Moreover, the period characterized by the $\Delta^{36}S/\Delta^{33}S$ slope of ~–1.5 seems to correspond to mid-Archean glaciation (2.9~2.8 Ga Pongola glaciation: Young et al., 1998). This correspondence may suggest a potential link between atmospheric composition and climatic changes during the late Archean era.

Paleo Archean geological record of atmospheric chemistry

The Chapter 5 present a new discovery of 3.4-3.5 Ga sulfur isotope anomalies. This discovery fill in the significant time gap of the previous sulfur isotope records before 3.0 Ga. As discussed in Chapter 4, we detect the paleo Archean $\Delta^{36}S/\Delta^{33}S$ slope changes for the first time. These observed slopes (–1.0 to –0.4) are shallower than late Archean slopes (–1.5 to –0.9). Based on photochemical experiments (Whithill and Ono, 2013; Endo et al., 2016), shallower slopes during the 3.4-3.5 Ga indicate the paleo Archean atmosphere possibly more reductive than the late Archean. Moreover, any $\Delta^{36}S$-$\Delta^{33}S$ array does not

intersect the origin ($\Delta^{36}S = \Delta^{33}S = 0$), and these intercepts are lower than sulfate intercept (barite deposited at 3.5-3.4 Ga). Since the SO_2 photochemical reactions originate from igneous sulfur ($\Delta^{36}S = \Delta^{33}S = 0$), the observed negative intercept strongly support the microbial sulfate reduction at that time.

References

Altabet, M. A., Bishop, J. K. B., & McCarthy, J. J., 1992, Differences in particulate nitrogen concentration and isotopic composition for samples collected by bottles and large-volume pumps in Gulf Stream warm-core rings and the Sargasso Sea. Deep Sea Research Part A. Oceanographic Research Papers, 39, S405-S417.

Beaumont, V., & Robert, F. (1999). Nitrogen isotope ratios of kerogens in Precambrian cherts: a record of the evolution of atmosphere chemistry. Precambrian Research, 96(1), 63-82.

Bekker, A., Holland, H. D., Wang, P. L., Rumble, D. I. I. I., Stein, H. J., Hannah, J. L., ... & Beukes, N. J., 2004, Dating the rise of atmospheric oxygen. Nature, 427 (6970), 117-120.

Brocks, J. J., Buick, R., Summons, R. E., & Logan, G. A., 2003, A reconstruction of Archean biological diversity based on molecular fossils from the 2.78 to 2.45 billion-year-old Mount Bruce Supergroup, Hamersley Basin, Western Australia. Geochimica et Cosmochimica Acta, 67 (22), 4321-4335.

Brocks, J. J., Love, G. D., Summons, R. E., Knoll, A. H., Logan, G. A., & Bowden, S. A., 2005, Biomarker evidence for green and purple sulphur bacteria in a stratified Palaeoproterozoic sea. Nature, 437 (7060), 866-870.

Canfield, D. E., Habicht, K. S., & Thamdrup, B. O., 2000, The Archean sulfur cycle and the early history of atmospheric oxygen. Science, 288 (5466), 658-661.

Canfield, D. E., 2005, The early history of atmospheric oxygen: homage to Robert M. Garrels. Annu. Rev. Earth Planet. Sci., 33, 1-36.

Chadwick, B., Ramakrishnan, M., Viswanatha, M.N., 1981. The stratigraphy and structure of the Chitradurga region: an illustration of cover–basement interaction in the late Archaean evolution of the Karnataka craton, southern India. Precambrian Research 16, 31–54.

Chadwick, B., Ramakrishnan, M., Vasudev, V. N., & Viswanatha, M. N., 1989, Facies distributions and structure of a Dharwar volcanosedimentary basin: evidence for late Archaean transpression in southern India?. Journal of the Geological Society, 146(5), 825-834.

Chardon, D., Jayananda, M., & Peucat, J. J., 2011, Lateral constrictional flow of hot orogenic crust: Insights from the Neoarchean of south India, geological and geophysical implications for orogenic plateaux. Geochemistry, Geophysics, Geosystems, 12 (2).

Cheney, E.S., 1996. Sequence stratigraphy and plate tectonic significance of the Transvaal succession of southern Africa and its equivalent inWestern Australia. Precambrian Research 79, 3–24.

Condie, K. C., Belousova, E., Griffin, W. L., & Sircombe, K. N., 2009, Granitoid events in space and time: constraints from igneous and detrital zircon age spectra. Gondwana Research, 15 (3), 228-242.

Coplen, T. B., Hopple, J. A., Boehike, J. K., Peiser, H. S., & Rieder, S. E., 2002, Compilation of minimum and maximum isotope ratios of selected elements in naturally occurring terrestrial materials and reagents. Water Resources Investigations Report. United States Geological Survey, (4222), 112.

Crosby, H. A., Roden, E. E., Johnson, C. M., & Beard, B. L., 2007, The mechanisms of iron isotope fractionation produced during dissimilatory Fe (III) reduction by Shewanella putrefaciens and Geobacter sulfurreducens. Geobiology, 5 (2), 169-189.

de Wit, M. J., Furnes, H., & Robins, B., 2011, Geology and tectonostratigraphy of the Onverwacht Suite, Barberton greenstone belt, South Africa. Precambrian Research, 186 (1), 1-27.

de Wit, M. J., & Furnes, H., 2016, 3.5-Ga hydrothermal fields and diamictites in the Barberton Greenstone Belt—Paleoarchean crust in cold environments. Science advances, 2 (2), e1500368.

Endo, Y., Ueno, Y., Aoyama, S., Danielache, S. O., 2016. Sulfur isotope fractionation by broadband UV radiation to optically thin SO 2 under reducing atmosphere. Earth and Planetary Science Letters, 453, 9-22.Farquhar, J., Bao, H., Thiemens, M., 2000. Atmospheric influence of earth’s earliest sulfur cycle. Science, 289, 756-759.

Farquhar, J., Savarino, J., Airieau, S., Thiemens, M. H., 2001. Observation of wavelength-sensitive mass-independent sulfur isotope effects during SO2 photolysis: Implications for the early atmosphere. Journal of Geophysical Research, 106, 32829-32839.

Farquhar, J., Peters, M., Johnston, D. T., Strauss, H., Masterson, A., Wiechert, U., Kaufman, A. J., 2007. Isotopic evidence for Mesoarchaean anoxia and changing atmospheric sulphur chemistry. Nature, 449 (7163), 706–709.

Furnes, H., de Wit, M. J., Robins, B., & Sandstå, N. R., 2011, Volcanic evolution of the upper Onverwacht Suite, Barberton greenstone belt, South Africa. Precambrian Research, 186 (1), 28-50.

Furnes, H., Robins, B., & de Wit, M. J., 2012, Geochemistry and petrology of lavas in the upper Onverwacht Suite, Barberton Mountain Land, South Africa. South African Journal of Geology, 115 (2), 171-210.

Guo, Q. J., Strauss, H., Kaufman, A. J., Schroder, S., Gutzmer, J., Wing, B., Baker, M. A., Bekker, A., Jin, Q. S., Kim, S. T., Farquhar, J., 2009. Reconstructing Earth's surface oxidation across the Archean-Proterozoic transition. Geology 37 (5), 399–402.

Hayes, J. M., 2001, Fractionation of carbon and hydrogen isotopes in biosynthetic processes. Reviews in mineralogy and geochemistry, 43 (1), 225-277.

Hokada, T., Horie, K., Satish-Kumar, M., Ueno, Y., Nasheeth, A., Mishima, K., & Shiraishi, K., 2013, An appraisal of Archaean supracrustal sequences in Chitradurga schist belt, western Dharwar craton, southern India. Precambrian Research, 227, 99-119.

Holland, H. D., 2002, Volcanic gases, black smokers, and the Great Oxidation Event. Geochimica et Cosmochimica Acta, 66 (21), 3811-3826.

Holland, H. D., 2006, The oxygenation of the atmosphere and oceans. Philosophical Transactions of the Royal Society B: Biological Sciences, 361 (1470), 903-915.

Jayananda, M., Chardon, D., Peucat, J. J., & Capdevila, R., 2006, 2.61 Ga potassic granites and crustal reworking in the western Dharwar craton, southern India: tectonic, geochronologic and geochemical constraints. Precambrian Research, 150 (1), 1-26.

Jayananda, M., Peucat, J. J., Chardon, D., Rao, B. K., Fanning, C. M., & Corfu, F., 2013, Neoarchean greenstone volcanism and continental growth, Dharwar craton, southern India: constraints from SIMS U–Pb zircon geochronology and Nd isotopes.

Precambrian Research, 227, 55-76.

Johnson, C. M., Roden, E. E., Welch, S. A., & Beard, B. L., 2005, Experimental constraints on Fe isotope fractionation during magnetite and Fe carbonate formation coupled to dissimilatory hydrous ferric oxide reduction. Geochimica et Cosmochimica Acta, 69 (4), 963-993.

Johnson, C. M., Beard, B. L., & Roden, E. E., 2008, The iron isotope fingerprints of redox and biogeochemical cycling in modern and ancient Earth. Annu. Rev. Earth Planet. Sci., 36, 457-493.

Kasting, J. F., 1993, Earth's early atmosphere. SCIENCE-NEW YORK THEN WASHINGTON-, 259, 920-920.

Kasting, J. F., 2001. The rise of atmospheric oxygen. Science, 293 (5531), 819-820.

Kasting, J. F., & Siefert, J. L., 2002. Life and the evolution of Earth's atmosphere. Science, 296(5570), 1066-1068.

Kaufman, A. J., Corsetti, F. A., & Varni, M. A., 2007. The effect of rising atmospheric oxygen on carbon and sulfur isotope anomalies in the Neoproterozoic Johnnie Formation, Death Valley, USA. Chemical Geology, 237 (1), 47-63.

Kung, C. C., Hayatsu, R., Studier, M. H., & Clayton, R. N., 1979. Nitrogen isotope fractionations in the Fischer-Tropsch synthesis and in the Miller-Urey reaction. Earth and Planetary Science Letters, 46 (1), 141-146.

Kurzweil, F., Claire, M., Thomazo, C., Peters, M., Hannington, M., & Strauss, H., 2013. Atmospheric sulfur rearrangement 2.7 billion years ago: Evidence for oxygenic photosynthesis. Earth and Planetary Science Letters, 366, 17-26.

Naqvi, S. M., & Hussain, S. M., 1973. Geochemistry of Dharwar metavolcanics and composition of the primeval crust of the peninsular India. Geochimica et Cosmochimica Acta, 37 (1), 159-164.

Naqvi, S. M., & Rogers, J. J. W., 1987. Precambrian geology of India. Oxford University Press.

Ojakangas, R. W., Srinivasan, R., Hegde, V. S., Chandrakant, S. M., & Srikantia, S. V., 2014. The Talya Conglomerate: an Archean (~ 2.7 Ga) Glaciomarine Formation, Western Dharwar Craton, Southern India. Current Science, 106, 387-396.

Ono, S., Eigenbrode, J. L., Pavlov, A. A., Kharecha, P., Rumble, D., Kasting, J. F.,

Freeman, K. H., 2003. New insights into Archean sulfur cycle from mass-independent sulfur isotope records from the Hamersley Basin, Australia. Earth and Planetary Science Letters, 213, 15-30.

Ono, S., Beukes, N. J., Rumble, D., Fogel, M. L., 2006. Early evolution of atmospheric oxygen from multiple-sulfur and carbon isotope records of the 2.9 Ga Mozaan Group of the Pongola Supergroup, Southern Africa. South African Journal of Geology 109 (1–2), 97–108.

Ono, S., Beukes, N. J., Rumble, D., 2009. Origin of two distinct multiple-sulfur isotope compositions of pyrite in the 2.5Ga Klein Naute Formation, Griqualand West Basin, South Africa. Precambrian Research, 169, 48-57.

Papineau, D., Mojzsis, S. J., & Schmitt, A. K., 2007. Multiple sulfur isotopes from Paleoproterozoic Huronian interglacial sediments and the rise of atmospheric oxygen. Earth and Planetary Science Letters, 255 (1), 188-212.

Pavlov, A. A., & Kasting, J. F., 2002. Mass-independent fractionation of sulfur isotopes in Archean sediments: strong evidence for an anoxic Archean atmosphere. Astrobiology, 2 (1), 27-41.

Raase, P., Raith, M., Ackermand, D., & Lal, R. K., 1986. Progressive metamorphism of mafic rocks from greenschist to granulite facies in the Dharwar Craton of South India. The Journal of Geology, 261-282.

Rasmussen, B., Fletcher, I. R., Brocks, J. J., & Kilburn, M. R. (2008). Reassessing the first appearance of eukaryotes and cyanobacteria. Nature, 455 (7216), 1101-1104.

Sagan, C., & Mullen, G., 1972. Earth and Mars: Evolution of atmospheres and surface temperatures. Science, 177 (4043), 52-56.

Seshadri, T. S., Chaudhuri, A., Babu, P. H., & Chayapathi, N., 1981. Chitradurga belt. Mem. Geol. Surv. India, 112, 163-198.

Srikantia, S. V., 1992. Glacial and Fluvial Geomorphology of Western Himalaya. Geological Society of India, 39 (4), 355-355.

Thomazo, C., Ader, M., Farquhar, J., & Philippot, P., 2009. Methanotrophs regulated atmospheric sulfur isotope anomalies during the Mesoarchean (Tumbiana Formation, Western Australia). Earth and Planetary Science Letters, 279 (1), 65-75.

Watanabe, Y., Farquhar, J., & Ohmoto, H., 2009. Anomalous fractionations of sulfur

isotopes during thermochemical sulfate reduction. Science, 324 (5925), 370-373.

Yoshiya, K., Nishizawa, M., Sawaki, Y., Ueno, Y., Komiya, T., Yamada, K., ... & Maruyama, S., 2012. In situ iron isotope analyses of pyrite and organic carbon isotope ratios in the Fortescue Group: Metabolic variations of a Late Archean ecosystem. Precambrian Research, 212, 169-193.

Young, G. M., Brunn, V. V., Gold, D. J., & Minter, W. E. L., 1998. Earth's oldest reported glaciation: physical and chemical evidence from the Archean Mozaan Group (~2.9 Ga) of South Africa. The Journal of geology, 106 (5), 523-538.

Young, G. M., Nesbitt, H. W., & Bosman, S. A., 2009. Stratigraphy, tectonic setting and age of Archean supracrustal rocks in the north-central part of the North Spirit Lake greenstone belt, NW Superior province, Canada. Precambrian Research, 174 (1), 1-15.

Zerkle, A. L., Claire, M. W., Domagal-Goldman, S. D., Farquhar, J., & Poulton, S. W., 2012. A bistable organic-rich atmosphere on the Neoarchaean Earth. Nature Geoscience, 5 (5), 359-363.

Chapter 2

Geology of Chitradruga Schist Belt, Western Dharwar Craton, Southern India: Stratigraphy, geochemistry, geochronology, metamorphic petrology and geological setting

Abstract

In order to understand late Archean tectonic and climatic systems prior to the Great Oxidation Event, we focus on volcano-sedimentary sequences of the Dharwar Supergroup, distributed in the Chitradurga Schist Belt, Western Dharwar craton, Southern India. Although many previous studies described lithology and deformation structures, and provided tectonics history of this belt, the intense deformations and severe alteration make stratigraphical study complicated, and led to many interpretations of the stratigraphy of the Dharwar Supergroup. In order to accurately compare stratigraphy with other Archean craton and discuss the late Archean earth's evolution, it is necessary to reconstruct detail litho- and chrono-stratigraphy by systematic geological study. Thus, we carried out a systematic field work, detailed litho- chrono-stratigraphical study and metamorphic petrology of the Chitradurga Schist Belt. A synthesis of new and existing data reveals that a major unconformity separate the rocks of the Chitradurga Schist Belt into two units. While the precise age range of the rocks present in each unit is largely unknown, we argue here that the status of the traditional classification such as Bababudan Group, Vanivilas Formation, Ingaldhal Formation and Hiriyur Formation of the Dharwar Supergroup should be divided into two unit. The lower unit consists of basal conglomerate, stromatolitic carbonate, silici-clastics with conglomerate (known as Talya Conglomerate), chert/BIFs, and thick pillowed basalt in ascending order, indicating a rift margin environment at ~2.8-2.7 Ga. The upper unit unconformably overlies the pillow lava, and consists of conglomerate/sandstone, basaltic lava, BIFs and silici-clastic sequences with some mafic volcanic layers. Especially, age frequency in the upper unit (Hiriyur Formation) shows a peak around 2.54 Ga, suggesting that young granite intrusive rocks occurred in the hinterland.

In the Chitradurga Schist Belt between 3.0 and 2.5 Ga tectonic processes appear to have operated similar to those within modern plate boundaries.

2-1. Introduction

The late Archaean suprasrustal greenstone belts attract broad interests in understanding the paleo-environmental evolution before the Great Oxidation Event (GOE; Holland et al., 2002, 2006). The Chitradurga Schist Belt (CSB) in the Western

Dharwar Craton (WDC), Southern India, provides robust rock-based benchmarks for studies on early Earth, because 3.0–2.5 Ga Archean supracrustal rocks within the CSB are well-preserved. For more than 100 years, Dharwar Supergroup has been scrutinized by a number of researchers (e.g. reviews by Seshadri et al., 1981). An extensive amount of previous work resulted in conflicting interpretations of the tectonic evolution of the CSB.

The CSB is a type locality of Chitradurga Group which is upper unit of Dharwar Supergroup. The stratigraphy was well summarized in Seshadri et al. (1981), Naqvi (1973, 1985), and Chadwick et al. (1981). The rocks occurring on both sides of the belt are shallow-water sediments like current-bedded quartzites and stromatolites, and, as yet there is no unequivocal evidence to separate them from the main mass of the schist belt, which is designated as Chitradurga Group (e.g. Seshadri et al., 1981; Rao et al., 1995). However, due to the many folds and extensive alteration in the CSB which disrupt the original succession, and lack of systematic study, the stratigraphical classification of these rocks is unsolved and debated.

The tectonic context of CSB is also a subject of debate. Chardon et al. (1996, 1998) and Choukroune et al. (1995, 1997) claimed that its evolution was controlled by non-uniformitarian sagduction: passive sinking of volcanic and sedimentary basins into basement gneisses with no crustal shortening. However, many Archean continental growth had been dominantly controlled by plate tectonics including arc magmatism, subduction–accretion processes, and plume-related intra-plate magmatism (Kroner, 1981; Sleep, 1992). This uniformitarian plate tectonic model (Krogstad et al., 1989; Chadwick et al., 2000, 2003, 2007; Moyen et al., 2001, 2003; Jayananda et al., 2013; Manikyamba et al., 2014) have been presented to explain general geological framework of the Dharwar Craton. Several recent papers reported geochemical data of volcanic rocks in different greenstone terranes of the eastern and WDC and interpreted that they were either erupted from mantle plume or at convergent margin settings. Eruption related to the mantle plume at continental margin has been suggested through the geochemical characteristics of mafic–ultramafic sequences (Manikyamba et al., 2008, 2013; Manikyamba and Kerrich, 2011).

One of the research aims is to reassessment complex geological structure of the

CSB and build the paleo-depositional environments in which the volcano-sedimentary sequences of the Dharwar Supergroup formed. Firstly, we provide an overview of the current status of the stratigraphy and structure in the CSB, as focusing on the Dharwar Supergroup. The basis of this chapter is a new geological map, stratigraphic columns and restored sections (Figs. 2-1,2 and 3) that well illustrate the internal stratigraphy of CSB. The map covers center of the CSB without southern and northern part. This may reveal what kind of tectonics operated at that time, and will be useful for further late Archean tectono-climatic studies. Detailed stratigraphic reconstruction, zircon Pb-Pb age distribution, and metamorphic petrological study provides crucial information about tectonic history of the CSB.

2-2. General geology and stratigraphy of the Dharwar supracrustal rocks

The Dharwar Craton (DC) in southern India consists of Archaean gneisses of tonalitic-trondhjemitic-granodioritic (TTG) composition, volcano-sedimentary sequences, and calc-alkaline to high-potassic granitoids (Chadwick et al., 2000; Jayananda et al., 2006; 2008). The DC is divided into two blocks, Western Dharwar Craton (WDC) and Eastern Dharwar Cratons (EDC). Chadwick et al. (1996) suggested that a major mylonitic ductile shear zone (~400 km long) separates the EDC (high-temperature metamorphic terrain) from the WDC (low-temperature metamorphic terrain). This shear zone (Chitradurga Shear Zone; CSZ) between WDC and EDC extends from the west of Bangalore through the eastern margin of the Chitradurga Schist belt to the west coast of India (Naqvi 1973). The WDC is dominated by an older basement rock (Peninsular gneiss interlayered with >3.0 Ga Sargur Group) which is unconformably overlain by Dharwar Supergroup (2.9-2.6 Ga) than EDC. Dharwar Supergroup are distributed in the Chitradurga, Bababudan, Shimoga, and Western Ghat Greenstone Belts. High-potassic granitic plutons (2.61Ga) are minor within the WDC. The Peninsular gneiss well crops out in the southern region of the WDC. In contrast, the EDC comprises a younger TTG basement rock (2.7 Ga) with small remnants of >3.0 Ga TTG suites, thin elongated 3.0-2.5 Ga greenstone belts, and abundant 2.55-2.52 Ga calc-alkaline to high-potassic intrusions (Jayananda et al., 2006). The peak pressure and temperature conditions for late Archean regional metamorphism in the Dharwar Craton were estimated to be 0.3-

0.5 GPa and ~400°C, whereas those for southernmost parts of the craton were 0.8–0.9 GPa and ~800°C, respectively (Raith et al., 1982; Hansen et al., 1984b, 1995; Raase et al., 1986).

The Chitradurga Schist Belt (CSB) extends over 400 km with an average width of 15 km (Fig. 2-1). The CSB consists of two generations of greenstone sequences: >3.0 Ga older greenstone sequences known as Sargur Group (Radhakrishna 1967; Viswanatha and Ramakrishnan 1976) and 2.9-2.5 Ga younger volcano-sedimentary sequences known as Dharwar Supergroup (e.g. Ramakrishnan and Swaminath 1976; Swami Nath et al. 1976; Viswanatha and Ramakrishnan 1976; Radhakrishna and Naqvi 1986). This division is also simply based on their amphibolite-facies metamorphism of Sargur Group. Both of the greenstone sequences are surrounded by >3.0 Ga TTG gneiss (Chadwick et al., 2000; Jayananda et al., 2006). In generally, the Dharwar Supergroup is separated into lower part (Bababudan Group) and upper part (Chitradurga Group) by an unconformity (Ramakrishnan, 1980). However, the subdivision of the Dharwar Supergroup into the lower Bababudan and upper Chitradurga Groups is difficult due to the absence of an unequivocal marker horizon between them. Swami Nath and Ramakrishnan (1981) proposed that the Talya polymictic conglomerates that are composed of highly disrupted sequence with greywacke matrix define the base of the Chitradurga Group. Chadwick et al. (1981) suggested that the BIF in the CSB is a marker horizon between the Bababudan and Chitradurga Group. On the other hand, Radhakrishna (1983) proposed that the Bababudan and Chitradurga Groups had formed in two different depositional environments at the same time. According to Naqvi (1973, 1985), there is no time gap between the Bababudan and Chitradurga Groups.

2-2-1. Sargur Group

The oldest Sargur Group comprises komatiite, amphibolites, BIF, garnet-biotite schist with kyanite, sillimanite, and stauorolite, calc-silicate and fuchsite quartzite with barite (Swaminath and Ramakrshnan, 1981). The Sargur Group is exposed along the western and eastern margins in the CSB. In the western part near the Gotti Hosahalli, several quartzite layers occur interlayered with serpentinized komatiite. In contrast, marble and ferruginous chert layers are associated with amphibolites in the eastern part.

Metamorphic condition of Sargur Group is estimated to be in the high-P gradient based on the appearance of kyanite and lack of biotite in quartzite (Hokada et al., 2013). U-Pb ages of zircons from metapelitic rocks and quartzite of Sargur Group show the peak age of 2949-3580 Ma (Nutman et al., 1992). Sm-Nd age of 3352 ± 110 Ma was reported from the komatiite by Jayananda et al. (2008), which is considered as a formation age of the Sargur group. Furthermore, monazite U-Th-Pb dating of kyanite-muscovite quartzite sample yield a metamorphic age of 3200-3000 Ma (Hokada et al., 2013).

2-2-2. Bababudan Group

The type area of the Bababudan Group is in 100 km southwest of the CSB, called as Bababudan Schist Belt (Chadwick et al., 1985). The base of the Bababudan Group is marked by a prominent but thin horizon of quartz-pebble conglomerate, which marks a profound unconformity between the basement of TTG gneisses and the Dharwar Supergroup. On the other hand, the Bababudan Group is exposed in only Kibbanahalli Arm of southern CSB and Mayakonda Band in the western margin of CSB. The Kibbabahalli Arm is a synclinal arm wrapping around the Chikkanayakanahalli (CNK Halli) gneissic. The basal conglomerate is overlain by metabasalt-quartzite successions with subordinate amounts of BIF. Locally, agglomerates and volcanic breccias are seen within the metabasalts. The Kibbanahalli Arm was interpreted as a decollement earlier, but it appears to be a synclinal keel that unconformably overlies the basement gneisses containing Sargur enclaves. Quartzite-metabasalt alternations that overlie the basal conglomerate are well exposed from Mayakonda to Vanivilasa Sagara at the western margin of the Chitradurga belt. Polymict conglomerate is exposed along a faulted strip. This conglomerate is overlain by alternated amygdule-bearing metabasalt and cross-bedded quartzite, phyllites, and BIF (Swaminath and Ramakrshnan, 1981). Typical Bababudan succession is also exposed in the Brahmasagara (Halekal) outlier in the northeast of Mayakonda. Depositional age of the Bababudan Group is constrained to be younger than 3137 ± 7 Ma and 3178 ± 61 Ma. The former is based on the youngest detrital zircon grain, and the latter is determined with a monazite U-Th-Pb dating, respectively (Hokada et al., 2013). Mafic metavolcanics in this Group yield a less-constrained whole rock isochrone Sm-Nd age of 2747 ± 15 Ma (Kumar et al., 1996).

2-2-3. Chitradurga Group

The Chitradurga Group is composed of Vanivilas, Ingaldhal and Hiriyur formations, in ascending order (e.g. Seshadri et al., 1981). The Vanivilas Formation occurs at the lowermost part of the Chitradurga Group in the earlier nomenclature of Vanivilas Series (Rama Rao, 1932) and Vanivilas group (Iyengar, 1976). The basal rock unit, called as Talya conglomerate, is a thick (maximum thickness in over 1 km) oligomictic conglomerate. The origin of this conglomerate is variaou arguments; an earlier sedimentary conglomerate (e.g. Sreenivas and Srinivasan, 1968), a volcanic origin (Iyengar, 1901), a mixed pyroclastic and hydroelastic origin (Ziauddin, 1975). Srikantia et al. (1992) and Ojakangas et al. (2014) interpreted the Talya conglomerate as glaciomarine diamictites, but this is highly debatable (see Chapter 3). Above the Talya conglomerate, the Vanivilas Group consists of quartz arenite, phyllite, limestone/dolostone, manganese formations and BIF. The arenites are cross-bedded and exhibit ripple mark at some sequences. Limestones are stromatolite bearing. Locally, the carbonates turn to be brownish weathering dolostones. Partially Manganese is concentrated in carbonates, phyllites, cherts, and BIF. Hokada et al. (2013) reported the yougnest U-Pb detrital zircon age of 3220 ± 3 Ma from a pelitic rock from the Vanivilas Formation, suggesting that the depositional age was younger than 3220 Ma. They also reported monazite U-Th-Pb age of 2255-2484 Ma, which is interpreted as a metamorphic age for this Formation (Hokada et al., 2013).

The Ingaldhal Formation overlies the BIF and associated phyllite near the Chitradurga anticline (Seshadri et al., 1981). The formation consists preponderantly of basic volcanic rocks with subordinate intermediate and acidic volcanic rocks. These are closely associated with pyroclastic such as volcanic breccia agglomerate and tuff. The Chitradurga anticline is principally composed of a chert-greenstone complex, in which the thick basaltic volcanic suite is intercalated with two typical BIF. Chadwick et al. (1981) indicated that the basalt which stratigraphically underlies the BIF in the Chitradurga anticline corresponds to the Bababudan Group and Vanivilas Formation (Chitradurga Group) exposed in the western margin. They indicated the basalt, phyllite, and acid volcanic/pyroclastic overlying the BIF belong to the Ingaldhal Formation. Meta

felsic volcanics intruded in thick pillow lava in the south of CSB. Zircons separated from this felsic volcanics yielded a U-Pb age of 2676 ± 10 Ma (Hokada et al., 2013), indicating that Ingaldhal Formation and sedimentary rocks under the Ingaldhal Formation were deposited older than at least 2.68 Ga.

The volcanic suite of Ingaldhal Formation is overlain by a thick sedimentary pile, which is interspersed with minor volcanics. The sedimentary pile is composed of a greywacke argillite suite containing several interbeds of polymict conglomerate (Seshadri et al., 1981). The associated volcanics and pyroclastics are mainly andesitic to basaltic and less commonly acidic. This major lithological unit is exposed on the eastern part of the main schist belt and is called as Hiriyur Formation. The Hiriyur Formation starts with a major polymict conglomerate member known as the K. M. Kere Conglomerate, and its equivalents near G.R Halli. The K. M. Kere Conglomerate is the basal conglomerate of the Hiriyur Formation. In the K. M. Kere Conglomerate, some grading structures from conglomerate through sandstone to mudstone repeated several times. The K. M. Kere Conglomerate is overlain by a thick pile of greywacke which is followed upward by vast thickness of siltstone and phyllite interbedded with polymict conglomerates (Aimangala conglomerate). The U-Pb ages of detrital zircon from metasandstone in K. M. Kere conglomerate indicate the clastic sediments deposited after 2633 ± 12 Ma (Hokada et al., 2013). The eastern margin of the Hiryur Formation bounded by Eastern Dharwar Craton that is collided at ~2.5 Ga based on granite age. Numerous east-west-trending dyke swarms cross cut the entire CSB after 2369 Ma (French et al., 2010). The mineral assemblages in pelitic and psammitic samples implied that metamorphic conditions of all formations in the Chitradurga Group are relatively low-grade (Hokada et al., 2013).

2-3. New geological map and key sections through the Dharwar Supergroup

Fig. 2-1 shows a revised geological map of the CSB. The area consists predominantly of metasediments and mafic volcanic rocks and minor part of ferruginous chert, BIF, oligomictic and polymictic conglomerate, felsic volcanic rock, and carbonate rock. A cross-section is also reconstructed in which the dips of the bedding and igneous layering are generally sub-vertical. We have performed geological survey including field mappings over 5 years from 2011, together with detailed logging, sampling, and

petrological study. 15 logged sections are marked on the map, and are compiled in the Fig. 2-2. The several faults and fold are described in the Fig. 2-1. Clear contacts between each unit are rarely exposed in the field. The geological features of individual sections are summarized below.

Sections 1 and 2 are W-E trending in the western limb of the CSB. Conglomerate called “Neralekatte Conglomerate”, which is composed of quartz-pebble, occurs at the bottom of the sections (Chadwick et al., 1981). This conglomerate is overlain by basic volcanic lava, pelite, and cross-bedded quartzite, which are followed by Talya conglomerate. The Talya conglomerate layer here is *ca.* 1 km thick, alternating with a coarse-grained sandstone. Clasts, up to 50 cm in size, show a variation from extremely angular to well-rounded and spherical. The conglomerates exhibit unsorted and matrix-supported textures, and well-sorted and grain-supported texture in places. Talya conglomerate shows fining-upward succession and is followed by carbonaceous BIF.

Section 3 is near Sadarahalli and at west limb of anticline. This section has been interpreted as stratigraphic way up to the west, because of the westward dipping succession. The sedimentary sequences unconformably overlie the Penisular Gneiss and end with the mylonatized fault between the PG and metasandstone. This section comprises a ~0.8 km thick pile, which is composed predominantly of sedimentary rocks and starts from an unsorted, 10 m thick, conglomerate layer. Quartzite and vein quartz clasts are dominant within this conglomerate layer. This conglomerate layer is followed by banded ferruginous chert. We interpret that this conglomerate is equivalent to the Talya conglomerate in the Sections 1 and 2, because of similarity in characteristic of the conglomerate and stratigraphic sequences. The banded ferruginous chert is overlain by a 200 m thick laminated sandstone. This sandstone gradually changes to diamictite. In this section, clasts in the diamictite units just above the conformity are poorly sorted, monomictic in composition, and angular to rounded shapes. Some clasts look like dropstone, which is characterized by the folded layer below the clast, and this feature suggests a glacial origin (see Chapter 3).

Section 4 occurs from eastern part of Sirankatte dome through the CSB to the east. The sedimentary rocks in this section unconformably overlie the Sirankatte granite-gneiss complex and are truncated at the Chitradurga Shear Zone. The contact with the Sirankatte

dome is marked by a ~10 m thick quartizte-conglomerate which unconformably overlies the the granite-gneiss. We interpret it as a basal conglomerate corresponding to Neralekatte conglomerate at western limb of the CSB. The conglomerate is followed by chemogenic units of marble (calcitic-dolomitic, often interbedded with chert), Fe-Mn formations, and BIF and phyllite. This dolomic marble is alternating with chert and quartzite layers. These chemogenic units are totally *ca.* 2 km thick and overlain by a basic volcanic rock interlayered with several thick ferruginous chert horizons. The basic volcanic sequence shows agglomeratic, pillow, variolitic, and vesicular structures, and it is followed by a volcanoclastic sediment. On the other hand, Sections 4d, 4e, and 5 include a thin conglomerate layer (Figs. 2-5c and d) just below the BIF. Quartzite and vein quartz are predominant as clasts in this conglomerate layer, which is poorly sorted just like the Talya conglomerate. We interpret that this conglomerate is equivalent to the Talya conglomerate, because of the similarity of sequences (Fig. 2-2). The basic volcanic rocks and volcanoclastic sediment are overlain by an apploximately 1.5 km thick polymict conglomerate, known as K. M. Kere conglomerate of the bottom layer of Hiriyur Formation (Seshadri et al., 1981). This conglomerate in the Section 4 is dominated by well-rounded basaltic clast (Fig. 2-6c) in contrast to Sections 6 and 7 K. M. Kere conglomerate, which include granite, BIF, black chert and basaltic clasts (Fig. 2-6b). At the exposure of the contact between the volcanoclastic sediment and K. M. Kere conglomerate, highly sheared cataclasite occurs, suggesting a tectonic boundary. This conglomerate is followed by carbonated basic volcanic rocks and a coarse cross-laminated sandstone.

Sections 6 and 7 occur at eastern limb of the Chitradurga anticline. Thick pillow basalt (Fig. 2-4g) with ocelli occur throughout the bottom part of the sequence. The bottom of this sequence is truncated by the intrusion of Chitradruga granite. This section consists predominantly of basic volcanic rocks and BIF or banded ferruginous shale. Sedimentary rocks at the section 6a strike E-W and dip moderately to the south in the Chitradruga anticline, while those in the sections 6b, 7a, and 7b strike N-S and dip to the east. In these sections, the pillow structures indicate that the stratigraphic way-up are to the south. This means outward younging polarity of the sequences from Chitradurga Granite. Thin komatiitic basalt lava rests on the first BIF, and is overlain by several BIF,

pyroclastic-volcanoclastic sediments, thin conglomerate layers, and a ~5 km thick basic volcanic rock. These conglomerates are characterized by unsorted angular BIF, chet, quartz, and basalt pebble (Fig. 2-6a), indicating the derivation from the underlying BIF. These basic volcanic rocks show agglomeratic, pillow, variolitic, vesicular, and brecciated structures. In the Sections 6b, 7a, and 7b, the basic volcanic rocks and clastic rock units are overlain by the *ca.* 500 m thick K. M. Kere conglomerate unit. The boundary between the lower and uppers unit shows a tectonic contact defined as a sheared cataclasite. Pebbles in the K. M. Kere conglomerate are well sorted and show various shapes and sizes (Fig. 2-6b). The pebbles include fragments of massive and schistose lavas, banded ferruginous chert, black chert, granite, quartzite and, vein quartz, all of them indicative of derivation from the underlying Ingaldhal and Vanivilas Formations and granite intrusion. The K. M. Kere conglomerate includes turbidite sequences. A severely carbonated basalt rests on the conglomerate, and it is followed by BIF, laminated greywacke, and Aimangala conglomerate (Fig. 2-6d). The Aimangala conglomerate is poorly sorted and consists of rounded pebbles of metabasalt, granite, BIF, black chert, and vein quartz.

Scction 8 occur at the east of the Chitradurga granite. This section consists predominantly of basic volcanic rocks which are highly carbonated. This basic volcanic rocks are overlaid by thin ferruginous chert and feruginou shale. The contact is rarely exposed.

Successions in Section 9 dip eastward at the southern part of the CSB. This section occurs at eastern limb of the anticline, and sequences start from a thick dolostone This dolostone exhibits clear stromatolite textures (Fig. 2-4b) and is followed by a basic volcanic rock interlayered with two thick ferruginous chert horizons. The upper part of this section includes a diamictite layer, that is similar to Aimanagala diamictite.

2-4. Structural Geology

The revised setting of the structures is shown in Figure 2-7. The syncline on the east of the CSB is inferred from graded bedding and pillow orientation. The anticline of the main outcrop of the Chitradurga Granite marks the inferred extension of the Chitradurga arc axial trace shown in Fig. 2-1. The Sirankatte dome formed of basement gneiss is also shown. An integration of our new findings and existing data reveals that at least three

major N-S trending faults and an unconformity separate the volcaniclastic sediment and upper sandstone of the CSB (Fig. 2-1). The first major fault occurs at the west of Chitradurga anticline. This thrust fault extends from the western margin of the Chitradurga granite to the west of Sirankatte dome. The exact contact is rarely exposed, but conversely this is attributed to the existence of this fault. The second fault occurs at the center of CSB, extending with the N-S strike (Figs. 2-8a, b). The cataclasitetes generally indicate the thrust fault boundary, but the characteristics of conglomerates which include clasts from underlying units indicates that the eastern brock across the boundary is overlying sediment by an unconformity. The third major fault occurs at the eastern part of CSB, and it separates the metasediments from metabsasalts (Fig. 2-8c). The fault strikes NW-SE, and extends at least 40 km. This fault was previously documented by Chadwick et al. (2007) as Medikeripura High-strain Zone (Fig. 2-1; MHZ). This fault was related to sinistral shear within a high strain zone, which is indicated by sporadic outcrops of fissile metabasalts and ultramylonitic greywackes. (Chadwick et al., 2007). The MHZ is cut by the later Chitradurga Shear Zone (CSZ; Fig. 2-1).

As described in Figure 2-1, there are many fold structures in the CSB. The well-known major double plunging antiformal fold is called Chitradurga anticline, which occurs here as the steeply plunging fold whose axial trace extends to southeast of the Chitradurga Granite and around Sirankatte dome (Fig. 2-1; e.g. Naqvi, 1973; Chadwick et al., 1981; Naha et al., 1991). Presence of conglomerate at the base of the sedimentary sequence and the stratigraphic way-up away from Sirankatte dome gneiss proves that the gneiss was a basement of the sedimentary rocks. We confirmed a number of repetitions of same sequence due to the small folds at the east of CSB (Fig. 2-1 and Fig. 2-4i). Especially, several series of tight folds occur within the volcanoclastic sediments (Fig. 2-1), indicating that original thickness of the volcanoclastic layer is thinner than the apparent thickness. Similar series of tight folds are observed in the Hiriyur sediment (east part of CSB). These repeated folds resulted in to E–W shortening of the sequences (Chardon et al., 2008, 2011).

As discussed above, several folds and faults in the CSB make it difficult to understand the original stratigraphy of the Dharwar Supergroup. However, our systematic

lithostratigraphic study demonstrated some similarities in each section, and enables us to reconstruct an integrated geologic column of the Dharwar Supergroup (Figs. 2-2 and 2-3). The major unconformity exists only under K. M. Kere conglomerate which includes clasts derived from underlying rocks (Fig. 2-2). Sedimentary environment changed through the major unconformity. The sediments just beneath the major unconformity are composed of black mudstones and volcanoclastic sediments (Fig. 2-9a), indicating a deep and distal marine environment. On the other hand, K. M. Kere conglomerate and overlying sediments include the well-rounded coarse and cross-laminated sandstones (Fig. 2-9b), indicating a proximal shallow marine environment. Thus, we emphasize here that the Dharwar Supergroup should be divided into two units by the unconformity below the Hiriyur Formation.

2-5. New classification of the Dharwar Supergroup

We reconstructed geological columns in whole CSB, from western limb of the Bababudan Group to the eastern margin. Fig. 2-1 is a revised geological map of the CSB, based on our geological survey, and Fig. 2-2 shows a compilation of the geological columns at individual sections.

2-5-1. The lower unit

The newly defined lower unit includes well-exposed volcano-sedimentary sequences of the CSB, that traditionally have been assigned as Bababudan Group, Vanivilas Formation, and Inghaldhal Formation (Figs. 2-2 and 2-3). Along the western limb of the CSB, a series of sedimentary rock is exposed as thin layers from the basal Peninsular Gneiss to top BIF (Fig. 2-1). These sedimentary rocks include cross-laminated ripple-marked quartzites (Fig. 2-4c), and the latter indicates the shallow marine environment. Presence of conglomerate at the base of the sedimentary sequence and the stratigraphic way-up, suggested by pillow shapes, proves that the gneiss was the basement of the sedimentary pile. The sedimentary sequences along the Sirankatte dome also starts from the basal conglomerate which is immediately covered by a thick dolostone (exhibiting stromatolitic textures in places). In contrast, along the southern part of the CSB, the sedimentary sequence is mainly composed of mafic volcanic rocks and overlying thick stromatolitic dolostones (Fig. 2-4b) which are believed to have been

deposited below the photic zone (Walter and Hofmann, 1983). These shallow marine sedimentary sequences are covered by the distinctive conglomerate called Talya conglomerate and BIF.

In generally, the Talya conglomerate marks the transition from Bababudan to Chitradurga Groups as a horizon of siliceous schists at western limb of CSB (e.g. Seshadri et al., 1981). The conglomerate is succeeded by shallow marine deposits of quartzite-stromatolitic carbonate-manganese formations (chert and carbonate). The shallow-water sequence gradually changes into the deep-water sequence including thick mudstone, cherts and widely deposited BIF (middle marker) that probably represents an offshore deposit. Except for some sections, BIF usefle key marker beds for the stratigraphic work, because they are well observed in sediments deposited from shallow shelf to offshore environments (Figs. 2-1 and 2-2).

Pillowed and massive basaltic lavas are dominant within the ~2000 m thick volcanic sequence in the Chitradurga anticline and east of Sirankatte dome (Fig. 2-1), known as Ingaldhal Formation (Ingaldhal volcanics). Rare komatiitic basalt occurs in the middle part of the volcanic sequence at sections 6 and 7. Compared to shallow marine sedimentary sequences under the middle BIF marker, the terrigenous sediments are less and thin in these volcanic sequences, suggesting deposition at the distal marine setting. In view of the geochemistry of the Ingaldhal basalt, the assemblage is interpreted as MORB-like signature (Enya et al., in prep.). A series of tightly folded pile of volcaniclastic sediment overlies both the shallow-water and deep-water sequences at the center of the CSB. These volcaniclastic sediments show the flame structure in places (Fig. 2-4e), indicating an unstable depositional environment.

2-5-2. The upper unit

Across the eastern part of the Chitradurga anticline, we categorized the clastic sequence of Hiriyur Formation, that well crop out at sections 4, 5, 6, and 7, as the upper unit of Dharwar Supergroup (Figs. 2-1 and 2-2). The sedimentary rocks unconformably overlie the Ingaldhal volcanics and volcaniclastic sediments, and they are truncated at the Chitradurga Shear Zone (CSZ) and Medikeripura High-strain Zone (MHZ; Chadwick et al., 2007) that separates the Hiriyur Formation from the Eastern Dharwar Craton. The

boundary under the K. M. Kere conglomerate shows a major unconformity, and is severely sheared. This contact is exposed along the middle of the CSB with a N-S trend, and extends from Chitradurga to Elladakere, although the exposure of K. M. Kere conglomerate is limited to section 5. This suggests that the unconformable contact between the upper and lower unit was reworked by later fault activities. The K. M. Kere conglomerate is overlain by a carbonated metavolcanic rock, BIF, and greywacke which is followed upward by thick siltstones and phyllites interbedded with polymict conglomerates of Aimangala.

2-6. Samples

We have collected four outcrop samples (three sedimentary rocks and one volcanic rock) for the zircon U-Pb geochronology, and their locations are shown in Fig. 2-10. Sample M21-16 was collected from matrix part of a conglomerate in the east of Sirnakatte dome, and is thought to stratigraphically correspond to the lower unit. The second sample, M22-2, was collected from matrix part of the Aimangala conglomerate near NH4 high way, and is thought to be correspond to the upper unit. The third sedimentary sample, M24-6, was collected from southern part of CSB. Due to severe deformations and the lack of marker horizons, the stratigraphic sequence within the package is uncertain. However, the tihck and horizontal bed indicates this metasandstone is composed of the Upper unit of the Dharwar Supergroup. The gneissic sample, 1215Y-7, was collected from Sirankatte dome.

2-7. Method

The analysis was performed using a sensitive high-resolution ion microprobe (SHRIMP II) at the National Institute of Polar Research, Tokyo, Japan. We followed the procedure described in Horie et al. (2012) for the sample preparation and zircon U-Pb analysis. Presence of zircon in the selected samples was confirmed by petrographic observation. We concentrated zircon grains using conventional mineral separation techniques, which include crushing and pulverizing followed by magnetic and heavy liquid separation. After these processes, zircons grains were hand-picked manually under binocular microscope and mounted together with standards in an epoxy resin disc. After

curing, these discs were polished until their midsections of the zircons were exposed. Cathodoluminescence (CL) images and Backscattered electron (BSE) images were taken using a scanning electron microprobe (SEM; JEOL JSM-5900LV) to examine the internal structures of the individual grains as well as to determine the appropriate analytical spots for each grain. The surfaces of grain mounts were washed with 2 % HCl to remove the lead contamination at the grain surface. Gold coating was also made prior to the analysis. We mainly followed the analytical protocol described in Compston et al. (1984), Williams (1998), and Horie et al. (2006). The procedure began by the emission of an O_2 primary ion beam of 1–3 nA, with a 10–15 μm diameter, to sputter the polished mount around each analytical spot. TEMORA2 ($^{206}Pb/^{238}U$ age = 416.8 Ma; Black et al. 2004) and SL13 (U concentration 238 ppm; Claoue-Long et al., 1995) were used as calibration standards. Data reduction of U–Pb were performed by using the SQUID 2 (Ludwig, 2009), which is similar to the description given in William (1998). Common Pb correction was made based on the measured ^{204}Pb as well as Pb isotope composition of the oceanic crust reported by Stacey and Kramers (1975). The pooled ages were determined using Isoplot/Ex software (Ludwig, 2008). In appraisal of the data, only concordant ones, defined by less than 10% discordancy were considered for further discussion. All the reported dates in this paper were derived from $^{207}Pb/^{206}Pb$ ratios. Uncertainty reported for individual analysis is at the 1σ level, and the pooled age calculated by weighted average is quoted at the 2σ level.

2-8. Results

In situ U–Pb zircon analyses for the conglomerate matrix of upper unit (M22-2) were performed at 36 spots on 32 grains. Results are shown in Figs. 2-12 and 2-13. Zircon grains are rounded and prismatic and show rounded shapes with their grain sizes ranging 50–100μm. Almost all zircon grains show oscillatory-zoned internal structures, indicating a magmatic origin (Fig. 2-11). A probability density diagram of concordant $^{207}Pb/^{206}Pb$ age shows multiple age peaks mainly centered at 2.54 Ga, 2.84 Ga, 3.09 Ga, 3.35 Ga, and 3.40 Ga (Fig. 2-12).

In situ U–Pb zircon analyses for the conglomerate matrix of lower unit (M21-16) were performed at 32 spots on 28 grains (Figs. 2-12 and 2-13). Zircon grains are rounded

and prismatic and show rounded shapes with their grain sizes ranging 50–100μm. Zircon grains show oscillatory-zoned internal structuresindicating a magmatic origin (Fig. 2-11). A probability density diagram of concordant $^{207}Pb/^{206}Pb$ age shows multiple age peaks mainly centered at 2.8 Ga, 3.01 Ga, 3.12 Ga, 3.25 Ga and 3.28 Ga (Fig. 2-12).

Zircon U–Pb dating was performed on the Sirankatte gneiss (1215Y-7). Results are shown in Figs. 2-12 and 2-13. A discordant $^{207}Pb/^{206}Pb$ age of 3229 ± 30 Ma was obtained by an upper intercept age on the Concordia curve (Fig. 2-11) (2σ uncertainties, MSWD= 20).

U–Pb zircon analysis was performed on metasediment of the upper unit (M24-6). Zircon crystals, whose sizes range from 50 to 150 μm, are prismatic and show rounded shapes. An age frequency diagram of concordant $^{207}Pb/^{206}Pb$ age shows multiple age peaks centered at 2.54 Ga, 2.98 Ga, and 3.2-3.4 Ga (Fig. 2-13).

2-9. Discussions

2-9-1. Provenance of sediments in the Dharwar Supergroup

Age spectrum of detrital zircons from a conglomerate can provide information about ancient provenance. We separated detrital zircons from 3 clastic sediments in the CSB. A number of 3.5-3.0 Ga grains are included in all the sedimentary rocks analyzed in this and previous studies (Figs. 2-12; concluding Sarma et al., 2012; Hokada et al., 2013; Nasheeth et al., 2015), and they were likely derived from surrounding TTG suites in the WDC (3.5-3.0 Ga; Chardon, 1997). We collected a sample from the Sirankatte dome gneiss as 1215Y-7, which yielded a weighted mean Pb/Pb age of 3172 ± 19 Ma (MSWD = 20). There is a basic problem whether the gneisses of Sirankatte dome were older or younger than the Dharwar Supergroup (e.g. Naha et al., 1995). Because it is difficult to explain the dome structure without plume followed by the upheaval. In this study, the newly obtained $^{207}Pb/^{206}Pb$ age of 3.2 Ga indicates that the Sirankatte dome gneiss was formed in parallel with the TTG gneisses, and was one of the sources of the zircons included in overlying sedimentary rocks.

The youngest age of detrital zircons in the lower unit is ca. 2.8 Ga, which constrains the maximum depositional age of the lower unit (Fig. 1-13). On the other hand, the upper limit is constrained by felsic intrusive rock of 2.67 Ga (Hokada et al., 2013) and 2.62 Ga

potassic plutons (Jayananda et al., 2006). Thus, the depositional age of Ingaldhal volcano-sedimentary sequence was between the 2.8 and 2.67 Ga. This age is consistent with the whole rock isochrone Sm-Nd age of mafic metavolcanics in this unit, that yielded 2747 ± 15 Ma for the mixed sample (Kumar et al., 1996).

On the other hand, we obtained Neoarchean populations (~2.54 Ga) from the matrix of Aimangala conglomerate in the upper unit of the Dharwar Supergroup (Fig. 2-13). This youngest age peak is consistent with the 2.6–2.5 Ga felsic intrusive occurring in the WDC (Nutman et al., 1996; Trendall et al., 1997; Chadwick et al., 2007; Sarma et al., 2011; Jayananda et al., 2006, 2013; Ram Mohan et al., 2014), indicating a derivation of materials from these intrusions. Previous studies also have reported Neoarchean detrital zircons from the upper unit (Hokada et al., 2013; Nasheeth et al., 2016). However, their ages are slightly older than those in this study (Fig. 2-12). Jayananda et al. (2013) reported a lot of data set of zircon U-Pb ages, determined with a SIMS, for felsic volcanic rocks occurring in seven greenschist belts within the Dharwar Craton. Their U-Pb ages are categorized into two stages magmatism (2.7–2.6 Ga and 2.58–2.54 Ga). Both age ranges are consistent with the Neoarchean zircon populations in the K. M. Kere conglomerate (2.68-2.63 Ga) and the Aimangala conglomerate (~2.5 Ga). This fact suggests that the upper unit include at least two magmatic events.

A metasandstone (M24-6) from the southern part of the CSB has zircons with ages ranging from 2.5 Ga to *ca.* 3.4 Ga (Fig. 2-12). The youngest peak of 2.6-2.55 Ga is same as that in the upper unit. Thus, this sediment is deposited at same time with Upper unit. The probability density diagram of $^{207}Pb/^{206}Pb$ age shows a large peak at 3.4-3.2 Ga, unlike the upper unit of M22-2. This might reflect the difference of hinterland: southern part of CSB was far from the young granites, therefore the detrital zircons from surrounding 3.4-3.2 Ga Peninsular gneiss tend to be enriched.

Traditionally sedimentary rocks occurring on both sides of the CSB have been interpreted as a successive sequence without major unconformities. Actually, no stratigraphic gap in sediments in between western and central part was documented in previous works (e.g. Seshadri et al., 1981; Rao et al., 1995). However, we newly identified a huge sedimentary gap at the bottom of the Hiriyur Formation, and separated the sediments into the upper and the lower units based on this sequence boundary. Age

frequencies of detrital zircons, in which the youngest Pb-Pb age of the lower unit is 300 My older than that of the upper unit, support the idea.

2-9-2. Metamorphic petrology

Dharwar Craton has been divided into eastern low pressure and western intermediate pressure metamorphic blocks (Swami Nath and Ramakrishnan, 1981). The boundary between the two brocks show a highly shear zone traced along the eastern margin of the CSB (Chadwick et al., 1989). Pichamuthu (1962) and Raase et al. (1986) have demonstrated that the grade of metamorphism in the late Archean supracrustal rocks increases from greenschist facies in the northern part to upper amphibolite facies in the southern part of the western block. On the other hand, Hokada et al. (2013) reported the distinct metamorphic conditions of each stratigraphic unit by pelitic metamorphic study, with most prominent difference observed in the Chitradurga Group. The lower unit of this group are metamorphosed under biotite-muscovite grade, whereas the upper unit at chlorite-muscovite grade. To understand the P-T regime of metamorphism in the CSB, we have examined the mafic volcanic rocks which distributed throughout the CSB.

2-9-2-1. Mineral isograds of the Chitradurga Schist Belt

The greenstones in the Chitradurga area underwent various extents of carbonatization but less carbonatized greenstones retain index secondary minerals such as chlorite (Chl), epidote (Ep), albite (Ab), oligoclase (Olg), calcite (Cc), Ca-amphibole and quartz (Qz) (Fig. 2-15). Under such greenstone facies metamorphism, original igneous textures and minerals are ubiquitously preserved, and fine-grained samples have intergranular, intersertal or hyaloophitic textures. The original igneous minerals in groundmass of fine-grained volcanic rocks are partly or completely replaced by secondary minerals such as chlorite, epidote, quartz, amphibolite and calcite. However, many igneous clinopyroxene are well preserved in some coarse-grained samples in the middle part of the Ingaldhal region (Fig. 2-14). Plagioclase is replaced by epidote, albite, sericite and calcite. Veins such as carbonate and quartz are also present but they are excluded from the following description because the cross-cutting relation indicates they were formed during later processes. We subdivided the Chitradurga area into three units,

from unit A to C, based on the mineral isograds in less carbonatized greenstones (Fig.2-17). The mineral parageneses in Units A, B and C are shown in Fig. 2-15. Unit A is defined by emergence of calcic plagioclase of oligoclase composition and Ca-amphibole; the typical mineral assemblage is Ab + Ep + Ca-amphibole + Qz ± Chl (Fig. 2-15). Unit B is defined by the actinolite (Act) in the greenstone; the typical mineral assemblage is Chl + Ep + Act + Qz + Ab. Unit C is defined by the emergence of pyroxene which are igneous origin; the mineral assemblage is Chl + Ep + Act + Ab + Qz + Cc (Fig. 2-15). Although they were shifted by secondary faults in some places, the boundaries of the metamorphic zonation among unit A to C are almost parallel to the lithological boundaries of BIF (Fig. 2-14). Carbonate minerals are ubiquitous throughout the area, but the modal amount decreases from unit A to C.

2-9-2-2. Mineral Chemistry

Chemical compositions of minerals were measured by an Electron Probe Micro Analyzer (JEOL-JXA-8800) at Tokyo Institute of Technology. All analyses were performed with an accelerating voltage of 15 kV, 12 nA beam current and a counting time of 10–40 s. Analytical conditions of the scanning microprobe were 15 kV accelerating voltage, 10 nA specimen current, and 60–80 s counting time. We analyzed approximately 3500 points in total.

The bulk composition of the metabasalt in the CSB were analyzed by the X-ray fluorescence technique for their major and trace element concentrations at the University of Niigata (Enya et al., in prep.). Mineral paragenesis generally depends not only on the metamorphic grade but also the effective bulk compositions. However, the major element concentrations are very similar on the Vijoen diagram (Fig. 2-16; Vijoen, 1982), indicating that the all metabasalts show tholeiite basalt composition.

2-9-2-2-1. Plagioclase

Secondary plagioclase is ubiquitous in units A, B and C, whereas the igneous calcic plagioclase is completely replaced by secondary sodic plagioclase, sericite, carbonates or epidote. The anorthite (An) content of the plagioclase from unit A to C is shown in Fig. 2-18 and Table 1. In units B and C, all plagioclase is albite, but in unit A have higher An

than those in units B and C. The An content ranges from 0.9% to 5.8% in unit B and from 1.4% to 14.9% in unit C. In unit A, albite and oligoclase coexist in some samples. In summary, the An content of plagioclase increases at unit A.

2-9-2-2-2. Calcic amphibole

Colorless to pale-green and fine-needle-like Ca-amphibole occurs in units A, B and C. The amphibole partially replaces the rim of relict clinopyroxene. Chemical compositions of Ca-amphibole in units A, B and C are plotted on the amphibole classification diagram (Figs. 2-19 and 2-20; Table 2). The Fe^{3+} content of amphibole was estimated from the stoichiometry based on a formula of 23 oxygen (Terabayashi, 1993).

2-9-2-2-3. Chlorite

Chlorite replaces igneous olivine, pyroxene, plagioclase and interstitial glass. It ubiquitously occurs in all units. The chlorite has large compositional variations within even a single metamorphic unit, but is relatively homogeneous in terms of the XFe [FeO/(FeO + MgO)] ratio in each sample.

2-9-2-3. Mineral composition

The intimate relationships between the secondary matrix minerals, such as chlorite, epidote, Ca-amphiboles, secondary plagioclases, are illustrated by their textures and modes of occurrence (Fig. 2-15), indicating that they crystallized simultaneously with each other. Accordingly, we assume chemical equilibrium of the secondary minerals was attained.

In general, the An content of plagioclase increases with increasing metamorphic grade at the greenschist–amphibolite transition (Maruyama et al., 1982). In the CSB, the An content of plagioclase increase from units B, C to A (Fig. 2-18).

The composition of Ca-amphiboles changes progressively and stratigraphically downwards (Fig. 2-18). In Units B and C, it is only actinolite, whereas both actinolite and hornblende coexist in unit A. Single phase hornblende is present in the southern part of Zone D in the lower gabbro unit. Within the greenschist and amphibolite facies zones, the development of the metabasalt assemblages is characterized by progressive growth and

compositional reequilibration of amphibole. The chemical composition of the amphiboles shows a marked change from actinolite in the greenschist facies zone (Units B and C) to hornblende in the amphibolite facies zone (Unit A), which results from an increase in the tschermakite components (Fig. 2-19).

2-9-2-4. Metamorphic temperature and progressive metamorphism of the Chitradurga Schist Belt

The metabasaltic rocks, unlike the metapelites in this traverse (Hokada et al., 2013), do not show dramatic changes in their mineral assemblages over a wide range of P-T conditions in the CSB (Fig. 2-17). Instead, continuous chemical changes occur, especially in amphibole and plagioclase. While the Units B, C show the lower greenschist facies metamorphism (~400 °C), amphibolite facies were obtained from Unit A. Indeed, the mineral assemblages in the metabasaltic rocks of the Unit A yielded temperature of 500-550 °C by hornblende-plagioclase thermometer of Holland and Blundy (1994). Thus, the metamorphic mineral of the present area can be classified into two units based on their relationship with the mineral compositions in the host rocks (Fig. 2-21).

The cause of amphibolite metamorphism widely debated. In generally, the progressive metamorphic zonation in the western part of the Dharwar craton was described in the early works (Rama Rao, 1936; Pichamuthu 1953; Raase et al., 1986). For the major crustal segment, north of the WDC, they indicated a continuous increase in metamorphic conditions from greenschist facies in the north to granulite facies in the south. On the other hand, Hokada et al. (2013) reported distinct metamorphic conditions of each stratigraphic unit by pelitic samples study; lower unit of Dharwar Supergroup are metamorphosed under biotite-muscovite grade, whereas the upper unit at chlorite-muscovite grade. They implied that the metamorphic conditions are not continuous from Chitradurga supracrustal rocks to underlying Sargur (and probably Bababudan as well). When combined with the results of the previous investigation by Hokada et al. (2013), our data suggests an increase in grade of metamorphism from greenschist facies at the central portion to amphibolite facies at the belt margin during the main granite intrusive (Chitradurga granite and Hosadurga granite possibly Arsikere granite; Fig. 2-1). This can be attributed to the steep thermal gradient produced by syn-kinematic granitoids, the

emplacement of which was broadly contemporaneous with the deformation and regional metamorphism of the supracrustal sequence. However, Hokada et al. (2013) indicated that the Sargur Group (and possibly Bababudan Group) underwent metamorphism of the biotite-muscovite grade before 3.0 Ga on monazite metamorphic age, while the overlying Chitradurga Group contain the c. 2.5-2.3 Ga monazites. This is inconsistent with the contact metamorphism by 2.6 Ga Chitradurga Granite intrusion. Hokada et al. (2013) also suggested the possibility of contamination of Sargur monazite into the Bababudan sediment. In either of the scenarios, this latest Archaean-early Proterozoic metamorphic episode, extensively recorded in Chitradurga Group, is not clear in underlying Bababudan and Sargur Groups, which imply some discontinuity in terms of regional metamorphic records within the Chitradurga Schist Belt. Further integrated field, petrographical and geochronological studies are required to evaluate the significance of this regional metamorphic event.

2-9-3. Tectonic framework

We have presented new observations from two different geological units in the Chitradurga Schist Belt, each separated by tectonic and instance unconformable contacts. The units all have complex internal geological relationships and histories that have not been fully appreciated before. Thus, the tectonic context of CSB is a subject of debate. Chardon et al. (1996, 1998) and Choukroune et al. (1995, 1997) claimed that its evolution was controlled by non-uniformitarian sagduction: passive sinking of volcanic and sedimentary basins into basement gneisses with no crustal shortening. On the other hand, uniformitarian plate tectonic model (Krogstad et al., 1989; Chadwick et al., 2000, 2003, 2007; Moyen et al., 2001, 2003; Jayananda et al., 2013; Manikyamba et al., 2014) have been presented to explain general geological framework of the Dharwar Craton. This model represents an east-to-west accretionary model of island arcs, or of an already-formed arc-granitic whole-batholith terrane, again from east to west, onto the WDC (Fig. 23). Our new litho-stratigraphic study and zircon age data together with published ages show the evolution of CSB at c. 2.8–2.67 Ga upper unit and 2.61–2.54 Ga lower unit (Fig. 2-24).

The lower unit started from basal conglomerate, basaltic lava, stromatolitic

carbonate, silici-clastics cross-laminated sandstone and oligomictic conglomerate indicates shallow marine environment caused by initial crustal extension (Fig. 2-24a and b). Follwing a thick mudstone, cyclic volcanoclastic sequence and widely deposited BIF indicate that the depositional setting must shifted from proximal to distal marine environment (Fig. 2-24c). It suggests the rift setting at ca. 2.8 Ga. After 2.7 Ga, basaltic and andesitic bimodal volcanism, and the emplacement of 2.62 Ga potassic plutons (Chitradurga Granite; Jayananda et al., 2006), indicate the start of subduction (Fig. 2-24d and e). A reorganization of the subduction (steepening or break-off of slabs) could have triggered the rise of a mega plume beneath the CSB, followed by the upheaval of the lower unit before 2.6 Ga. The rising plume caused the crustal reworking and regional metamorphism. The following upper unit (Hiriyur Formation) contains lower unit material such as basalt, BIF, shale, quartzite, and 2.7-2.54 Ga zircon grains. This suggest the erosion and redeposition of lower unit during 2.7-2.55 Ga (Fig. 1-24e). After 2.55 Ga, the collision of arc basalt of east of CSB. The Aimangala conglomerate and covered sediment possibly derived from this magmatism (Fig. 2-24f).

Recently, the major and trace element compositions and isotopic compositions of the three basalt units (see section 2-8-2, Fig. 2-14) suggest that they can be grouped into 2 geochemically distinct types (Enya et al., in prep). The first type of rocks occurring in the unit A and unit C are characterized by major elements having negative trends in binary diagrams versus MgO, flat REE pattern and trace element spider diagram similar to primitive mantle. The second group of rocks, occurring in the Unit B, on the other hand, have high trace element abundances, have negative trends in variation diagrams except for Cr and Ni, enriched compositions of LIL, LREE and slightly depleted HREE than the first type. In addition, Nd isotope ratios were different for the 2 types, the first type samples have positive epsilon Nd values, whereas the second type have negative values. Considering the Nd isotopic data, it was concluded that the compositional variations observed between the two types of volcanic rocks were cause by the difference in magma source in different tectonic settings. The Units A and C have likely oceanic ridge type volcanism as evidenced by the REE patterns and Nd isotopic ratio related to a possible upwelling mantle plume. On the other hand, the Unit B volcanism can be related to an arc setting possibly caused by subduction. These geochemical evidences support the

uniformitarian plate tectonic model of CSB. However, there is no geological evidence such as drastic and short term subduction. In either of the scenarios, this latest Archaean-early Proterozoic metamorphic episode, extensively recorded in CSB, is not clear. Further integrated field, petrographical and geochronological studies are required to evaluate the significance of this regional tectonic event.

2-10. Conclusions

We have reassessed the Archaean metasedimentary sequences of the Chitradurga Schist Belt in Western Dharwar Craton in terms of their stratigraphy, geochronology and geological setting with metamorphic conditions. Our chronology is largely consistent with that presented in previous zircon U–Pb dating studies (e.g. Hokada et al., 2013), but we have added finer resolution to the stratigraphic units. Moreover, the detail metamorphic petrological study has brought to light the following metamorphic feature of the Chitradurga Schist Belt. The conclusions of the present work can be summarized as follows:

We argue here that the status of the traditional classification such as Bababudan Group, Vanivilas Formation, Ingaldhal Formation and Hiriyur Formation of the Dharwar Supergroup should be divided into two units by an unconformity. The lower unit consists of basal conglomerate, stromatolitic carbonate, silici-clastics with diamictite (Talya conglomerate), chert/BIFs and thick pillowed basalt in ascending order, indicating that rift margin environment predominated at this time. The upper unit unconformably overlies the pillow lava, and consists of conglomerate/sandstone, mafic lava, BIFs and silici-clastic sequences. Especially, the age distribution in the upper unit (Hiriyur Formation) shows a peak age at around 2.55 Ga, suggesting the hinterland from the young granite intrusive.

The prograde metamorphic mineral composition, amphibole-plagioclase in metabasalts, which developed during the intrusive granite (regional metamorphism) yielded pressure and temperature in the Amphibolite facies. This data, when combined with the results of the previous investigation by Hokada et al., 2013, suggests an increase in grade of metamorphism from greenschist facies at the central portion to amphibolite facies at the belt margin during the main granite intrusive. This can be attributed to the

steep thermal gradient produced by syn-kinematic granitoids, the emplacement of which was broadly contemporaneous with the deformation and regional metamorphism of the supracrustal sequence.

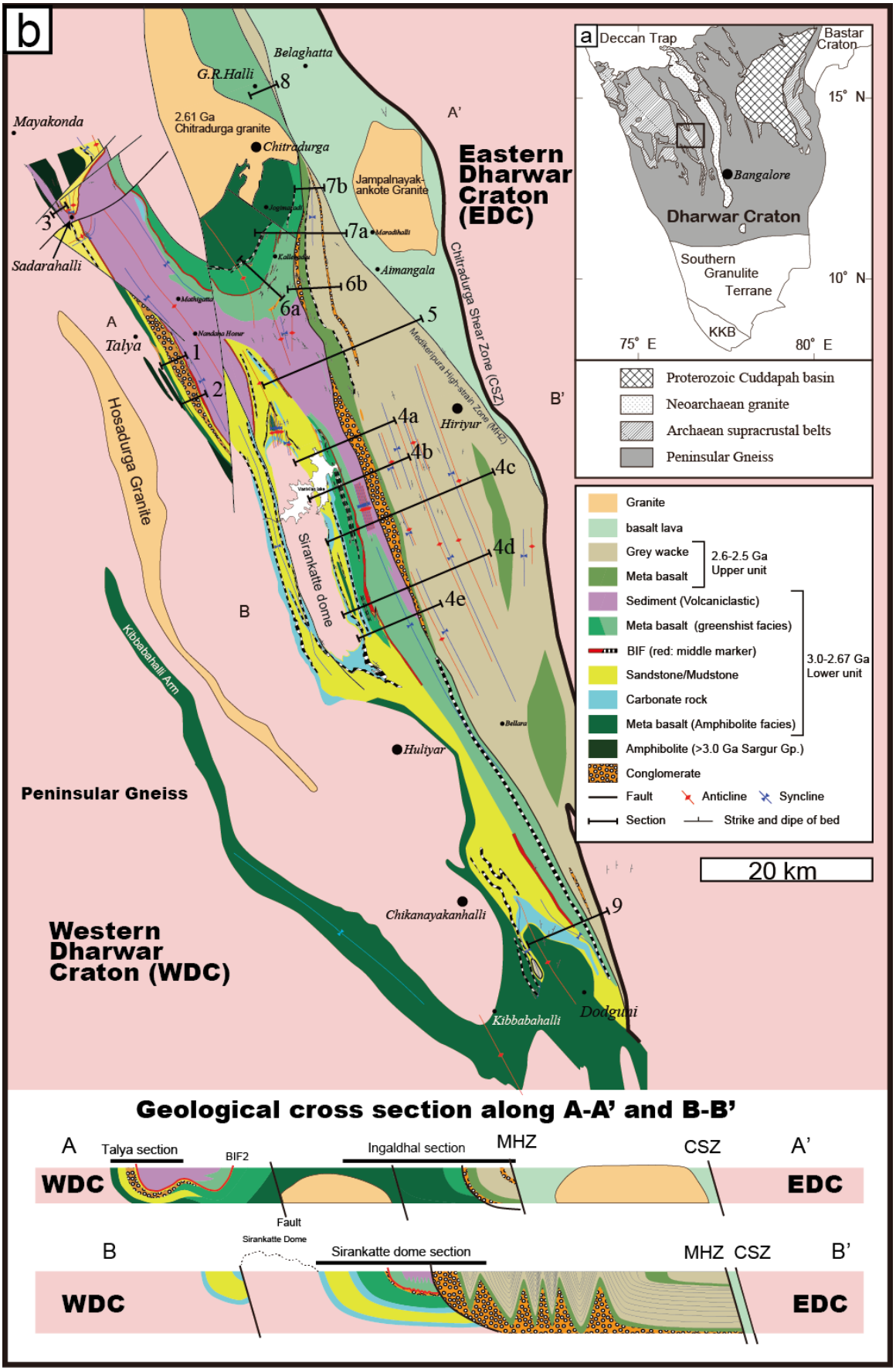

Fig. 2-1 Geologic map of the studied area, compiled from fieldwork carried out between 2010 and 2015, using enlarged aerial-photographs and topographic maps published by the Geological Survey of India,

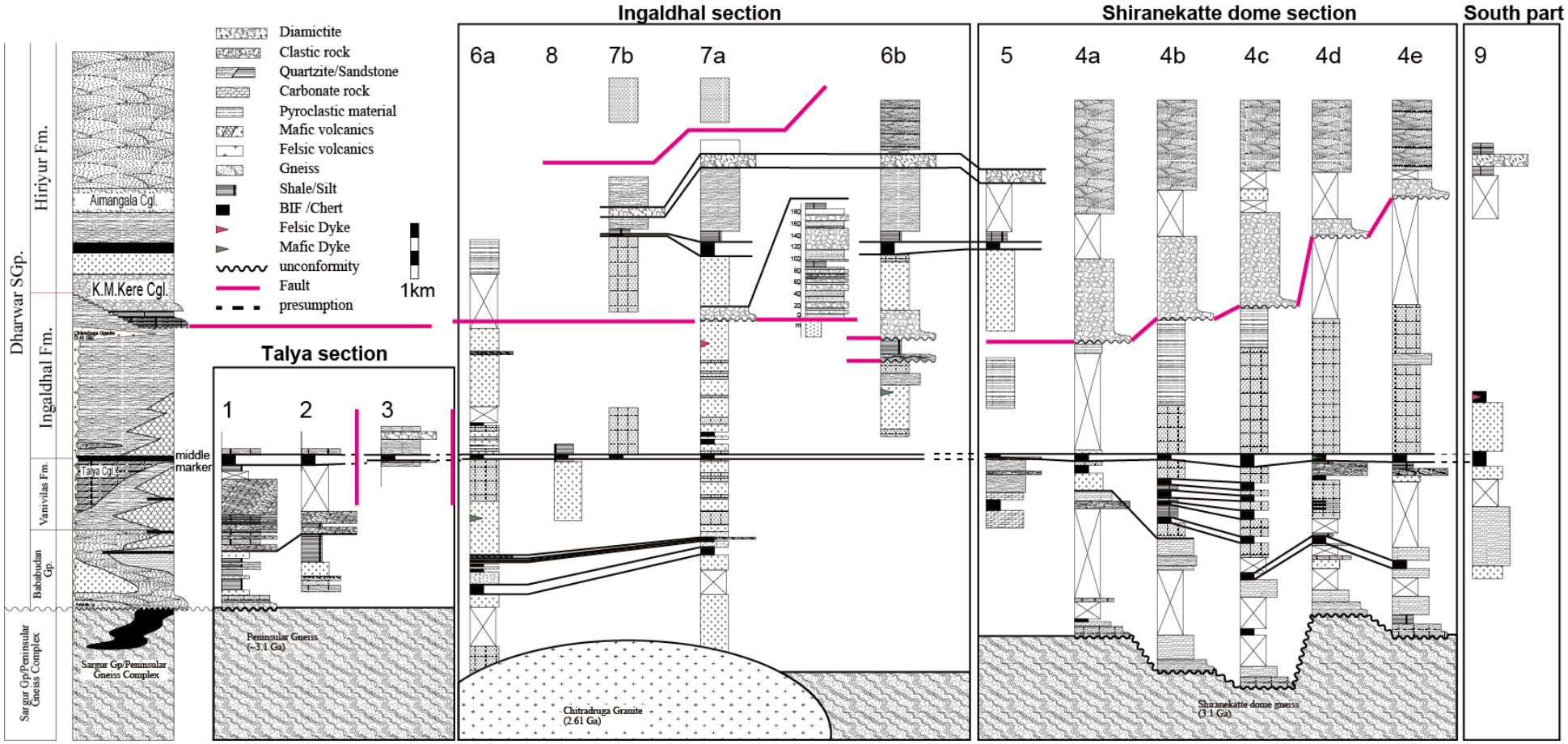

Fig. 2-2. Lithostratigraphic columns through the Dharwar Supergroup, compiled from logged sections, shown in Fig. 1-1.

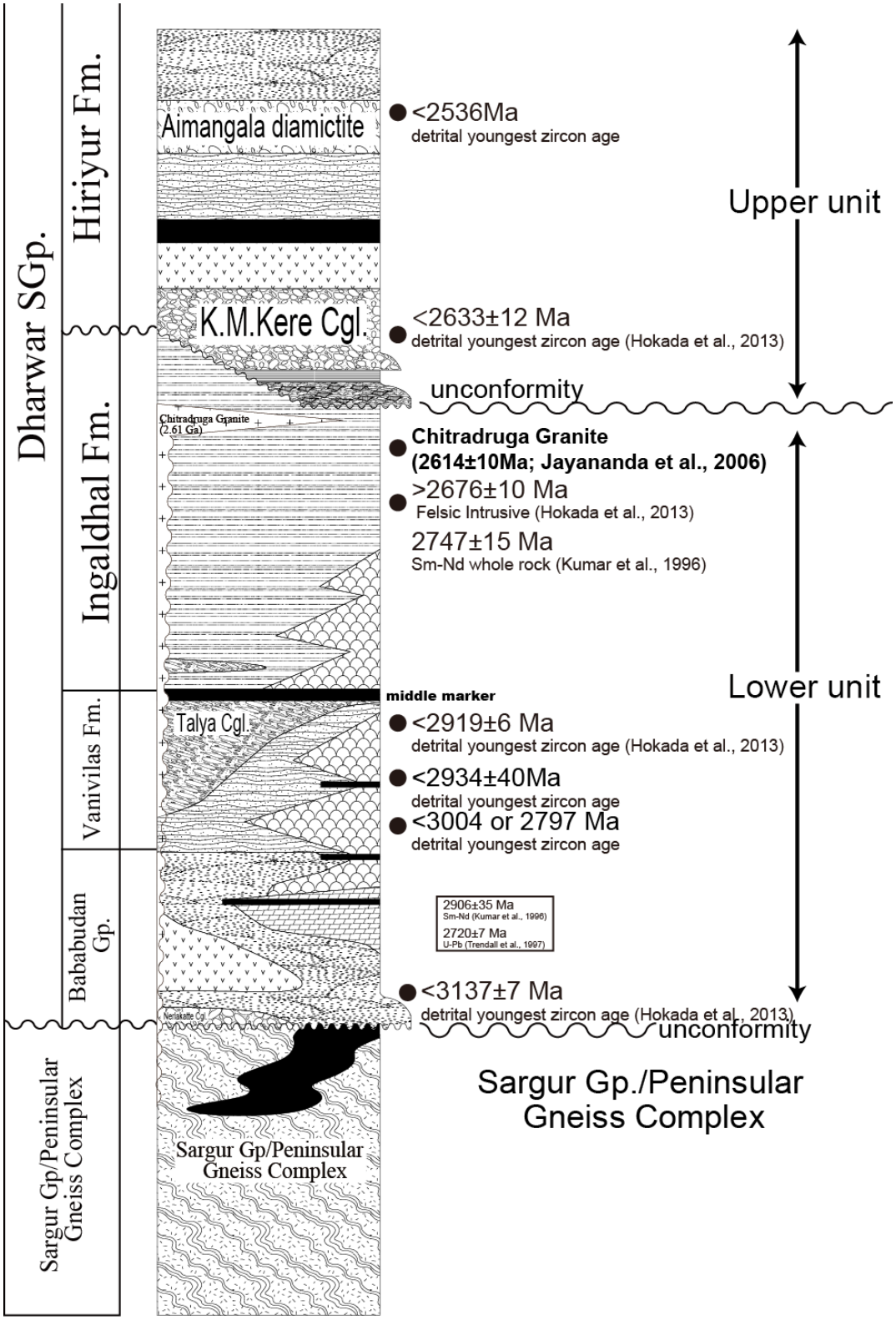

Fig. 2-3 Stratigraphic column of the Dharwar Supergroup as exposed in the Chitradurga Schist Belt. Compiled from mapping and the logged sections shown in Fig.1-2.

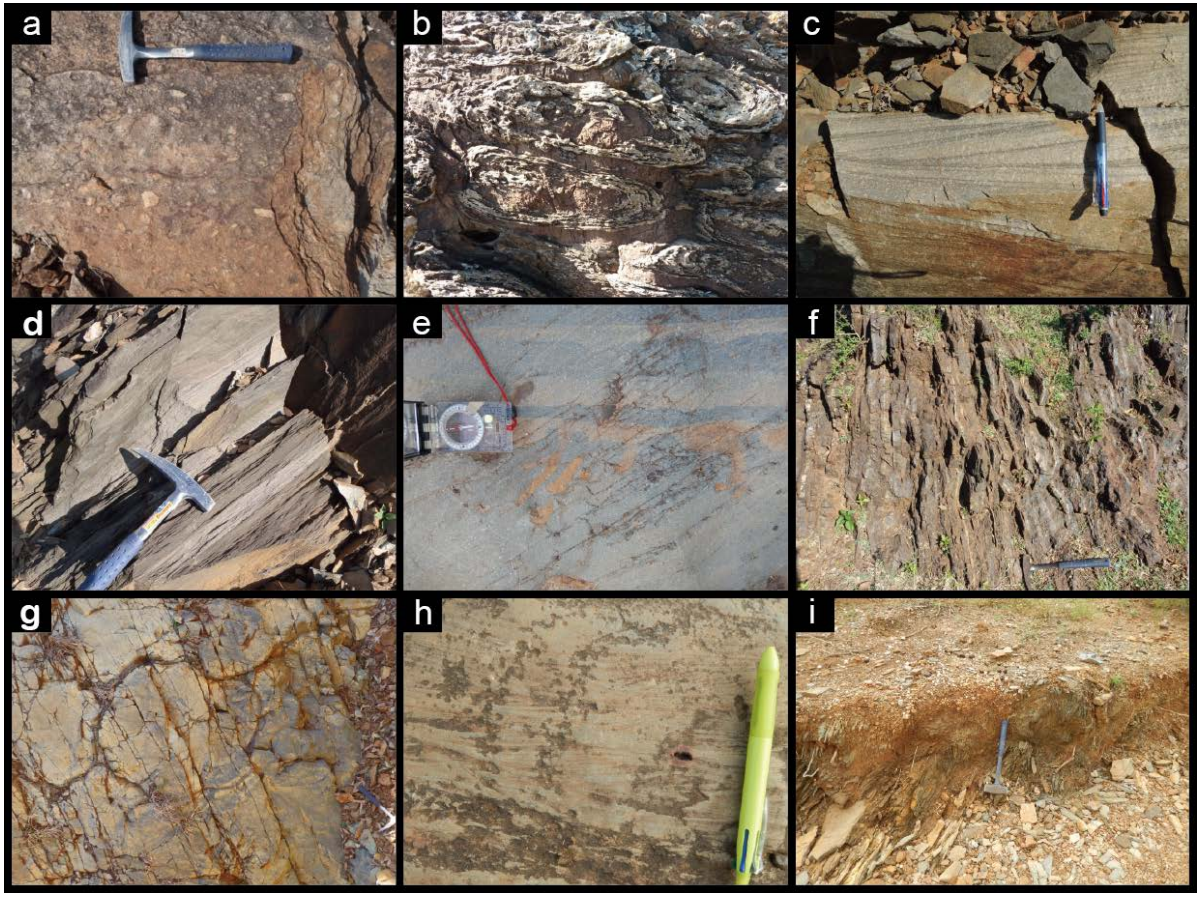

Fig. 2-4 Field photographs (a) Nerlakatte conglomerate which are basal conglomerate of Dharwar Supergroup (b) Dolostone with stromatolite texture (c) cross-laminated quartzite in Bababudan Group (d) mudstone in Lower Unit (e) Volacaniclastic sediments with flame structure (f) BIF (middle marker) (g) Typical pillow basalt (h) cross-laminated sandstone in Hiriyur Formation (i) series of tight folds in Hiriyur Formation

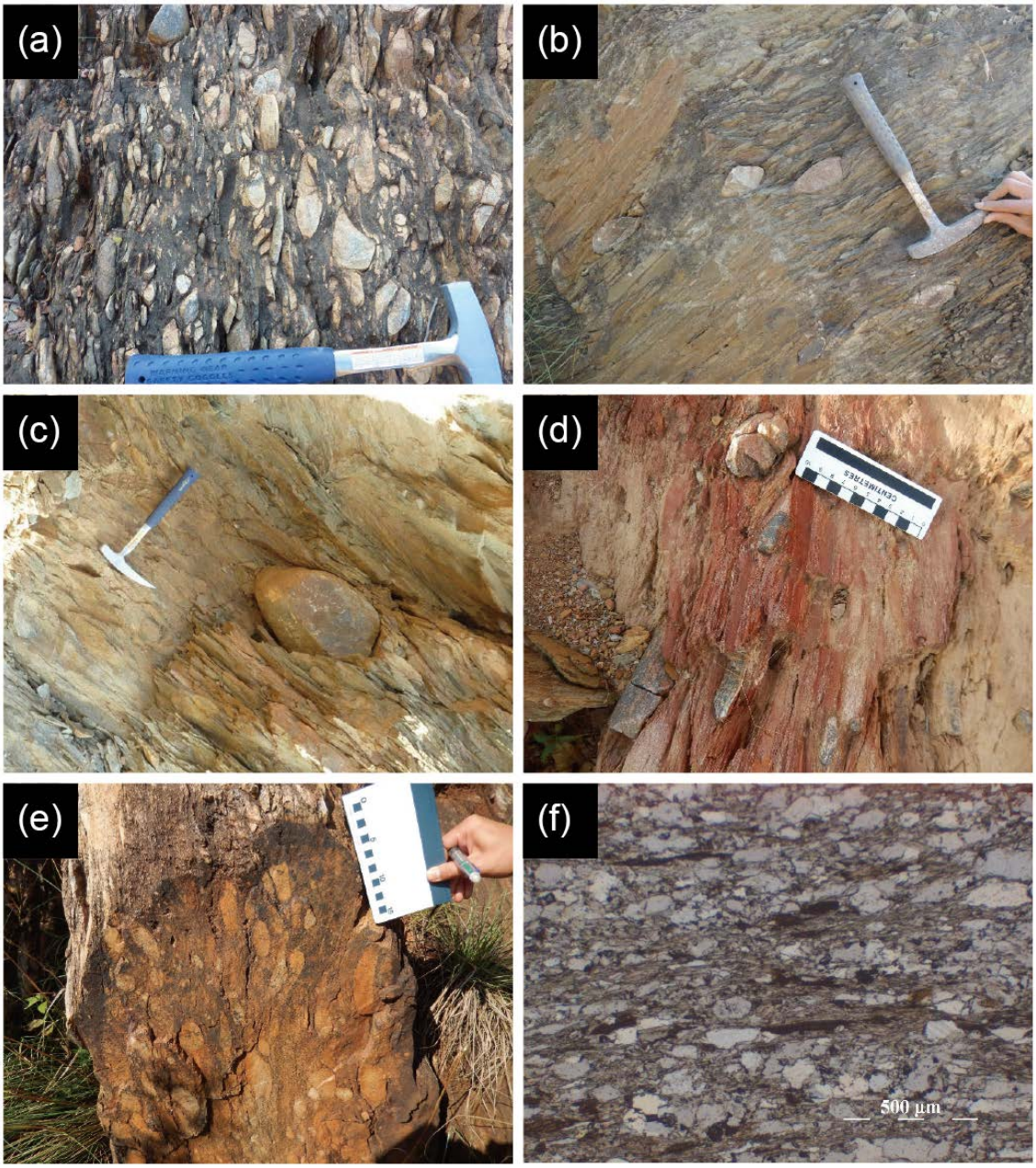

Fig. 2-5 Field photographs (a) typical Talya conglomerate in the western margin of the CSB (b) the conglomerate in the section 3 near Sadarahalli (c) Talya conglomerate along the Sirankatte dome (d) Talya conglomerate at Sirankatte dome north (e) Talya conglomerate north of CSB (f) photomicrograph of Talya conglomerate matrix.

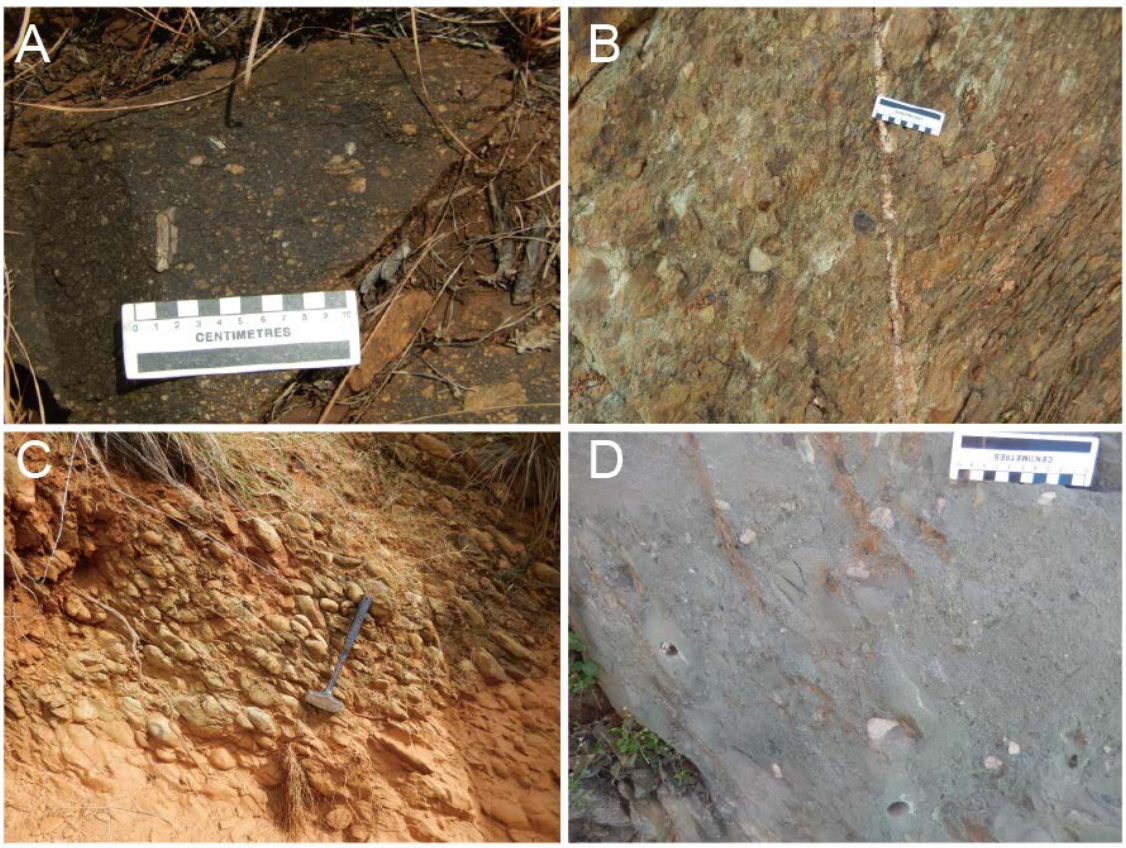

Fig. 2-6 Field photographs (A) breccia in the Ingaldhal suite (B) typical polymict conglomerate (K. M. Kere conglomerate) (c) K. M. Kere conglomerate dominated by rounded basalt clasts (d) Aimangala conglomerate

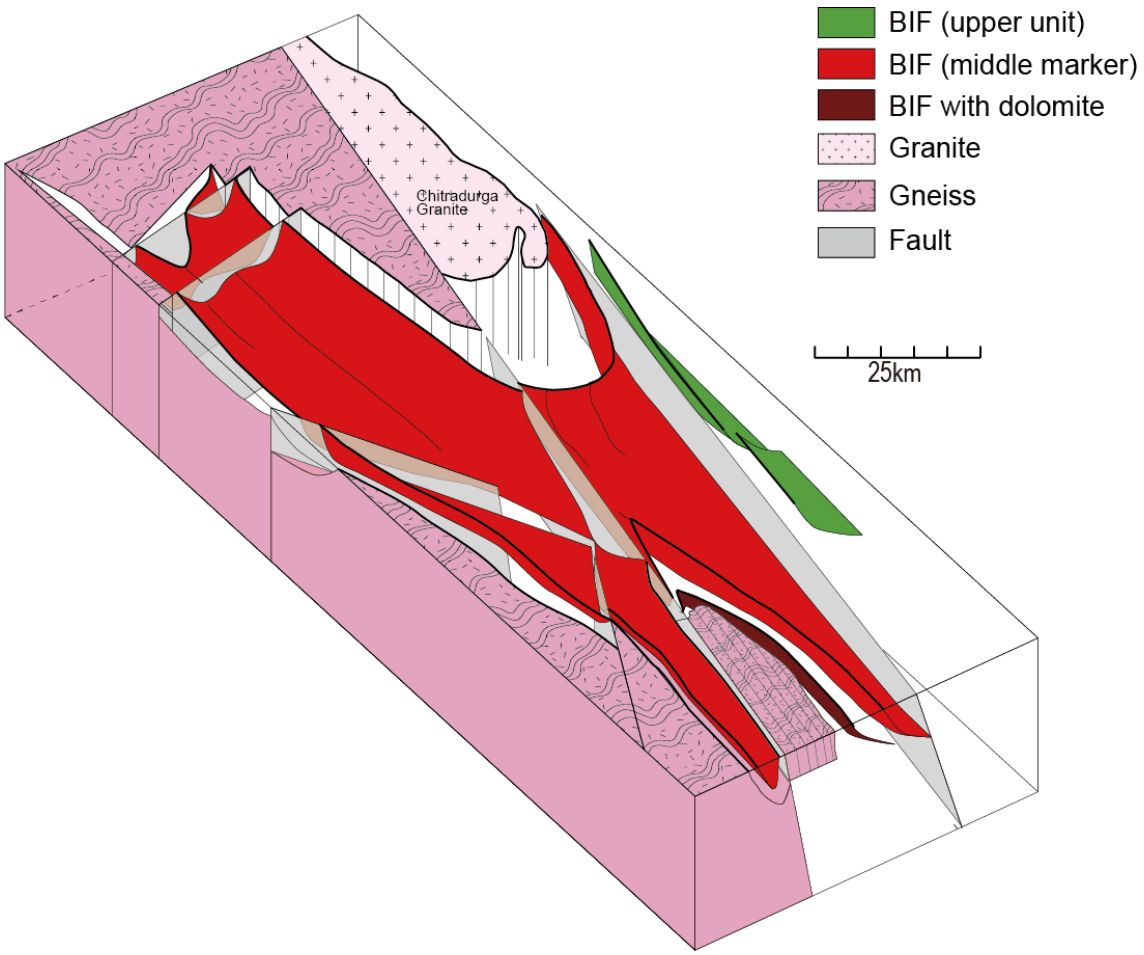

Fig. 2-7 Schematic representation of the Chitradurga structure to show spatial relations of the principal BIF markers (modified from Chadwick et al., 1981).

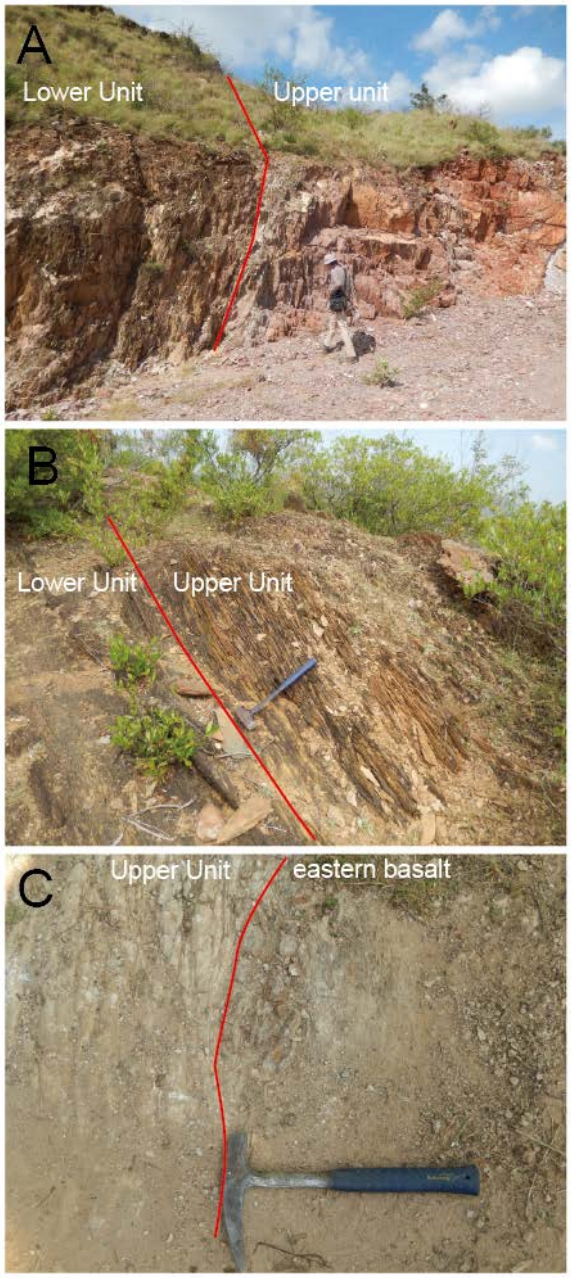

Fig. 2-8 Field photographs (A) (B) boundary of Upper unit and Lower unit (C) boundary of Upper unit and eastern basalt.

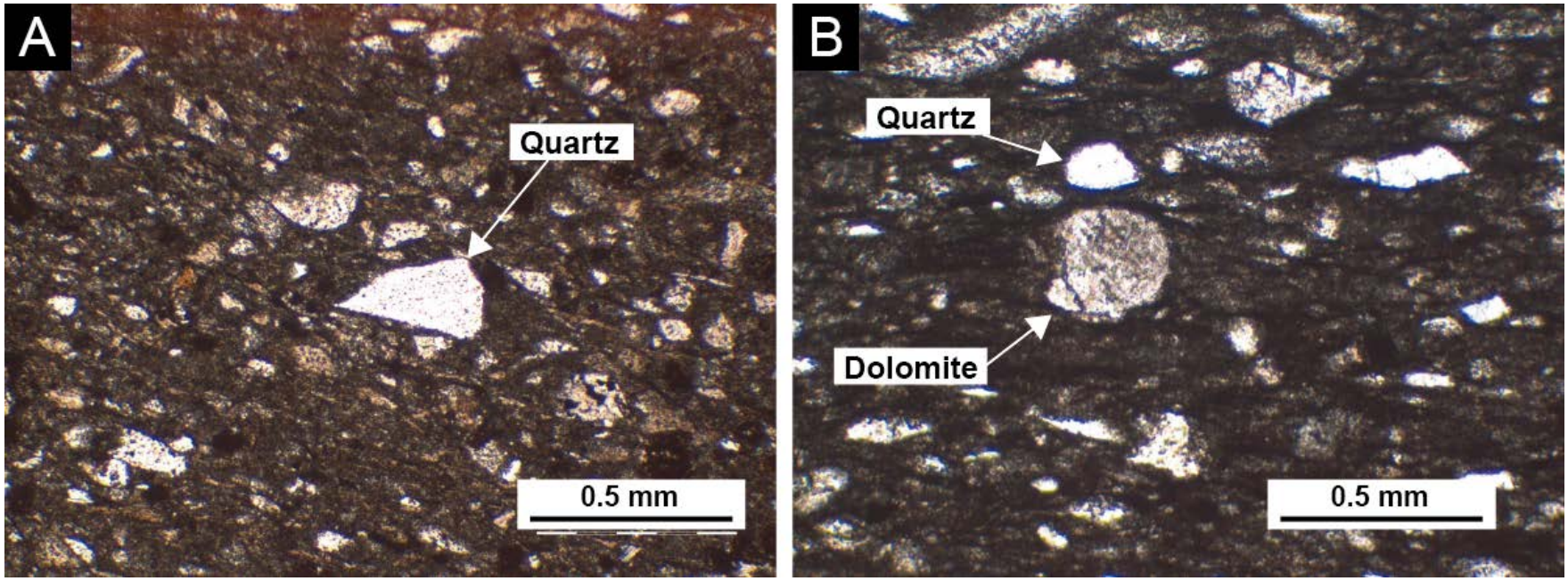

Fig. 2-9 Photomidrograph (A) volcaniclastic sediment in the central CSB, including glassy quartz (B) sandstone in the Upper Unit (Hiriyur Formation) including the rounded quartz and dolomite grain. This dolomite grain possibly come from lower unit.

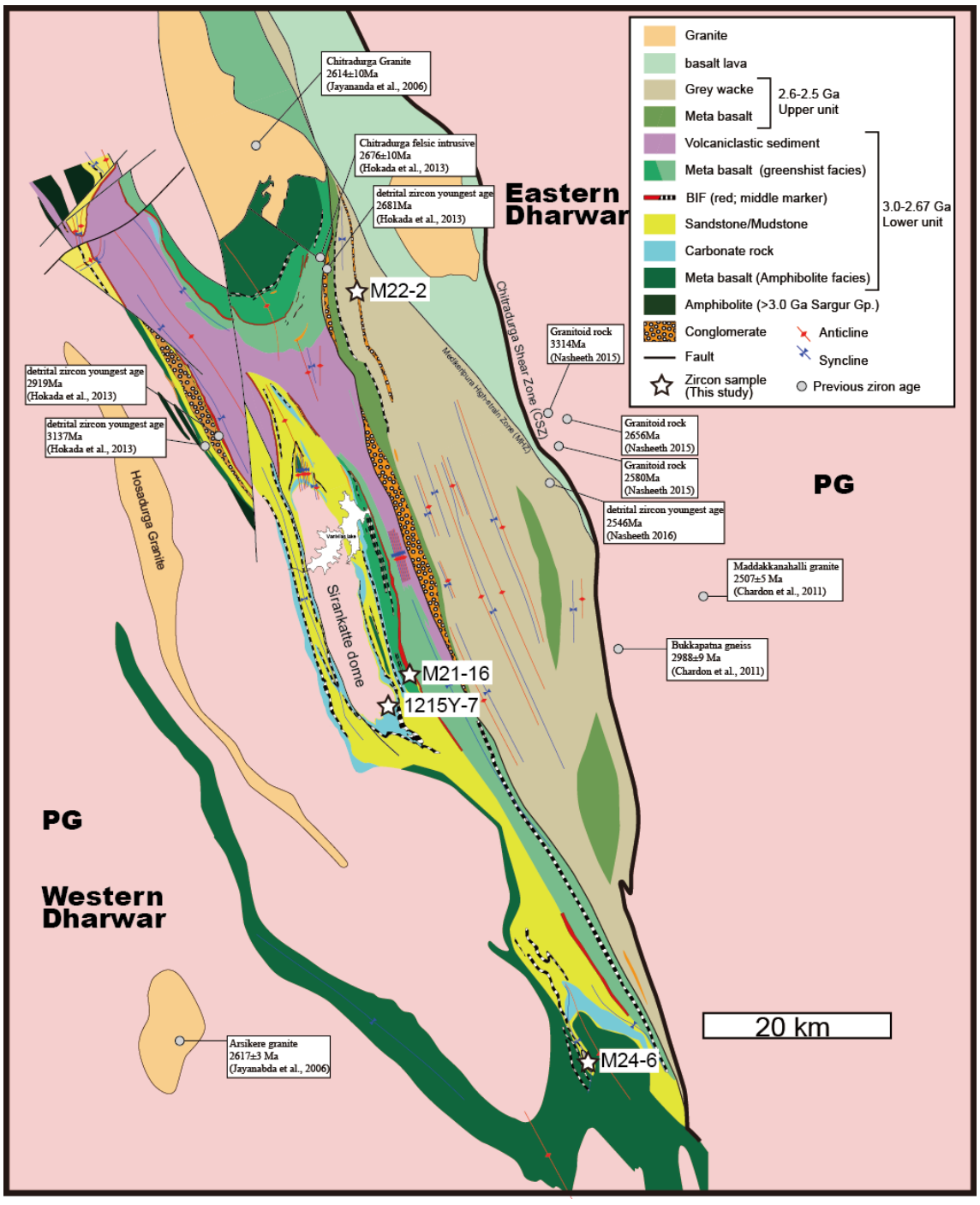

Fig. 2-10 Simplified geological sketch map of the Chitradurga Schist Belt. Stars and circles indicate the locations of the samples for which zircon ages were determined by ion microprobe and previou works, respectively.

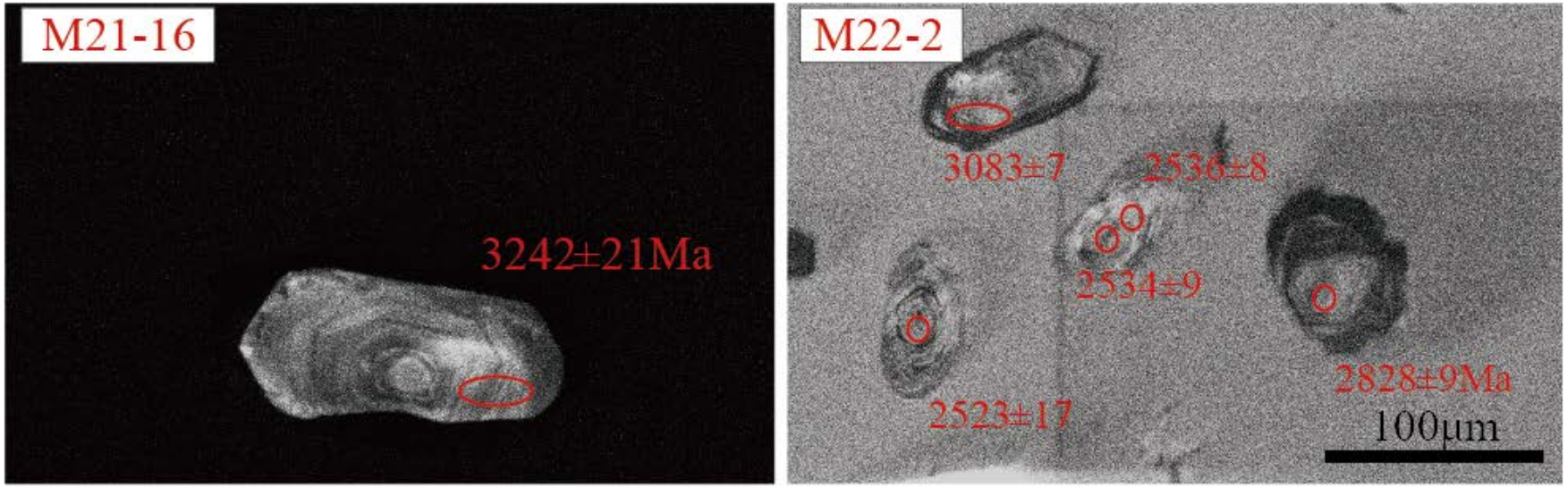

Fig. 2-11 (A) Cathodoluminescence image (CLI) of typical zircon grains in conglomerate matrix from the Lower and Upper Unit of Dharwar Supergroup. Zircons generally showed typical oscillatory zoning suggesting magmatic origin.

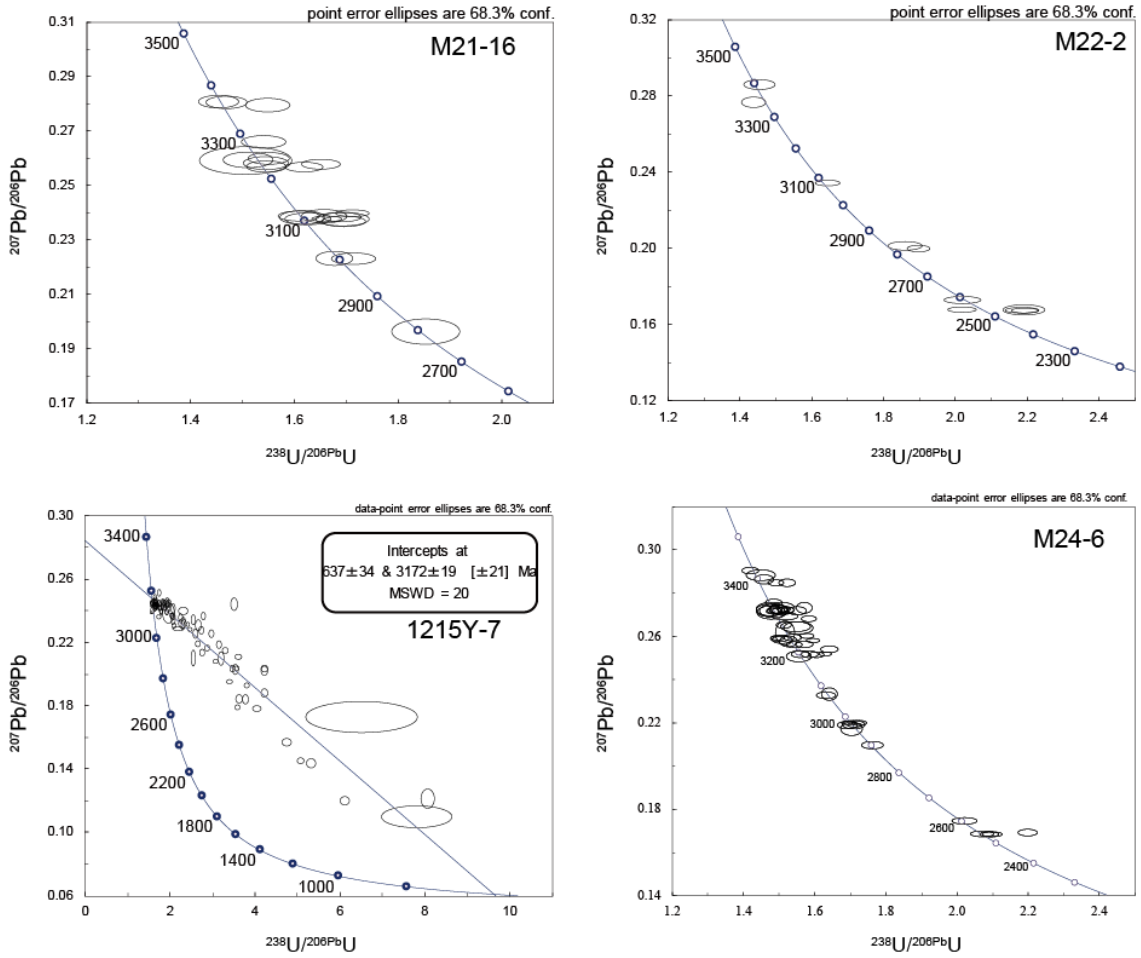

Fig. 2-12 Tera-Wasserburg concordia diagrams.

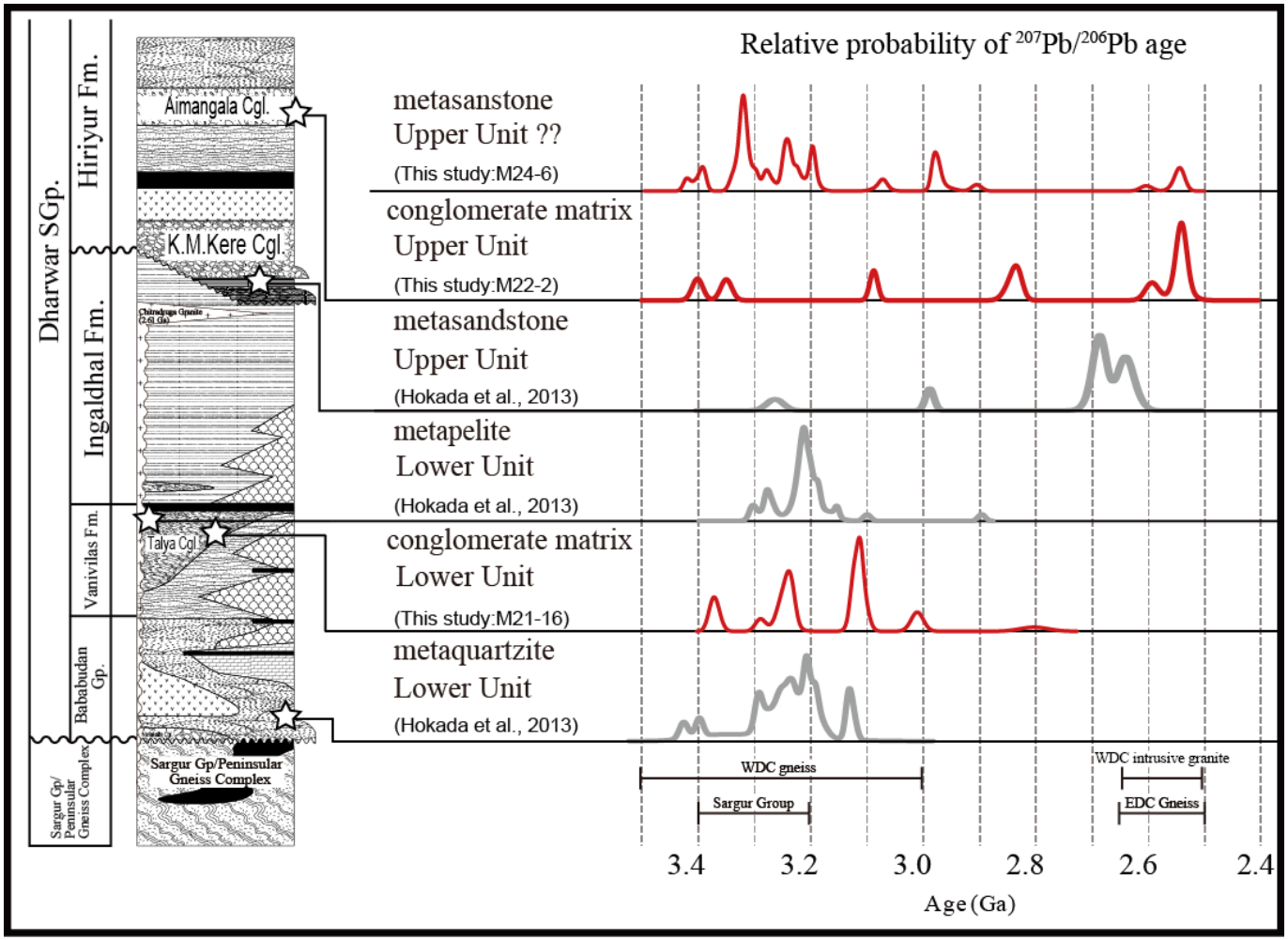

Fig. 2-13 probability density diagram of $^{207}Pb/^{206}Pb$ ages.

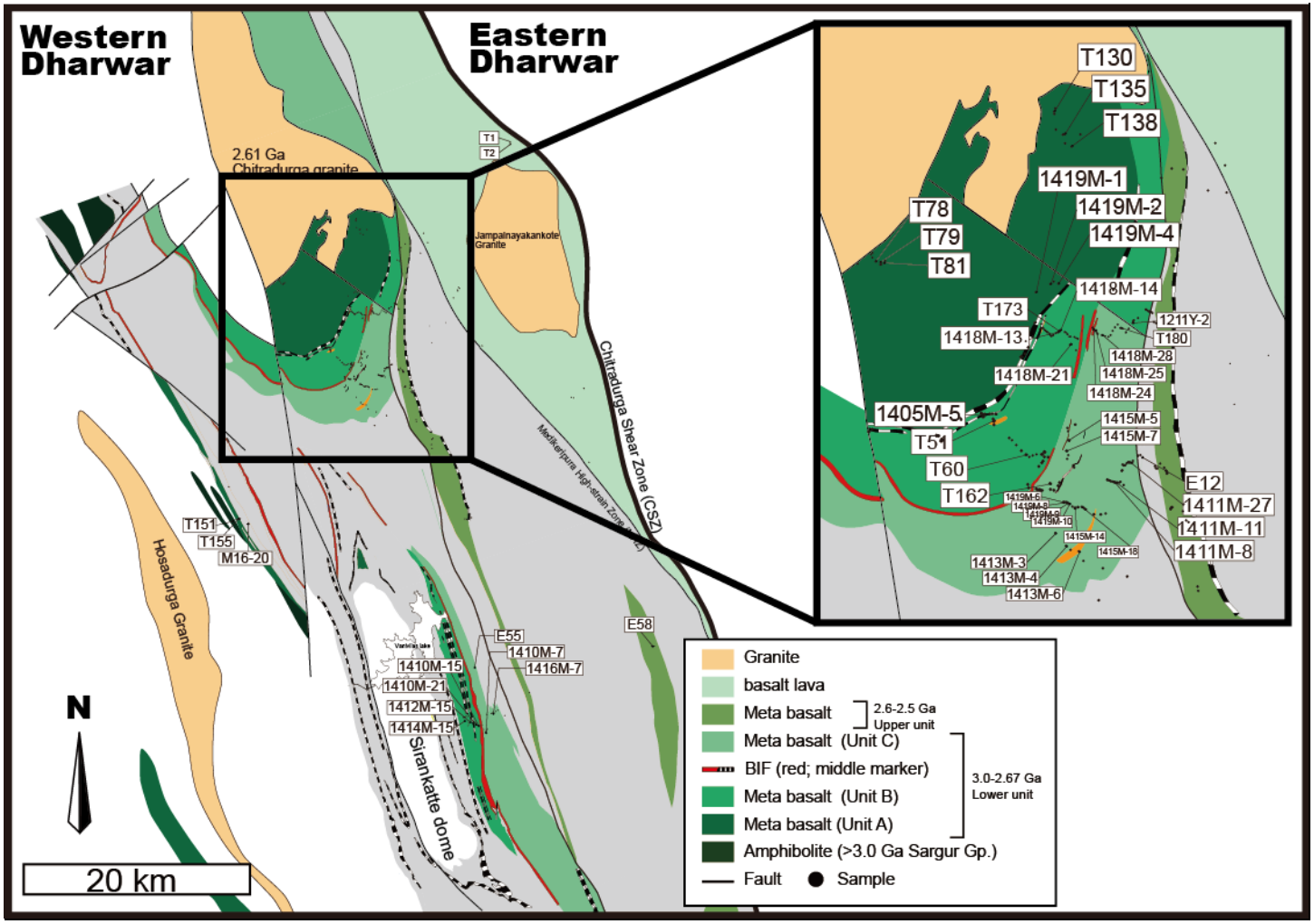

Fig. 2-14 Geological map of the Chitradurga Schist Belt and sample points.

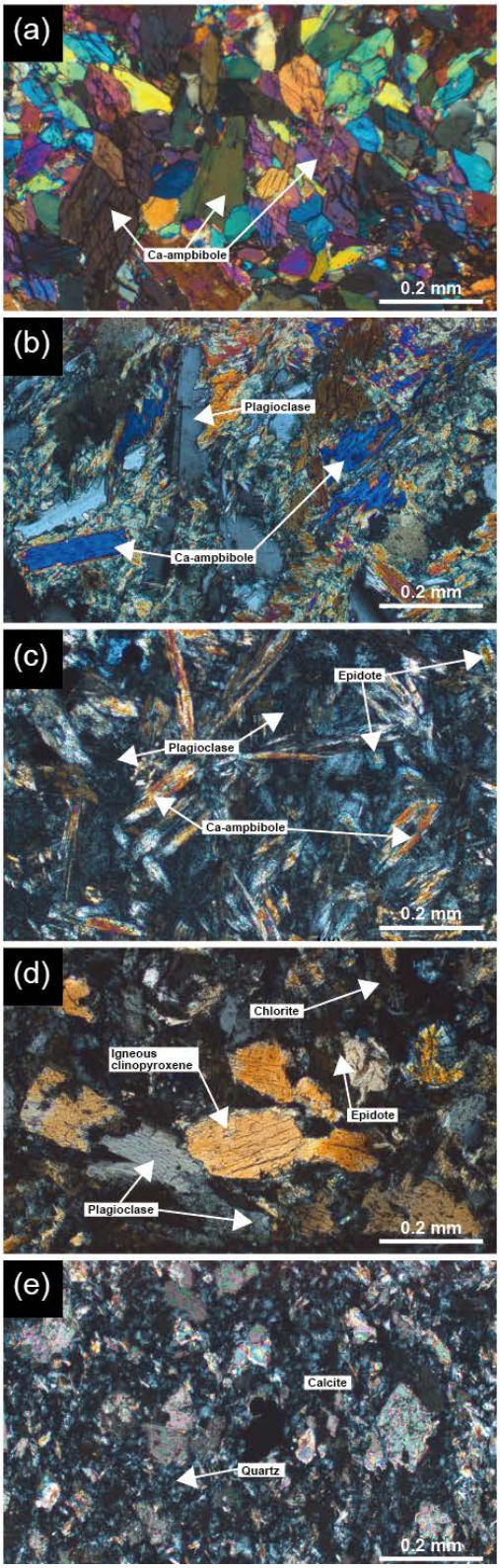

Fig. 2-15 Photomicrographs of greenstone (a) Amphibolite in Sargur Group (b) Unit A (c) Unit B (d) Unit C; Relict igneous clinopyroxene in a coarse-grained basaltic greenstone. (e) greenstones in upper Unit (Hiriyur Formation). The greenstones contain a lot of calcite coexisting with chlorite.

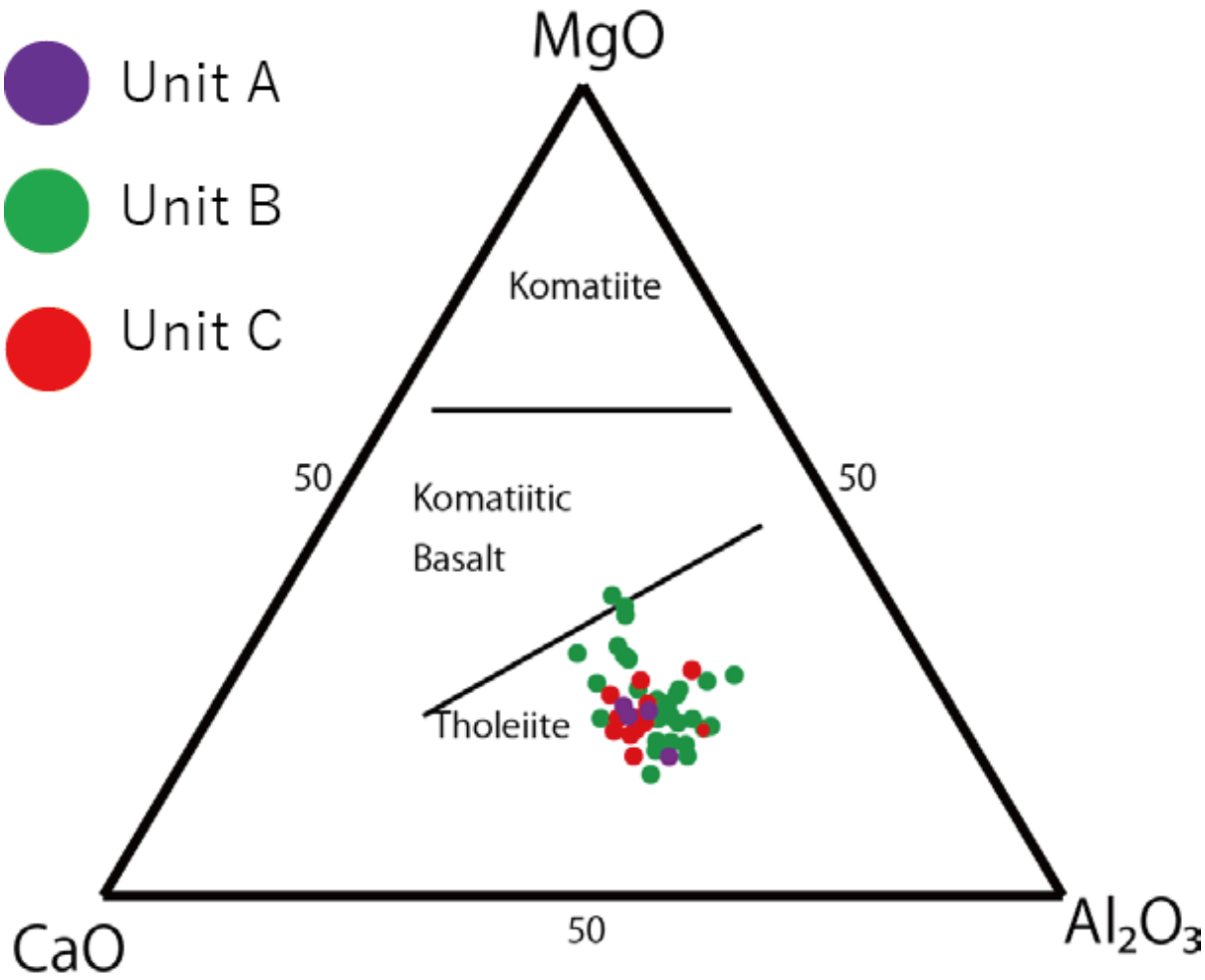

Fig. 2-16 Compositional variation of mafic colcanic rocks from Chitradurga Schist Belt, shown on diagram (Vijoen 1982).

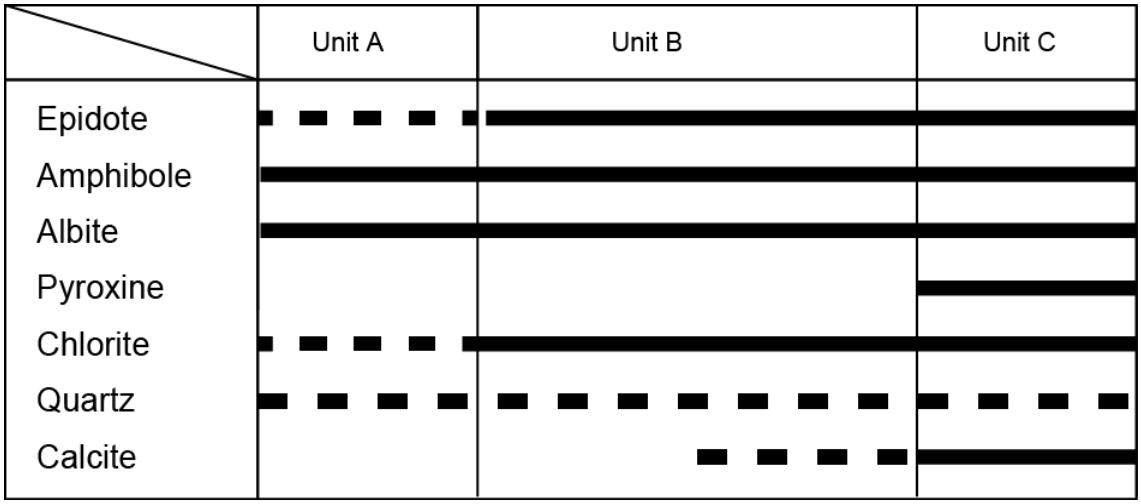

Fig. 2-17 Summary of the mineral parageneses in matrices and veins in the Chitradurga Schist belt.

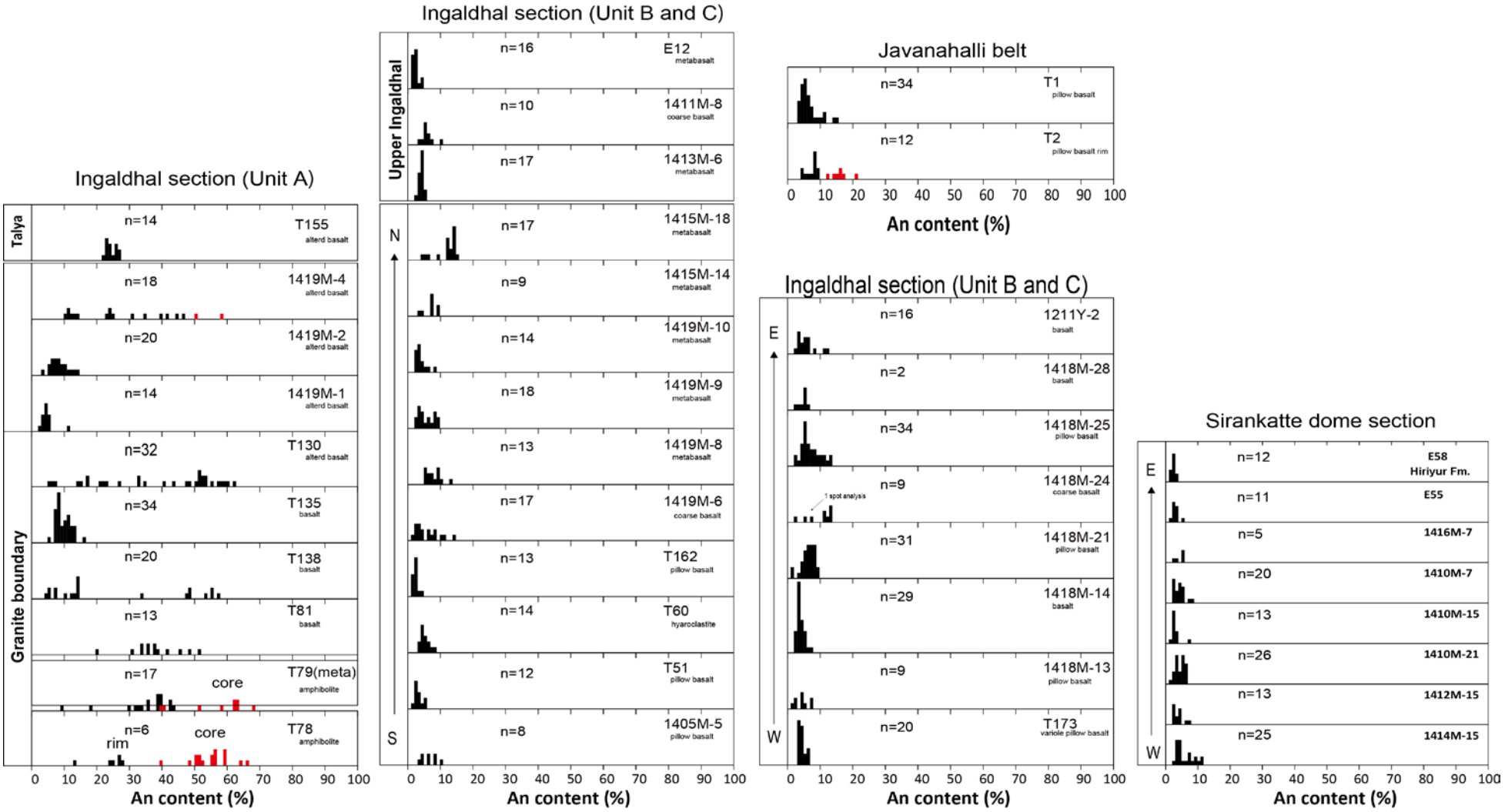

Fig. 2-18 Frequency diagrams of An content of secondary plagioclase in the Chitradurga Schist Belt.

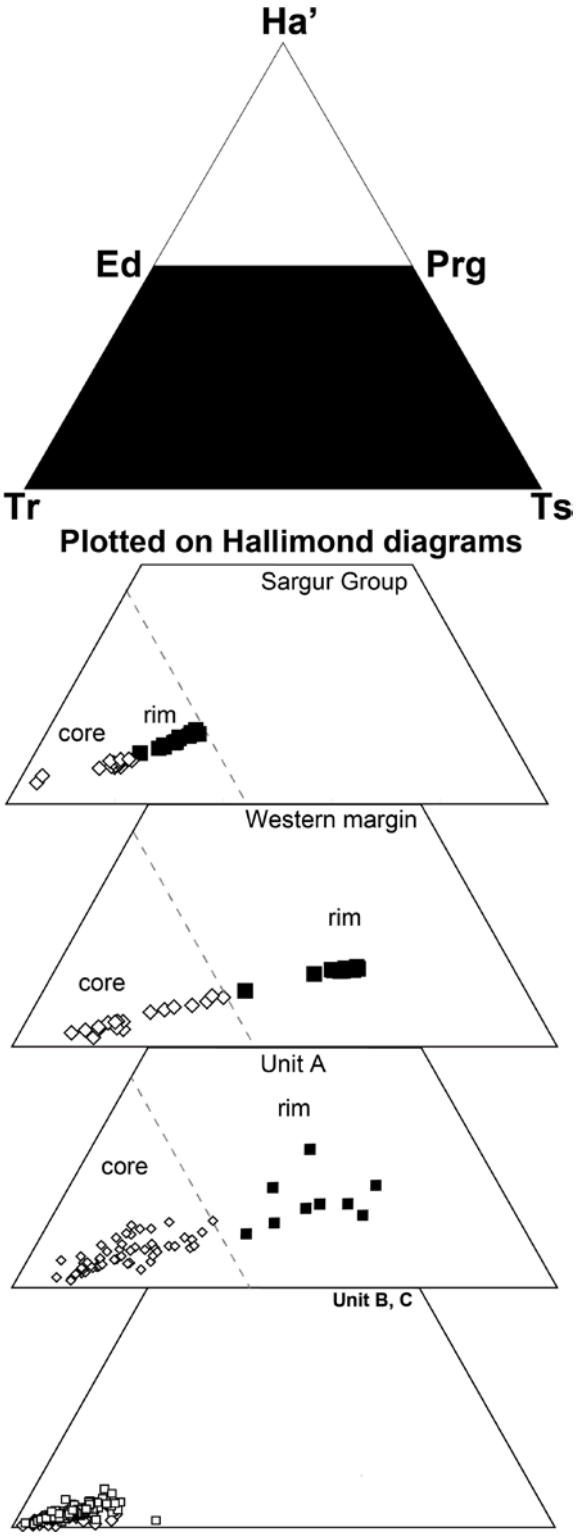

Fig. 2-19 Compositional variation of Ca-amphibolites in greenstones from Chitradurga Schist Belt, shown on quadrilateral diagram (Hallimond, 1943).

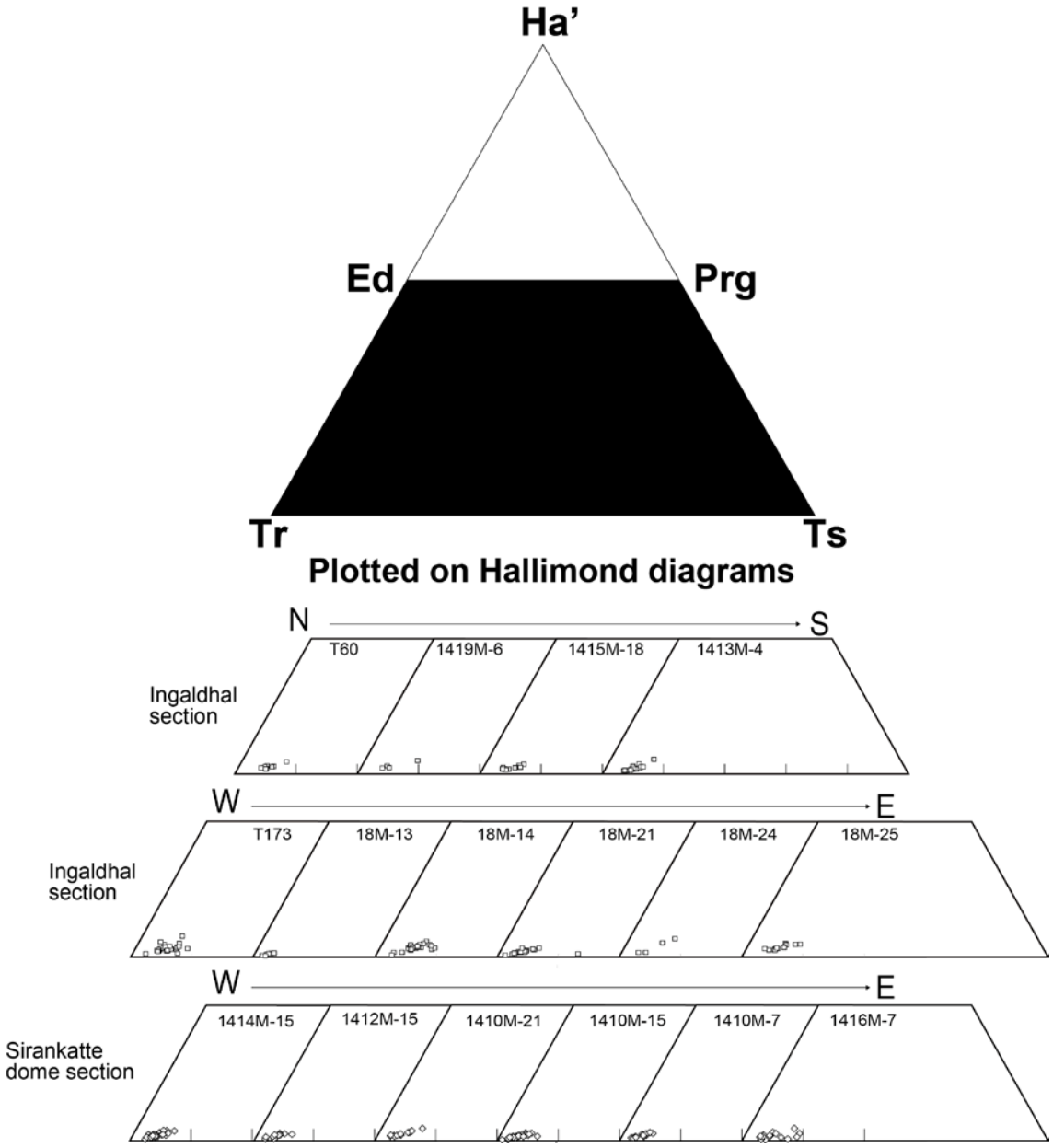

Fig. 2-20 Compositional variations of Ca-amphiboles in the Units B and C.

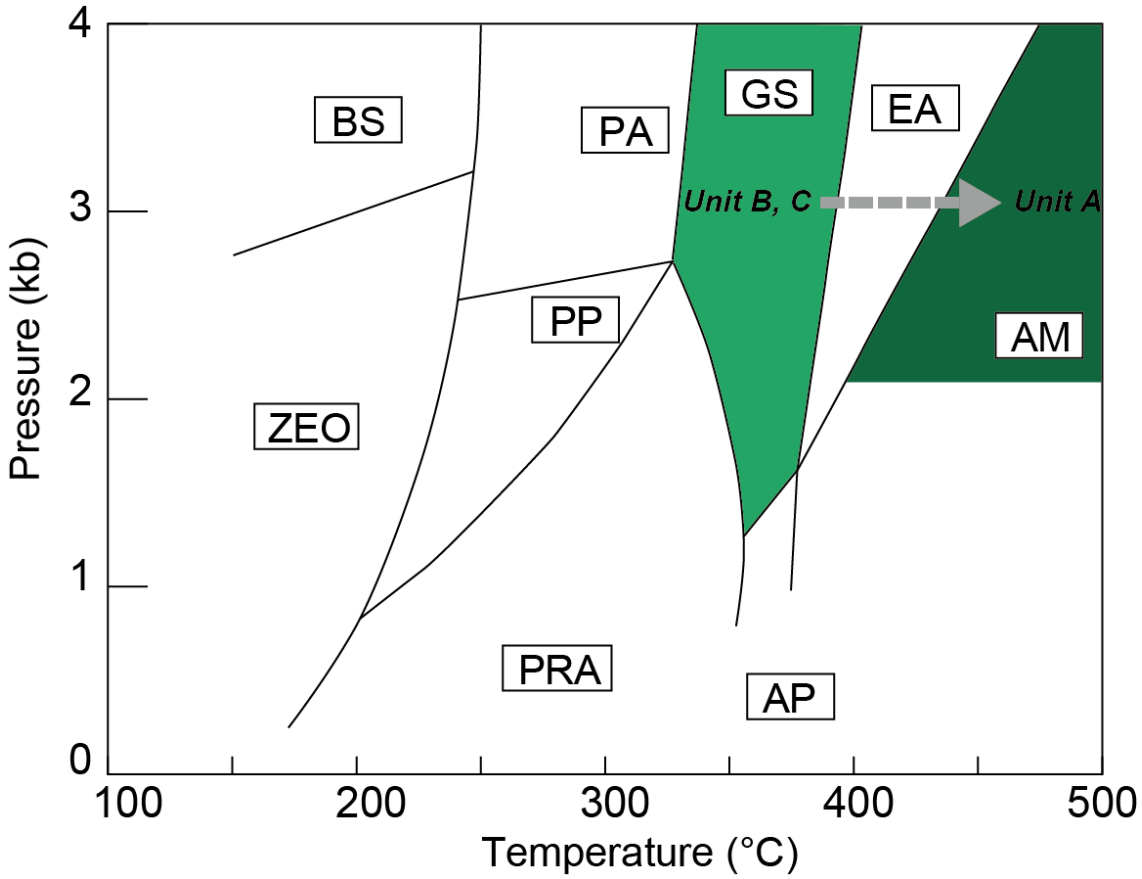

Fig. 2-21 A Pressure–temperature diagram of metamorphic reactions and metamorphic facies, modified after Liou et al. (1985)

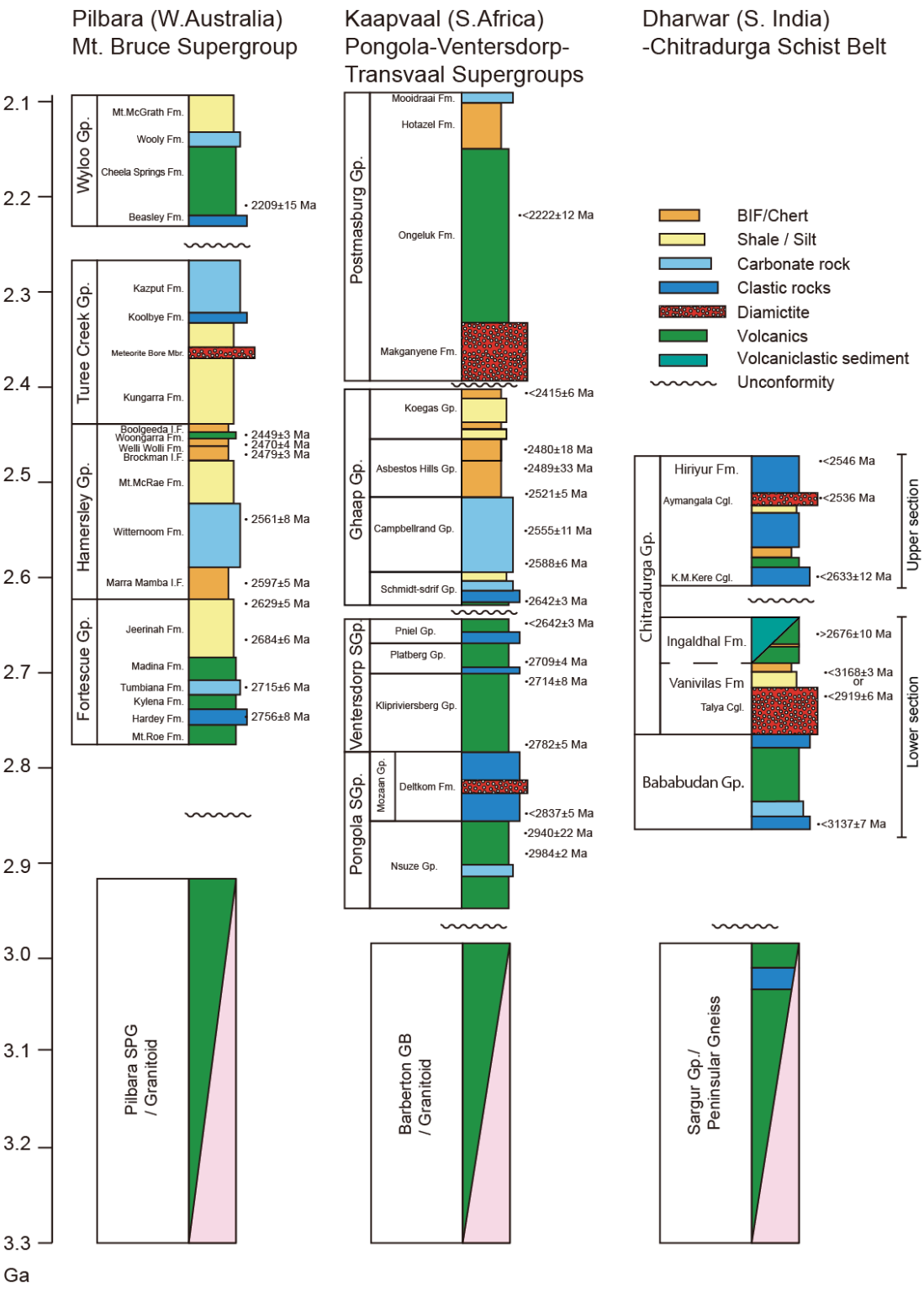

Fig. 2-22 Stratigraphic section of Chitradurga Schist Belt in Dharwar Craton compared with those of Pilbara Craton in Western Australia and Kaapvaal Craton in S. Africa (Cornell et al., 1996; Gutzmer et al., 1999; Nelson et al., 1999; Lindsay et al., 2003).

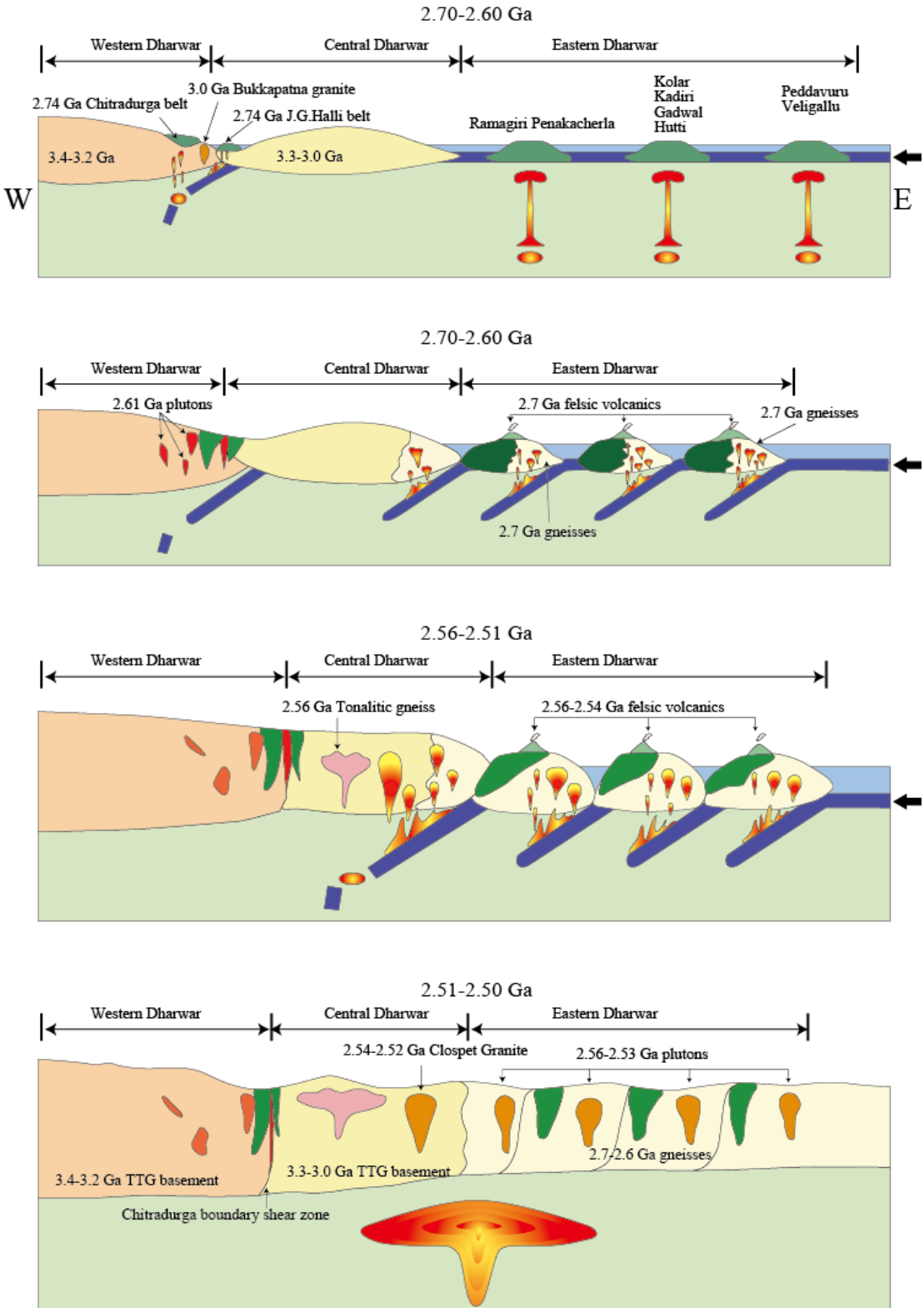

Fig. 2-23 Cartoon depicting a possible tectonic evolutionary model of the Western, central, and Eastern Dharwar cratons (after Jayananda et al., 2013).

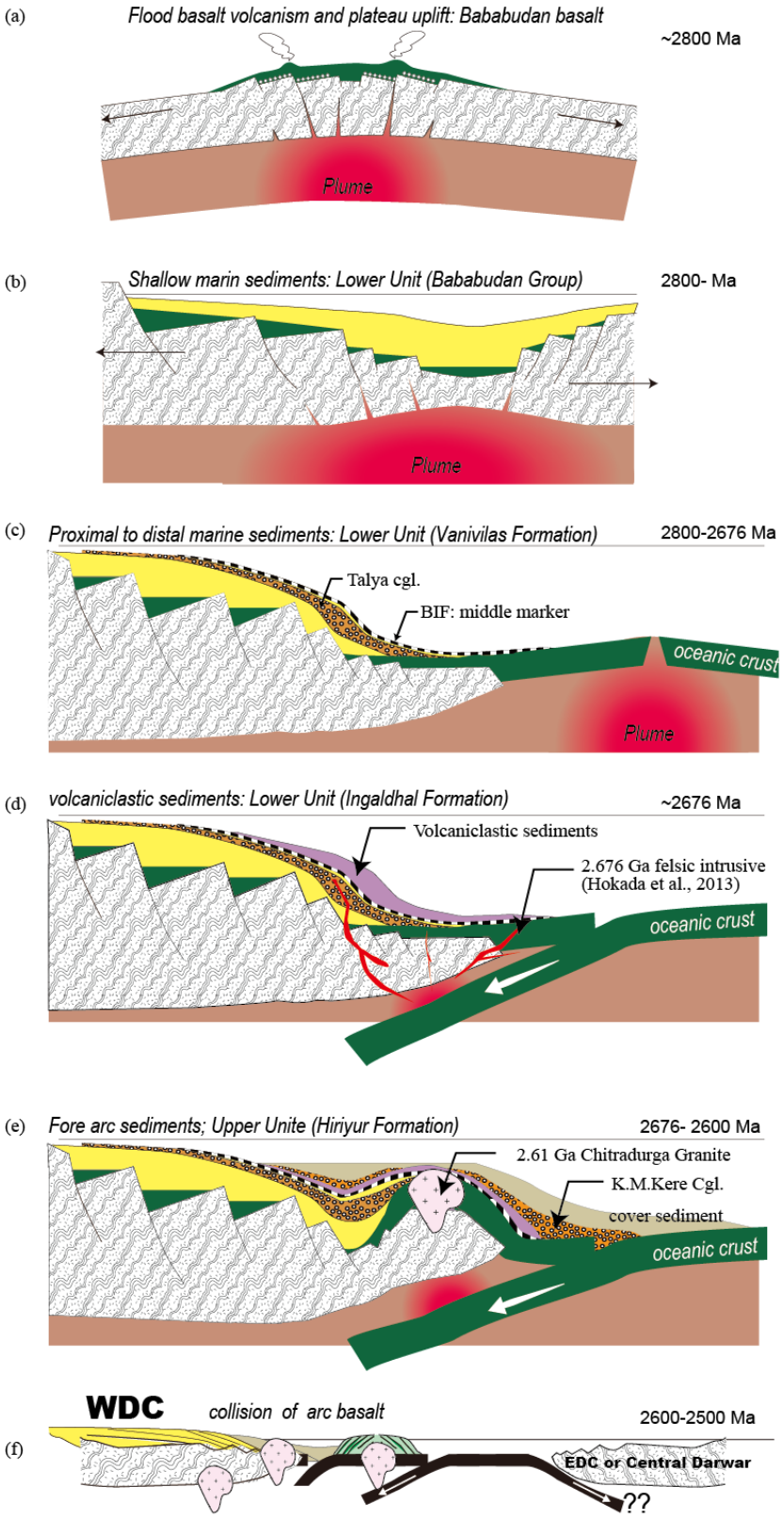

Fig. 2-24 (a–f) Cartoon showing the proposed tectonic model for 2.8–2.5 Ga greenstone volcanism in the Chitradurga Schist Belt.

Table 1.

Representative analyses of plagioclase from examined samples

Unit	A	A	A	A	B	B	B	B	C	C	C	C	C	C
Sp. No.	T130	T81	T79	T155	T51	T60	1418M-14	1418M-21	1418M-24	1211Y-2	T162	1419M-10	1415M-18	E12
Lithology	Lava	Lava	Lava	Lava	Lava	Lava	Lava	Lava	Lava	Lava	Lava	Lava	Lava	Lava
SiO_2	62.39	59.76	57.98	63.74	67.54	67.58	69.21	67.82	65.30	66.87	68.73	69.43	64.39	68.69
TiO_2	0.09	0.01	0.01	0.00	0.01	0.03	0.00	0.04	0.00	0.06	0.00	0.00	0.00	0.06
Al_2O_3	23.26	25.12	26.62	23.24	20.12	20.16	19.77	20.16	21.57	20.04	19.99	19.44	22.12	19.26
FeO	0.61	0.37	0.13	0.32	0.10	0.13	0.18	0.20	0.34	0.56	0.17	0.27	0.15	0.27
MnO	0.00	0.03	0.02	0.04	0.00	0.01	0.00	0.01	0.00	0.00	0.00	0.00	0.00	0.00
MgO	0.01	0.00	0.01	0.00	0.00	0.03	0.02	0.00	0.02	0.19	0.00	0.00	0.02	0.00
CaO	4.54	6.36	8.72	4.43	0.80	0.70	0.35	1.28	2.62	1.04	0.68	0.44	3.11	0.24
Na_2O	8.96	7.84	6.52	8.23	11.47	10.98	10.51	10.35	10.22	10.54	11.14	10.40	9.77	11.78
K_2O	0.04	0.05	0.06	0.04	0.06	0.42	0.03	0.16	0.06	0.07	0.02	0.03	0.07	0.03
Total	99.89	99.53	100.06	100.04	100.09	100.03	100.07	100.01	100.15	99.37	100.73	100.00	99.63	100.33
Si	2.70	2.67	2.59	2.81	2.96	2.96	3.00	2.96	2.87	2.95	2.98	3.02	2.85	2.99
Ti	0.00	0.00	0.00	0.00	0.00	0.00	0.00	0.00	0.00	0.00	0.00	0.00	0.00	0.00
Al	1.35	1.33	1.40	1.21	1.04	1.04	1.01	1.04	1.12	1.04	1.02	1.00	1.15	0.99
Fe	0.05	0.01	0.00	0.01	0.00	0.00	0.01	0.01	0.01	0.02	0.01	0.01	0.01	0.01
Mn	0.00	0.00	0.00	0.00	0.00	0.00	0.00	0.00	0.00	0.00	0.00	0.00	0.00	0.00
Mg	0.02	0.00	0.00	0.00	0.00	0.00	0.00	0.00	0.00	0.01	0.00	0.00	0.00	0.00
Ca	0.17	0.31	0.42	0.21	0.04	0.03	0.02	0.06	0.12	0.05	0.03	0.02	0.15	0.01
Na	0.55	0.68	0.57	0.70	0.97	0.93	0.89	0.88	0.87	0.90	0.94	0.88	0.84	1.00
K	0.09	0.00	0.00	0.00	0.00	0.02	0.00	0.01	0.00	0.00	0.00	0.00	0.00	0.00
Total	4.93	5.00	4.99	4.94	5.01	5.00	4.93	4.95	5.00	4.98	4.98	4.92	5.00	5.00
X An	23.05	30.96	42.50	22.94	3.70	3.41	1.79	6.41	12.40	5.14	3.27	2.27	14.98	1.09

Total Fe as Fe^{3+} and Fe^{2+}

Table 2.

Representative analyses of calcic amphibole from examined samples

Unit	Sargur	A	A	A	A	B	B	B	B	C	C	C	C	C
Sp. No.	T151	T130	T81	T79	T155	T51	T60	1418M-14	1418M-21	1418M-24	1211Y-2	1419M-10	1415M-18	E12
Mineral	Hbl	Hbl	Hbl	Hbl	Hbl	Act	Act	Act	Act	Act	Act	Act	Act	Act
Lithology	Lava	Lava	Lava	Lava	Lava	Lava	Lava	Lava	Lava	Lava	Lava	Lava	Lava	Lava
SiO_2	48.70	48.40	49.43	42.70	48.44	51.54	47.73	55.47	54.82	52.01	55.30	52.70	53.91	53.11
TiO_2	0.64	0.31	0.22	0.22	0.28	0.14	9.84	0.01	0.04	0.08	0.05	0.08	0.05	0.15
Al_2O_3	7.51	7.37	5.89	15.15	7.96	3.64	2.20	2.58	1.45	2.81	0.91	0.54	2.89	2.92
FeO	11.67	18.39	19.37	18.58	16.22	19.01	8.80	10.91	10.12	18.52	12.57	10.43	14.13	16.47
MnO	0.18	0.28	0.22	0.25	0.25	0.40	0.14	0.18	0.25	0.27	0.25	0.31	0.26	0.18
MgO	14.57	10.35	12.30	7.10	11.75	11.46	12.12	16.06	15.89	11.54	16.15	12.40	14.04	13.39
CaO	11.27	11.16	8.71	11.55	11.18	11.48	15.97	12.43	14.21	12.27	11.92	21.80	12.09	11.26
Na_2O	1.34	0.87	0.67	1.20	0.78	0.35	0.14	0.19	0.14	0.38	0.07	0.04	0.18	0.54
K_2O	0.44	0.19	0.06	0.47	0.19	0.16	0.13	0.10	0.06	0.07	0.05	0.00	0.08	0.04
Total	96.95	97.42	97.07	97.23	97.24	98.22	98.01	98.04	97.16	97.98	97.42	98.35	97.71	98.26
Si	7.06	7.12	7.04	6.38	7.05	7.51	6.99	7.86	7.88	7.66	7.88	7.70	7.76	7.62
Al(IV)	0.94	0.88	0.96	1.62	0.95	0.49	0.38	0.14	0.12	0.34	0.12	0.09	0.24	0.38
Al(VI)	0.34	0.40	0.03	1.04	0.41	0.13	0.00	0.29	0.12	0.14	0.04	0.00	0.25	0.12
Ti	0.07	0.03	0.02	0.03	0.03	0.02	1.08	0.00	0.00	0.01	0.01	0.01	0.00	0.02
Fe3+	0.50	0.61	2.03	0.40	0.74	0.62	0.00	0.00	0.00	0.19	0.40	0.00	0.19	0.60
Fe2+	0.92	1.65	0.28	1.92	1.24	1.69	1.08	1.29	1.22	2.09	1.09	1.28	1.51	1.38
Mn	0.02	0.03	0.03	0.03	0.03	0.05	0.02	0.02	0.03	0.03	0.03	0.04	0.03	0.02
Mg	3.15	2.27	2.61	1.58	2.55	2.49	2.65	3.39	3.40	2.53	3.43	2.70	3.01	2.87
Ca	1.75	1.76	1.33	1.85	1.74	1.79	2.51	1.89	2.19	1.94	1.82	3.42	1.86	1.73
Na(M4)	0.25	0.24	0.19	0.15	0.22	0.10	0.00	0.05	0.00	0.06	0.02	0.00	0.05	0.15
Na(A)	0.13	0.01	0.00	0.20	0.00	0.00	0.04	0.00	0.04	0.04	0.00	0.01	0.00	0.00
K	0.08	0.04	0.01	0.09	0.03	0.03	0.02	0.02	0.01	0.01	0.01	0.00	0.01	0.01
Total	15.21	15.04	14.53	15.28	15.00	14.92	14.77	14.96	15.02	15.06	14.85	15.25	14.93	14.89
Mg#	0.77	0.58	0.90	0.45	0.67	0.60	0.71	0.72	0.74	0.55	0.76	0.68	0.67	0.68
Ha'	15.54	10.83	8.15	14.60	9.71	4.63	2.01	2.53	1.90	5.12	0.96	0.55	2.49	6.94
Tr	55.86	59.66	66.04	28.07	58.51	80.01	89.06	86.83	92.22	83.15	95.16	97.38	85.40	80.63
Ts	26.38	28.02	21.69	56.13	30.34	14.82	9.33	10.49	6.04	11.56	3.79	2.30	11.94	11.35

Table 3
U–Pb data of zircons analyzed by SHRIMP.

U (ppm)	Th (ppm)	Th/U	^{206}Pb (ppm)	^{238}U/^{206}Pb	^{207}Pb/^{206}Pb	^{207}Pb/^{206}Pb age (Ma)	^{206}Pb/^{238}U age (Ma)	Disc. (%)
M22-2 diamictite matrix								
M22-2-1.1	1607	497	0.32	160	8.62	0.115	1880 ± 23	707 ± 11	66
M22-2-2.1	117	45	0.39	54	1.86	0.202	2839 ± 12	2776 ± 38	3
M22-2-3.1	708	558	0.81	243.00	2.50	0.25	3151 ± 8	2168 ± 19	37
M22-2-4.1	446	96	0.22	196.00	1.95	0.21	2938 ± 6	2664 ± 24	11
M22-2-1.2	1581	431	0.28	159.00	8.52	0.11	1825 ± 31	716 ± 7	64
M22-2-5.1	582	210	0.37	264.00	1.90	0.20	2828 ± 9	2731 ± 24	4
M22-2-6.1	1043	688	0.68	220.00	4.07	0.14	2220 ± 15	1416 ± 13	40
M22-2-6.2	852	466	0.56	254.00	2.88	0.16	2481 ± 9	1920 ± 18	26
M22-2-7.1	317	120	0.39	114.00	2.39	0.18	2613 ± 14	2257 ± 24	16
M22-2-8.1	128	68	0.55	45.00	2.44	0.18	2608 ± 16	2213 ± 31	18
M22-2-9.1	360	236	0.68	120.00	2.58	0.17	2504 ± 11	2110 ± 22	18
M22-2-10.1	117	114	1.01	46.00	2.19	0.17	2538 ± 18	2426 ± 36	5
M22-2-10.2	210	260	1.28	82.00	2.18	0.17	2536 ± 10	2431 ± 29	5
M22-2-11.1	399	428	1.11	129.00	2.65	0.17	2516 ± 10	2065 ± 21	21
M22-2-12.1	694	660	0.98	179.00	3.33	0.16	2406 ± 12	1694 ± 21	34
M22-2-13.1	288	211	0.75	104.00	2.39	0.17	2508 ± 14	2256 ± 25	12
M22-2-14.1	486	242	0.51	241.00	1.74	0.28	3355 ± 5	2934 ± 42	16
M22-2-15.1	105	89	0.88	46.00	1.94	0.26	3273 ± 11	2682 ± 41	22
M22-2-16.1	755	465	0.64	203.00	3.20	0.14	2214 ± 24	1754 ± 17	24
M22-2-17.1	400	218	0.56	142.00	2.42	0.17	2504 ± 11	2232 ± 23	13
M22-2-18.1	134	36	0.27	57.00	2.02	0.17	2589 ± 12	2595 ± 36	0
M22-2-19.1	735	96	0.13	263.00	2.40	0.23	3015 ± 8	2245 ± 20	30
M22-2-20.1	91	37	0.42	54.00	1.45	0.29	3397 ± 10	3377 ± 52	1
M22-2-21.1	938	381	0.42	267.00	3.02	0.22	2990 ± 7	1846 ± 16	44
M22-2-22.1	631	639	1.05	163	3.32	0.152	2370 ± 12	1699 ± 16	32
M22-2-23.1	546	288	0.54	137	3.44	0.172	2575 ± 15	1647 ± 57	41
M22-2-24.1	306	201	0.68	130	2.02	0.168	2539 ± 9	2596 ± 28	-3
M22-2-25.1	608	277	0.47	160	3.26	0.173	2592 ± 10	1725 ± 17	38
M22-2-26.1	2285	571	0.26	146	13.47	0.098	1587 ± 44	462 ± 9	73
M22-2-27.1	135	124	0.94	81	1.44	0.277	3346 ± 10	3407 ± 41	-2
M22-2-28.1	265	134	0.52	100	2.28	0.186	2710 ± 8	2348 ± 24	16
M22-2-29.1	587	632	1.11	186	2.71	0.161	2465 ± 8	2027 ± 18	21
M22-2-30.1	335	258	0.79	131	2.19	0.168	2534 ± 9	2424 ± 23	5

Table 4
U–Pb data of zircons analyzed by SHRIMP.

	U (ppm)	Th (ppm)	Th/U	^{206}Pb (ppm)	^{238}U/^{206}Pb	^{207}Pb/^{206}Pb	^{207}Pb/^{206}Pb age (Ma)	^{206}Pb/^{238}U age (Ma)	Disc. (%)
M22-2-30.2	552	265	0.5	192	2.47	0.168	2536 ± 8	2192 ± 19	16
M22-2-31.1	179	105	0.61	94	1.64	0.235	3083 ± 7	3066 ± 34	1
M22-2-32.1	589	765	1.34	176	2.88	0.167	2523 ± 17	1920 ± 17	28
M21-16 diamictite matrix									
M21-16-1.1	18	14	0.80	10	1.50	0.259	3242 ± 21	3285 ± 101	-2
M21-16-2.1	256	221	0.89	91	2.43	0.257	3229 ± 7	2221 ± 24	37
M21-16-3.1	134	59	0.46	72	1.61	0.239	3113 ± 8	3118 ± 40	0
M21-16-4.1	395	118	0.31	148	2.30	0.226	3022 ± 9	2326 ± 23	27
M21-16-5.1	341	170	0.51	166	1.76	0.284	3388 ± 23	2894 ± 76	18
M21-16-6.1	103	69	0.69	57	1.55	0.260	3247 ± 9	3210 ± 43	1
M21-16-7.1	289	222	0.79	145	1.71	0.240	3119 ± 6	2967 ± 30	6
M21-16-8.1	412	17	0.04	213	1.66	0.238	3106 ± 5	3038 ± 28	3
M21-16-9.1	126	83	0.68	64	1.69	0.237	3100 ± 9	2990 ± 39	4
M21-16-10.1	70	50	0.74	40	1.51	0.260	3244 ± 11	3277 ± 54	-1
M21-16-11.1	53	48	0.92	25	1.85	0.196	2797 ± 26	2783 ± 53	1
M21-16-12.1	127	70	0.57	64	1.71	0.223	3004 ± 10	2964 ± 39	2
M21-16-12.2	592	388	0.68	140	3.62	0.188	2723 ± 7	1571 ± 15	47
M21-16-13.1	96	32	0.34	54	1.54	0.266	3284 ± 9	3227 ± 46	2
M21-16-14.1	132	84	0.65	74	1.54	0.257	3229 ± 8	3218 ± 41	0
M21-16-15.1	200	94	0.49	103	1.68	0.223	3005 ± 12	3017 ± 34	0
M21-16-16.1	74	38	0.54	38	1.69	0.238	3105 ± 11	2994 ± 48	4
M21-16-16.2	174	84	0.50	88	1.69	0.239	3110 ± 7	2996 ± 35	5
M21-16-17.1	154	75	0.51	82	1.62	0.257	3227 ± 7	3102 ± 36	5
M21-16-18.1	312	151	0.50	153	1.75	0.266	3281 ± 5	2915 ± 38	14
M21-16-19.1	89	32	0.37	47	1.62	0.238	3106 ± 10	3092 ± 44	1
M21-16-19.2	98	47	0.50	51	1.66	0.239	3112 ± 11	3046 ± 43	3
M21-16-20.1	95	54	0.58	56	1.47	0.281	3366 ± 9	3349 ± 46	1
M21-16-20.2	101	68	0.70	60	1.45	0.281	3368 ± 9	3376 ± 47	0
M21-16-21.1	230	78	0.35	110	1.80	0.267	3286 ± 10	2850 ± 41	16
M21-16-22.1	84	51	0.63	47	1.54	0.258	3237 ± 9	3219 ± 47	1
M21-16-23.1	155	55	0.37	81	1.65	0.258	3234 ± 7	3054 ± 36	7
M21-16-24.1	1886	213	0.12	209	7.74	0.111	1809 ± 14	783 ± 7	60
M21-16-25.1	103	60	0.60	55	1.61	0.238	3109 ± 11	3109 ± 44	0
M21-16-26.1	223	132	0.61	108	1.77	0.255	3215 ± 7	2892 ± 31	12
M21-16-27.1	217	107	0.51	120	1.55	0.280	3361 ± 9	3214 ± 46	6
M21-16-28.1	405	124	0.32	76	4.60	0.209	2896 ± 15	1268 ± 39	62

References

Black, L. P., Kamo, S. L., Allen, C. M., Davis, D. W., Aleinikoff, J. N., Valley, J. W., ... & Foudoulis, C., 2004. Improved $^{206}Pb/^{238}U$ microprobe geochronology by the monitoring of a trace-element-related matrix effect; SHRIMP, ID–TIMS, ELA–ICP–MS and oxygen isotope documentation for a series of zircon standards. Chemical Geology, 205 (1), 115-140.

Chadwick, B., Ramakrishnan, M., Viswanatha, M.N., 1981. The stratigraphy and structure of the Chitradurga region: an illustration of cover–basement interaction in the late Archaean evolution of the Karnataka craton, southern India. Precambrian Research 16, 31–54.

Chadwick, B., Ramakrishnan, M., & Viswanatha, M. N., 1985. Bababudan-A Late Archaean Intracratonic Volcanosedimentary Basin, Karnataka, Southern India. Geological Society of India, 26(11), 769-801.

Chadwick, B., Ramakrishnan, M., Vasudev, V. N., & Viswanatha, M. N., 1989. Facies distributions and structure of a Dharwar volcanosedimentary basin: evidence for late Archaean transpression in southern India?. Journal of the Geological Society, 146(5), 825-834.

Chadwick, B., Vasudev, V. N., & Ahmed, N., 1996. The Sandur schist belt and its adjacent plutonic rocks implications for Late Archaean crustal evolution in Karnataka. Geological Society of India, 47 (1), 37-57.

Chadwick, B., Vasudev, V. N., Hegde, G. V., 2000. The Dharwar craton, southern India, interpreted as the result of Late Archaean oblique convergence. Precambrian Research, 99, 91–111.

Chadwick, B., Vasudev, V. N., & Hegde, G. V., 2003. The Chitradurga Schist Belt and its Adjacent Plutonic Rocks, NW of Thngabhadra, Karnataka: a Duplex in the Late Archaean Convergent Setting of the Dharwar Craton. Geological Society of India, 61 (6), 645-663.

Chadwick, B., Vasudev, V. N., Hegde, G. V., & Nutman, A. P., 2007. Structure and SHRIMP U/Pb zircon ages of granites adjacent to the Chitradurga schist belt: Implications for Neoarchaean convergence in the Dharwar craton, southern India. Geological Society of India, 69 (1), 5-24.

Chardon, D., Choukroune, P., & Jayananda, M., 1996. Strain patterns, decollement and incipient sagducted greenstone terrains in the Archaean Dharwar Craton (South India). Journal of Structural Geology, 18 (8), 991-1004.

Choukroune, P., Ludden, J. N., Chardon, D., Calvert, A. J., & Bouhallier, H., 1997. Archaean crustal growth and tectonic processes: a comparison of the Superior Province, Canada and the Dharwar Craton, India. Geological Society, London, Special Publications, 121 (1), 63-98.

Chardon, D., Choukroune, P., & Jayananda, M., 1998. Sinking of the Dharwar basin (South India): implications for Archaean tectonics. Precambrian Research, 91 (1), 15-39.

Chardon, D., & Jayananda, M., 2008. Three dimensional field perspective on deformation, flow, and growth of the lower continental crust (Dharwar craton, India). Tectonics, 27 (1).

Chardon, D., Jayananda, M., & Peucat, J. J., 2011. Lateral constrictional flow of hot orogenic crust: Insights from the Neoarchean of south India, geological and geophysical implications for orogenic plateaux. Geochemistry, Geophysics, Geosystems, 12 (2).

Choukroune, P., Ludden, J. N., Chardon, D., Calvert, A. J., & Bouhallier, H., 1997. Archaean crustal growth and tectonic processes: a comparison of the Superior Province, Canada and the Dharwar Craton, India. Geological Society, London, Special Publications, 121 (1), 63-98.

Claoué-Long, J. C., 1995. Two Carboniferous ages: a comparison of SHRIMP zircon dating with conventional zircon ages and $^{40}Ar/^{39}Ar$ analysis.

Compston, W.,Williams, I.S., Meyer, C.E., 1984. U–Pb geochronology of zircons from lunar breccia 73217 using a sensitive high-mass resolution ion microprobe. Journal of Geophysical Research 89, 525–534.

French, J. E., & Heaman, L. M., 2010. Precise U–Pb dating of Paleoproterozoic mafic dyke swarms of the Dharwar craton, India: implications for the existence of the Neoarchean supercraton Sclavia. Precambrian Research, 183 (3), 416-441.

Hansen, E. C., Newton, R. C., Janardhar, A. S., & Lindenberg, S., 1995. Differentiation of late Archean crust in the eastern Dharwar craton, Krishnagiri-Salem area, south

India. The Journal of Geology, 629-651.

Hansen, E. C., Newton, R. C., Janardhar, A. S., & Lindenberg, S., 1995. Differentiation of late Archean crust in the eastern Dharwar craton, Krishnagiri-Salem area, south India. The Journal of Geology, 629-651.

Hokada, T., Horie, K., Satish-Kumar, M., Ueno, Y., Nasheeth, A., Mishima, K., Shiraishi, K., 2013. An appraisal of Archaean supracrustal sequences in Chitradurga Schist Belt, Western Dharwar Craton, South India, Precambrian Research, 227, 99–119

Holland, H. D., 2002. Volcanic gases, black smokers, and the Great Oxidation Event. Geochimica et Cosmochimica Acta, 66, 3811–3826.

Holland, H. D., 2006. The oxygenation of the atmosphere and oceans. Philosophical Transactions of the Royal Society B: Biological Sciences, 361(1470), 903-915.

Horie, K., Hidaka, H., Gauthier-Lafaye, F., 2006. Elemental distribution in zircon: alteration and radiation-damage effects. Physics and Chemistry of the Earth 31, 587–592.

Horie, K., Hokada, T., Hiroi, Y., Motoyoshi, Y., & Shiraishi, K., 2012. Contrasting Archaean crustal records in western part of the Napier Complex, East Antarctica: New constraints from SHRIMP geochronology. Gondwana Research, 21 (4), 829-837.

Iyengar, S. V. P., 1976. The stratigraphy, structure and correlation of the Dharwar Supergroup. Geol. Surv. India Misc. Publ, 23 (2), 415-455.

Jayananda, M., Chardon, D., Peucat, J. J., Capdevila, R., 2006, 2.61 Ga potassic granites and crustal reworking in the western Dharwar craton, southern India: tectonic, geochronologic and geochemical constraints. Precambrian Research, 150, 1–26.

Jayananda, M., Kano, T., Peucat, J. J., Channabassappa, S., 2008, 3.35Ga komatiite volcanism in the western Dharwar craton, southern India: Constraints from Nd isotopes and whole rock geochemistry. Precambrian Research, 162, 160–179.

Jayananda, M., Peucat, J. J., Chardon, D., Rao, B. K., Fanning, C. M., & Corfu, F., 2013. Neoarchean greenstone volcanism and continental growth, Dharwar craton, southern India: constraints from SIMS U–Pb zircon geochronology and Nd isotopes. Precambrian Research, 227, 55-76.

Krogstad, E. J., Hanson, G. N., Balakrishnan, S., Rajamani, V., & Mukhopadhyay, D. K., 1989. Plate tectonics 2. 5 billion years ago- Evidence at Kolar, south India. Science,

243 (4896), 1337-1340.

Kröner, A., 1981. Precambrian plate tectonics. Developments in Precambrian geology, 4, 57-90.

Kumar, A., Rao, Y. B., Sivaraman, T. V., & Gopalan, K., 1996. Sm-Nd ages of Archaean metavolcanics of the Dharwar craton, South India. Precambrian Research, 80 (3), 205-216.

Ludwig, K. R., 2009. SQUID 2: a user's manual. Berkeley Geochronology Center Special Publication, 5, 110.

Manikyamba, C., Kerrich, R., Khanna, T. C., Krishna, A. K., & Satyanarayanan, M., 2008. Geochemical systematics of komatiite–tholeiite and adakitic-arc basalt associations: the role of a mantle plume and convergent margin in formation of the Sandur Superterrane, Dharwar craton, India. Lithos, 106 (1), 155-172.

Manikyamba, C., Kerrich, R., Polat, A., & Saha, A., 2013. Geochemistry of two stratigraphically-related ultramafic (komatiite) layers from the Neoarchean Sigegudda greenstone terrane, Western Dharwar Craton, India: evidence for compositional diversity in Archean mantle plumes. Lithos, 177, 120-135.

Manikyamba, C., Saha, A., Santosh, M., Ganguly, S., Singh, M. R., Rao, D. S., & Lingadevaru, M., 2014. Neoarchaean felsic volcanic rocks from the Shimoga greenstone belt, Dharwar Craton, India: geochemical fingerprints of crustal growth at an active continental margin. Precambrian Research, 252, 1-21.

Manikyamba, C., & Kerrich, R., 2011. Geochemistry of alkaline basalts and associated high-Mg basalts from the 2.7 Ga Penakacherla Terrane, Dharwar craton, India: an Archean depleted mantle-OIB array. Precambrian Research, 188 (1), 104-122.

Moyen, J. F., Nédélec, A., Martin, H., & Jayananda, M., 2001. Contrasted granite emplacement modes within an oblique crustal section: the Closepet Granite, South India. Physics and Chemistry of the Earth, Part A: Solid Earth and Geodesy, 26 (4), 295-301.

Moyen, J. F., Martin, H., Jayananda, M., & Auvray, B., 2003. Late Archaean granites: a typology based on the Dharwar Craton (India). Precambrian Research, 127 (1), 103-123.

Naha, K., Srinivasan, R., & Jayaram, S., 1991. Sedimentational, structural and migmatitic

history of the Archaean Dharwar tectonic province, southern India. Proceedings of the Indian Academy of Sciences-Earth and Planetary Sciences, 100 (4), 413-433.

Naqvi, S. M., & Hussain, S. M., 1973. Geochemistry of Dharwar metavolcanics and composition of the primeval crust of the peninsular India. Geochimica et Cosmochimica Acta, 37 (1), 159-164.

NAQVI, S., 1985. Journal Geological Society of India Vol. 26, Aug. 1985, pp. 511 lo 525 Chitradurga schist belt—an Archaean suture. Chitradurga Schist Belt, 511.

Nasheeth, A., Okudaira, T., Horie, K., Hokada, T., & SATISH–KUMAR, M., 2015. SHRIMP U–Pb zircon ages of granitoids adjacent to Chitradurga shear zone, Dharwar craton, South India and its tectonic implications. Journal of Mineralogical and Petrological Sciences, 110 (5), 224-234.

Nasheeth, A., Okudaira, T., Horie, K., Hokada, T., & Satish-Kumar, M., 2016. U-Pb SHRIMP ages of detrital zircons from Hiriyur Formation in Chitradurga greenstone belt and its implication to the Neoarchean evolution of Dharwar craton, south India. Journal of the Geological Society of India, 87 (1), 43-54.

Nutman, A. P., Chadwick, B., Ramakrishnan, M., & Viswanatha, M. N., 1992. SHRIMP U-Pb ages of detrital zircon in Sargur supracrustal rocks in western Karnataka, southern India. Geological Society of India, 39 (5), 367-374.

Ojakangas, R. W., Srinivasan, R., Hegde, V. S., Chandrakant, S. M., & Srikantia, S. V., 2014. The Talya Conglomerate: an Archean (~ 2.7 Ga) Glaciomarine Formation, Western Dharwar Craton, Southern India. Current Science, 106, 387-396.

Pichamuthu, C. S., 1962. Some observations on the structure, metamorphism, and geological evolution of Peninsular India. Geological Society of India, 3, 106-118.

Raase, P., Raith, M., Ackermand, D., Lal, R.K., 1986. Progressive metamorphism of mafic rocks from greenschist to granulite facies in the Dharwar craton of South India. Journal of Geology 94, 261–282.

Radhakrishna, B. P., 1967. The present status of geological, geophysical and geochemical studies in the Dharwar region. Government of Mysore, Department of Mines & Geology.

Radhakrishna, B. P., & Naqvi, S. M., 1986. Precambrian continental crust of India and its evolution. The Journal of Geology, 145-166.

Raith, M., Raase, P., Ackermand, D., & Lal, R. K., 1982. The Archean craton of southern India: metamorphic evolution and PT Conditions. Geologische Rundschau, 71(1), 280-290.

Ram Mohan, Sarma, D. S., McNaughton, N. J., Fletcher, I. R., Wilde, S. A., Siddiqui, M. A., ... & Kamo, S. L., 2014. SHRIMP zircon and titanite U-Pb ages, Lu-Hf isotope signatures and geochemical constraints for~ 2.56 Ga granitic magmatism in Western Dharwar Craton, Southern India: Evidence for short-lived Neoarchean episodic crustal growth?. Precambrian Research, 243, 197-220.

Rao, T. G., & Naqvi, S. M., 1995. Geochemistry, depositional environment and tectonic setting of the BIF's of the Late Archaean Chitradurga Schist Belt, India. Chemical Geology, 121 (1), 217-243.

Sarma, D. S., Fletcher, I. R., Rasmussen, B., McNaughton, N. J., Mohan, M. R., & Groves, D. I., 2011. Archaean gold mineralization synchronous with late cratonization of the Western Dharwar Craton, India: 2.52 Ga U–Pb ages of hydrothermal monazite and xenotime in gold deposits. Mineralium Deposita, 46 (3), 273-288.

Sarma, D. S., Mc Naughton, N. J., Belousova, E., Ram Mohan, M., & Fletcher, I. R., 2012. Zircon U-Pb ages and Hf-isotope systematic from the Gadag greenstone belt: Archean crustal growth in the western Dharwar craton, India. Gondwana Research, http://dx. doi. org/10.1016/j. gr, 1.

Seshadri, T. S., Chaudhuri, A., Babu, P. H., & Chayapathi, N., 1981. Chitradurga belt. Mem. Geol. Surv. India, 112, 163-198.

Sleep, N. H., 1992. Archean plate tectonics: what can be learned from continental geology? Canadian Journal of Earth Sciences, 29 (10), 2066-2071.

Sreenivas, B. L., & Srinivasan, R., 1968. Dharwar conglomerates of Mysore-a restudy. Geological Society of India, 9 (2), 197-205.

Srikantia, S. V., 1992. Glacial and Fluvial Geomorphology of Western Himalaya. Geological Society of India, 39 (4), 355-355.

Swami Nath, J., Ramakrishnan, M., & Viswanatha, M. N., 1976. Dharwar stratigraphic model and Karnataka craton evolution. Rec. Geol. Surv. India, 107 (2), 149-175.

Stacey, J. T., & Kramers, 1. (1975). Approximation of terrestrial lead isotope evolution by a two-stage model. Earth and planetary science letters, 26 (2), 207-221.

Terabayashi, M., 1993. Compositional evolution in Ca‐amphibole in the Karmutsen metabasites, Vancouver Island, British Columbia, Canada. Journal of Metamorphic Geology, 11 (5), 677-690.

Trendall, A. F., De Laeter, J. R., Nelson, D. R., & Rao, Y. B., 1997. Further zircon U-Pb age data for the Daginkatte formation, Dharwar Supergroup, Karnataka craton. Geological Society of India, 50 (1), 25-30.

Viljoen, M. J., Viljoen, R. P., & Pearton, T. N., 1982. The nature and distribution of Archaean komatiite volcanics in South Africa. Komatiites, Allen and Unwin, London, 53-79.

Viswanatha, M. N., & Ramakrishnan, M., 1976. The pre-Dharwar supracrustal rocks of Sargur Schist Complex in southern Karnataka and their tectono-metamorphic significance. Indian Mineralogist, 16, 48-65.

Walter, M. R., & Hofmann, H. J., 1983. The palaeontology and palaeoecology of Precambrian iron-formations. Developments in Precambrian Geology, 6, 373-400.

Williams, I.S., 1998. U–Th–Pb geochronology by ion microprobe. In: McKibben, M.A., Shanks III, W.C., Ridley, W.I. (Eds.), Applications of Microanalytical Techniques to Understanding Mineralizing Processes. Reviews in Economic Geology, vol. 7, pp. 1–35.

Ziauddin, M., & Yadav, P. K., 1975. Acid charnockite (metasomatic) near Sivasamudram, Karnataka State. Geological Society of India, 16 (2), 215-219.

Chapter 3

Potential glacial deposit in the Dharwar Supergroup, Southern India

Abstract

The late Archean volcano-sedimentary rocks of the Dharwar Supergroup exposed at Western Dharwar Craton, Southern India, contains several unmistakable diamictite (i.e. matrix-supported conglomerate) which exhibit depositional features that allow the sequences to be interpreted as a glacial origin. In this study, we found the newly glacial sedimentary sequences near the Sadarahalli, north west of Chitradurga Schist Belt, interbedded with mudstone and sandstone units. The entire thickness of this glacial diamictite within the middle formation of the Chitradurga Group, is exposed in a 100m thick measured section. The Sadarahalli diamictite has unusual concentration of boulder size clasts and preserve an original matrix texture of laminate mudstone and fine sandstone, especially impact of dropstone on sea-bed caused the fold. This conglomerate can be compared with the glacial diamictites in glaciomarine environment.

3-1. Introduction

The climate change during the Archean is not fully understood because the unavailability and destruction of older rock exposures by erosion and tectonic deformation through time (Crowell, 1983; Eyles, 1993). The oldest deposits of suspected glacial origin in the Southern African region were first described from diamictites in the 2.9 Ga Witwatersrand Supergroup, South Africa (e.g. Tankard et al., 1982; Crowell, 1983). Subsequent work on the Southern African subcontinent in Archean deposits of the Pongola Supergroup (Mozaan group) of South Africa and Swaziland, involved a glacial interpretation for part of the sequence which they ultimately termed the Earth's oldest reported glaciation (Von Brunn and Gold, 1993; Young et al., 1998). Moreover, several researchers reported glaciogenic sediments at 3.5 Ga Onverwacht Suite, South Africa, ~2.7 Ga Stillwater Complex, USA and ~2.8 Ga Nuywane Formation, Botswana (de Wit et al., 2016; Modie, 2002). Both these deposits may represent temporary and regional glaciations, but their suggestion did not receive general acceptance. Thus, the Archean glacial deposit may not strictly qualify as glacio-epochs.

However, Archean was much colder as a consequence of a 'faint young sun' with an output 25–30% lower than that of today (Sagan et al., 1972). Some workers suggested that glaciation was only prevented by greenhouse gases such as CO_2, NH_3 or CH_4

(Caldeira and Kasting, 1992 and Zahnle and Sleep, 2002). High CH_4 concentrations, along with enhanced CO_2 levels, could have produced enough greenhouse warming to counter low solar luminosity and keep the Archean Earth warm (Pavlov et al., 2000). However, at $CH_4/CO_2 > \sim 0.1$, the anti-greenhouse effect is stronger than the greenhouse effect and increases in the CH_4 flux should have caused cooling (Domagal-Goldman et a., 2008). If Archean Earth' surface is cold, then glacially influenced strata should be widespread and preserved elsewhere other than on the Kaapvaal Craton and Botswana but this does not appear to be the case (Eyles, 2008). The geodynamic setting indicates a passive margin setting. A systematic search is needed for new deposits in other basins.

This section discusses the interpretation of the depositional environment of a late Archaean volcanogenic sedimentary sequence that belongs to the Vanivilas-Ingaldhal Formation of the Dharwar Supergroup exposed in Southern India. Rocks assigned to the Dharwar Supergroup are preserved in a N-S striking ridge exposed at Chitradurga Schist Belt (Fig. 3-1). Recent geological field investigations revealed the occurrence of depositional features that resemble glacial attributes in the Vanivilas Formation (Ojakangas et al., 2014). In this regard, this chapter presents an interpretation of the depositional processes that prevailed during accumulation of the Vanivilas-Ingaldhal formation, by considering the data in a sedimentological and glaciogenic perspective.

3-2. Geological outline

In the Dharwar Craton of the southern Indian, 2.8-2.5 Ga Neoarchean volcano-sedimentary sequence constituting the Dharwar Supergroup accumulated on 3.5–3.0 Ga Sarugur greenstone-TTG complex. The Dharwar Supergroup is divided into two unit of the lower unit (traditionally Bababudan Group, Vanivilas Formation and Ingaldhal Formation) and the upper unit (traditionally Hiriyur Formation). The lower Dharwar Supergroup was intruded by 2.6–2.5 Ga granitoids (e.g. Jayananda et al., 2006). A simplified lithostratigraphy is shown in Fig. 2-2, which based on our detailed fieldwork over 5 years. The depositional age of lower unit is estimated at 2.8-2.67 Ga by detrital zircon Pb/Pb age and felsic volcanic intrusive of 2.67 Ga (see Chapter 1 and Hokada et al., 2013). The youngest age of detrital zircons in the upper unit are 2.63 or 2.53 Ga, suggesting the depositional age of upper unit is younger than ~2.6 Ga.

3-3. Stratigraphy

The dimamictites described in this chapter form part of the Dharwar Supergroup, which includes a thick dominantly volcano-sedimentary sequence. According to Chapter 2, the thick volcano-sedimentary succession of the lower unit of Dharwar Supergroup deposited at early rift setting. The sandstone of Bababudan Group appears to have been derived from the surrounding Peninsular gneiss (Hokada et al., 2013). Four major conglomerates have been recognized within the Dharwar Supergroup: Neralekatte conglomerate, Talya conglomerate, K. M. Kere conglomerate and Aimangara conglomerate. Other than the reported conglomerate, we found new diamicittie which possibly glacial orign.

3-3-1. Neralekatte Conglomerate

In the CSB the basal conglomerate is known as the 'Neralekatte Congolmerate' (Chadwick et al., 1981), which distribute on the west end of the CSB. The pebbles consist mostly of vein quartz, but there are rare clasts of quartzite and fuchsite quartzite, the latter derived from enclaves of Sargur metasediments in the basement gneisses (Chadwick et al., 1981). Sedimentary contacts with the Peninsular Gneiss and Sargur enclaves are exposed only rarely. This conglomerate might deposit in the initial rift zone.

3-3-2. Talya conglomerate

Talya conglomerate is 800 m thick but boundaries are transitional with increase of the chlorite-biotite-quartz-plagioclase matrix into overlying homogeneous siliceous schist and BIF. Unsorted, rounded-angular clasts, up to 1 m in size, consist of almost quartzite, quartz pebble conglomerate (Fig. 3-3). The matrix is generally cleaved. Becaulse the conglomerate appears to wide range of the CSB, it is useful to key bed of Dharwar Supergroup (Fig. 3-2). The origin of the Talya conglomerate is controversial (Ziauddin, 1975), but its extensive outcrop and lateral variation indicate deposition as a large lenticular mass whose formation envisaged as the result of rapid uplift of the sedimentary cover and its basement to the west (Chadwick et al., 1981). The conglomerate probably formed as a large subaqueous slump breccia that slid off the uplifted area, the slip being triggered by seismic shocks contemporaneous with the uplift

(Chadwick et al., 1981).

On the other hand, Srikantia (1992) and Ojakangas et al. (2014) interpreted that The Talya Conglomerate and the lower Kaldurga are interpreted as a glaciomarine unit deposited on a marine shelf (or possibly on the slope/abyssal plain) by rainout of iceberg-rafted coarse detritus. However, we could not detect the glaciogenic evidence. Thus, it is difficult to believe them.

3-3-3. Sadarahalli diamictite

Sadarahalli diamictite is 100 m thick overlaying the Talya conglomerate and BIF sequences in Section 3 (Fig. 3-2). The Section 3 is near Sadarahalli and at west limb of anticline. This section has been interpreted as stratigraphic way up to the west, because of the westward dipping succession (Fig. 3-1c). The sedimentary sequences end with the mylonatized fault between the PG and metasandstone (Fig. 3-1c). This section comprises a ~0.8 km thick pile, which is composed predominantly of sedimentary rocks and starts from an unsorted, 10 m thick, conglomerate. Quartzite and vein quartz clasts are dominant within this conglomerate layer (Fig. 3-3b). This conglomerate layer is followed by banded ferruginous chert. We interpret that this conglomerate is equivalent to the Talya conglomerate in the Sections 1 and 2, because of similarity in characteristic of the conglomerate and stratigraphic sequences (Fig. 3-2). The banded ferruginous chert is overlain by a 200 m thick laminated sandstone. This sandstone gradually changes to diamictite. Unsorted, rounded-angular clasts, up to 1 m in size, consist of almost quartzite, quartz pebble. This diamictite layer has not been reported so far. The possibility of the glacial diamictite is discussed below.

3-3-4. K. M. Kere conglomerate

It extends from east of lngaldhal to south of Elladakere for a length of about 40 km and has a width varying from a few meters to as much as 1 km (Seshadri et al., 1981). It shows wide variations in the composition of matrix and pebbles along strike and dip. An assortment of pebbles of various shapes and sizes, embedded in matrices of vastly different character, constitutes the conglomerate. The pebbles consist of massive and schistose lavas, banded ferruginous chert, black chert, black shale, grnnite, gneiss,

quartzite and vein quartz (Fig. 3-3e), all of them indicative of derivation from the older lngaldhal, Vanivilas, Bababudan Group and the gneissic complex and young granites. This suggest that redposition of lower sedimentary unit. The pebble composition in a given area is variable depending on the geology of the hinterland. While the mafic pebbles are absent in the Gownahalli area of middle of CSB, they occur in abundance in the south and northward (Fig. 3-1b). Except for the banded chert and black chert, most other pebbles show a high degree of roundness. The matrix varies from pelitic to carbonated sand and corresponds to the compositional range of greywacke-argillite suite. But at places it is distinctly tuffaceous. The K. M. Kere conglomerate includes several non-pebbly phyllites with sandy and calcareous partings.

3-3-5. Aimangala conglomerate

To the east of the Ingaldhal, the greywacke-argillite suite encloses the unsorted polymict conglomerate of Aimangala, exposed between D. S. Halli and NH4. This conglomerate consists of boulders and pebbles of mostly massive and schistose lavas, massive grey granite, banded ferruginous chert, black chert, and vein quartz (Fig. 3-3f). The size distribution of pebbles is bimodal, the cherts and quartz pebbles being 5-6 cm in diameter, whereas lavas and granite boulders are 16-20 cm in diameter. This conglomerate was also considered by earlier workers as a major unit useful for classifying the rocks of the Chitradurga schist belt (e.g. Seshadri et al., 1981). But it is seen that the conglomerate is conformable in attitude with the surrounding rocks which themselves form an inseparable unit of greywacke- argillite suite. Therefore, this conglomerate has no great stratigraphic significance.

3-4. Analyses

The petrographic study was performed on polished thin sections using a microscope. Scanning electron microscope (Hitachi SEM 3400N), equipped with an EDS, was used to study morphological characteristics.

3-5. Evidence for glaciation

Diamictite can deposit by a variety of processes (e.g. Schermerhorn, 1974). Thus, a glacial origin should not be inferred without appropriate supporting criteria. In the

Sadarahalli diamictite of middle Dharwar Supergroup a case for glacial influence is based on the occurrence of drop stone texture in the laminated shale, in addition to the recognition of large, oversized sedimentary clasts and isolated pebbles preserved in finely laminated mudstone/sandstone facies. This bed differs from other conglomerates in the Dharwar Supergroup.

Figure 3-5 shows the photomicrographs of Talya conglomerate matrix and Sadarahalli diamictite matrix. The Sadarahalli diamicitite matrix show the alternating with fine-grained sandy layer and muddy layer (Fig. 3-5b). This muddy layer is composed of Al, K and Fe (Fig. 3-6). While this diamictite suffers severe alteration, the enrich of Al and K in the muddy bed possibly indicates not alteration origin but deposition of mudstone at that time. The alteration of fine-grained sandstone and mudstone within mm scale indicate that this diamictite does not deposit as slump or subaqueous mudflow. This diamictite possibly deposited at distal marine environment. On the other hand, the Talya conglomerate does not show alternation of sand and mudstone (Fig. 3-5a). Thus, the possibility of slump or subaqueous mudflow remains at Talya conglomerate.

The recognition of dropstones in laminated shale has been considered throughout the geological literature as good criterion to infer glaciation (Crowell, 1983; Edwards, 1986; Eyles, 1993). These attributes also seem to form the most common and significant features that correlate ancient glacial deposits to modern glacial deposits. The occurrence of oversized sedimentary clasts within finely laminated mudstone and sandstone facies in the lower unit of Dharwar Supergroup (Fig. 3-4). Clasts that show evidence of forceful emplacement (dropstones) strongly suggest presence of floating ice. Figures 3-4c and d is a typical dropstone texture. The clast (a well-rounded quartzite) has penetrated at least ~3 cm (post-compaction thickness) into laminated to fine-bedded mudstones. On the both side, a 1 cm-thick layer has been almost entirely squeezed out beneath the clast. They also show small fold structures and brecciation of the laminated mudstone. The disturbance extends for at least 2 cm laterally from the edge of the quartzite clast, with small folds verging away from the clast. These compactional and fold features are developed on both sides of the clast, indicating vertical emplacement into unconsolidated or partly consolidated laminated muddy sediments. The features of the quartzite cast are illustrated on the accompanying sketch (Fig. 3-4d). The most likely mode of emplacement is from

clast-charged floating glacier ice. The large size of some clasts also suggests glacial activity.

3-6. Correlation with Pongola glaciation

Figure 3-6 shows the lithostratigraphic sequence of the Dharwar Craton (Southern India) compared with that of Kaapvaal Craton (South Africa). The new physical evidence support a glacial interpretation of the 2.8-2.7 Ga Sadarahalli diamictite which occurs at the middle of Dharwar Supergroup. This evidence of 2.8-2.7 Ga glaciation, together with the 2.9-2.8 Ga Pongola glaciation (Young et al., 1998), indicate the climate cooling era at 2.9-2.7 Ga. This consistent with the presumed ‘‘faint young sun’’ suggested for Archean times would have resulted in cold climatic conditions (Sagan and Mullen, 1972; Kasting, 1993).

3-7. Conclusions

Consideration of limited geological information from the Sadarahalli diamictite has given insight into the palaeoenvironment at the time of deposition of the sedimentary facies. Physical evidence supporting a glacial origin for the Sadarahalli diamictite includes the dropstones within laminated-to-finely bedded sequences.

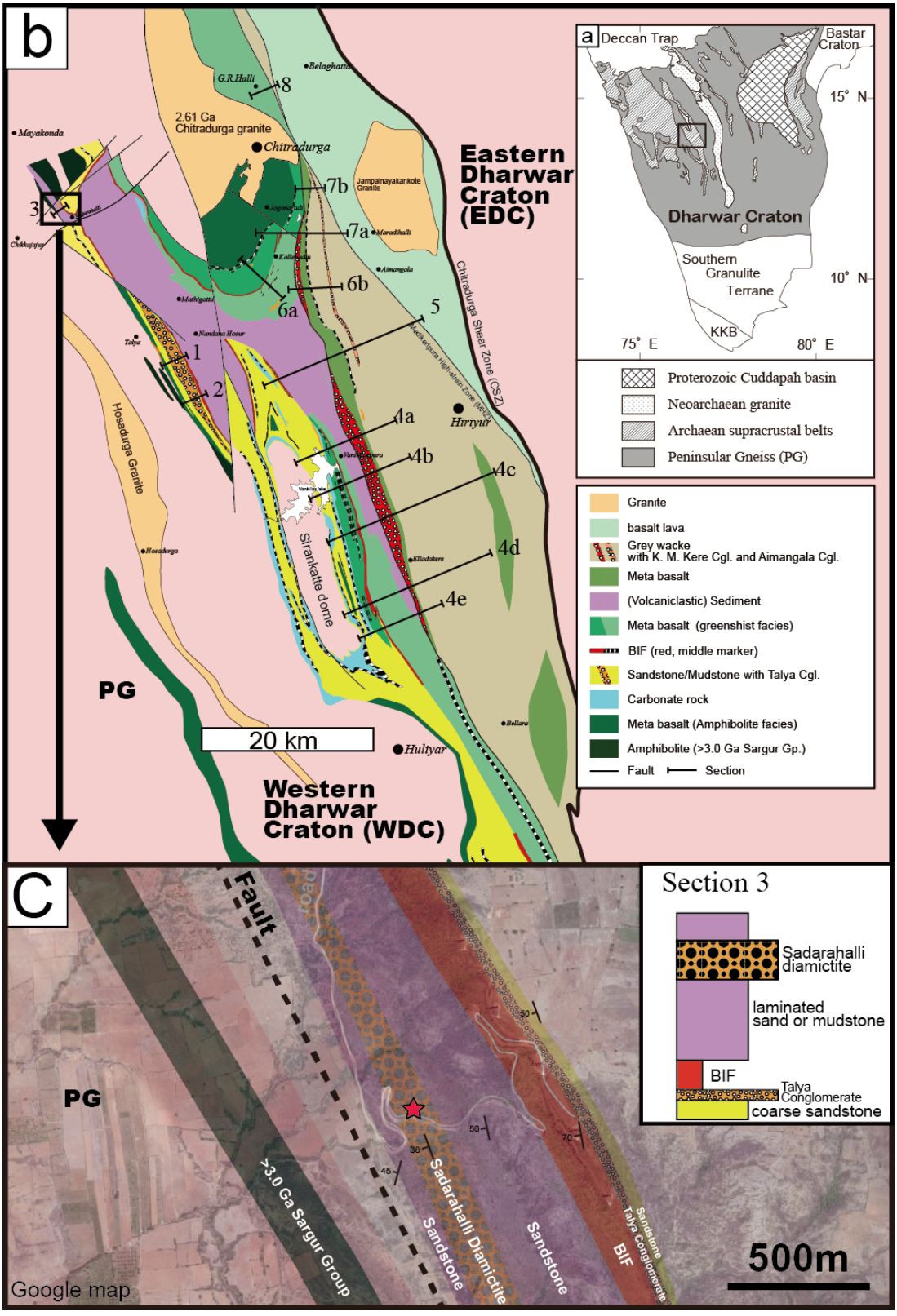

Fig. 3-1 Geologic map of the studied area. Star shows a type locarity of doropstone texture.

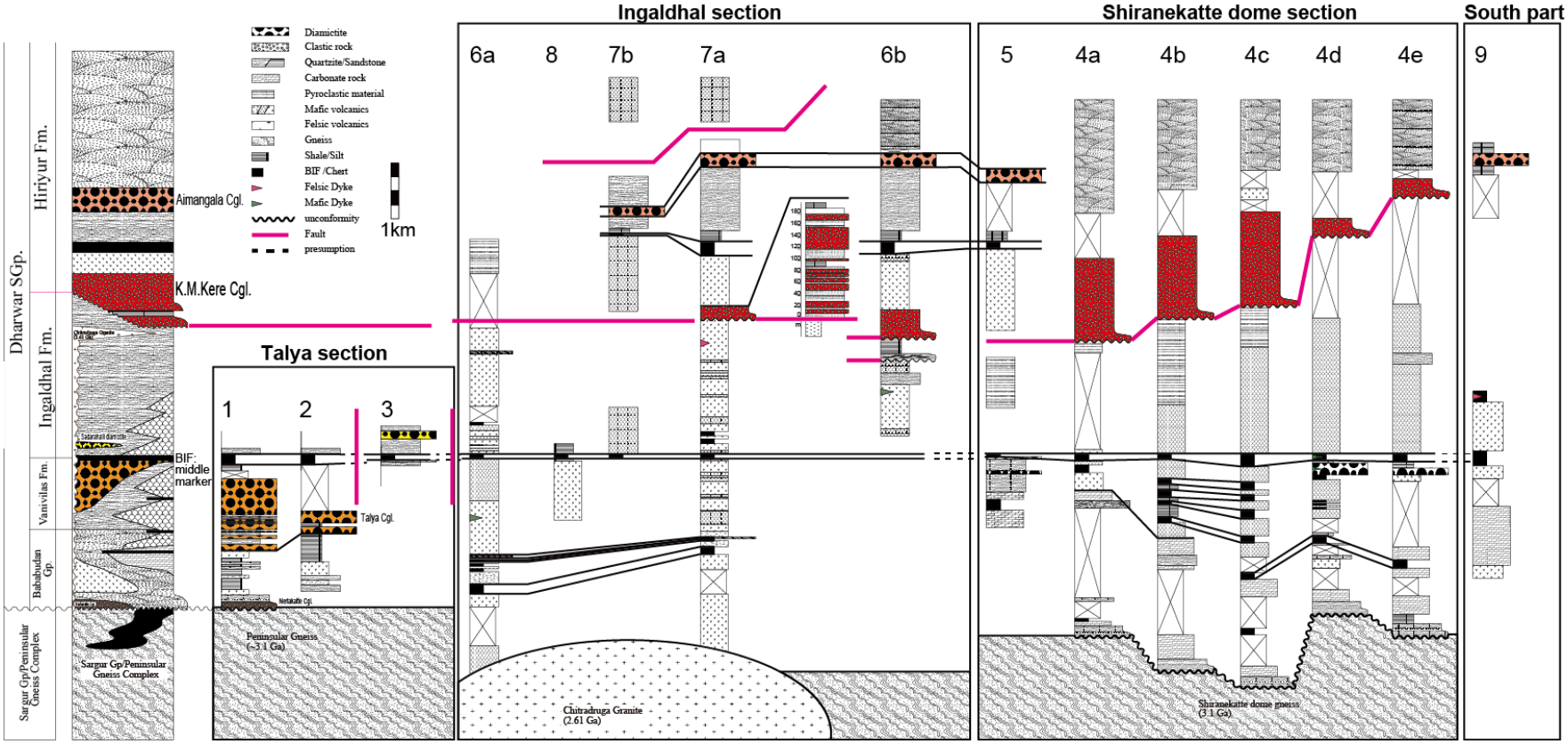

Fig. 3-2 Lithostratigraphic columns through the Dharwar Supergroup, compiled from logged sections, shown in Fig. 3-1.

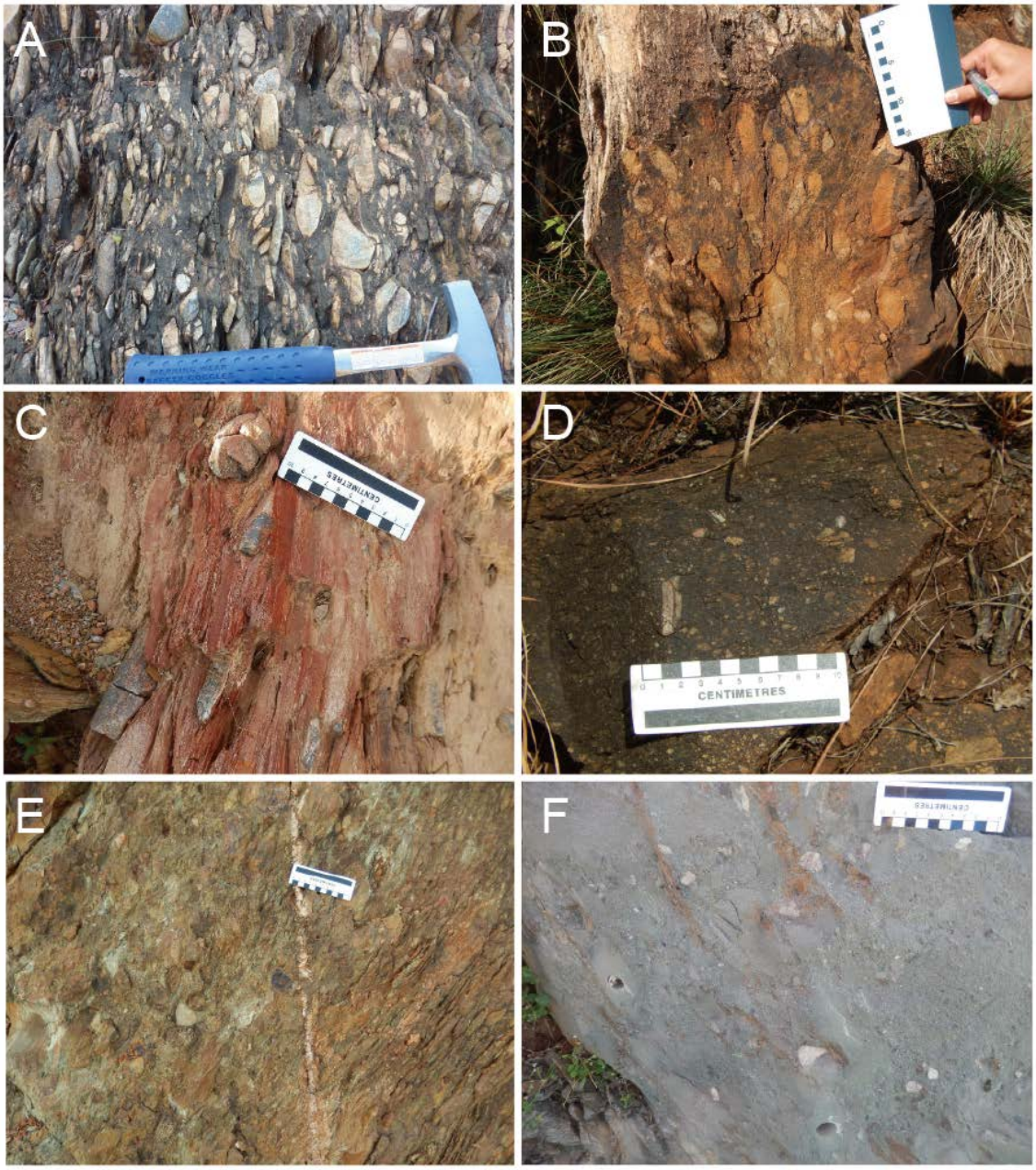

Fig. 3-3 Field photographs (A) Talya conglomertate near Talya (B) Talya conglomerate near Sadarahalli (C) Talya conglomerate near Sirankatte dome (D) Conglomerate interlayered with Basalt lava at Ingaldhal (E) K. M. Kere conglomerate (F) Aimangala conglomerate

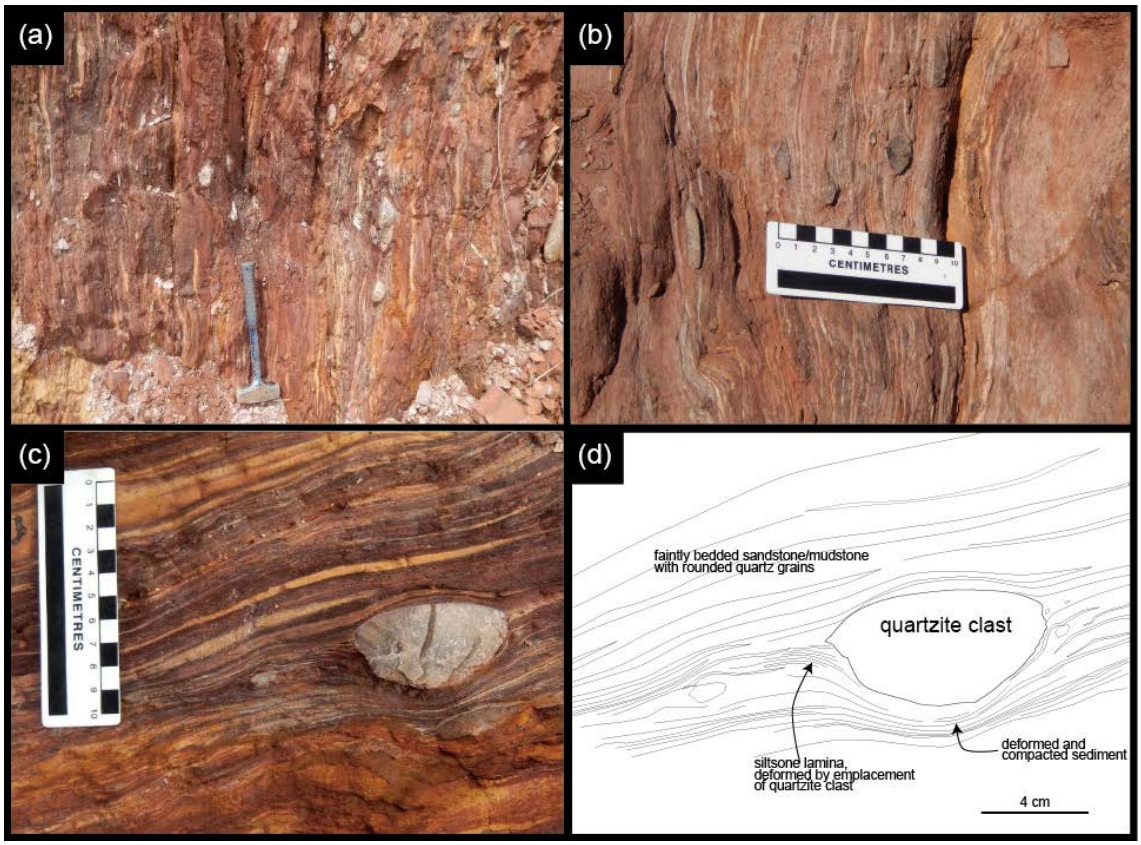

Fig. 3-4 Field photographs of a dropstone in laminated, finely bedded ferruginous sandstone/mudstones in the Sadarahalli diamictite (A, B, C). Scale in cm. Sketch of the dropstone shown in (d), to highlight important features.

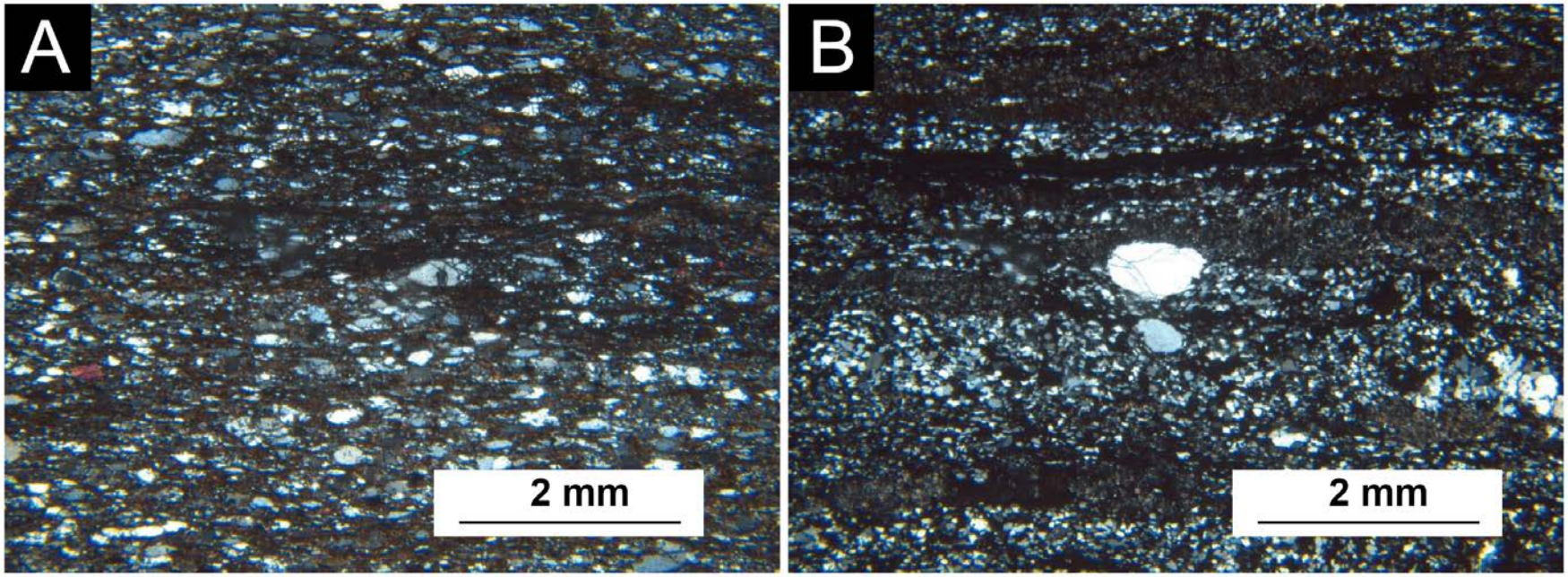

Fig. 3-5 Photomicrograph of the (A) Talya conglomerate matrix and (B) Sadarahalli diamictite matrix.

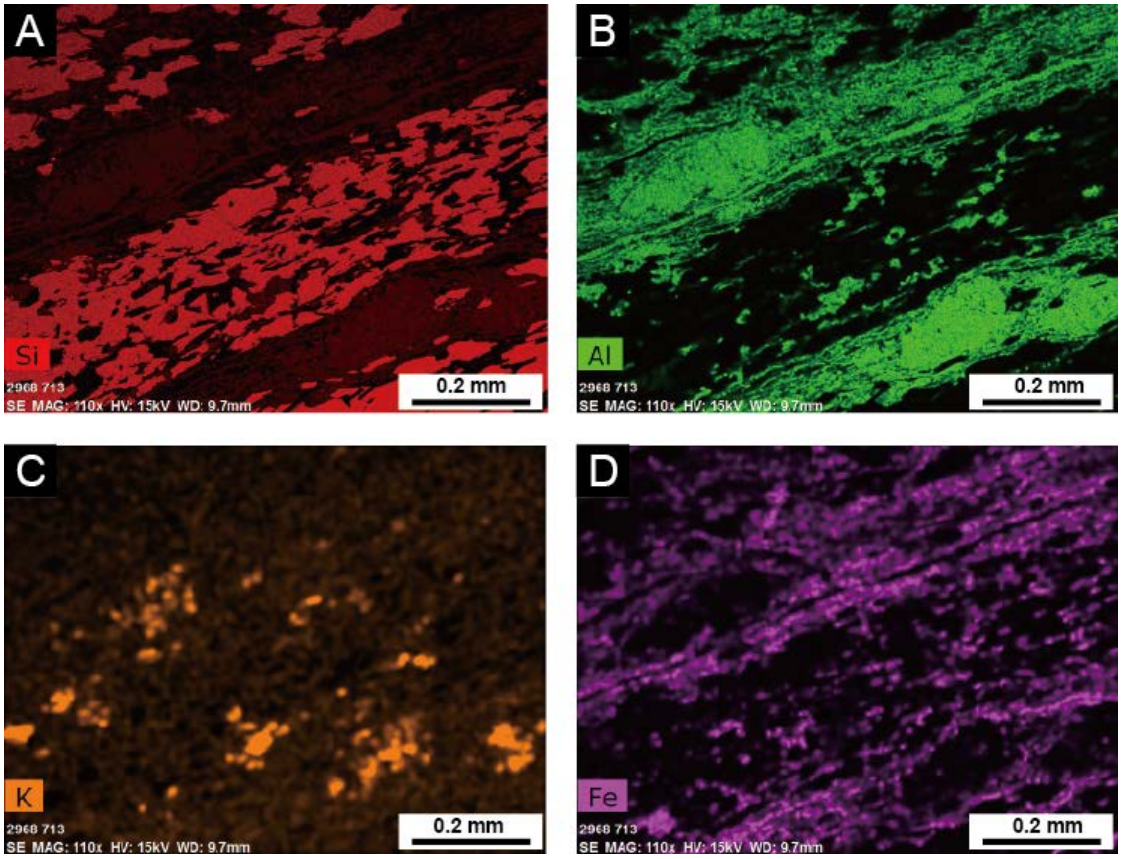

Fig. 3-6 Compositional variation in Si, Al, K and Fe within a Sadarahalli diamictite matrix

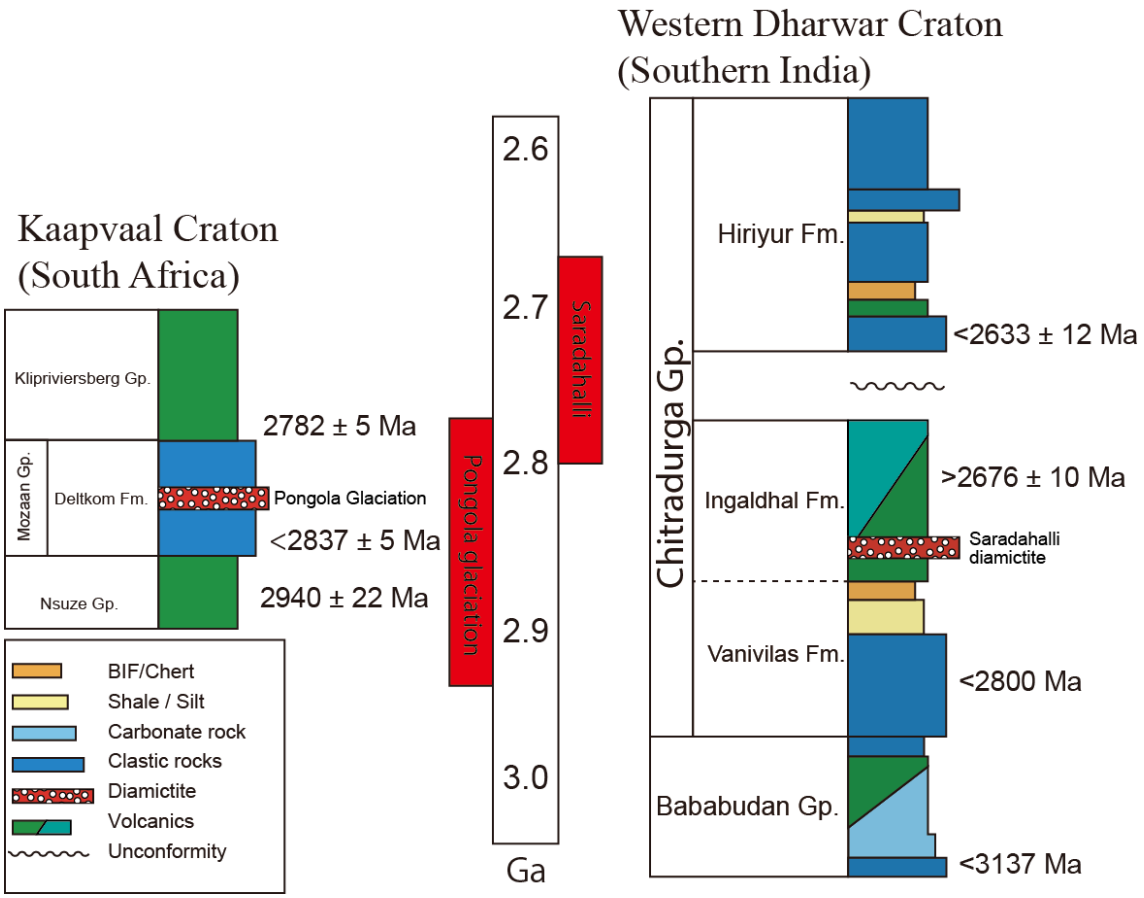

Fig. 3-7 Stratigraphic section of Chitradurga Schist Belt in Dharwar Craton compared with Kaapvaal Craton in S. Africa (Cornell et al., 1996; Gutzmer et al., 1999; Nelson et al., 1999; Lindsay et al., 2003; Hoakda et al., 2013).

References

Caldeira, K., & Kasting, J. F., 1992. Susceptibility of the early Earth to irreversible glaciation caused by carbon dioxide clouds.

Chadwick, B., Ramakrishnan, M., & Viswanatha, M. N., 1981. Structural and Metamorphic Relatioms Between Sargur and Dharwar Supracrustal Rocks and Peninsular Gneiss in Central Karnataka. Geological Society of India, 22 (12), 557-569.

Crowell, J. C., 1983. Ice ages recorded on Gondwanan continents: Geological Society of South Africa Transactions, v. 86. Crowell23786Ice ages recorded on Gondwanan continents 1983, 237-262.

de Wit, M. J., & Furnes, H., 2016. 3.5-Ga hydrothermal fields and diamictites in the Barberton Greenstone Belt—Paleoarchean crust in cold environments. Science advances, 2 (2), e1500368.

Domagal-Goldman, S. D., Kasting, J. F., Johnston, D. T., & Farquhar, J., 2008. Organic haze, glaciations and multiple sulfur isotopes in the Mid-Archean Era. Earth and Planetary Science Letters, 269 (1), 29-40.

Edwards, M. B., 1986. Glacial environments. Sedimentary environments and facies, 445-470.

Eyles, N., 1993. Earth's glacial record and its tectonic setting. Earth-Science Reviews, 35 (1-2), 1-248.

Eyles, N., 2008. Glacio-epochs and the supercontinent cycle after~ 3.0 Ga: tectonic boundary conditions for glaciation. Palaeogeography, Palaeoclimatology, Palaeoecology, 258 (1), 89-129.

Hokada, T., Horie, K., Satish-Kumar, M., Ueno, Y., Nasheeth, A., Mishima, K., & Shiraishi, K., 2013. An appraisal of Archaean supracrustal sequences in Chitradurga schist belt, western Dharwar craton, southern India. Precambrian Research, 227, 99-119.

Jayananda, M., Chardon, D., Peucat, J. J., & Capdevila, R., 2006. 2.61 Ga potassic granites and crustal reworking in the western Dharwar craton, southern India: tectonic, geochronologic and geochemical constraints. Precambrian Research, 150(1), 1-26.

Kasting, J. F., 1993. Earth's early atmosphere. SCIENCE-NEW YORK THEN WASHINGTON-, 259, 920-920.

Modie, B. N., 2002. Glacial records in Botswana. In 16th Int. Sedim. Congr., Johannesburg (South Africa), Abstracts (p. 261).

Ojakangas, R. W., Srinivasan, R., Hegde, V. S., Chandrakant, S. M., & Srikantia, S. V., 2014. The Talya Conglomerate: an Archean (~ 2.7 Ga) Glaciomarine Formation, Western Dharwar Craton, Southern India. Current Science, 106, 387-396.

Pavlov, A. A., Kasting, J. F., Brown, L. L., Rages, K. A., & Freedman, R., 2000. Greenhouse warming by CH 4 in the atmosphere of early Earth. Journal of Geophysical Research, 105 (11), 981-11.

Sagan, C., & Mullen, G., 1972. Earth and Mars: Evolution of atmospheres and surface temperatures. Science, 177 (4043), 52-56.

Schermerhorn, L. J. G., 1983. Late Proterozoic glaciation in the light of CO2 depletion in the atmosphere. Geological Society of America Memoirs, 161, 309-317.

Seshadri, T. S., Chaudhuri, A., Babu, P. H., & Chayapathi, N., 1981. Chitradurga belt. Mem. Geol. Surv. India, 112, 163-198.

Srikantia, S. V., 1992. Glacial and Fluvial Geomorphology of Western Himalaya. Geological Society of India, 39 (4), 355-355.

Tankard, A. J., Jackson, M. P. A., Eriksson, K. A., Hobday, D. K., Hunter, D. R., & Minter, W. E. L., 1982. 3.5 Billion years of Crustal Evolution in Southern Africa.

Von Brunn, V., & Gold, D. J. C., 1993. Diamictite in the Archaean Pongola sequence of southern Africa. Journal of African Earth Sciences (and the Middle East), 16(3), 367-374.

Young, G. M., Brunn, V. V., Gold, D. J., & Minter, W. E. L., 1998. Earth's oldest reported glaciation: physical and chemical evidence from the Archean Mozaan Group (~2.9 Ga) of South Africa. The Journal of geology, 106 (5), 523-538.

Zahnle, K., & Sleep, N. H., 2002. Carbon dioxide cycling through the mantle and implications for the climate of ancient Earth. Geological Society, London, Special Publications, 199(1), 231-257.

Ziauddin, M., 1975. The acid volcanic and pyroclastic rocks (Champion Gneiss and Autoclastic agglomerate) of the Kolar Schist Belt (Karnataka and Andhra States) in Studies in Precambrians, (Ed.) C.

Chapter 4

Multiple sulfur isotope geochemistry of the Dharwar Supergroup, Southern India

Abstract

Earth's tectonic and climatic systems may have changed fundamentally before the Great Oxidation Event (GOE) at about 2.3 Ga. Sulfur Mass Independent Fractionation (S-MIF) has demonstrated that Earth's atmosphere was virtually oxygen-free before the GOE. During 3.0 to 2.4 Ga, the change in $\Delta^{33}S$ and $\Delta^{36}S$ signals may reflect the perturbation of atmospheric chemistry, though the mechanisms of the change are uncertain. Here, we reported multiple sulfur isotopic studies of Archean volcano-sedimentary sequences of the Dharwar Supergroup, distributed in the Chitradurga Schist Belt (CSB), Southern India. New field mapping and zircon U-Pb dating allows us to reconstruct detailed lithostratigraphy of the Dharwar Supergroup. The lower unit consists of post-3.0 Ga conglomerate, stromatolitic carbonate, siliciclastics with diamictite, chert/BIF and pillowed basalt in ascending order, all of which are older than the 2676 Ma dacite dyke that had intruded into the lower unit. The upper unit unconformably overlies the pillow basalts at the top of the lower unit, and consists of conglomerate/sandstone with ~ 2600 Ma detrital zircons, komatiitic basalt, BIF and siliciclastic sequence with mafic volcanics. Sulfur isotope analysis of extracted sulfides show MIF signals ($\Delta^{33}S > +1‰$) with clear $\Delta^{33}S$-$\Delta^{36}S$ correlations. The lower group of the Dharwar Supergroup shows a $\Delta^{36}S/\Delta^{33}S$ slope of –1.48, the middle group shows –1.16 and –1.07, and the upper group shows –0.94. Reassessment of all the Archean S-MIF records from sedimentary rocks indicates that the $\Delta^{36}S/\Delta^{33}S$ slope systematically changed during the Archean period. The observed trend in the Indian section is similar to those of its Pilbara-Kaapvaal equivalents, thus it could reflect a global atmospheric signature. Moreover, the isotopic trend seems to correlate with mid-Archean glaciation. Thus, the $\Delta^{36}S/\Delta^{33}S$ slope could be a useful tracer for atmospheric chemistry and its link with climate change before the GOE.

4-1. Introduction

The late Archean is an important period regarding the Earth's environmental changes. Before the GOE, the atmosphere was probably reducing with trace amounts of molecular oxygen based on the presence of sulfur mass independent fractionation (S-MIF) in pre-2.3 Ga rocks (Farquhar et al., 2000). Sulfur has 4 stable isotopes (^{32}S, ^{33}S, ^{34}S and ^{36}S). Isotope fractionations by biological or inorganic processes show mass-

dependent fractionation ($\delta^{33}S \approx 0.5 \times \delta^{34}S$; $\delta^{36}S \approx 1.9 \times \delta^{36}S$; Hulston and Thode, 1965). S-MIF is known to be produced by SO_2 photolysis in a low oxygen atmosphere based on previous photochemical experiments (Farquhar et al., 2001; Ono et al., 2013; Endo et al., 2015). Based on atmospheric model calculations, it has been hypothesized that the SO_2 photolysis in an anoxic atmosphere would have resulted in two isotopically distinct sulfur aerosols (i.e. sulfate with negative $\Delta^{33}S$ and elemental sulfur with positive $\Delta^{33}S$) that were transferred to and preserved in sediments when the atmosphere was anoxic ($O_2 < 1$ ppm; Pavlov and Kasting, 2002; Ono et al., 2003).

The Archean $\Delta^{33}S$ record exhibits clear changes in the magnitude of MIF over time: minimum $\Delta^{33}S$ at around 2.9 Ga, subsequent large $\Delta^{33}S$ variations culminating at 2.5 Ga, followed by its sudden drop in the Paleoproterozoic. The change in $\Delta^{33}S$ signature may possibly reflect a fluctuation in oxygen levels (Ono et al., 2006a), the presence of large volcanic eruptions (Ohmoto et al., 2006), speciation of volcanic gasses (SO_2/H_2S ratio; Halevy et al., 2010) and/or other changes in atmospheric chemistry (Farquhar et al., 2007; Domagal-Goldman et al., 2008; Thomazo et al., 2009; Zerkle et al., 2012; Claire et al., 2014). In addition, the atmospheric $\Delta^{33}S$ value can be diluted by mixing it with mass-dependent sulfur compounds (Ono et al., 2003, Penniston-Dorland et al., 2008, Guy et al., 2012). So far, it has been difficult to decouple the $\Delta^{33}S$ variations caused by atmospheric processes from other reactions in subsequent processes (biology, photolysis, mixing, open system, etc.) before sedimentation (Halevy et al., 2013).

The $\Delta^{36}S/\Delta^{33}S$ ratio may be able to give us additional information about past atmospheric chemistry because mass dependent processes cannot change the $\Delta^{36}S/\Delta^{33}S$ ratio significantly. Farquhar et al. (2007) used $\Delta^{36}S/\Delta^{33}S$ to distinguish MIF and MDF processes. Mass dependent processes can also produce small non-zero $\Delta^{36}S$ and $\Delta^{33}S$ values, but show a characteristic $\Delta^{36}S/\Delta^{33}S$ ratio theoretically predicted at about –7 (Ono et al., 2006b). On the other hand, mass independent processes that occurred during the Archean show a different $\Delta^{36}S/\Delta^{33}S$ ratio from –1 to –1.5. The mechanism to change the $\Delta^{36}S/\Delta^{33}S$ ratio is still uncertain, though it could potentially reflect the change in atmospheric chemistry before the GOE event (Farquhar et al., 2007).

Geographically, most of the Archean MIF records measured so far are mainly derived from Pilbara Craton, Western Australia and Kaapvaal Craton, South Africa.

However, several paleomagnetic and lithostratigraphic studies suggested that Pilbara and Kaapvaal Craton might have been part of the same continent during the late Archean (e.g., Cheney et al., 1996). Therefore, it is possible that the $\Delta^{36}S/\Delta^{33}S$ ratio may only reflect local changes and not necessarily global events. In order to distinguish the local and global signatures, it is necessary to study other late Archean sections around the world.

Apart from the two cratons, 3.2 to 2.5 Ga volcano-sedimentary sequences are well exposed in continuous stratigraphic successions in the Chitradurga Schist Belt (CSB) in Western Dharwar Craton, Southern India (Fig. 1; e.g. Swaminath and Ramakrishnan, 1981). Our previous lithostratigraphic and geochronological investigations (Hokada et al., 2013) suggest that the depositional setting of the Dharwar Supergroup is different from that of its Pilbara-Kaapvaal equivalent during the late Archean (Fig. 2). For example, the manganiferous nature of the Chitradurga BIF is not observed in its Pilbara-Kaapvaal counterparts. The lithostratigraphic difference and metamorphic history suggest that the Dharwar Craton was geographically separate from the Pilbara-Kaapvaal Craton (Hokada et al., 2013). Moreover, Bleeker et al. (2003) suggested that Dharwar Craton was part of the Slave Craton, which was different from Kaapvaal Craton at ~2.6 Ga.

In this paper, we report detailed lithostratigraphy of the Dharwar Supergroup that appeared in the CSB together with multiple sulfur isotope geochemistry of the strata. We have conducted a detailed field mapping in the schist belt during several field seasons that have been carried out since 2010. Based on our sedimentological observations, we discuss the link between depositional settings and the multiple sulfur isotope record, and then test the global nature of the S-MIF signals by comparing the data from Pilbara and Kaapvaal Cratons.

4-2. Geological setting

The Dharwar Craton of southern India consists of Archean gneiss of tonalitic-trondhjemitic-granodioritic (TTG) composition, volcano-sedimentary sequences and calc-alkaline to high-potassic granitoids (Chadwick et al., 2000; Jayananda et al., 2006). The Dharwar Craton has been divided into two blocks: Western Dharwar and Eastern Dharwar Cratons. The Western Dharwar Craton is dominated by an older basement (Peninsular Gneiss interlayered with >3.0 Ga Sargur Group), which is unconformably

overlain by Dharwar Supergroup (2.9-2.6 Ga). High-potassic granitic plutons (2.61Ga) are minor parts of Western Dharwar Craton. The Peninsular Gneiss occurs mainly in the southern part of this region. In contrast, the Eastern Dharwar Craton comprises a younger TTG basement (2.7 Ga) with small remnants of >3.0 Ga TTG, thin elongated 2.7 Ga greenstone belts and abundant 2.55-2.52 Ga calc-alkaline to high-potassic intrusions (Jayananda et al., 2006).

The Chitradurga Schist Belt (CSB) is located at the eastern margin of the Western Dharwar Craton where the two cratons are separated by the steep mylonitic zone, Chitradurga Shear Zone (CSZ; Fig. 4-1). The CSB is the type locality of the Chitradurga Group that comprises the upper part of the Dharwar Supergroup. Well preserved late Archean sedimentary sequences and structures are exposed in this schist belt.

4-2-1. Chitradurga Schist Belt (CSB)

The CSB extends to a length of over 400 km with an average width of 15 km and attains a maximum width of 40 km in the central region (Fig. 4-1). Three important steeply-dipping faults cut across the entire CSB (Fig. 4-1). The CSB consists of two generations of greenstone sequences: >3.0 Ga older greenstone sequences known as the Sargur Group and 2.9-2.5 Ga younger volcano-sedimentary sequences known as the Dharwar Supergroup. Both of the greenstone-sedimentary sequences are surrounded by >3.0 Ga TTG gneiss (Chadwick et al., 2000; Jayananda et al., 2006). Generally, the Dharwar Supergroup is divided into two groups: Bababudan Group and Chitradurga Group. The Chitradurga Group is divided into three formations: Vanivilas Formation, Ingaldhal Formation, and Hiriyur Formation, in ascending order (Swaminath and Ramakrishnan, 1981). Based on our field mapping of over 5 years, including detailed logging, sampling and petrological study, the Dharwar Supergroup is subdivided into a lower unit (Bababudan Group, Vanivilas Formation and Ingaldhal Formation) and an upper unit (Hiriyur Formation), which are separated by a major unconformity (Hokada et al., 2013).

The Sargur Group, which is the oldest group in the Dharwar Craton, comprises komatiite, tholeiitic amphibolites, BIF, garnet-biotite schist with kyanite, sillimanite and staurolite, calc-silicate and fuchsite quartzite with barite (Swaminath and Ramakrishnan,

1981). The Sargur Group is only exposed along the western and eastern margins in the CSB. The metamorphic conditions of the Sargur Group are estimated to be low-T/high-P based on the appearance of kyanite and lack of biotite in quartzite (Hokada et al., 2013). A Sm-Nd age of 3352 ± 110 Ma from komatiite was reported by Jayananda et al. (2008), which is considered to be the formation age of the Sargur Group. Furthermore, monazite U-Th-Pb dates of kyanite-muscovite quartzite samples yield a comparable age of 3200-3000 Ma (Hokada et al., 2013).

The Bababudan Group is the lowest part of the Dharwar Supergroup. The basal conglomerate of the Bababudan Group, named Neralekatte conglomerate, overlies the Peninsular Gneiss with a profound unconformity. The conglomerate is overlain by alternated amygdular metabasalt and cross-bedded quartzite, pelite and BIF (Swaminath and Ramakrishnan, 1981). In the CSB, the Bababudan Group is exposed in a narrow zone near southeast Talya, on the eastern flank of the Sirankatte dome and the southern part of the CSB. Carbonate and dolomitic BIF layers are exposed on the eastern side of Sirankatte dome, and well-preserved stromatolites were observed on the southern flank of the CSB (Fig. 1). The occurrence of the stromatolite and cross-bedded sandstones suggest that the depositional setting of the Bababudan Group is a shallow marine environment such as a marginal basin (Drury, 1983). The depositional age of the Bababudan Group is estimated to be younger than 3137 ± 7 Ma and 3178 ± 61 Ma based on detrital zircon U-Pb dates and monazite U-Th-Pb dates, respectively (Hokada et al., 2013).

Vanivilas Formation is the lowest unit of the Chitradurga Group. Predominant polymict conglomerate marks the transition from the Bababudan to the Chitradurga Groups through a horizon of siliceous schists. The basal rock unit, called Talya conglomerate, is a partially thick oligomictic diamictite distributed in the western margin of the CSB and the eastern limb of the Sirankatte dome. The lithologies of the Vanivilas Formation change from stromatolitic carbonates to conglomerate, chlorite schist, quartzite, ferruginous chert and BIF (Swaminath and Ramakrishnan, 1981), suggesting that the depositional setting shifted from a shallow marine to a distal marine environment. BIF and Talya conglomerate are useful in determining the stratigraphic relation of the Vanivilas Formation to other locations in the CSB. The depositional age of the Vanivilas Formation is estimated to be younger than 3168 ± 7 Ma or 2919 Ma based on detrital

zircon U-Pb dates (Hokada et al., 2013). On the other hand, Naqvi (1985) suggests there is no time gap between the Bababudan and Chitradurga Group. Moreover, Radhakrishna (1983) proposed that, within this belt, the Bababudan and Chitradurga Groups are merely two different facies that formed in two different environments at the same time.

Ingaldhal Formation conformably overlies the Vanivilas Formation. This formation comprises basic pillow lavas, volcaniclastic sediments and BIF (Swaminath and Ramakrishnan, 1981). It is mainly exposed in the central part of the CSB. The thick pillow lava of the Ingaldhal Formation was often intruded by metafelsic volcanics. Zircons from these felsic volcanics yielded a U-Pb age of 2676 ± 10 Ma (Hokada et al., 2013), indicating that the Ingaldhal Formation was deposited before 2.68 Ga.

Hiriyur Formation occurs mainly in the eastern part of the CSB. The K. M. Kere conglomerate is the basal conglomerate of the Hiriyur Formation that unconformably overlies the Ingaldhal Formation. In the K. M. Kere conglomerate, a fining-upward sequence of conglomerate-sandstone-mudstone is repeated several times. These clastic rocks are overlain by mafic volcanic rocks, BIF and laminated greywacke in stratigraphic order. The U-Pb ages of detrital zircon from metasandstone in the K. M. Kere conglomerate indicate that the clastic sediments were deposited after 2633 ± 12 Ma (Hokada et al., 2013). The youngest U-Pb ages of detrital zircon from metagreywacke in the Hiriyur Formation indicates that the clastic sediments were deposited after 2546Ma (Nasheeth et al., 2016). The eastern margin of the Hiriyur Formation was bound by the Eastern Dharwar Craton that collided with the CSB at ~2.5 Ga based on geochronology of granites (Jayananda et al., 2013). Numerous east-west-trending dyke swarms younger than 2369 Ma cross cut the entire CSB (French et al., 2010). The mineral assemblages in pelitic and psammitic units imply that the metamorphic conditions of all formations in the Chitradurga Group are relatively low-grade (Hokada et al., 2013).

4-2-3. Samples

In this study, the stratigraphy of the Dharwar Supergroup in the CSB followed earlier studies (Chadwick et al., 1981) and the field relations observed in our own field work. To evaluate the sulfur isotope composition across the Dharwar Supergroup, we studied several stratigraphic sections from the CSB. The stratigraphic correlation for these

sections was made using 3 banded iron formations and 4 conglomerate layers as key beds. The base of the K. M. Kere conglomerate is a major unconformity between the upper unit (Hiriyur Formation) and the lower unit (Bababudan Group and Vanivilas Formation). A total of 44 sedimentary rocks and 3 igneous rocks containing sulfide minerals were selected for sulfur isotope analyses in this study. Sample localities are shown in Figs 1 and 2.

A total of 8 samples (7 quartzites and 1 marble) were collected from the Sargur Group in the same area and were analyzed for sulfur isotopes (Fig. 1). Quartzite and fuchsite quartzite samples composed of kyanite + muscovite + quartz were collected from a quarry south of Talya where quartzite with kyanite layers are interbedded. Sheared amphibolites and Peninsular Gneiss are exposed in the surrounding area. The marble layer is ~10 m thick and is interlayered with amphibolites. Fine euhedral pyrites are found in the quartzite.

Fifteen carbonate rocks of the Bababudan Group were analyzed from two sections in the CSB. The 11 samples were analyzed from the eastern part of the Sirankatte dome, where ~200 m thick dolomite were exposed. The remaining 4 samples were collected from the southern part of the CSB. The carbonate rocks include disseminated pyrites with a few anhedral pyrites in the fine laminae (Fig. 4-3). ~1 m thick layers of dolomitic sandstone and black chert were observed interlayered within the dolomite. The dolomite layer shows gradational contact with overlying mudstone and is subsequently overlain by metabasalt and BIF.

A total of 7 samples from the Vanivilas Formation were used for sulfur isotope analyses. Three samples (09st2, 08st1-1, 08st3-3) were collected from the western limb of the CSB, while one sample is from a black quartz pebble in the Talya conglomerate. Three carbonate rocks (1210Y-11, 1210Y-5, 10st4-4) and a chert sample (15st5-2) were collected from the eastern part of the Sirankatte dome. All Vanivilas Formation samples are from the Talya conglomerate layer.

Thirteen samples were analyzed from the Ingaldhal Formation. Six samples (E50, E51, E54, 12st3-4, 12st4, 10st6-1) were collected from volcanic rocks and cover volcaniclastic sediments (Fig. 4-1). Seven samples (1414M-5, 1414M-6, 1414M-7) were collected from a BIF layer within the pillow basalts.

From the Hiriyur Formation, 13 samples were used for analyses. The samples are mainly from three sections (Fig. 4-1). Four clastic samples (11st6-2, 1211Y-9, 1213Y-6 and 13st3-2) were collected along the basal rock unit (K.M. Kere conglomerate) of the Hiriyur Formation, which occurs above the pillow lava of the Ingaldhal Formation. 11st6-1 is a black chert pebble from the K. M. Kere conglomerate, thought to have originated from ferruginous chert interlayered in pillow lava. A black chert (13st1-2) was collected from just below the BIF, suggesting distal marine sediments. Seven proximal mudstone samples (22st3-1, 22st3-2, 22st3-3 and M15-57a, b, c) that were collected from the pyrite-bearing mudstone are intercalated with coarse cross-laminated sandstone, suggesting a proximal marine setting.

The Dharwar Supergroup has experienced low-grade metamorphism (Hokada et al., 2013). Sulfide minerals occur mainly as disseminated pyrite or recrystallized euhedral pyrite (Fig. 3). Disseminated pyrite ranges from a few μm to a few mm in diameter. Diagenetic pyrite can display a number of different morphologies and sizes, from very fine-grained crystallites to large concretions and nodules. Most pyrite grains seem to have been recrystallized during metamorphism, though the samples are carefully selected to avoid veins, fractures and lithological contacts.

4-3. Sulfur Isotope Analysis

Rock samples were cut into slabs and the weathered surfaces were removed. Slabs were crushed into small chips about 1 cm^3. The chips were ultrasonically cleaned with distilled water. Cleaned chips were dried in an oven at 100ºC overnight, and were then crushed using a stainless-steel mortar, and subsequently powdered with an agate mortar. Sulfide was extracted using a method modified from Hsieh and Shieh (1997). A powdered rock sample (2-10 g) and alkaline Zn trap (3:5 mixture of 0.2M zinc acetate and 2M NaOH solution) were placed in a glass bottle with two stopcocks. The bottle was initially purged by nitrogen gas, and then the sample was reacted with 15 ml 5M HCl at room temperature. In this process, acid volatile sulfur (AVS) was selectively converted to H_2S. The H_2S was precipitated as zinc acetate in an alkaline Zn trap. Our samples have only a small amount of AVS, and thus were not processed further. Subsequently, the sample powder was reacted with 20 ml chromium (II) solution with HCl for >24 h at room

temperature (Canfield et al., 1986). In this process, chromium (II)-reducible sulfur (CRS) was converted to ZnS similar to AVS. In the case of low sulfide content, more than 20 g of sample powder is required to yield enough sulfur for isotope analysis. In this case, we extracted sulfide in several batches with the same alkaline Zn trap. The ZnS was then converted to silver sulfide (Ag_2S) by reaction with 0.1 M $AgNO_3$ solution. The Ag_2S precipitate was cleaned by repeated centrifugation using distilled water and dried at 80ºC overnight.

The Ag_2S powder (0.1 - 2 mg) is converted into SF_6 by reaction with about 300 torr of purified elemental fluorine overnight in a nickel reaction vessel (Ueno et al., 2015). The resulting SF_6 was purified by vacuum line and gas chromatography. Purified SF_6 was introduced into a mass spectrometer to measure sulfur isotopes ($^{32}SF_5^+$, $^{33}SF_5^+$, $^{34}SF_5^+$ and $^{36}SF_5^+$). Large volume (6 - 8 μmol) samples were measured using a normal inlet system of the Thermo-Fischer MAT-253 mass spectrometer, whereas smaller volume samples (<4 μmol) were measured using an external micro-volume inlet directly connected by a capillary tube to the ionization chamber of the mass spectrometer. All data are reported in ‰ as

$$\delta^{34}S = 1000 \times ({}^{34}R_{sample}/{}^{34}R_{standard} - 1)\ ‰ \quad (1)$$

$$\Delta^{33}S = 1000 \times \ln(\delta^{33}S/1000 + 1) - 0.515 \times 1000 \times \ln(\delta^{34}S/1000 + 1)\ ‰ \quad (2)$$

$$\Delta^{36}S = 1000 \times \ln(\delta^{36}S/1000 + 1) - 1.90 \times 1000 \times \ln(\delta^{34}S/1000 + 1)\ ‰ \quad (3)$$

These values are normalized against V-CDT, assuming IAEA-S1 has a composition on the VCDT scale of $\delta^{34}S = -0.3‰$, $\Delta^{33}S = 0.100‰$, and $\Delta^{36}S = -0.91‰$ (Ding et al., 2001; Ono et al., 2007). The analytical reproducibility of $\delta^{34}S$, $\Delta^{33}S$, and $\Delta^{36}S$ values, based on replicate analysis of IAEA-S1, S2, S3 and other in-house silver sulfide standards, is better than ±0.4‰, ±0.02‰ and ±0.5‰, respectively. Note that the definition of capital delta value is different from that used in some previous works ($\Delta^{33}S = \delta^{33}S - 1000 \times [(1 + \delta^{34}S/1000)^{0.515} - 1]$, $\Delta^{36}S = \delta^{36}S - 1000 \times [(1 + \delta^{34}S/1000)^{0.90} - 1]$; Farquhar et al., 2000; Johnston et al., 2007). These two definitions yield practically identical values when variations in $\delta^{34}S$ values are smaller than ±10‰ (Ono et al., 2007).

4-4. Results

The results of isotope analysis are shown in Table 1 and Figs. 4-4 and 4-5. The

sedimentary sulfides of the Dharwar Supergroup show clear mass independent fractionation from –1.2‰ to +3.9‰ for $\Delta^{33}S$ values, except for Sargur Group ($\Delta^{33}S$ = –0.2‰ to +0.1‰). The extreme $\Delta^{33}S$ values were found in the upper Ingaldhal Formation and the youngest Hiriyur formation. The $\delta^{34}S$ values had a narrow range and were within ±5‰, except for carbonates from the Bababudan Group and BIF from the Ingaldhal Formation, which show a wider range of $\delta^{34}S$ values from –10.9‰ to +19.4‰ (Figs. 4-4 and 4-5). In general, the $\Delta^{36}S$ values are negatively correlated with the $\Delta^{33}S$ values (Fig. 4-5). In each stratigraphic unit, the $\Delta^{36}S$-$\Delta^{33}S$ relation shows a distinct trend: The Bababudan Group, Vanivilas Formation, Ingaldhal Formation and Hiriyur Formation show a $\Delta^{36}S/\Delta^{33}S$ slope of –1.48 ± 0.21, –1.16 ± 0.13, –1.07 ± 0.13 and –0.94 ± 0.06, respectively. These $\Delta^{36}S/\Delta^{33}S$ slopes are within the range of previously reported values from the late Archean strata (Farquhar et al., 2000, 2007, Kaufman et al., 2007; Zerkle et al., 2012; Ono et al., 2009; Thomazo et al., 2009; Izon et al., 2015). In order to compare our results with the previous data from Pilbara and Kaapvaal Craton, we have recalculated the published $\Delta^{33}S$ and $\Delta^{36}S$ values according to the logarithmic definition and obtained a $\Delta^{36}S/\Delta^{33}S$ ratio for each stratigraphic unit (Table 2, Fig. 4-7B).

4-5. Discussion

4-5-1. Multiple sulfur isotope ratio in open marine environment

Total sulfide in the 2.6-2.5 Ga Hiriyur Formation shows correlations between $\Delta^{33}S$ and $\Delta^{36}S$ ($\Delta^{36}S = -0.94\Delta^{33}S - 0.23$; $R^2 = 0.97$), even though the sulfides are from various types of sedimentary rocks including BIF, chert, mudstone and sandstone (Fig. 4-5A). These sedimentary rocks are deposited in various environmental settings; for example, chert and BIF are likely deposited in a distal marine environment, whereas clastic rocks are in a more proximal marine environment. The constant $\Delta^{36}S/\Delta^{33}S$ ratios irrespective of depositional settings indicate that the MIF-yielding mechanism was not local and constant during the period from 2.6 to 2.5 Ga. The MIF signal is mixed in the ocean, which supports the theory that the S-MIF originated from atmospheric chemistry at that time. Based on atmospheric model calculations, it has been hypothesized that the SO_2 photolysis in an anoxic atmosphere would have produced two isotopically distinct sulfur aerosols (i.e. sulfate with negative $\Delta^{33}S$ and elemental sulfur with positive $\Delta^{33}S$; Ono et

al., 2003). Subsequently, these isotopic anomalies could have been transferred to and preserved in sediments.

In the Hiriyur Formation, a BIF sample has the largest positive $\Delta^{33}S$ values ($\Delta^{33}S$ = +3.9‰), whereas the clastic rocks in this formation show smaller $\Delta^{33}S$ values ($\Delta^{33}S$ < ±1‰). The positive $\Delta^{33}S$ values were likely derived from SO resulting from $SO_2 + h\nu \rightarrow$ SO + O (Ono et al., 2003). The elemental sulfur resulting from the SO could have been introduced into the ocean and undergone disproportionation into sulfide and sulfate, either by biotic or abiotic processes (Ono et al., 2003). Thereafter, the sulfide reacted with Fe^{2+} to form pyrite, particularly from ferruginous seawater where the BIF was deposited. Although both abiotic and biotic disproportionation reactions may involve isotope fractionation, these processes are mass dependent and thus do not yield MIF (Johnston et al., 2007). Thus, the large positive $\Delta^{33}S$ value in the BIF likely reflects the $\Delta^{33}S$ value of the atmospheric input. The inferred atmospheric origin is consistent with the depositional age of the Hiriyur Formation when a large positive $\Delta^{33}S$ signal has been reported from various other strata of 2.6-2.5 Ga age (Kaufman et al., 2007; Zerkle et al., 2012; Izon et al., 2015).

On the other hand, the negative and smaller $\Delta^{33}S$ values in clastic rocks suggest the contribution of mass-dependent sulfur ($\Delta^{33}S$ = 0‰) or a negative $\Delta^{33}S$ component that can be derived from sulfate aerosol (Ono et al., 2003). The sulfate deposition into the ocean could have been converted into sulfide through microbial sulfate reduction. When these sulfides with negative $\Delta^{33}S$ values are incorporated into the sulfide pool, they dilute the positive $\Delta^{33}S$ values in the proximal marine environment. If we assume microbial sulfate reduction, the observed narrow range of $\delta^{34}S$ values from −1.3‰ to 2.9‰ in the Hiriyur Formation (Fig. 4-4) suggest low sulfate concentration favoring smaller isotopic fractionation during microbial reduction, which is consistent with previous estimations of seawater sulfate concentration being below 200 μM, or possibly 2.5 μM, depending on the species (Habicht et al., 2002; Crowe et al., 2014; Bradley et al., 2016). Alternatively, input of igneous sulfur may also dilute the S-MIF signal and produce the small $\Delta^{33}S$ values as well as small scatter of $\delta^{34}S$ values. However, small but clearly negative $\Delta^{33}S$ values cannot be explained by mixing of the igneous sulfur.

In contrast, Paris et al. (2014) reported that carbonate-associated sulfate (CAS) of

2.55 Ga microbial carbonate shows positive $\Delta^{33}S$ values. This may suggest that the late Archean seawater sulfate acquired a positive $\Delta^{33}S$ value at least temporally or locally. The seawater isotopic composition is discussed in the subsequent sections.

During the period from 2.8 to 2.7 Ga, the sedimentary sulfides of the Vanivilas Formation also show a negative correlation between $\Delta^{33}S$ and $\Delta^{36}S$ ($\Delta^{36}S = -1.16 + \Delta^{33}S - 0.08$; $R^2 = 0.94$) (Fig. 4-5E), though the $\Delta^{36}S/\Delta^{33}S$ ratio has a smaller slope than that of the Hiriyur Formation. The cause of the variations in the slope will be discussed in detail later. Similar to the Hiriyur Formation, sulfides in the distal marine settings in the Vanivilas Formation show larger and more positive $\Delta^{33}S$ values in comparison to the proximal clastic sediments (Fig. 4-5). The similarity in isotopic distribution pattern suggests that similar MIF-yielding mechanisms and preservation processes would have operated during the older period.

4-5-2. Microbial sulfate reduction in closed marine environment

The sedimentary sulfides in carbonate rocks of the Bababudan Group (3.0-2.7 Ga) show both positive and negative $\Delta^{33}S$, and a wide range of $\delta^{34}S$ (from −2.4‰ to +19‰) (Fig. 4-4). The non-zero $\Delta^{33}S$ values indicate the contribution of atmospheric sulfur components. Nevertheless, the photochemical reaction alone cannot explain the wide range of $\delta^{34}S$ values in the carbonate rocks because the $\delta^{34}S$ values do not linearly correlate with $\Delta^{33}S$ values (Fig. 4-5H). Instead, the wide range of $\delta^{34}S$ values with negative $\Delta^{33}S$ may have resulted from a mass dependent fractionation such as microbial sulfate reduction. If microbial sulfate reduction under elevated sulfate concentrations occurred during the deposition of the Bababudan carbonate rocks, the negative $\Delta^{33}S$ values were derived from sulfate. The sulfide that was produced by the microbial sulfate reduction has reacted with dissolved Fe^{2+} and been deposited in the sedimentary rocks as sulfides. Assignment of negative $\Delta^{33}S$ values for Archean seawater sulfate is consistent with the previous interpretation that atmospheric sulfate aerosol acquired negative $\Delta^{33}S$ values (Farquhar et al., 2000; Pavlov and Kasting, 2002; Ono et al., 2003). On the other hand, the observed ^{34}S-enrichment up to +19‰ of sulfide in the Bababudan carbonate exceeded the previous estimate of seawater sulfate ($\delta^{34}S$ value from +5‰ to +15‰; Ono et al., 2003; Ueno et al., 2008) in the Archean. This indicates sulfate reduction in a closed

system with respect to seawater sulfate. The sedimentary environment of the Bababudan carbonate is consistent with the restricted shallow marine environment.

The sedimentary sulfide in the Bababudan carbonate rocks show the $\Delta^{33}S$ values from −1‰ to +1‰ with a $\Delta^{36}S/\Delta^{33}S$ slope of −1.48 ± 0.21 ($R^2 = 0.83$) (Fig. 4-5G). If the observed $\Delta^{36}S/\Delta^{33}S$ ratio preserves the initial photochemical reaction ratio, the mixing between photochemical sulfur should have exhibited a linear $\Delta^{36}S/\Delta^{33}S$ array. However, the $\Delta^{36}S$-$\Delta^{33}S$ relation is rather scattered, especially for sulfide with the negative $\Delta^{33}S$ values (Fig. 4-6B). This may suggest the influence of secondary mass-dependent fractionation such as microbial sulfate reduction. Mass-dependent processes can also produce small non-zero $\Delta^{36}S$ and $\Delta^{33}S$ values characterized by a $\Delta^{36}S/\Delta^{33}S$ ratio theoretically predicted to be about –7 (Ono et al., 2006b). Zhelezinskaia et al. (2014) also reported $\Delta^{36}S/\Delta^{33}S = –7$ by in situ analysis of pyrites in 2.5 Ga carbonate sequence (Babatal Formation, Brazil), suggesting the activity of microbial sulfate reduction at that time.

In order to evaluate the isotopic evolution through microbial sulfate reduction, we calculate the isotopic composition of cumulative sulfide produced by sulfate reduction assuming a closed system using batch Rayleigh equations in quadruple sulfur isotopes:

$$(\delta^{3x}S_{sulfide}/1000 + 1) = (\delta^{3x}S_{BS}/1000 + 1) \times (1 - f^{3x\alpha})/(1 - f) \quad (4)$$

where $^{3x}\alpha$ is the fractionation factor, $\delta^{3x}S_{BS}$ is the initial isotopic composition of sulfate in Bababudan basin, $\delta^{3x}S_{sulfide}$ is the cumulative sulfur isotopic compositions of the product sulfide, and f is the remaining fraction of sulfate. Note that we measure bulk or averaged isotopic composition of each sedimentary layer rather than measure each grain of pyrite in the sediment. Thus, we aim to compare measured bulk isotopic composition with estimated accumulative sulfides as a function of the remaining fraction of the sulfate pool, rather than calculating the isotopic evolution of each pyrite grain. Combining Eqs. (2), (3) and (4), the $\Delta^{33}S$ and $\Delta^{36}S$ values of accumulative sulfide can be written as the following equation:

$$\Delta^{33}S_{sulfide} = 1000 \cdot \ln\{(1 - f^{33\alpha})/(1 - f)\} - 0.515 \times 1000 \cdot \ln\{(1 - f^{34\alpha})/(1 - f)\} + \Delta^{33}S_{ss} \quad (5)$$

$$\Delta^{36}S_{sulfide} = 1000 \cdot \ln\{(1 - f^{36\alpha})/(1 - f)\} - 1.9 \times 1000 \cdot \ln\{(1 - f^{34\alpha})/(1 - f)\} + \Delta^{36}S_{ss} \quad (6)$$

To explain the wide range of $\delta^{34}S$ of sedimentary sulfide in the Bababudan carbonates, we use a $^{34}\alpha = 0.9707$ using a maximal spread in $\delta^{34}S$ between sulfate and sulfide during the microbial sulfate reduction (Johnston et al., 2007). Furthermore, in order to explain the observed $\Delta^{33}S$ and $\Delta^{36}S$ values of the Bababudan carbonate, we use $^{33}\alpha = 0.9849$ and $^{36}\alpha = 0.9432$ that are the most fractionated values observed so far in previous incubation experiments of microbial sulfate reduction (Johnston et al., 2007).

The magnitude of the effect on $\delta^{34}S$, $\Delta^{33}S$ and $\Delta^{36}S$ during a mixing of two sulfur pools (A and B), producing a new sulfur pool C is given as

$$\ln (\delta^{34}S_C/1000 + 1) = f' \times \ln (\delta^{34}S_A/1000 + 1) + (1 - f') \times \ln (\delta^{34}S_B/1000 + 1),$$

$$\Delta^{33}S_C = 1000 \times \ln \{f' (^{33}\alpha - 1) + 1\} - 0.515 \times 1000 \times \ln \{f' (^{34}\alpha - 1) + 1\} + \Delta^{33}S_B,$$

$$\Delta^{36}S_C = 1000 \times \ln \{f' (^{36}\alpha - 1) + 1\} - 1.9 \times 1000 \times \ln \{f' (^{34}\alpha - 1) + 1\} + \Delta^{36}S_B,$$

where f' is the ^{32}S normalized mixing ratio of the two initial sulfur reservoirs (Ono et al., 2006b). The observed $\delta^{34}S$, $\Delta^{33}S$ and $\Delta^{36}S$ values in the Bababudan carbonates were explained by considering a mixing of (A) the sulfide generated from microbial sulfate reduction from a negative $\Delta^{33}S$ sulfate pool and (B) a sulfide showing a positive $\Delta^{33}S$ value derived from the atmosphere.

Using the batch distillation model, the observed ^{34}S-enrichment of the sulfides in the Bababudan carbonate can be explained if the $\delta^{34}S$ and $\Delta^{33}S$ values of Bababudan sulfate are from +23‰ to +33‰ and from −1.0‰ to −1.7‰, respectively (Fig. 6A). This estimated $\delta^{34}S$ value of Bababudan sulfate is larger than those of the previously estimated Archean sulfates (+5 to +15‰; Ono et al., 2003), whereas the $\Delta^{33}S$ value is close to them. This difference between Bababudan sulfate and estimated Archean seawater sulfate $\delta^{34}S$ values may possibly reflect a residual pool of sulfate driven strongly by the Rayleigh effects, causing isotopic heterogeneity in a water column. The observed ^{34}S-enriched sulfides indicate that most sulfate had been reduced, perhaps in a restricted ocean basin. On the other hand, the scattered $\delta^{34}S$ sulfide values imply that the system is not completely closed. Thus, the observed $\delta^{34}S$ values reflect that the Bababudan deposition occurred in a marginal marine environment, consistent with the geological evidence.

Using the batch distillation model, we also explain the scatter around the $\Delta^{36}S/\Delta^{33}S$ slope of −1.5 for the sulfides in the Bababudan carbonate (Fig. 4-6). The Bababudan sulfide with negative $\Delta^{33}S$ values was generated from atmospheric sulfate (AS) through

microbial sulfate reduction (MSR). Thus, the observed isotopic compositions of sulfide in the Bababudan carbonate reflect mixing between the atmospheric sulfide (AS') and MSR sulfide. Using the batch distillation model, Fig. 6B shows the results of calculations for the evolution of sulfur isotope compositions and the possible mixing range. An estimated $\Delta^{36}S$ value of Bababudan sulfate (from +3.5‰ to +2.3‰) can explain the observed variations in the sulfide in the Bababudan carbonate. Assuming the observed sulfide with the highest $\Delta^{33}S$ value represents the initial atmospheric $\Delta^{36}S/\Delta^{33}S$ ratio in elemental sulfur, the estimated $\Delta^{36}S/\Delta^{33}S$ ratio of Bababudan sulfate deviates from the atmospheric fractionation line ($\Delta^{36}S/\Delta^{33}S = -1.5$) (Fig. 4-6C). This deviation may result from MSR activity. The sulfide generated by MSR reacted with Fe^{2+} to form pyrite and was deposited in sediments. Residual seawater sulfate (SWS) must be enriched in ^{34}S by the microbial fractionation (f = 0.4 and 0.5). This $\delta^{34}S$-enriched seawater (Bababudan sulfate: $\delta^{34}S$ = +23‰; Fig. 4-6) could be the source of the sulfide deposited in the Bababudan restricted basin.

4-5-3. Multiple sulfur isotope ratio in Ingaldhal Formation

The observed sulfides in the Ingaldhal BIF show negative $\Delta^{33}S$ (−1.2‰ to −0.9‰) and scattered $\delta^{34}S$ values from −4.9‰ to −10.9‰ and $\Delta^{36}S$ values from +0.0‰ to −1.9‰. The observed constant negative $\Delta^{33}S$ and negative $\delta^{34}S$ with about 6‰ variation are all consistent with microbial sulfate reduction. The $\Delta^{36}S$ variation down to −1.9‰ (Fig. 4-5C) can also be produced by microbial sulfate reduction, particularly in an open system, which is in contrast with Bababudan carbonate where all the pyrites are on the same trend ($\Delta^{36}S = -1.5\ \Delta^{33}S$; Fig. 4-5G) even though both the pyrites in Ingaldhal BIF and Bababudan carbonate would have been formed by sulfate reduction. The Bababudan pyrites show more positive $\delta^{34}S$ with larger variation (>20‰) than those of Ingaldhal BIF. The difference may have resulted from the contrasting depositional settings. Ingaldhal BIF deposited in an open marine setting where sulfate reduction would have proceeded in an open system, whereas Bababudan stromatolitic carbonate was deposited in a shallower photic zone where sulfate may have been limited in the restricted basin.

On the other hand, volcaniclastic sediment in the Ingaldhal Formation shows large positive $\Delta^{33}S$ values (+2.4‰ to +3.9‰). The volcaniclastic sediments seem to capture the

positive $\Delta^{33}S$ source better than anything else in Dharwar Supergroup. If the $\Delta^{36}S/\Delta^{33}S$ slope has been produced by mixing between the igneous sulfide and atmospheric sulfide, the slope is –1.07 ± 0.13 at ~2.7 Ga.

4-5-4 Global $\Delta^{36}S/\Delta^{33}S$ trend

The sedimentary sulfides in the Dharwar Supergroup show a distinct $\Delta^{36}S/\Delta^{33}S$ change in their slope from –1.48 ± 0.21 to −0.94 ± 0.06 through the late Archean. As discussed above, the S-MIF was originally generated from atmospheric reactions, however, it is not certain whether the change in $\Delta^{36}S/\Delta^{33}S$ slope reflects the atmospheric chemistry or if it is related to other processes that were operating during the Archean. To ascertain the characteristics of the $\Delta^{36}S/\Delta^{33}S$ slope in the late Archean, we compared the Dharwar $\Delta^{36}S/\Delta^{33}S$ slope with that of Kaapvaal and Pilbara Cratons. The slope changes have also been reported from other Archean Cratons (Fig. 4-7B). For example, in the Pilbara Craton, the slopes changed from −1.57 ± 0.14 to – 0.86 ± 0.08 at 2.6-2.7 Ga (Kaufman et al., 2007; Thomazo et al., 2009) and from −0.81 ± 0.02 to −1.06 ± 0.06 at 2.5 Ga (Kaufman et al., 2007). In the Kaapvaal Craton, South Africa, the slopes changed from −1.40 ± 0.72 to – 1.00 ± 0.04 at 2.7-2.5 Ga (Farquhar et al., 2007; Zerkle et al., 2012), from −0.96 ± 0.04 to −1.24 ± 0.05 at 2.6-2.5 Ga (Zerkle et al., 2012; Ono et al., 2009a) and from −0.86 ± 0.08 to −1.52 ± 0.17 at 2.45 Ga (Kaufman et al., 2007). Moreover, Izon et al. (2015) reported several slopes from Kaapvaal and Pilbara Craton at 2.7-2.5 Ga. Similarly, our data from the Bababudan Group and Vanivilas Formation suggests that the slopes before 2.7 Ga were steeper than the slopes after 2.7 Ga (Fig. 4-7B). Such a global signature suggests that the steep slopes before 2.7 Ga shared the same cause, possibly the atmospheric chemistry. On the other hand, after 2.7 Ga, the high-resolution stratigraphic studies of core samples showed some stratigraphical variation of $\Delta^{36}S/\Delta^{33}S$ slopes from ~−0.9 to ~−1.5 (Kaufman e al., 2007; Ono et al., 2009a; Zerkle et al., 2012). Considering the changes of the $\Delta^{36}S/\Delta^{33}S$ slope at 2.7-2.4 Ga in the Kaapvaal and Pilbara Craton, the slopes converge on ~−0.9 at ~2.5 Ga (Fig. 4-7B). Although there were some slope changes for a shorter duration on a smaller scale, the similarities in the slope between the Hiriyur Formation and Pilbara, Kaapvaal Craton suggest that slopes of −0.9 at ~2.5 Ga are a global signature. Kurzweil et al. (2013) also suggested a major

rearrangement in atmospheric chemistry at ~2.73-2.71 Ga from Kidd Creek area, Canada. Thus, the $\Delta^{36}S/\Delta^{33}S$ slope shift from −1.5 to −0.9 at ~2.7 Ga is generated by a global trend strongly controlled by the changing atmospheric chemistry rather than a local and trivial event.

4-5-5. Cause of the $\Delta^{36}S/\Delta^{33}S$ trend

The $\Delta^{36}S/\Delta^{33}S$ slope change at 2.7 Ga was global and could have been caused by changing atmospheric chemistry. However, the observed $\Delta^{36}S/\Delta^{33}S$ slopes from –0.9 to –1.5 are dissimilar to photochemical experimental results (Whitehill and Ono, 2012), whereas no MIF-yielding mechanism was found except for the photochemical reactions. The photochemical experiment results of Whitehill and Ono (2012) indicate that light of 250-330 nm wavelength produces elemental sulfur with a positive $\Delta^{36}S/\Delta^{33}S$ ratio (0.64 ± 0.03) by photoexcitation, and the 190-220 nm band and the 250-330 nm region produces negative $\Delta^{36}S/\Delta^{33}S$ values (–1.90) by SO_2 self-shielding. To explain the Archean $\Delta^{36}S/\Delta^{33}S$ slopes, we propose a mixing of two different photochemical channels: photolysis in the 190-220 nm band and photo-excitation in the 250-330 nm band (Fig. 8B). These changes probably reflect both the intensity of volcanic SO_2 emissions and the concentration of reducing gasses under the O_2-free atmosphere (Endo et al., 2016). Based on the atmospheric mixing model, the SO_2 self-shielding rate and photoexcitation rate grew after 2.7 Ga. This increase in volcanic emissions of reduced gas and SO_2 gas can be supported by the occurrence of major plume events in the Archean at ~2.77 to ~2.7 Ga (Isley and Abbot, 1999).

Not only the $\Delta^{36}S/\Delta^{33}S$ trend, but also the magnitude and variation of $\Delta^{33}S$ values changed through time (Figs. 4-7 and 4-8). The MIF sulfide is dominant in the 2.7-2.5 Ga Archean sedimentary rocks, in contrast to the dominance of MDF or small MIF sulfide during 3.0-2.7 Ga (Figs. 8C and D). This change might have been caused by an increase in production rate of S_8 (Ono et al., 2003). In an ambient atmosphere, optical thickness of SO_2 is unlikely to be high enough to cause the isotopic self-shielding, thus it cannot explain the observed high $\Delta^{33}S$ values in the late Archean sediments (Ono et al., 2013; Endo et al., 2016). Instead, the large S-MIF can be produced after extensive volcanism when pSO_2 is high enough to cause considerable S-MIF by isotopic self-shielding in

volcanic plumes. Thus, together with the change in the $\Delta^{36}S/\Delta^{33}S$ slopes, the atmosphere may have been reducing with higher volcanic SO_2 input after 2.7 Ga.

On the other hand, the atmospheric conditions before 2.7 Ga could have been under low pSO_2 and contained less reducing gas, though the pO_2 level would still be low enough to produce S-MIF. The lower volcanic activity and somewhat oxidizing conditions might have restricted the formation of S-MIF (Ono et al., 2006a) and could have caused the mid Archean glaciation. Indeed, there are reports of glacial sediment in the Vanivilas Formation before 2.7 Ga (Ojakangas et al., 2014). Several authors reported the anomalous $\Delta^{36}S/\Delta^{33}S$ ratios in the Witwatersrand Supergroup and Pongola Supergroup, Kaapvaal Craton, South Africa (Ono et al., 2006a; Farquhar et al., 2007; Guy et al., 2012). These multiple sulfur isotope ratios in the sedimentary sulfide are scattered and do not show a linear array. Ono et al. (2006a) suggested a short scale photosynthetic oxidation event at 2.9 Ga, which destabilized the methane-rich Archean atmosphere and triggered the Pongola glaciation, though this needs to be tested.

In any case, our new long-term record of the late Archean from Dharwar Supergroup suggests that the variation and magnitude of $\Delta^{33}S$ together with a change in the $\Delta^{36}S/\Delta^{33}S$ slope reflect the drastic changes in the climatic system. For further constraints, it is necessary to investigate more systematic isotope chemostratigraphy of the rocks in the same time interval as that of Dharwar Supergroup, as well as mechanisms of atmospheric S-MIF through studies involving photochemical experiments and theoretical modeling.

4-6. Conclusions

Our high-precision quadruple sulfur isotope data from the Chitradurga Schist Belt, Western Dharwar Craton, southern India suggested the following new results and insights.

1. All samples in the Dharwar Supergroup exhibit a clear MIF signature ($\Delta^{33}S$ = –1.2 to +3.9‰) with $\Delta^{36}S/\Delta^{33}S$ slope from –0.9 to –1.5, suggesting that the mixing of atmospheric sulfur and MDF components was responsible for the observed isotopic variation.
2. Comparing the $\Delta^{36}S/\Delta^{33}S$ arrays reported from the Kaapvaal Craton, South Africa and Pilbara Craton, Western Australia with our new data from Dharwar Supergroup, the

$\Delta^{36}S/\Delta^{33}S$ slopes seem to change globally from –1.5 to –0.9 through the late Archean. The global nature of the trend supports the hypothesis that the $\Delta^{36}S/\Delta^{33}S$ slope reflects the change in atmospheric chemistry through the late Archean.

3. The $\Delta^{33}S/\delta^{34}S$ distribution pattern and a wide range of $\delta^{34}S$ values suggest that microbial sulfate reduction was active in a low sulfate environment in the Bababudan Basin.

These results strengthen the use of S-MIF signals to trace the change of atmospheric chemistry before the Great Oxidation Event. The change in $\Delta^{36}S/\Delta^{33}S$ ratio may serve as a clue for monitoring volcanic activity and the amount of reducing gas in the atmosphere. The period characterized by the $\Delta^{36}S/\Delta^{33}S$ slope of ~ -1.5 seems to correspond to mid-Archean (2.9~2.8 Ga Pongola glaciation: Young et al., 1998). This correlation may suggest a potential link between atmospheric chemistry changes and climate during the Archean and Paleoproterozoic.

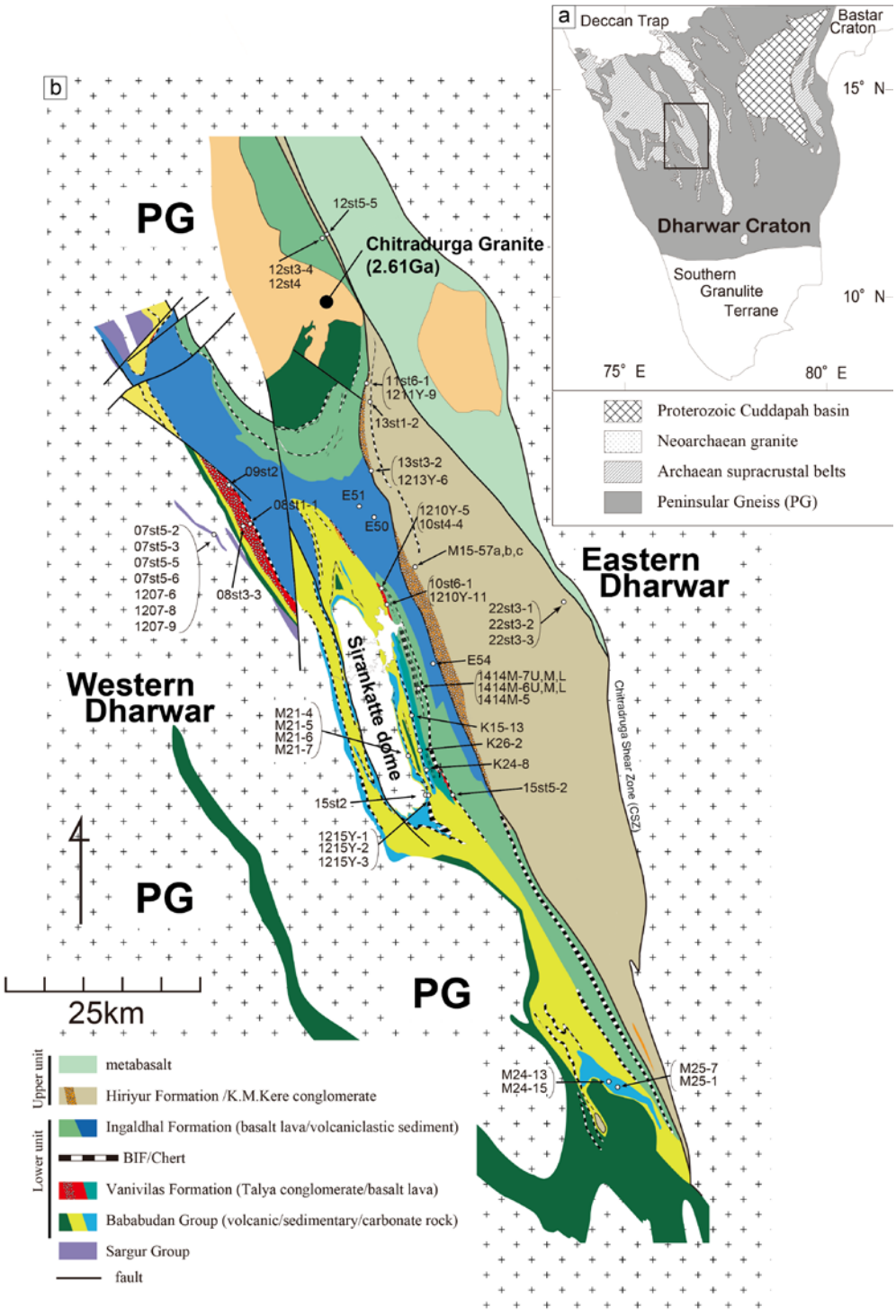

Fig. 4-1 (a) Sketch map showing the position of the Dharwar craton in South India, with the Dharwar Craton. (b) Simplified geological sketch map of the CSB. Circle indicate the locations of the samples in which sulfur isotope were analyzed by MAT253.

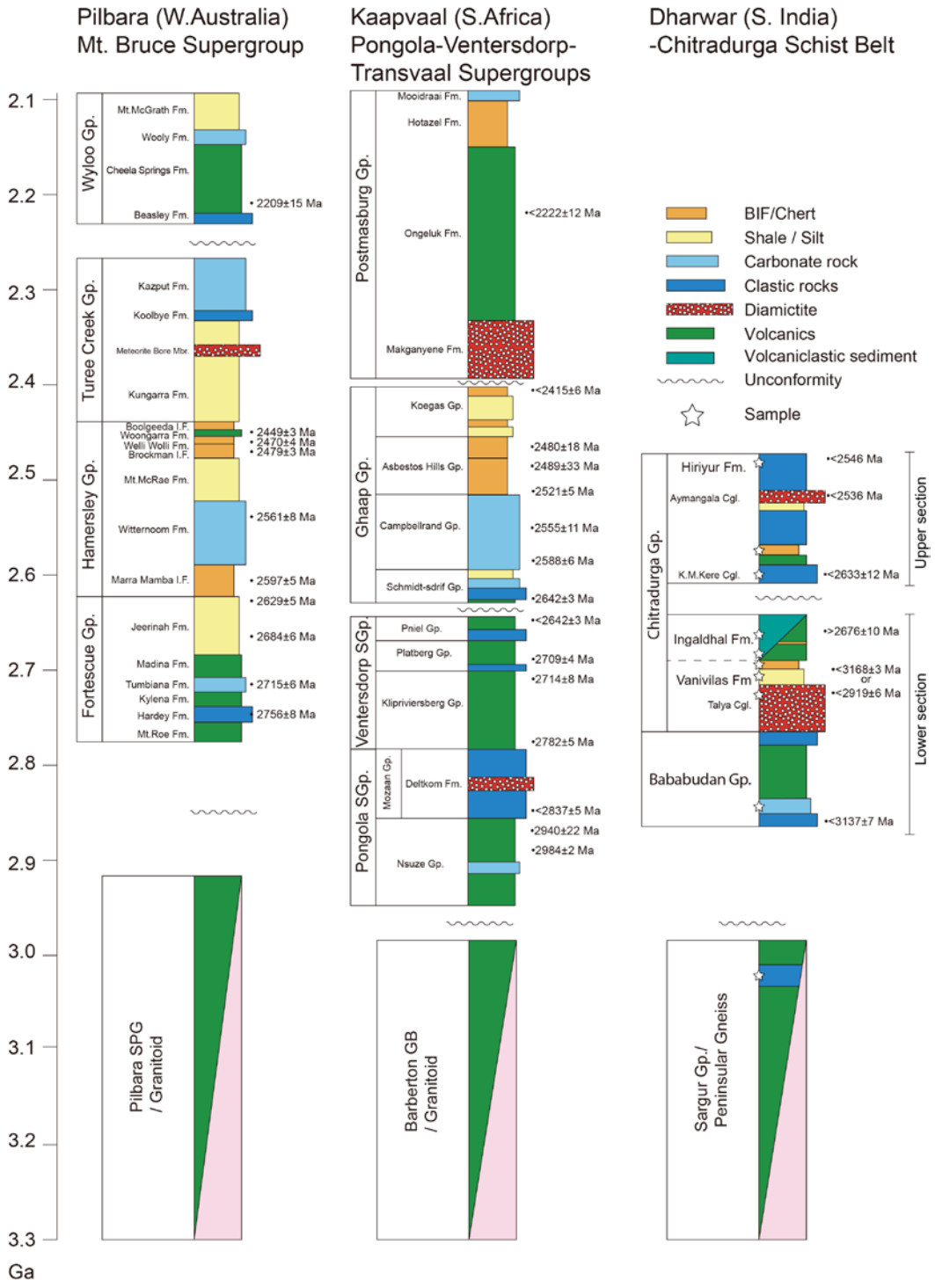

Fig. 4-2 Stratigraphic section of CSB in Dharwar Craton compared with those of Pilbara Craton in Western Australia and Kaapvaal Craton in S. Africa. Star symbols in the Chitradurga section define the stratigraphic position of the samples selected for quadruple sulfur isotope studies. The figure is modified from Hokada et al. (2013).

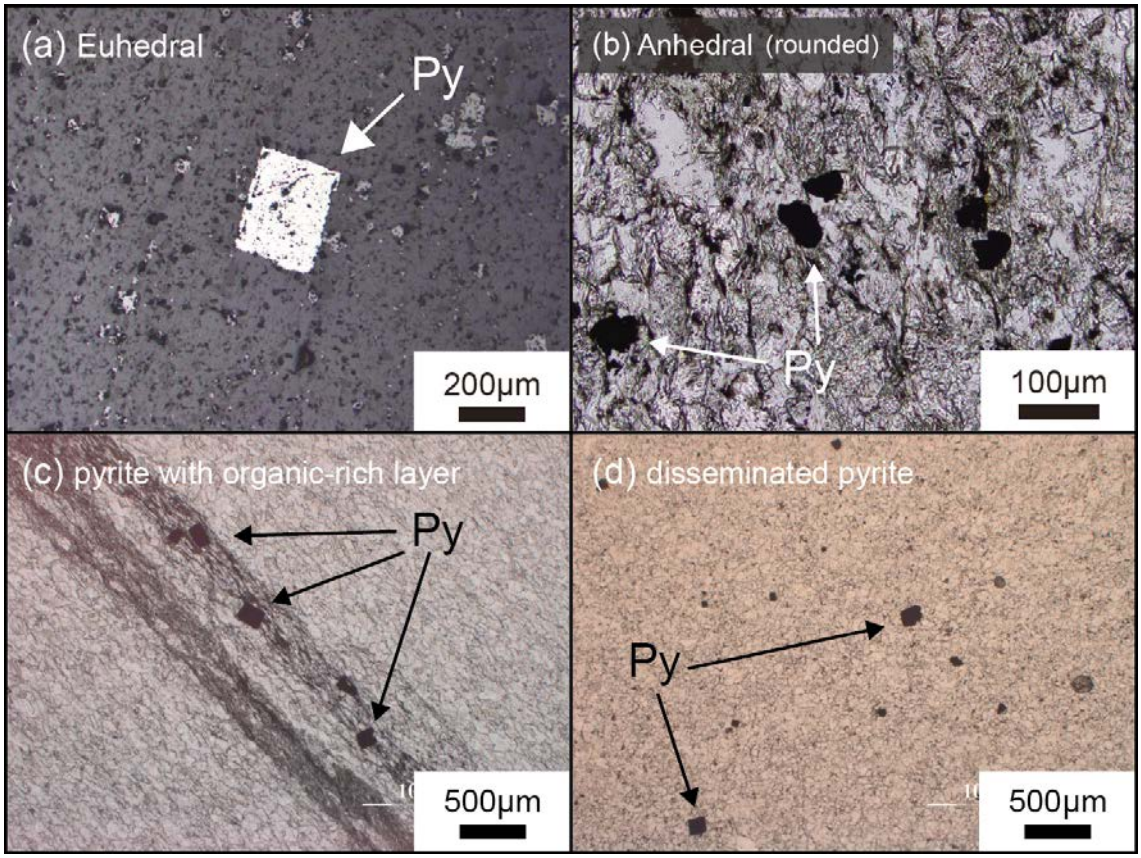

Fig. 4-3 Pyrite textures observed in Dharwar Supergroup, showing (a) Euhedral pyrite (b) Anhedral pyrite (c) euhedral pyrite associated with organic-rich layer in the dolostone (d) disseminated pyrite in the carbonate rocks.

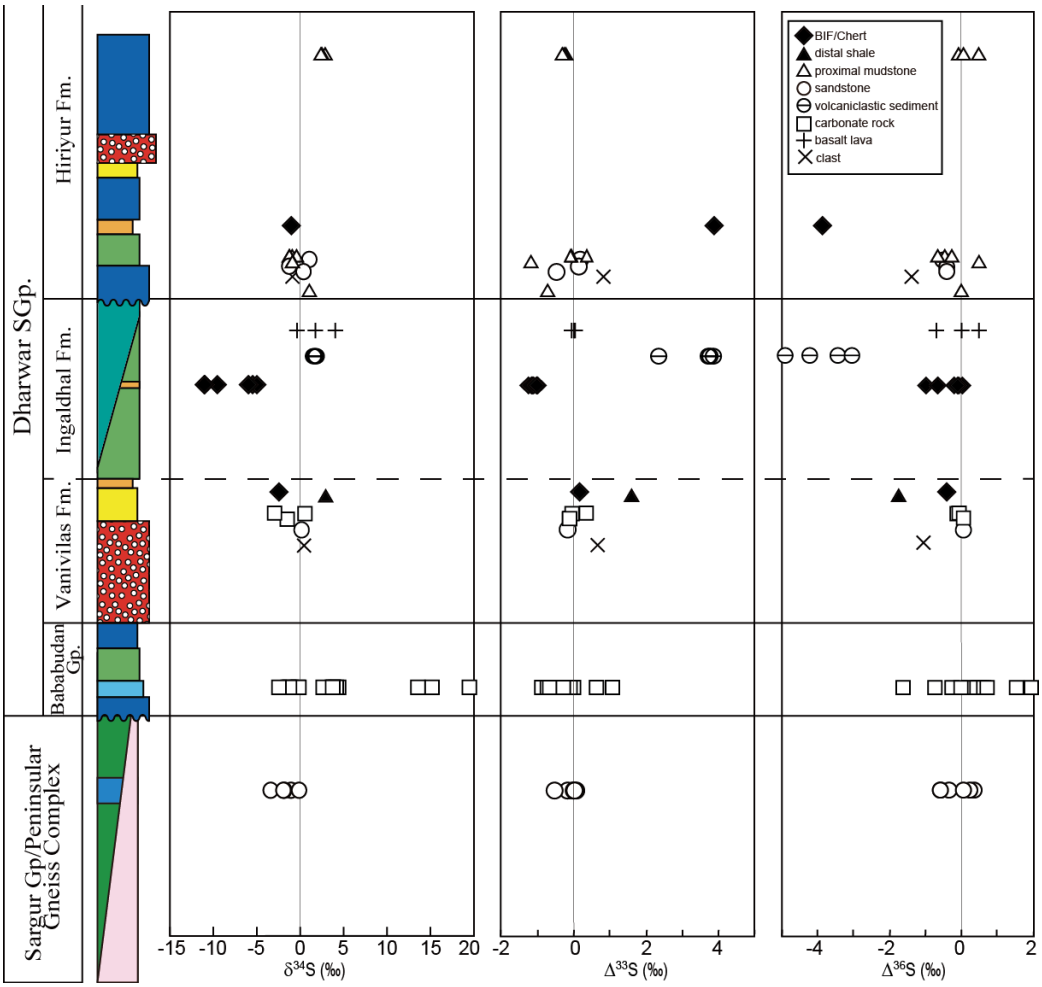

Fig. 4-4 Stratigraphic records of multiple sulfur isotopes in sedimentary lithofacies of the Dharwar Supergroup.

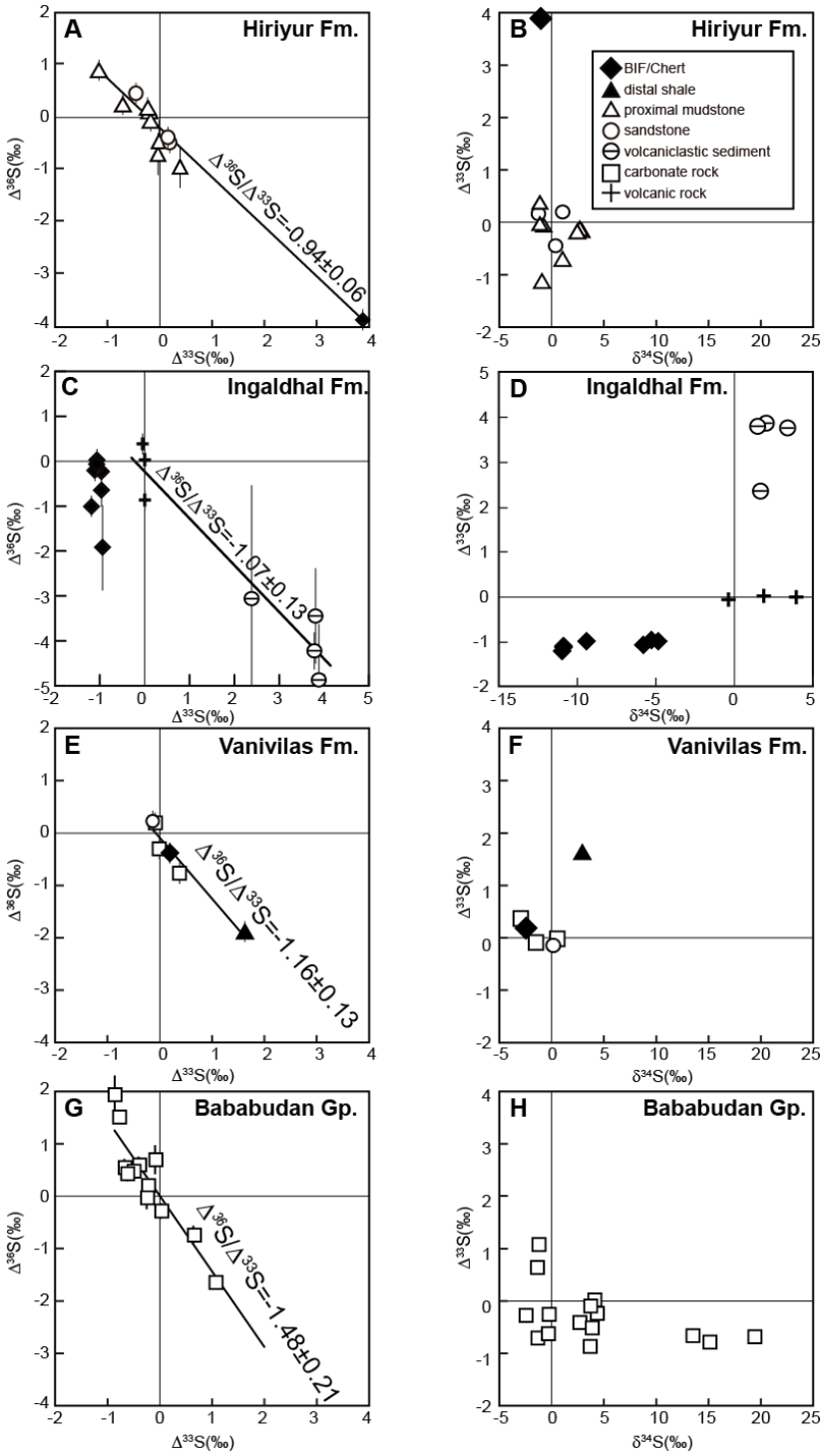

Fig. 4-5 Plots of $\delta^{34}S$, $\Delta^{33}S$ and $\Delta^{36}S$ for each formation in the Dharwar Supergroup. (a) (b) Hiriyur Formation, (c)(d) Ingaldhal Formation, (e)(f) Vanivilas Formation, (g)(h) Bababudan Group, respectively. Solid lines show the regression lines, which originate from atmospheric photochemical reactions. Error bars for isotopic compositions represent analytical reproducibility based on the repeated analysis of standard Ag_2S sample.

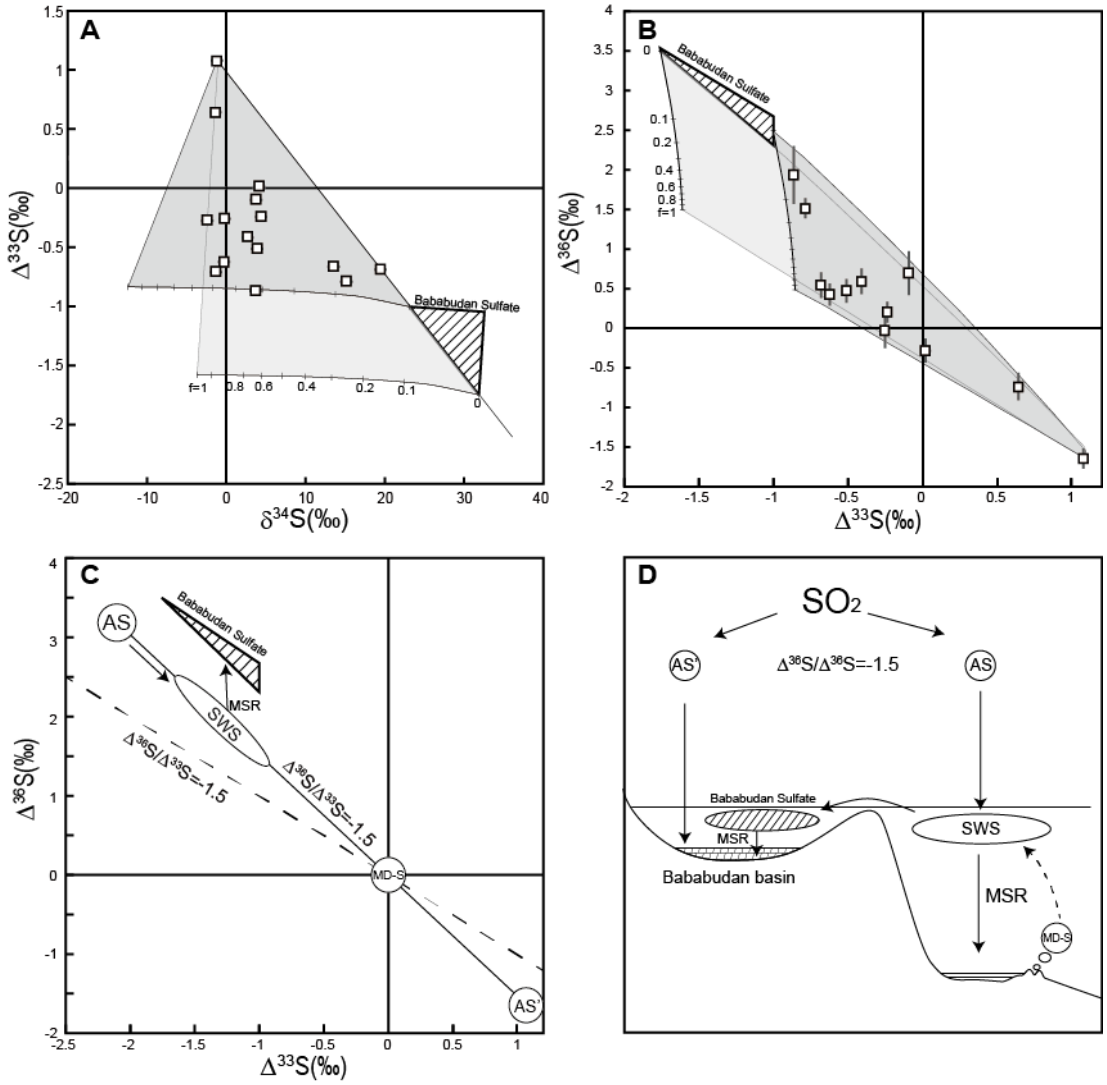

Fig. 4-6 (a) Relationship between $\delta^{34}S$ and $\Delta^{33}S$ values of sulfide in the Bababudan carbonate. (b) Relationship $\Delta^{33}S$ and $\Delta^{36}S$ values. The shaded area shows the calculated area from a Rayleigh distribution model assuming a closed system. F is fractionation. (c) (d) Quadruple sulfur isotope systematics for the Bababudan basin. Atmospheric sulfate (AS), atmospheric sulfide (AS'), Bababudan sulfate and seawater sulfate (SWS) are inferred. Oblique line represents inferred atmospheric $\Delta^{33}S$ /$\Delta^{36}S$ slope. Dashed line represents Archean reference array ($\Delta^{36}S = -1\ \Delta^{33}S$). MSR represents the microbial sulfate reduction. Some arrows represent inferred MDF and MIF processes starting from atmospheric sulfur.

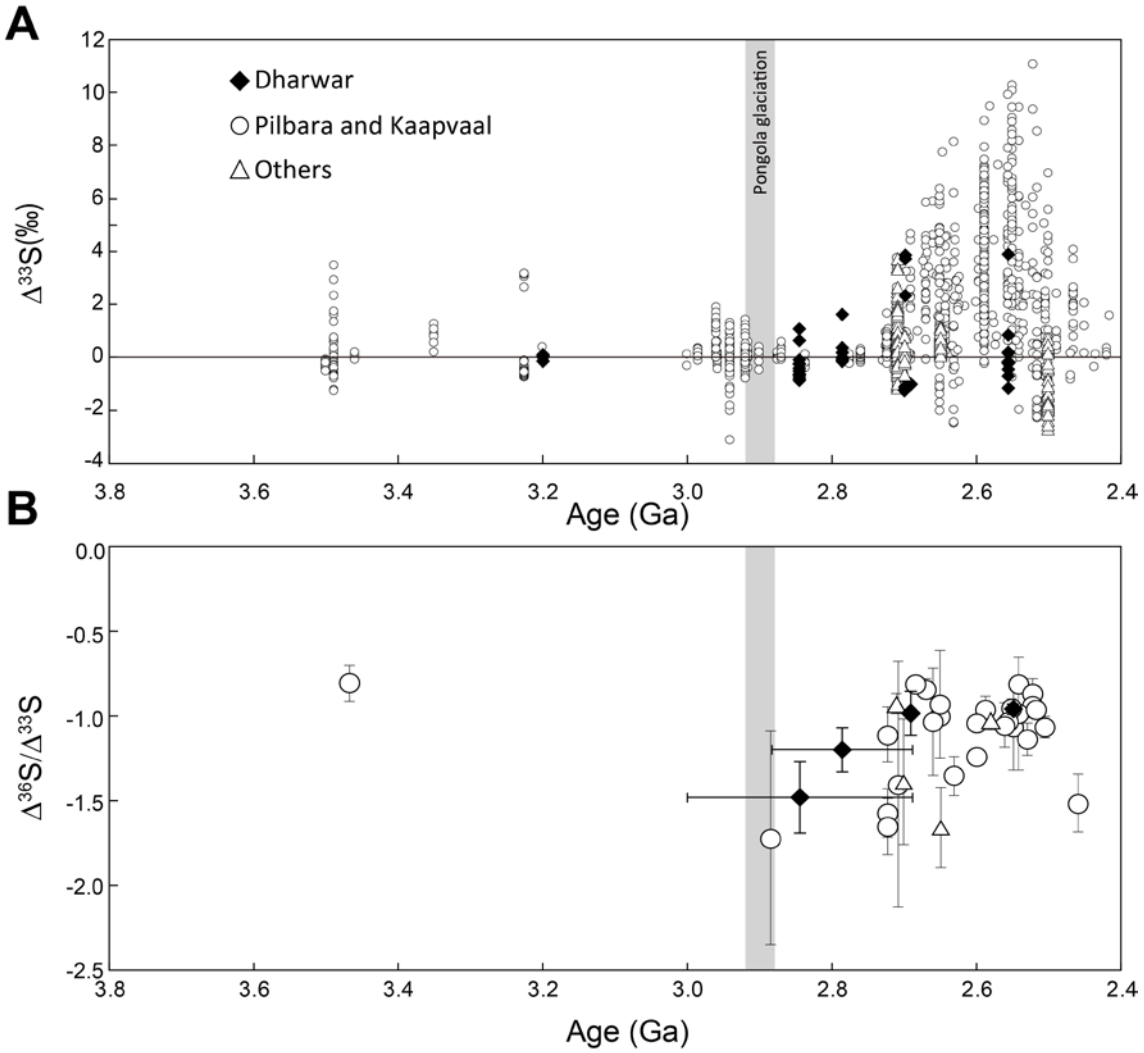

Fig. 4-7 (a) Secular variation of $\Delta^{33}S$ values. The data of this study is illustrated by black diamonds. (b) Evolution of $\Delta^{36}S$ /$\Delta^{33}S$ slope. The data of this study is illustrated by black diamonds. Literature data (closed circles) are from Ueno et al. (2008), Kaufman et al. (2007), Farquhar et al. (2007), Thomazo et al. (2009), Ono et al. (2009), Kurzweil et al. (2013), Zerkle et al. (2012), Guy et al. (2012), Zhelezinslaia et al. (2014), Izon et al. (2015) and Tsuruoka (MSc thesis).

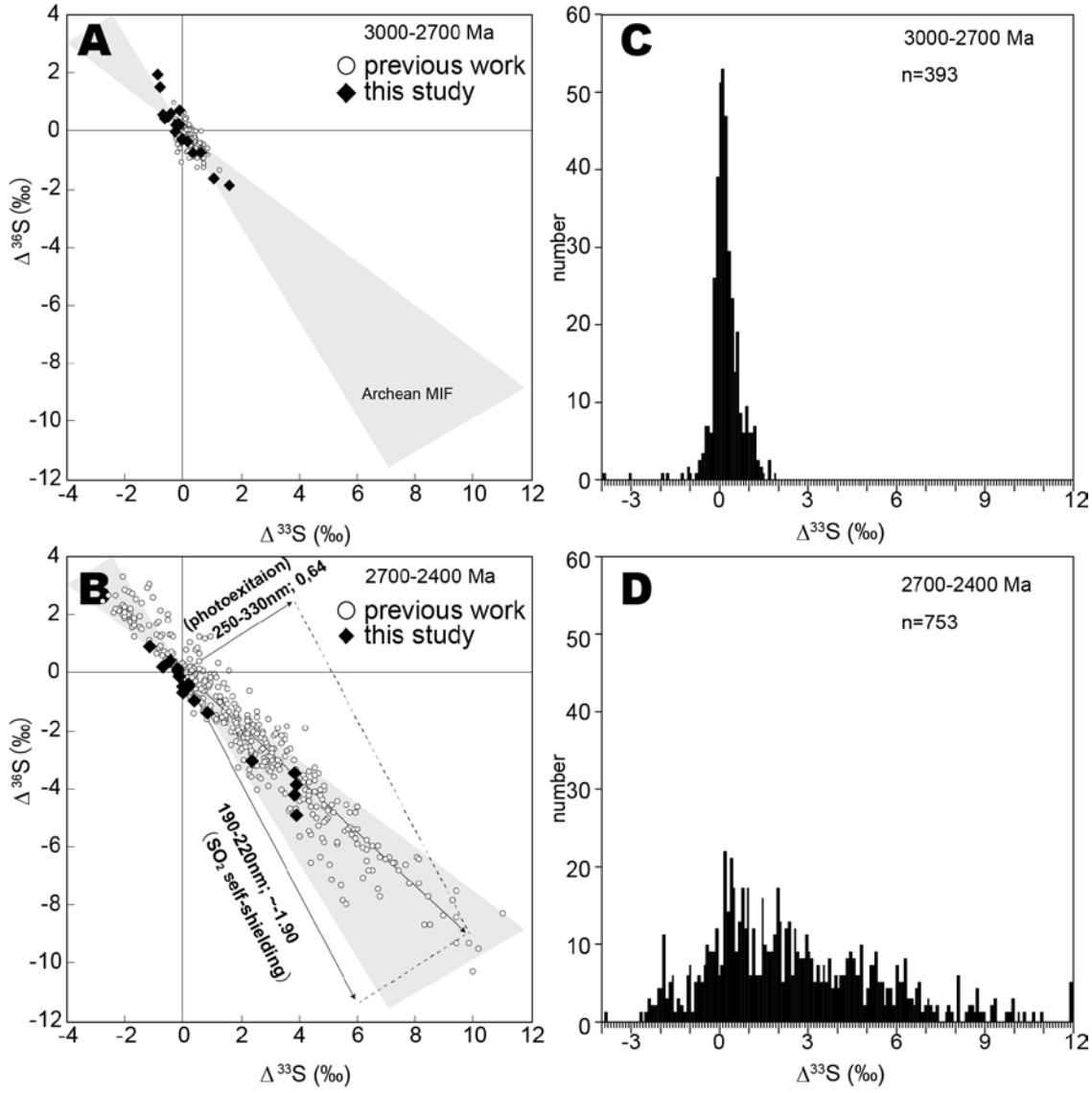

Fig. 4-8 Relationship between $\Delta^{36}S$ and $\Delta^{33}S$ values of the late Archean sulfides. The gray area indicates the Archean S-MIF area with $\Delta^{36}S/\Delta^{33}S = -0.9$ to -1.5. Dharwar data is illustrated by black diamonds and circles show published data. The positive arrow indicates the photoexcitation line ($\Delta^{36}S/\Delta^{33}S$ ratio of $+0.64 \pm 0.03$) and the negative arrow indicates the SO_2 self-shielding lines ($\Delta^{36}S/\Delta^{33}S$ ratio of -1.90) (Whitehill and Ono, 2012). Sulfur isotope variation of $\Delta^{36}S/\Delta^{33}S$ plot can be explained by these two experimental slopes. (a) 3.0 to 2.7 Ga (b) 2.7 to 2.4 Ga. (c) and (d) Frequency distribution of $\Delta^{33}S$ values of the late Archean sedimentary rocks.

Table 1.
Results of Isotope analysis in the Dharwar Supergroup

Sample	Rock name	Unit	SF6 (μmol)	$\delta^{34}S$ (‰)	$\Delta^{33}S$ (‰)	$\Delta^{36}S$ (‰)
22st3-1	Proximal mudstone	Hiriyur	3.52	2.45	-0.22	0.13
22st3-2	Proximal mudstone	Hiriyur	6.44	2.69	-0.17	-0.09
22st3-3	Proximal mudstone	Hiriyur	7.03	2.87	-0.19	0.08
13st1-2	Black chert	Hiriyur	6.71	-1.02	3.89	-3.86
13st3-2	Sandstone	Hiriyur	6.75	1.06	0.2	-0.48
12st5-5	Proximal mudstone	Hiriyur	7.33	-0.91	-1.16	0.9
11st6-2	Sandstone	Hiriyur	8.21	0.38	-0.45	0.46
1211Y-9	Proximal mudstone	Hiriyur	7.02	1.04	-0.7	0.24
1213Y-6	Sandstone	Hiriyur	6.17	-1.26	0.16	-0.38
11st6-1	Chert pebble (K. M. Kere conglomerate)	Hiriyur	8.9	-0.89	0.84	-1.37
M15-57a	Proximal mudstone	Hiriyur	0.22	-1.09	-0.01	-0.44
M15-57b	Proximal mudstone	Hiriyur	0.1	-1.17	0.38	-0.92
M15-57c	Proximal mudstone	Hiriyur	0.18	-0.79	-0.04	-0.69
E50	Volcaniclastic sediment	Ingaldhal	0.05	2.00	3.88	-4.88
E51-1	Volcaniclastic sediment	Ingaldhal	0.07	1.44	3.81	-3.44
E51-2	Volcaniclastic sediment	Ingaldhal	0.07	3.27	3.79	-4.22
E54	Volcaniclastic sediment	Ingaldhal	0.03	1.58	2.38	-3.05
12st3-4	Quartz vein in metabasalt	Ingaldhal	9.1	1.84	0.02	-0.86
12st4	Metabasalt	Ingaldhal	0.22	-0.37	-0.04	0.41
10st6-1	Metabasalt	Ingaldhal	n.d.	3.97	0.00	0.04
1414m-7u	BIF	Ingaldhal	0.33	-10.93	-1.20	-0.99
1414M-7m	BIF	Ingaldhal	0.23	-10.87	-1.08	-0.07
1414M-7L	BIF	Ingaldhal	0.22	-10.90	-1.12	-0.19
1414m-6u	BIF	Ingaldhal	0.25	-5.77	-1.07	0.02
1414m-6M	BIF	Ingaldhal	0.16	-4.88	-0.98	-0.22
1414m-6L	BIF	Ingaldhal	0.34	-5.30	-0.96	-1.92
1414m-5	BIF	Ingaldhal	0.26	-9.42	-0.98	-0.64
08st1-1	Distal shale	Vanivillus	0.35	2.94	1.62	-1.88
09st2	Sandstone	Vanivillus	0.42	0.16	-0.15	0.24
15st5-2	Chert	Vanivillus	7.16	-2.44	0.18	-0.37
08st3-3	Black chert pebble (Talya conglomerate)	Vanivillus	4.69	0.44	0.68	-1.09
1210Y-11	Siliceous layer in dolostone	Vanivillus	4.77	-1.5	-0.09	0.21
1210Y-5	Siliceous layer in dolostone	Vanivillus	3.52	-2.95	0.37	-0.76
10st4-4	Dolostone	Vanivillus	7.07	0.54	-0.02	-0.29
1215Y-1	Dolostone	Bababudan	1.39	13.51	-0.66	n.d.
1215Y-2	Dolostone	Bababudan	4.7	3.88	-0.51	0.47
1215Y-3	Dolostone	Bababudan	0.92	-2.43	-0.27	n.d.
M21-4	Dolostone (Siliceous layer)	Bababudan	4.7	-1.35	0.64	-0.74
M21-5	Dolostone	Bababudan	3.01	19.44	-0.68	0.55
M21-6	Dolostone	Bababudan	4.7	15.13	-0.79	1.51
M21-7	Dolostone (Siliceous layer)	Bababudan	3.03	3.69	-0.87	1.94
M24-13	Dolostone	Bababudan	4.05	2.69	-0.41	0.59
M24-15	Marble	Bababudan	3.19	-1.19	1.08	-1.65
M25-1	Dolostone	Bababudan	2.3	3.74	-0.09	0.7
M25-7	Dolostone	Bababudan	2.23	-0.24	-0.26	-0.03
M25-8	Dolostone	Bababudan	1.04	-1.31	-0.71	n.d.
K15-13	Dolostone	Bababudan	4.28	-0.31	-0.63	0.43
k24-8	Dolostone	Bababudan	2.3	4.12	0.02	-0.29
K26-2	Black chert with dolostone	Bababudan	4.19	4.37	-0.24	0.2
07st5-2	Quartzite	Sargur	7.38	-1.05	0.09	-0.37
07st5-3	Quartzite	Sargur	8.9	-1.83	0.01	0.15
07st5-5	Quartzite	Sargur	9.22	-3.39	-0.15	-0.47
07st5-6	Quartzite	Sargur	8.21	-1.93	0.02	0.06
16st1-5	Marble	Sargur	8.46	-0.12	0.05	0.33
1207-6	Quartzite	Sargur	3.34	-0.3	0.11	-0.85
1207-8	Quartzite	Sargur	4.15	-2.79	-0.13	-0.23
1207-9	Quartzite	Sargur	3.11	-1.76	0.04	-0.29

n.d.: not reported due to large error/low bulk rock S content

Table 2.

Published slopes in Δ33S versus Δ36S, for Kaapvaal Craton, South Africa and Pilbara Craton, Western Australia

Stratigraphic position	number	$\Delta^{36}S/\Delta^{33}S$[a]	error	R^2	Age (Ma)	Reference
Upper Mt.McRae Formation, Western Australia	24	-1.06	0.06	0.93	2504	Kaufman et al., 2007
Under Mt.McRae Formation, Western Australia	19	-0.81	0.02	0.99	2541	Kaufman et al., 2007
Kuruman Iron Formation, South Africa	15	-1.52	0.17	0.86	2460	Kaufman et al., 2007
Gamohaan Formation, South Africa	8	-0.86	0.08	0.95	2521	Kaufman et al., 2007
Upper Nauga Formation, South Africa	15	-1.07	0.26	0.57	2549	Zerkle et al., 2012
Lower Nauga Formation, South Africa	21	-0.96	0.08	0.88	2588	Zerkle et al., 2012
Monteville Formation, South Africa	23	-1.24	0.05	0.97	2600	Zerkle et al., 2012
Lokammona Formation, South Africa	10	-1.00	0.04	0.99	2650	Zerkle et al., 2012
Babatal Formation, Brasil	68	-1.03	0.05	0.85	2580	Zhelezinskaia et al., 2014
Gamohaan Formation, South Africa	3	-0.94	0.07	0.99	2521	Izon et al., 2015
Kogelbeen Formation, South Africa	3	-1.14	0.09	0.99	2530	Izon et al., 2015
Papkuil Formation, South Africa	5	2.14	2.87	0.16	2535	Izon et al., 2015[b]
Klipfontein Heuwel Formation, South Africa	4	-0.99	0.33	0.81	2540	Izon et al., 2015
Fairfield Formation, South Africa	2	-1.61	0.00	1.00	2545	Izon et al., 2015[c]
Reivilo Formation, South Africa	25	-0.95	0.05	0.94	2550	Izon et al., 2015
Monteville Formation, South Africa	27	-1.04	0.05	0.94	2555	Izon et al., 2015
Lokammona Formation, South Africa	3	-0.93	0.32	0.90	2650	Izon et al., 2015
Boomplaas Formation, South Africa	3	-1.03	0.32	0.91	2660	Izon et al., 2015
Vryburg Formation, South Africa	21	-0.84	0.06	0.91	2670	Izon et al., 2015
Wittenoom Formation, Western Austraria	15	-1.05	0.13	0.84	2561	Izon et al., 2015
MMIF, Western Austraria	8	-1.04	0.04	0.99	2600	Izon et al., 2015
Jeerinah Formation, Western Austraria	25	-0.81	0.05	0.92	2684	Izon et al., 2015
Tumbiana Formation, Western Australia	8	-1.11	0.16	0.89	2724	Izon et al., 2015
Carawine Dolomite, Western Austraria	11	-1.35	0.11	0.94	2630	Izon et al., 2015
Nauga/Klein Naute Formation, South Africa	29	-0.96	0.04	0.96	2516	Ono et al., 2009
Kidd Creek Formation, Canada	62	-0.93	0.06	0.81	2730-2711	Kurzweil et al., 2013
Tumbiana Formation, Western Australia	30	-1.57	0.14	0.82	2724	Thomazo et al., 2009
Manjeri Formation, Zimbabwe	6	-1.39	0.37	0.78	2700	Thomazo et al., 2013
Cheshire Formation, Zimbabwe	22	-1.66	0.24	0.71	2650	Thomazo et al., 2013
Duitschland/Rooihoogte Formation, South Africa	22	-0.96		0.98	2300-2600	Guo et al., 2009
Ventersdorp Formation, South Africa	3	-1.40	0.72	0.79	2709	Farquhar et al., 2007
Tumbiana Formation, Western Australia	8	-1.65	0.17	0.98	2724	Farquhar et al., 2007
Witwatersrand Supergroup, South Africa	19	-0.87	0.52	0.14	2849-2985	Farquhar et al., 2007[b]
Mozaan Group, South Africa	8	-1.11	0.07	0.83	2960-2840	Ono et al., 2006[b]
Jeppestown Subgroup, South Africa	6	-0.39	0.11	0.89	2914	Guy et al., 2012[b]
Government Subgroup, South Africa	26	-0.94	0.26	0.76	2940	Guy et al., 2012[b]
Hospital Hill Subgroup, South Africa	8	-0.74	0.63	0.57	2985	Guy et al., 2012[b]
Nsuzu Group	13	-1.72	0.63	0.45	2885	Tsuruoka, MSc thesis.
Dresser Formation, Western Australia	14	-0.81	0.10	0.86	3470	Ueno et al., 2008
Hiriyur Formation, Southern India	11	-0.93	0.06	0.97	2550	This study
Ingaldhal Formation, Southern India	4	-1.07	0.13	0.93	2670	This study
Vanivilas Formation, Southern India	7	-1.20	0.13	0.94	2800	This study
Bababudan Group, Southern India	15	-1.48	0.21	0.83	2900	This study

a. $\delta^{34}S = 1000 \times ({}^{34}R_{sample}/{}^{34}R_{standard} - 1)$

$\Delta^{33}S = 1000 \times \ln(\delta^{33}S/1000 + 1) - 0.515 \times 1000 \times \ln(\delta^{34}S/1000 + 1)$

$\Delta^{36}S = 1000 \times \ln(\delta^{36}S/1000 + 1) - 1.90 \times 1000 \times \ln(\delta^{34}S/1000 + 1)$

b. The trend does not intersect the origin of the $\Delta^{33}S$-$\Delta^{36}S$ plot and scattered $\Delta^{36}S$, indicating later mass-dependent isotope effects.

c. This trend is lacking in the number.

References

Bleeker, W. 2003. The late Archean record: a puzzle in ca. 35 pieces. Lithos, 71(2), 99-134.

Bradley, A. S., Leavitt, W. D., Schmidt, M., Knoll, A. H., Girguis, P. R., Johnston, D. T., 2016. Patterns of sulfur isotope fractionation during microbial sulfate reduction. Geobiology, 14 (1), 91-101.

Canfield, D. E., Raiswell, R., Westrich, J. T., Reaves, C. M., Berner, R. A., 1986. The use of chromium reduction in the analysis of reduced inorganic sulfur in sediments and shales. Chemical Geology, 54, 149–155.

Chadwick, B., Ramakrishnan, M., Viswanatha, M. N., 1981. The stratigraphy and structure of the Chitradurga region: an illustration of cover–basement interaction in the late Archaean evolution of the Karnataka craton, southern India. Precambrian Research 16, 31–54.

Chadwick, B., Vasudev, V. N., Hegde, G. V., 2000. The Dharwar craton, southern India, interpreted as the result of Late Archaean oblique convergence. Precambrian Research, 99, 91–111.

Cheney, E. S., 1996. Sequence stratigraphy and plate tectonic significance of the Transvaal succession of southern Africa and its equivalent in Western Australia. Precambrian Research 79, 3–24.

Claire, M. W., Catling, D. C., Zahnle, K. J., 2006. Biogeochemical modelling of the rise in atmospheric oxygen. Geobiology 4 (4), 239–269.

Claire, M. W., Kasting, J. F., Domagal-Goldman, S. D., Stüeken, E. E., Buick, R., Meadows, V. S., 2014. Modeling the signature of sulfur mass-independent fractionation produced in the Archean atmosphere. Geochimica et Cosmochimica Acta, 141, 365-380.

Crowe, S.A., Paris, G., Katsev, S., Jones, C., Kim, S.-T., Zerkle, A.L., Nomosatryo, S., Fowle, D.A., Adkins, J.F., Sessions, A.L., Farquhar, J., Canfield, D.E., 2014. Sulfate was a trace constituent of Archean seawater. Science 346, 735–739.

Ding, T., Valkiers, S., Kipphardt, H., De Bievre, P., Taylor, P. D. P., Gonfiantini, R., Krouse, R., 2001. Calibrated sulfur isotope abundance ratios of three IAEA sulfur isotope reference materials and V-CDT with a reassessment of the atomic weight of

sulfur. Geochimica et Cosmochimica Acta, 65, 2433-2437.

Domagal-Goldman, S. D., Kasting, J. F., Johnston, D. T., Farquhar, J., 2008. Organic haze, glaciations and multiple sulfur isotopes in the Mid-Archean Era. Earth and Planetary Science Letters, 269, 29-40.

Drury, S. A., 1983. A regional tectonic study of the Archaean Chitradurga greenstone belt, Karnataka, based on LANDSAT interpretation. Geological Society of India, 24(4), 167-184.

Endo, Y., Danielache, S., Ueno, Y., Hattori, S., Johnson, M. S., Yoshida, N., Kjaergaard, H. G., 2015. Photoabsorption cross-section measurements of ^{32}S, ^{33}S, ^{34}S and ^{36}S sulfur dioxide from 190 to 220 nm. Journal of Geophysical Research: Atmospheres 120: doi:10.1002/2014JD021671.

Endo, Y., Ueno, Y., Aoyama, S., Danielache, S. O., 2016. Sulfur isotope fractionation by broadband UV radiation to optically thin SO 2 under reducing atmosphere. Earth and Planetary Science Letters, 453, 9-22.Farquhar, J., Bao, H., Thiemens, M., 2000. Atmospheric influence of earth's earliest sulfur cycle. Science, 289, 756-759.

Farquhar, J., Savarino, J., Airieau, S., Thiemens, M. H., 2001. Observation of wavelength-sensitive mass-independent sulfur isotope effects during SO2 photolysis: Implications for the early atmosphere. Journal of Geophysical Research, 106, 32829-32839.

Farquhar, J., Peters, M., Johnston, D. T., Strauss, H., Masterson, A., Wiechert, U., Kaufman, A. J., 2007. Isotopic evidence for Mesoarchaean anoxia and changing atmospheric sulphur chemistry. Nature, 449 (7163), 706–709.

French, J. E., & Heaman, L. M., 2010. Precise U–Pb dating of Paleoproterozoic mafic dyke swarms of the Dharwar craton, India: implications for the existence of the Neoarchean supercraton Sclavia. Precambrian Research, 183(3), 416-441.

Guo, Q. J., Strauss, H., Kaufman, A. J., Schroder, S., Gutzmer, J., Wing, B., Baker, M. A., Bekker, A., Jin, Q. S., Kim, S. T., Farquhar, J., 2009. Reconstructing Earth's surface oxidation across the Archean-Proterozoic transition. Geology 37 (5), 399–402.

Guy, B. M., Ono, S., Gutzmer, J., Kaufman, A. J., Lin, Y., Fogel, M. L., Beukes, N. J., 2012. A multiple sulfur and organic carbon isotope record from non-conglomeratic sedimentary rocks of the Mesoarchean Witwatersrand Supergroup, South Africa. Precambrian Research, 216-219, 208-231.

Habicht, K. S., Gade, M., Thamdrup, B., Berg, P., Canfield, D. E., 2002. Calibration of sulfate levels in the Archean ocean. Science, 298 (5602), 2372-2374.

Halevy, I., Johnston, D. T., Schrag, D. P., 2010. Explaining the structure of the Archean mass-independent sulfur isotope record. Science, 329 (5988), 204–207.

Halevy, I., 2013. Production, preservation, and biological processing of mass-independent sulfur isotope fractionation in the Archean surface environment. Proceedings of the National Academy of Sciences, 110 (44), 17644-17649.

Hokada, T., Horie, K., Satish-Kumar, M., Ueno, Y., Nasheeth, A., Mishima, K., Shiraishi, K., 2013. An appraisal of Archaean supracrustal sequences in Chitradurga Schist Belt, Western Dharwar Craton, Southern India. Precambrian Research, 227, 99–119

Hsieh, Y. P., Shieh, Y. N., 1997. Analysis of reduced inorganic sulfur by diffusion methods: improved apparatus and evaluation for sulfur isotopic studies. Chemical Geology, 137, 255–261.

Hulston, J. R., & Thode, H. G. 1965. Variations in the S33, S34, and S36 contents of meteorites and their relation to chemical and nuclear effects. Journal of Geophysical Research, 70(14), 3475-3484.

Isley, A. E., Abbott, D. H., 1999. Plume-related mafic volcanism and the deposition of banded iron formation. Journal of Geophysical Research: Solid Earth, 104(B7), 15461-15477.

Izon, G., Zerkle, A. L., Zhelezinskaia, I., Farquhar, J., Newton, R. J., Poulton, S. W., Eigenbrode, J. L., Claire, M. W., 2015. Multiple oscillations in Neoarchaean atmospheric chemistry. Earth and Planetary Science Letters, 431, 264-273.

Jayananda, M., Chardon, D., Peucat, J. J., Capdevila, R., 2006. 2.61 Ga potassic granites and crustal reworking in the western Dharwar craton, southern India: tectonic, geochronologic and geochemical constraints. Precambrian Research, 150, 1–26.

Jayananda, M., Kano, T., Peucat, J. J., Channabasappa, S., 2008. 3.35Ga komatiite volcanism in the western Dharwar craton, southern India: Constraints from Nd isotopes and whole rock geochemistry. Precambrian Research, 162, 160–179.

Jayananda, M., Peucat, J. J., Chardon, D., Rao, B. K., Fanning, C. M., & Corfu, F., 2013. Neoarchean greenstone volcanism and continental growth, Dharwar craton, southern India: constraints from SIMS U–Pb zircon geochronology and Nd isotopes.

Precambrian Research, 227, 55–76.

Johnston, D. T., Farquhar, J., Canfield, D. E., 2007. Sulfur isotope insights into microbial sulfate reduction: when microbes meet models. Geochimica et Cosmochimica Acta, 71 (16), 3929-3947.

Kaufman, A. J., Johnston, D. T., Farquhar, J., Masterson, A. L., Lyons, T. W., Bates, S., Anbar, A. D., Arnold, G. L., Garvin, J., Buick, R., 2007. Late Archean biospheric oxygenation and atmospheric evolution. Science, 317, 1900–1903.

Kurzweil, F., Claire, M., Thomazo, C., Peters, M., Hannington, M., Strauss, H., 2013. Atmospheric sulfur rearrangement 2.7 billion years ago: Evidence for oxygenic photosynthesis. Earth and Planetary Science Letters, 366, 17-26.

Naqvi, S. M., 1985. Chitradurga schist belt-an Archaean suture (?). Geological Society of India, 26(8), 511-525.

Nasheeth, A., Okudaira, T., Horie, K., Hokada, T., Satish-Kumar, M., 2016. U-Pb SHRIMP ages of detrital zircons from Hiriyur Formation in Chitradurga greenstone belt and its implication to the Neoarchean evolution of Dharwar craton, south India. Journal of the Geological Society of India, 87(1), 43-54.

Ohmoto, H., Watanabe, Y., Ikemi, H., Poulson, S. R., Taylor, B. E., 2006. Sulphur isotope evidence for an oxic Archaean atmosphere. Nature, 442, 908-911.

Ojakangas, R. W., Srinivasan, R., Hegde, V. S., Chandrakant, S. M., Srikantia, S. V., 2014. The Talya Conglomerate: an Archean (~ 2.7 Ga) Glaciomarine Formation, Western Dharwar Craton, Southern India. Current Science, 106, 387-396.

Ono, S., Eigenbrode, J. L., Pavlov, A. A., Kharecha, P., Rumble, D., Kasting, J. F., Freeman, K. H., 2003. New insights into Archean sulfur cycle from mass-independent sulfur isotope records from the Hamersley Basin, Australia. Earth and Planetary Science Letters, 213, 15-30.

Ono, S., Beukes, N. J., Rumble, D., Fogel, M. L., 2006a. Early evolution of atmospheric oxygen from multiple-sulfur and carbon isotope records of the 2.9 Ga Mozaan Group of the Pongola Supergroup, Southern Africa. South African Journal of Geology 109 (1–2), 97–108.

Ono, S., Wing, B., Johnston, D., Farquhar, J., Rumble, D., 2006b. Mass-dependent fractionation of quadruple stable sulfur isotope system as a new tracer of sulfur

biogeochemical cycles. Geochimica Et Cosmochimica Acta 70 (9), 2238–2252.

Ono, S., Shanks, W. C., Rouxel, O. J., Rumble, D., 2007. S-33 constraints on the seawater sulfate contribution in modern seafloor hydrothermal vent sulfides. Geochimica et Cosmochimica Acta, 71, 1170-1182.

Ono, S., Beukes, N. J., Rumble, D., 2009a. Origin of two distinct multiple-sulfur isotope compositions of pyrite in the 2.5Ga Klein Naute Formation, Griqualand West Basin, South Africa. Precambrian Research, 169, 48-57.

Ono, S., Kaufman, A. J., Farquhar, J., Sumner, D. Y., Beukes, N. J., 2009b. Lithofacies control on multiple-sulfur isotope records and Neoarchean sulfur cycles. Precambrian Research, 169, 58-67.

Ono, S., Whitehill, A. R., Lyons, J. R., 2013. Contribution of isotopologue self-shielding to sulfur mass-independent fractionation during sulfur dioxide photolysis. Journal of Geophysical Research: Atmosphere 118: 2444-2454.

Paris, G., Adkins, J. F., Sessions, A. L., Webb, S. M., & Fischer, W. W., 2014. Neoarchean carbonate–associated sulfate records positive Δ33S anomalies. Science, 346 (6210), 739-741.

Pavlov, A. A., Kasting, J. F., 2002. Mass-independent fractionation of sulfur isotopes in Archean sediments: Strong evidence for an anoxic Archean atmosphere. Astrobiology, 2, 27-41.

Penniston-Dorland, S. C., Wing, B. A., Nex, P. A. M., Kinnaird, J. A., Farquhar, J., Brown, M., Sharman, E. R., 2008. Multiple sulfur isotopes reveal a magmatic origin for the Platreef platinum group element deposit, Bushveld Complex, South Africa. Geology, 36, 979–982.

Radhakrishna, B. P., 1983. Archaean granite-greenstone terrain of the South Indian shield. Geological Soc. of India, 4, 1-46.

Rasmussen, B., Buick, R., 1999. Redox state of the Archean atmosphere: evidence from detrital heavy minerals in ca. 3250-2750Ma sandstones from Pilbara Craton, Australia. Geology, 27, 115-118.

Sagan, C., Chyba, C., 1997. The early faint sun paradox: organic shielding of ultraviolet-labile greenhouse gases. Science, 276 (5316), 1217–1221.

Swaminath, J., Ramakrishnan, M., 1981. Early Precambrian supracrustals of southern

Karnataka. Mem. Geol. Surv. India, 112, 1-363.

Thomazo, C., Ader, M., Farquhar, J., Philippot, P., 2009. Methanotrophs regulated atmospheric sulfur isotope anomalies during the Mesoarchean (Tumbiana Formation, Western Australia). Earth and Planetary Science Letters, 279, 65-75.

Ueno, Y., Ono, S., Rumble, D., Maruyama, S., 2008. Quadruple sulfur isotope analysis of ca. 3.5 Ga Dresser Formation: New evidence for microbial sulfate reduction in the early Archean. Geochimica et Cosmochimica Acta, 72, 5675-5691.

Ueno, Y., Aoyama, S., Endo, Y., Matsu'ura, F., & Foriel, J., 2015. Rapid quadruple sulfur isotope analysis at the sub-micromole level by a flash heating with CoF 3. Chemical Geology, 419, 29-35.

Whitehill A. R., Ono, S., 2012. Excitation band dependence of sulfur isotope mass-independent fractionation during photochemistry of sulfur dioxide using broadband light sources. Geochim. Cosmochim. Acta, 94, 238–253.

Young, G. M., Von Brunn, V., Gold, D. J. C., Minter, W. E. L., 1998. Earth's oldest reported glaciation: physical and chemical evidence from the Archean Mozoan Group (~2.9 Ga) of South Africa. Journal of Geology, 106, 523–538.

Zerkle, A. L., Claire, M. W., Domagal-Goldman, S. D., Farquhar, J., Poulton, S. W., 2012. A bistable organic-rich atmosphere on the Neoarchaean Earth. Nat. Geosci., 5(4), 359-363.

Zhelezinskaia, I., Kaufman, A. J., Farquhar, J., & Cliff, J., 2014. Large sulfur isotope fractionations associated with Neoarchean microbial sulfate reduction. Science, 346 (6210), 742-744.

Chapter 5

Multiple sulfur isotope geochemistry of the Onverwacht Suite, South Africa

Abstract

Records of sulfur mass independent fractionation (S-MIF) preserved in Archean sedimentary rocks could be a useful tracer for Archean sulfur cycles. Recently, high-resolution stratigraphic studies of the quadruple sulfur isotopes provide a comprehensive analysis of the Neoarchean (2.5 -3.0 Ga) marine sulfur cycle, which in turn can help our understanding of both atmospheric and biological processes during that time. However, there are only few reports of high-resolution stratigraphic studies of these isotopes from the Paleoarchean period (>3.0 Ga). Here, we report on ca.3.45 Ga sedimentary sulfides that are well preserved in the lower sequences of the Barberton Greenstone Belt, South Africa. Sulfur isotope analysis extracted from sulfides reveal a clear MIF ($\Delta^{33}S$ = +0.2 to +2.4‰). The Noisy Complex, comprising fluvial sediments and glacial diamictities, show vertical $\delta^{34}S$-$\Delta^{33}S$ correlation with a $\Delta^{36}S/\Delta^{33}S$ slope of −0.7. In contrast, deep (>2 km) marine cherts of the Kromberg Complex show positive $\delta^{34}S$-$\Delta^{33}S$ correlation with some negative $\Delta^{36}S/\Delta^{33}S$ slopes (−1.0 to −0.4). Moreover, these observed sulfides in any complex show the lack of igneous sulfur composition ($\Delta^{36}S = \Delta^{36}S$ = 0‰) and negative intercept of the $\Delta^{36}S$-$\Delta^{33}S$ plot. In this study, to explain the observed variation in $\delta^{34}S$, $\Delta^{33}S$ and $\Delta^{36}S$, we adopt the mixing model between the atmospheric sulfur and biogenic sulfide. The negative $\Delta^{36}S$ intercept and the wide range of $\delta^{34}S$ might reflect the microbial sulfate reduction. The $\delta^{34}S$-$\Delta^{33}S$ plot from each complex possibly reflect variations in local environments and/or microbial sulfate reduction rate. Although the $\Delta^{33}S/\Delta^{36}S$ arrays are influenced by biogenic sulfide mixing, a rotation of the arrays into different slopes from −0.4 to −0.8 across the Onverwacht Suite implies a change in the nature of the primary S-MIF signature, possibly reflecting the perturbation of atmospheric gas species at Paleoarchean.

5-1. Introduction

Sulfur mass independent fractionation (S-MIF) in the Archean sedimentary rocks could be a useful tracer for Archean sulfur cycles. The origin of the S-MIF is believed to have resulted from SO_2 photolysis by UV radiation in a low oxygen atmosphere, as supported by photochemical experiments in the laboratory (Farquhar et al., 2001; Pavlov and Kasting, 2000; Ono et al., 2003). Quadruple sulfur isotope ratios especially enable us

to explore the details of the composition of Archean reductive atmosphere. During the Neoarchean (3.0-2.5 Ga), mass-independent processes created $\Delta^{36}S/\Delta^{33}S$ ratios that vary between –0.9 to –1.5 as high-resolution chemo-stratigraphic studies of sulfur isotopes (Kaufman et al., 2007; Zerkle et al., 2012; Kurzweil et al., 2013; Mishima et al., in review.). The mechanism that changed the $\Delta^{36}S/\Delta^{33}S$ ratio are still under debate, but likely reflect changes in atmospheric chemistry before the 2.3 Ga great oxidation event (Farquhar et al., 2007).

On the other hand, sulfide before 3.0 Ga has been studied to search for sulfur isotopic evidence of microbial sulfur cycling. Three different pathways of microbial sulfur metabolism have been proposed previously for life in the Paleoarchean: elemental sulfur disproportionation (Philippot et al., 2007), sulfate reduction (Shen et al., 2001, 2009; Ueno et al., 2008), and sulfide oxidation (Wacey et al.,2011b). Although the Paleoarchean $\Delta^{36}S/\Delta^{33}S$ slopes of ~ −0.9 (Ueno et al., 2008; Roerdink et al., 2013) were reported from barite and sedimentary sulfide, the results lacked stratigraphic details such as reported by Zerkle et al. (2012) and Kaufman et al. (2007). Therefore, to compare Paleo- and Neo-archean data accurately, detailed stratigraphically-linked sulfur isotope analyses prior to 3.0 Ga is needed.

In this study, we build upon insights into the behavior of the Paleoarchean biosphere and atmosphere gained from bulk sulfur four-isotope analysis of sulfide from the 3.5-3.4 Ga Onverwacht Suite of the Barberton Greenstone Belt, South Africa. Previously three sulfur isotopes (^{32}S, ^{33}S, ^{34}S) ion-microprobe measurements were reported from stratigraphic sections in core samples (Grosch and McLoughlin, 2013), which revealed the largest range and most negative $\delta^{34}S$ (−55‰) so far reported from an Archean terrain. Grosch and McLoughlin (2013) suggested these observations revealed a potential tectonic control on atmospheric, geodynamic and hydrothermal environments on sulfate reducing microbes in the Paleoarchean.

Here, we analyzed quadruple sulfur isotopes (^{32}S, ^{33}S, ^{34}S and ^{36}S) in disseminated pyrite from chert, sandstone and diamictite sampled with high-resolution stratigraphic accuracy in the middle Onverwacht Suite, and focus on their $\Delta^{33}S$-$\Delta^{36}S$ relationships.

Our new multiple sulfur isotope data provide a new test for evaluating the atmospheric- versus mass-dependent models for the origin of their variations. Recently,

Roerdink et al. (2016) propose interactions between abiotic and biological processes in the 3.2 Ga Londozi hydrothermal system of the upper Onverwacht Suite, suggesting the reworking of atmospheric $\Delta^{36}S/\Delta^{33}S$ signals. Mass-dependent process produce slight, yet distinctive deviations from $\Delta^{36}S = -\Delta^{33}S$ (Shen et al., 2009; Johnston et al., 2005, 2007). In view of these insights, we discuss our new results in context of the origin of the atmospheric composition of the Paleoarchean >3.4 Ga.

5-2. Geological setting

The Barberton Greenstone Belt (BGB) is one of the best field laboratories for early earth studies because its Paleoarchean supracrustal rocks are well-preserved, mostly at low metamorphic grade, and in many places, relatively undeformation (Furness et al., 2011, 2012; de Wit et al., 2011, 2016). The BGB forms part of the eastern most margin of the Kaapvaal Craton as a NE–SW trending tectono-metamorphic belt on the border between South Africa and Swaziland (Fig. 5-1). The belt is structurally subdivided into two parts, namely a TTG (tonalite–trondhjemite–granitoid) gneiss terrain and a supracrustal greenstone sequence of mafic–ultramafic and clastic-volcaniclastic rocks (e.g. Brandl and de Wit, 1997).

5-3. Stratigraphy and samples

The volcano-sedimentary sequences of the Barberton greenstone belt have been subdivided traditionally into three stratigraphic sequences: the Onverwacht, Fig Tree and Moodies Groups (Viljoen and Viljoen, 1969). More recently the Onverwacht sequence has been subdivided into a number of tectonostratigrahic complexes and collectively referred to as the Onverwacht Suite (OS; de Wit et al., 2011; Furness et al 2011). The OS formed between ca. 3550 and 3300 Ma, and consists predominantly of deep water ultramafic and mafic volcanic rocks (komatiites, komatiitic basalts, basalts) and volcaniclastic cherts, and volumetrically lesser felsic volcanic and sedimentary rocks that formed in shallow marine to subaerial environments. The overlying Fig Tree Group, 3260-3230 Ma in age, consists of deep to shallow marine sandstone and shale with minor jaspilitic banded iron formation and mafic/felsic volcanic rocks. The Moodies Group was deposited between 3227-3220 Ma and consists of shallow-marine to fluvial sandstone and

conglomerate with minor shale and banded iron formation.

The Onverwacht Suite has been subdivided into seven tectonostratigraphic complexes; the Sandspruit, Theespruit, Komati, Hooggenoeg, Noisy, Kromberg and Mendon complexes (formerly formations e.g. Lowe and Byerly, 1999; Viljoen and Viljoen, 1969). The complexes are best developed in the southwestern part of the belt, northeast of Tjakastad. Metamorphic grade is mainly greenschist facies (Grosh et al., 2011; de Wit and Furness 2016), but locally reaches amphibolite facies close to the contact with surrounding granitoid intrusions. (e.g. Schoene et al., 2009)

The volcanic sequences of the Hoogenoeg Complex comprise mainly tholeiitic basalts, with minor komatiites and basaltic komatiites, episodically interbedded with up to 10 chert sequences. The volcanics are dominated by pillow lavas with vesicularity that indicates eruption depths of 2-4 km (Furnes et al., 2011). The stratigraphically lowest chert layer is known as the Middle Marker, which together with its underlying tectonically disrupted lava sequence, defines the tectonic boundary between the underlying Komati Complex and the overlying Hooggenoeg Complex (de Wit et al., 2011). By contrast the stratigraphically highest chert horizon defines the uppermost boundary between the Hooggenoeg Complex and the unconformably overlying Noisy Complex (de Wit et al., 2011). The Middle Marker has yielded U/Pb date of 3472 ± 5 Ma on detrital zircons (Armstrong et al., 1990). Four samples were collected from the black chert that just caps the top of the Hooggenoeg pillow basalts along the Komati River (chert 10 of de Wit et al., 2011). This chert layer is locally ~1 m thick, and is composed of fine-grained quartz (Fig.5-2e).

The Noisy Complex sedimentary sequence is well-exposed along the Komati River on the SE-limb (known here as the Etimambeni formation), where it unconformably overlies the Hooggenoeg Complex. It comprises with ~200 m of poorly bedded diamictites and fluvial conglomerates, overlain by well bedded sandstones, siltstones and laminated cherts, suggesting shallow marine environment to (Lowe and Knauth, 1977; de Wit et al., 2011), and in parts as subaerial deposits (de Wit and Furness, 2011, 2016). The Noisy unconformity cuts down at least 1.5-2 km into the Hooggenoeg pillow lavas (de Wit et al., 2011). In field outcrop, the diamictite is poorly sorted, matrix-supported and many of the clasts are rhyo-dacitic to granitic in composition. Zircons from a large dacitic

intrusion in the Noisy Complex have yielded a concordant U/Pb SHRIMP date of 3445 ± 5 Ma (de Wit et al., 1987). A total 9 samples were collected from the Etimambeni Formation of the Noisy Complex: 7 samples were collected from the out-crop rocks along the Komati River; and 2 samples were collected from core drilled duringthe Barberton Scientific Drilling Project (BSDP; Grosch et al., 2011). These samples are sandstones and mudstones that include very angular to angular feldspar grains (Fig.5-2d). The Noisy sequence has an upper contact with the Kromberg Complex that is inferred to be a thrust (the Etimambeni thrust, de Wit et al., 2011; Grosh et al., 2011).

The Kromberg Complex is in tectonic contact with the underlying Noisy Complex. Another major tectonic zone defines its boundary with the overlying Mendon Complex. Mafic to ultramafic intrusive rocks occupy most of this ca. 1.5 km thick magmatic complex, but in the lower and upper parts of the complex, well-exposed volcanic sequences occur. The stratigraphically lowest volcanic sequence of the Kromberg Complex comprises rocks of the ca. 150 m of slightly vesicular pillow lavas and massive units in the bottom and the top, whereas the uppermost part of the complex comprises mostly massive lava flows. This oceanic sequence, which formed at depth of 1.8-4.0 km (Furnes et al., 2011), is similar in composition to the Hoogenoeg Complex, but with greater volume of (sheeted) intrusions and with fewer interlayered cherts (Lowe and Byerly, 1999; de Wit et al., 2011, 2016).

Thirteen outcrop samples were collected from Kromberg Complex along the Komati River, of which 9 samples were collected from a black-brown chert layer (~30 m thick) that comprises and predominantly fine quartz with sporadic carbonates (dolomite and calcite; Fig. 5-2c). A further 4 samples were taken from the chert with laminated carbonates (Mg-siderite) and very fine quartz (Fig. 5-2b). We also collected samples of drill cores retrieved from two locations during the BSDP. The lower drill hole transected the lower sequences of the Noisy Complex and the upper pillow lavas of the Hooggenoeg Complex (Grosch et al. 2009a, b). The upper drill hole transects the contact between the Mendon Complex and the upper Kromberg Complex, including a thick sequence of chert of the lowermost Mendon Complex (formerly the Buck Ridge chert, but locally known as the Komatti bridge chert). The upper sequences of the of Kromberg Complex contain carbonate sequence, that alternate with mafic-ultramafic units. Carbonated samples from

this upper drill hole were also selected for the sulfur isotopic analyses.

5-4. Method

Rock samples were cut into slabs and surfaces were removed. Slabs were crushed into small chips of about 1 cm^3. The chips were ultrasonically cleaned with distilled water, then dried overnight in an oven at 100ºC and thereafter crushed using stainless mortar and subsequently powdered by an agate mortar. Sulfide was extracted by a method modified after Hsieh and Shieh (1997). Powdered rock sample (2-10 g) and an alkaline Zn-trap (3:5 mixture of 0.2 M zinc, acetate and 2 M NaOH solution) were placed in a glass bottle with two stopcocks. The bottle was initially purged by nitrogen, and then each sample was dissolved with 20 ml 5 M HCl at room temperature. During this process, acid volatile sulfur (AVS) was selectively converted to H_2S. The H_2S was precipitated as zinc acetate (ZnS) in an alkaline Zn-trap. Thereafter the sample powders were exposed to 20 ml chromium (II) solution with HCl for > 24h at room temperature (e.g. Canfield et al., 1986). In this process, chromium (II)-reducible sulfur (CRS) was converted ZnS. In samples with a low sulfide content, more than 20 g of sample powder was required to yield sufficient sulfur for isotope analysis. In achieve this, we extracted sulfide in several batches with the same alkaline Zn-trap. The ZnS was then converted to silver sulfide (Ag_2S) through reaction with 0.1 M $AgNO_3$ solution. The Ag_2S precipitate was cleaned by repeated centrifugation using distilled water, and then dried at 80ºC overnight.

The Ag_2S powder (0.1-2 mg) was converted to SF_6 through reaction with about 300 torr of purified elemental fluorine overnight in a nickel reaction vessel. Thereafter the SF_6 was purified by gas chromatography (Aoyama et al., 2014), and then inserted into the mass spectrometer (Thermo-Fischer MAT-253) to measure $^{32}SF_5^+$, $^{33}SF_5$, $^{+34}SF_5$and $^{+36}SF_5^+$. All data are reported in ‰ as:

$$\delta^{34}S = ({}^{34}R_{sample}/{}^{34}R_{standard} - 1) \times 1000\ ‰$$

$$\Delta^{33}S = [\ln(\delta^{33}S/1000 + 1) - 0.515 \times \ln(\delta^{34}S/1000 + 1)] \times 1000\ ‰$$

$$\Delta^{36}S = [\ln(\delta^{36}S/1000 + 1) - 1.90 \times \ln(\delta^{34}S/1000 + 1)] \times 1000\ ‰$$

These values are normalized against VCDT, assuming IAEA-S1 has a composition on the VCDT scale of $\delta^{34}S$ = –0.3‰, $\Delta^{33}S$ = +0.100‰, and $\Delta^{36}S$ = –0.91‰ (Ding et al., 2001; Ono et al., 2007). The analytical reproducibility of $\delta^{34}S$, $\Delta^{33}S$, and $\Delta^{36}S$ values, based on

replicate analysis of IAEA-S1, S2, S3 and other in-house silver sulfide standers, is better than ±0.4‰, ±0.02‰ and ±0.2‰, respectively.

5-5. Result

Results of isotope analysis are shown in Table 1 and Figs. 5-3 and 5-4. Two samples in the Noisy complex did not yield enough SF_6 after the fluoridation processes for ^{36}S measurements. The sedimentary sulfides of the Onverwacht Suite show clear mass independent fractionation (MIF) from +0.15‰ to +2.4‰ for $\Delta^{33}S$ values. The $\delta^{34}S$ values are within ±5‰ (Fig. 5-3). These $\delta^{34}S$ and $\Delta^{33}S$ values are within the range of previous in situ SIMS measurement on core samples Onverwacht Suite from a wide range of hydrothermal volcanic and sedimentary rocks in the same locations as those samples for the present study (Grosch & McLoughlin, 2013). By contrast, two volcanic lava in the Kromberg Complex show $\Delta^{33}S$ of +0.18‰ to +0.29‰, $\delta^{34}S$ of −0.17‰ to 0.48‰.

Each Complex shows a distinctive correlation between $\delta^{34}S$ and $\Delta^{33}S$: the Noisy clastic sediments reveal a vertical tend; the Kromberg chert show a positive trend and Kromberg carbonate show week negative trend (Figs. 5-4 and 5-5). The $\Delta^{33}S$-$\Delta^{36}S$ correlations of each stratigraphic unit show distinctive trends (Noisy clastic sediments: $\Delta^{36}S = -0.72 \times \Delta^{33}S - 0.64$; Kromberg upper chert: $\Delta^{36}S = -0.77 \times \Delta^{33}S - 0.61$; Kromberg lower chert: $\Delta^{36}S = -0.36 \times \Delta^{33}S - 0.51$; Kromberg carbonate: $\Delta^{36}S = -1.00 \times \Delta^{33}S - 0.2$). These $\Delta^{36}S/\Delta^{33}S$ slopes are slightly different from our earlier analyses of the 3.5 Ga Dresser Formation, Western Australia ($\Delta^{36}S/\Delta^{33}S = -0.9$; Ueno et al., 2008).

5-6. Discussion

5-6-1. Mass-Independent Sulfur Isotope Signature

A striking feature of our sedimentary sulfide analyses are its positive $\Delta^{33}S$ values ($\Delta^{33}S$; +0.15‰ to +2.43‰) and negative trends between $\Delta^{33}S$ and $\Delta^{36}S$, despite the fact that the sulfides are from various type of rocks such as chert, sandstone, mudstone and carbonated rocks. Larger $\Delta^{33}S$ (> 1‰) values are observed in both the Kromberg chert and Noisy diamictite layer, suggesting that the MIF-yielding mechanism is not influenced by depositional environments (e.g. deep or shallow/subaerial). This supports the hypothesis that the S-MIF originated from atmospheric chemistry at that time, prior to

deposition. Based on atmospheric model calculations, it has been hypothesized that the SO_2 photolysis in an anoxic atmosphere would have produced two isotopically distinct sulfur aerosols (i.e. sulfate with negative $\Delta^{33}S$, and elemental sulfur with positive $\Delta^{33}S$; e.g. Farquhar et al., 2000; Ono et al., 2003). Thereafter, these isotopic anomalies were transported to, and preserved in, both shallow and deep marine sediments.

5-6-2. Deep marine environment (Hooggenoeg and Kromberg Complexes)

The disseminated sulfides embedded in chert from Kromberg Complex show positive $\Delta^{33}S$ values and a distinct correlation between $\Delta^{33}S$, $\delta^{34}S$ and $\Delta^{36}S$ (Fig. 5-4). The upper chert shows a positive trend that widens toward the bottom of the $\Delta^{33}S$-$\delta^{34}S$ plot, whereas the lower chert show a positive linear array ($\Delta^{33}S = 0.57 \times \delta^{34}S + 1.4$; $R^2 = 0.83$). Previous studies interpreted the positive correlation of $\delta^{34}S$-$\Delta^{33}S$ as due to mixing between two atmospheric components – a sulfate aerosol component with negative $\delta^{34}S$ and $\Delta^{33}S$, and another component (suggested to be S8) with a positive $\delta^{34}S$ and $\Delta^{33}S$ (Ono et al., 2003; Ueno et al., 2008). Although all observed sulfides show positive $\Delta^{33}S$ values, the extension of the observed $\delta^{34}S$-$\Delta^{33}S$ slope is consistent with an estimated biogenic sulfide derived from open-system sulfate reduction (Ono et al., 2003). This suggests the possibility of the mixing between photochemical sulfide and biogenic sulfide. The widening variation of $\delta^{34}S$ in upper chert might reflect the changes of sulfate reduction rate or local sulfate concentrations.

Not only the $\delta^{34}S$-$\Delta^{33}S$ trend, but also the $\Delta^{36}S/\Delta^{33}S$ trends support microbial sulfate reduction in the Kromberg chert. These observed $\Delta^{36}S/\Delta^{33}S$ arrays intersect a $\Delta^{36}S$ axes of ~−0.5‰ (Figs. 5-5d and 5-5f). This conflicts with the requirement of such an Archean reference array to intersect with a composition of the bulk silicate Earth with $\Delta^{36}S = \Delta^{36}S = 0$‰. If the atmospheric sulfur isotope record is preserved directly in the sediments, the $\Delta^{36}S$-$\Delta^{33}S$ correlation should intercept through the bulk silicate Earth values. Therefore, to explain the negative intercept of the $\Delta^{36}S/\Delta^{33}S$ arrays, one must assume mixing with biogenic sulfide (Fig. 5-6). The $\Delta^{36}S$ values are relatively easily changed by microbial sulfate reduction (Ono et al., 2006; Johnston et al., 2005, 2007; Ueno et al., 2008; Shen et al., 2009), while it is difficult to change the $\Delta^{33}S$ values by mass-dependent processes. These sulfides must have been mixed in during hydrothermal activities in documented

hydrothermal vents on the deep-sea floor (de Wit et al., 2016). In agreement with the $\delta^{34}S$-$\Delta^{33}S$ plot, the upper Kromberg chert show a lesser wide slope compared to the linear array in the lower chert, possibly reflecting the changes of sulfate reduction rate, or local variable sulfate concentrations as discussed above.

On the other hand, the majority of sulfides in the carbonated rocks of the upper Kromberg Complex have a negative correlation in the second quadrant of $\Delta^{33}S$-$\delta^{34}S$ diagram (Fig. 5a); this is similar to the previous SIMS analyses of samples form the Kromberg Complex (Grosch and McLoughlin, 2013). The negative slope in the second quadrant of $\Delta^{33}S$-$\delta^{34}S$ diagram is similar to the trend observed in microscopic sulfide from the Dresser Formation, Western Australia (Philippot et al., 2007) and felsic volcanic ash-derived sulfide at 3.2 Ga Mapepe Formation in South Africa (Philippot et al., 2012), while the observed $\Delta^{33}S$-$\delta^{34}S$ trends do not seem to be a general characteristic during the Archaean. Although they interpret these negative array as the photodissociation of sulfur dioxide that was released into the atmosphere by short-lived but intense bursts of subaerial volcanic activity, the mechanism behind the negative array is more difficult to understand in the depositional context. However, the negative covariation between $\Delta^{33}S$ and $\delta^{34}S$ in sulfide from Kromberg carbonate layers (possibly reflecting primary siliceous deposits), indicates that the array is not related to volcanic event, which argues against a link between the $\Delta^{33}S$-$\delta^{34}S$ correlation and felsic volcanic eruptions (Philippot et al., 2012). On the other hand, the heterogeneity of the sulfur isotope ratio in the Kromberg carbonates possibly represents some specific biological processes such as sulfate reduction, or small amounts of oxidative recycling via sulfur compound disproportionation. This biological process might affect the $\Delta^{36}S$-$\Delta^{33}S$ plot as revealed by the scattered $\Delta^{36}S$ values.

5-6-3. Fluvial to shallow marine environment (Noisy Complex)

Analyzed samples of Noisy Complex that represent fluvial material such as sandstone, mudstone and glacial diamictite, show positive $\Delta^{33}S$ values (+0.15‰ to +1.94‰) and a vertical correlation between $\delta^{34}S$ and $\Delta^{33}S$ (Fig. 5-5g) that is slightly different from trends observed in Kromberg Complex. However, the observed $\Delta^{36}S/\Delta^{33}S$ trend reveals a linear array and negative intercept of the $\Delta^{36}S$ axes of ~−0.6‰ that is

similar to Kromberg chert, suggesting the effect of biogenic sulfide. Thus, we interpret the observed vertical trend in $\delta^{34}S$-$\Delta^{33}S$ plot as the mixing of atmospheric sulfide and biogenic sulfide similar to that of the Kromberg chert trends. The difference of the sulfur isotope fractionation between the Kromberg chert and Noisy clastic rocks may reflect the local depositional context. Roerdink et al. (2013) also reported a negative trend of $\delta^{34}S$-$\Delta^{33}S$ in sedimentary sulfide (barite) of 3.2 Ga Mapepe Formation. They also conclude that the negative array in $\delta^{34}S$-$\Delta^{33}S$ probably represents variable degrees of mixing between two biogenic sulfide pools during pyrite formation. On the other hand, Guy et al. (2012) suggest that the crustal sulfate reservoir from volcanic degassing or oxidative weathering of sulfide minerals ($\delta^{34}S$ = 0‰ to +5‰) is a likely end-member of the mixing array in sedimentary sulfide that would produce the negative trend. However, the negative $\Delta^{36}S$ intercept strongly supports the activity of the microbial sulfate reductions in the Noisy fluvial depositional to subaerial settings (Fig. 5-6). The similar isotopic composition between the predicted biogenic sulfide and sulfate indicates sulfate reduction in a closed system with respect to seawater sulfate or low sulfate condition [SO_4^{2-}] < 200μM (e.g. Habicht et al., 2002, Roerdink et al., 2013).

5-6-4. Paleoarchean $\Delta^{36}S/\Delta^{33}S$ slope change

Changes in atmospheric photochemical source reactions have been discussed on the basis of observed relationships between $\Delta^{33}S$ and $\Delta^{36}S$ measured in other Archean sequences because the $\Delta^{36}S/\Delta^{33}S$ slopes are changed globally (Kaufman et al., 2007; Ono et al., 2009a; Zerkle et al., 2012; Kurzweil et al., 2013; Mishima et al., in review.). In this study, we provide the first evidence of the $\Delta^{33}S/\Delta^{36}S$ slope changes, here from -1.0 ± 0.2 to -0.4 ± 0.04 through the 3.5-3.4 Ga Onverwacht Suite (Fig. 5-7). Although the $\Delta^{33}S/\Delta^{36}S$ arrays are influenced by biogenic sulfide mixing, a rotation of the arrays into different slopes implies a change in the nature of the primary S-MIF signature. Moreover, Kromberg cherts reveal a different $\Delta^{36}S/\Delta^{33}S$ slope within the one chert unit: the upper chert samples have a slope of -0.8 ± 0.1, lower chert samples have a slope of -0.4 ± 0.04. Thus, it appears that the $\Delta^{36}S/\Delta^{33}S$ slope changed within the stratigraphic ascending order in the Kromberg chert, similar to the Neoarchean sedimentary rocks (Kaufman et al., 2007; Zerkle et al., 2012). Thus, the observed $\Delta^{36}S/\Delta^{33}S$ slope variation between the

Kromberg upper and lower cherts may indicate an unstable atmosphere at ca. 3.4 Ga.

By contrast, the observed slope of −0.4 in the upper Kromberg chert are clearly shallower than slopes reported from Neoarchean sedimentary rocks ($\Delta^{33}S/\Delta^{36}S$ = −0.9 to −1.8; Kaufman et al. 2007; Farquhar et al., 2007; Ono et al. 2006, 2009; Kurzweil et al.,2013; Zerkle et al., 2012; Guy et al.,2012; Thomassot et al., 2015; Zhelezinskaia et al.,2014; Williford et al., 2016; Mishima et al., in review) (Fig. 5-7). The photochemical experiment results of Whitehill and Ono (2012) indicate that light of 250-330 nm wavelength produces elemental sulfur with a positive $\Delta^{36}S/\Delta^{33}S$ ratio (0.64 ± 0.03) by photoexcitation, and that the bands in the 190-220 nm the 250-330 nm regions produce negative $\Delta^{36}S/\Delta^{33}S$ values (–1.90) by SO_2 self-shielding (Fig. 5-7). The $\Delta^{36}S/\Delta^{33}S$ slopes of Archean sedimentary sulfide could be explained by mixing the signature of the 190-220 nm band and the 250-330 nm band (Whitehill and Ono, 2012; Endo et al., 2016). These changes probably reflect both the intensity of volcanic SO_2 emissions and the concentration of reducing gasses under the O_2-free atmosphere (Endo et al., 2016). Based on such an atmospheric reaction mixing model, comparing the Neoarchean steep slope (−0.9 to −1.8) and the Paleoarchean shallow slope (−1.0 to −0.4), suggests that the Paleoarchean atmosphere seems to be more reduced than the Neoarchean. This change may possibly link to the evolution of oxygenic photosynthesis (Brocks et al., 2003, 2005; Canfield, 2005; Rasmussen et al., 2008).

5-6-5. Implications for intercept of $\Delta^{36}S$-$\Delta^{33}S$

We explained above that the negative intercept of $\Delta^{36}S$-$\Delta^{33}S$ array in the Onverwacht Suite sulfides as due to the mixing with biogenic sulfides. However, non-zero intercepts have not been revealed in previous studies because of the imprecision of ^{36}S measurements. High precision measurements of ^{36}S could only recently be obtained, thus allowing discussions about the $\Delta^{36}S/\Delta^{33}S$ slope changes linked to high resolution stratigraphy. Here we also compile all published quadruple sulfur isotope data and recalculated the intercepts of $\Delta^{36}S$ axes ($\Delta^{36}S/\Delta^{33}S_0$; Table 2, Fig. 5-6).

Prior to ca. 3.2 Ga, all sulfide intercepts are lower than $\Delta^{36}S/\Delta^{33}S_0 = 0$, and intercepts of sulfate (barite deposit) are higher than intercept $\Delta^{36}S/\Delta^{33}S_0 = 0$. This could be explained by fractionation during sulfate reduction, which is necessary to increase $\Delta^{33}S$

and decrease $\Delta^{36}S$ of the pyrites relative to a host sulfate (e.g. Ono et al., 2006; Johnston et al., 2007; Ueno et al., 2008). After ca.2.7 Ga, sulfide intercepts appear to a positive value ($\Delta^{36}S/\Delta^{33}S_0$= ~+0.5 at 2.7 Ga. Sulfide produced by equilibrium hydrothermal reduction (100-200 °C) of sulfate, or 2 components mixing of this sulfide with juvenile sulfur, would produce only small ^{36}S enrichments relative to the mass-independent fractionation array (Shen et al., 2009). Furthermore, laboratory experiments with sulfur disproportionators produces mixing products that have slightly more positive $\Delta^{36}S$ relative to the mass-independent fractionation array (Johnston et al., 2005, 2007). Thus, according to the magnitude of $\Delta^{33}S$ change (Johnston et al., 2011) and the $\Delta^{36}S/\Delta^{33}S$ slope change at 2.7 Ga (Kurzweil et al., 2013; Mishima et al., in review), the timing of sulfide intercept change is possibly related to the change of Archean sulfur cycling.

5-7. Conclusions

High-resolution quadruple sulfur isotope analysis of sedimentary sulfide within the ~ 3.4-3.5 Ga Onverwacht Suite of the Barberton Greenstone Belt, South Africa, reveal previously undocumented stratigraphic changes in $\delta^{34}S/\Delta^{33}S$ and $\Delta^{36}S/\Delta^{33}S$ ratio.

First, shallow/subaerial clastic rocks of the Noisy Complex and laminated deep water chert in Kromberg Complex show two distinctive $\delta^{34}S$-$\Delta^{33}S$ trends. The difference may reflect the activities of microbial sulfate reduction in these two different depositional settings. Any $\Delta^{36}S$-$\Delta^{33}S$ array does not intersect the origin ($\Delta^{36}S = \Delta^{33}S = 0$), and these intercepts are lower than sulfate intercept (barite deposited at 3.5-3.4 Ga). Since the SO_2 photochemical reactions originate from igneous sulfur ($\Delta^{36}S = \Delta^{33}S = 0$), the observed negative intercept strongly support the microbial sulfate reduction at that time.

Second, we detect a Paleoarchean $\Delta^{36}S/\Delta^{33}S$ slope change. The observed slopes of −1.0 to −0.4 are shallower than reported slopes from the Neoarchean (2.5-3.0 Ga). Based on the recently photochemical experiment (Whithill and Ono, 2013; Endo et al., 2016), the Paleoarchean atmosphere was therefore possibly more reductive than during the Neoarchean.

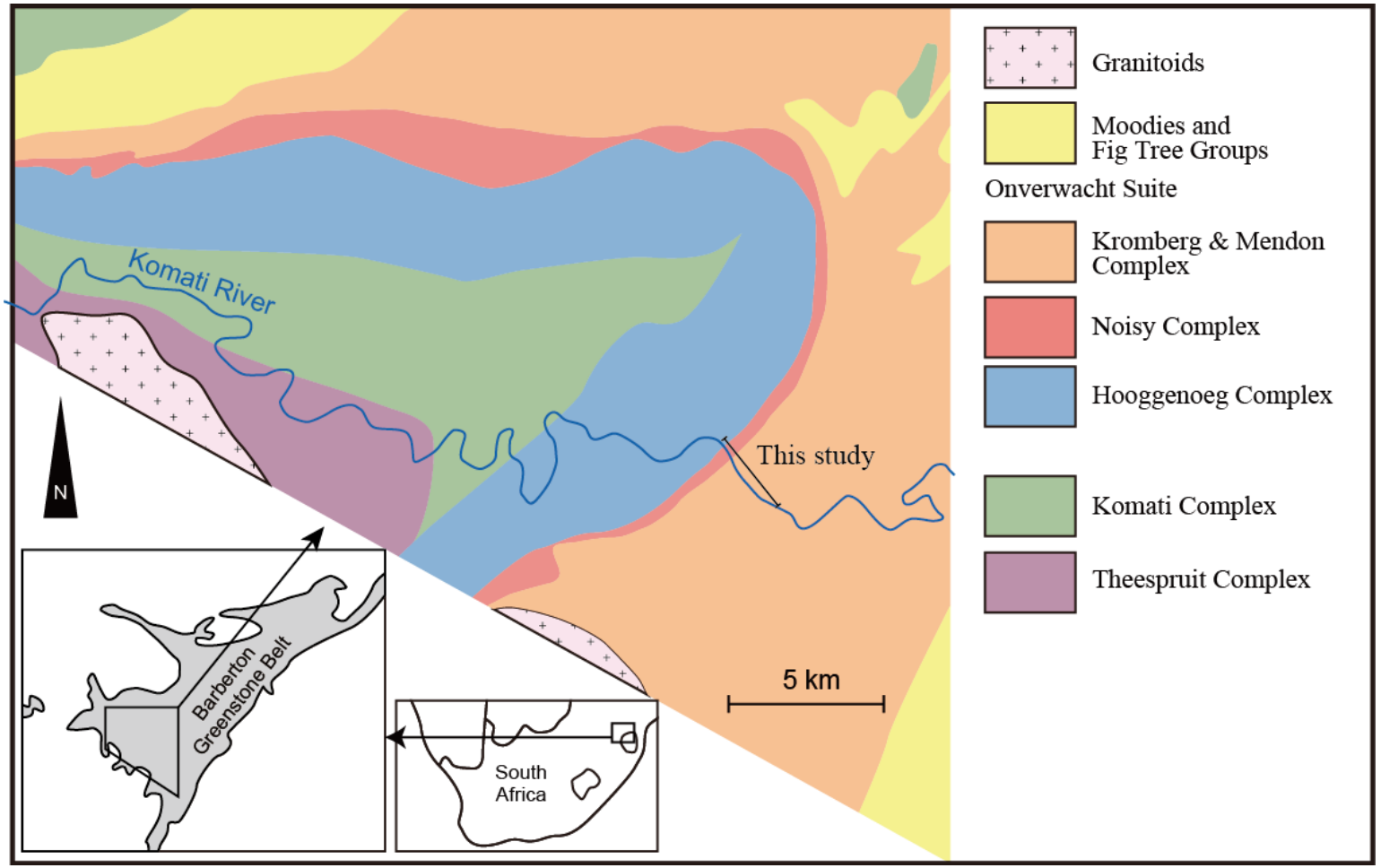

Fig. 5-1 Simplified geological map of the Barberton Greenstone Belt, South Africa. (Modified after de Wit et al.,2011).

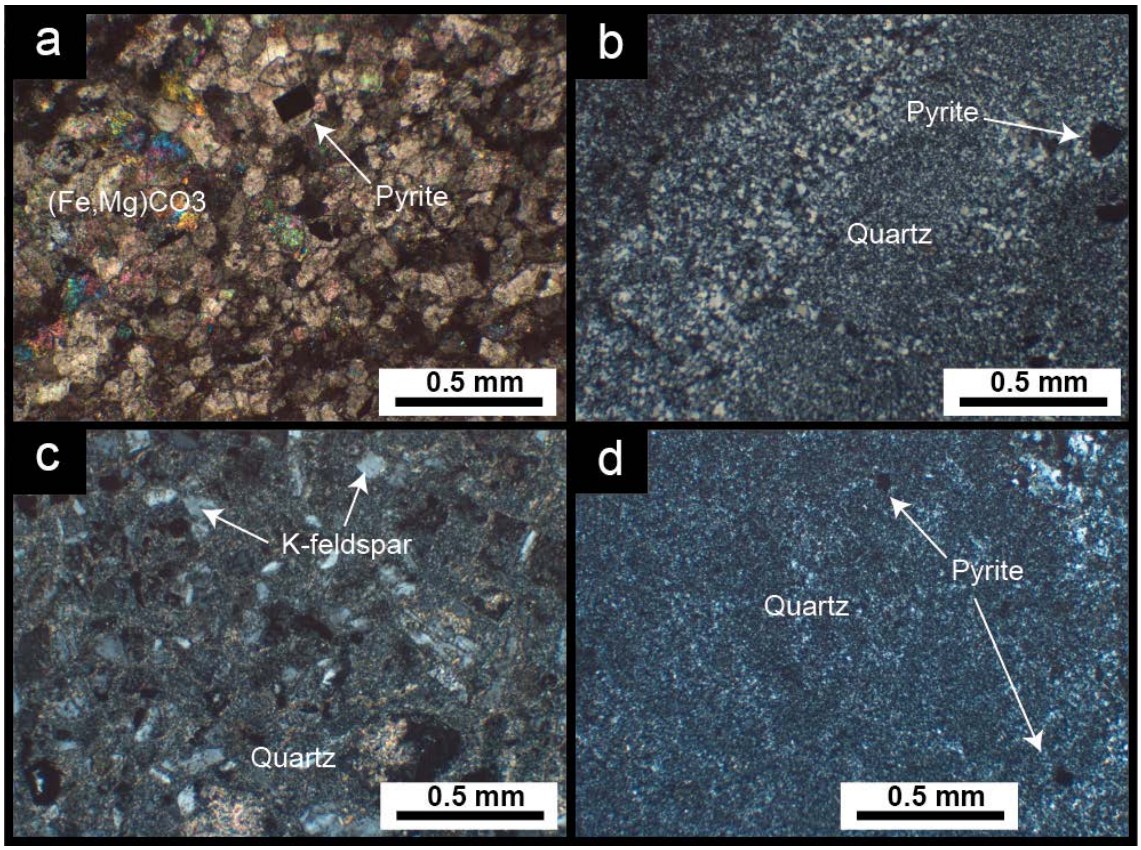

Fig. 5-2 Rock textures observed in Onverwacht Suite, showing (a) carbonate rock in the Kromberg complex (b) layered chert in the Kromberg Complex (c) diamictite matrix in the Noisy Complex (d) chert in the Hoogenoeg Complex.

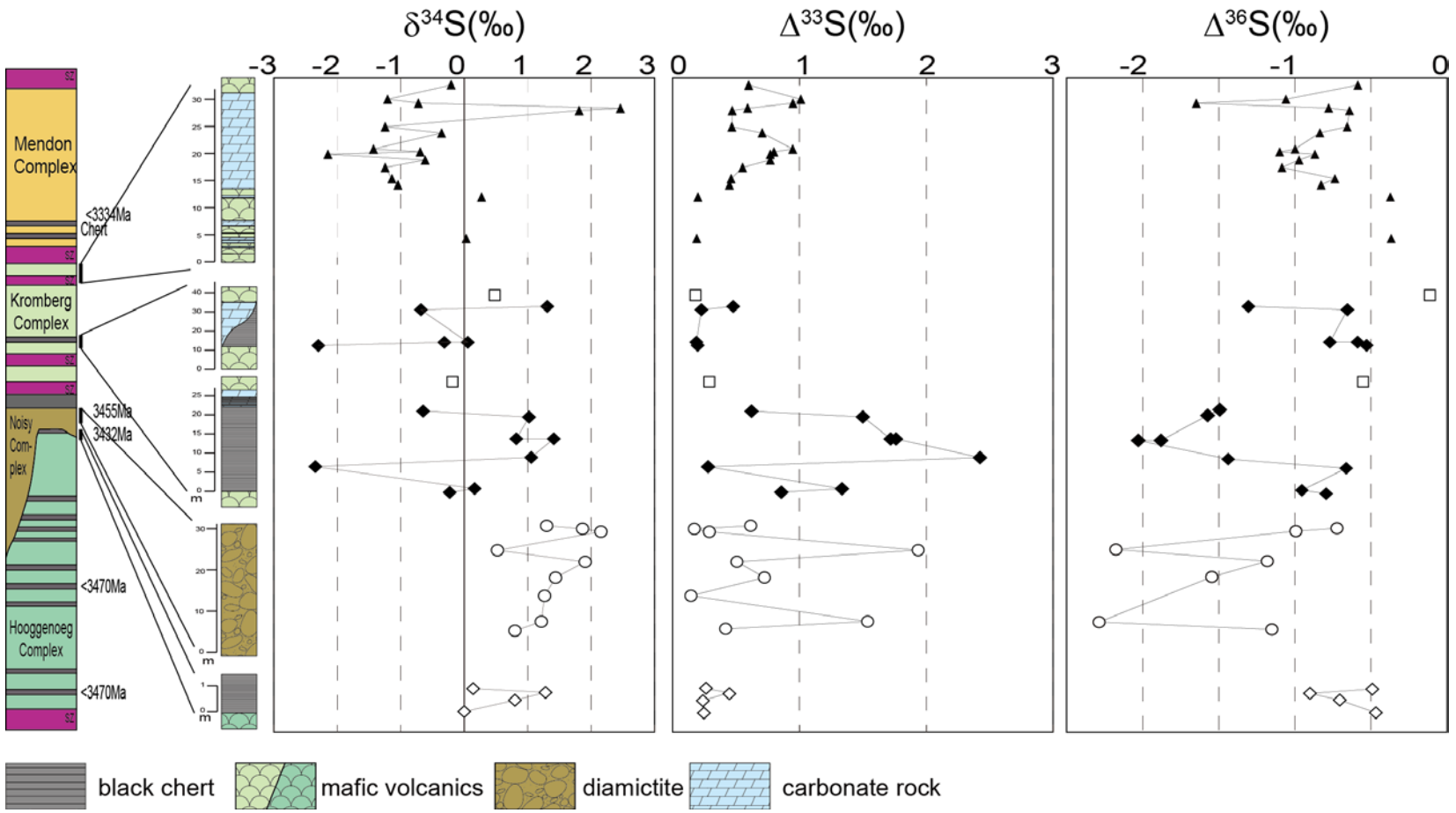

Fig. 5-3 The column shows stratigraphy in the Paleoarchean Onverwacht Suite, Barberton Greenstone belt, South Africa, with the main shear zones (SZ), several chert units and stratigraphic records of multiple sulfur isotopes (modified from de Wit et al., 2011).

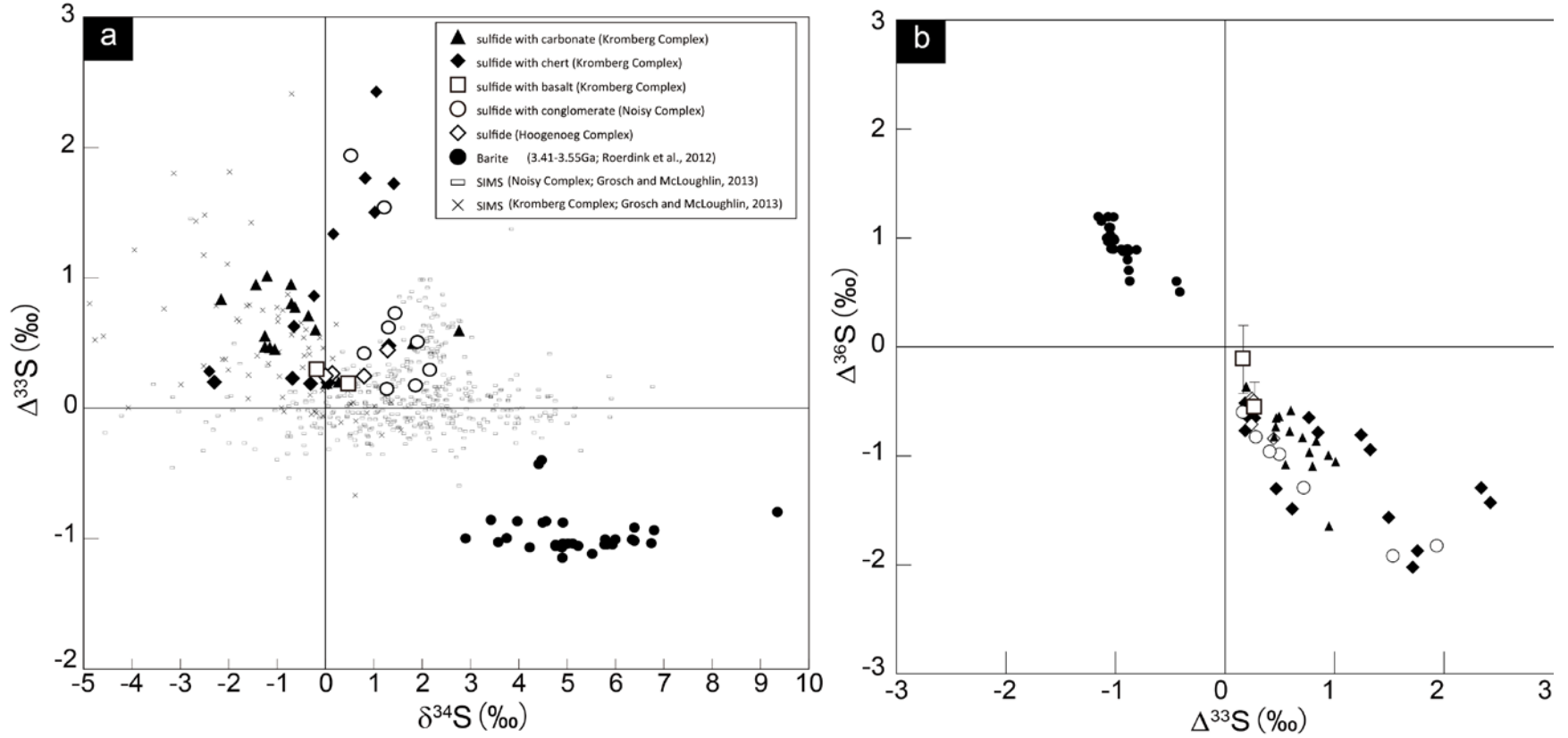

Fig.5-4 Cross-plot of (a) $\delta^{34}S$ vs. $\Delta^{33}S$ and (b) $\Delta^{33}S$ vs. $\Delta^{36}S$ for Onverwacht Suite, Barberton Greenstone Belt, South Africa. Each symbol shows stratigraphic position (Fig. 3). Our samples confirm previous reports for the barite and sedimentary sulfide in the BGB (Roerdink et al., 2012; Grosch and Mcloughlin, 2013).

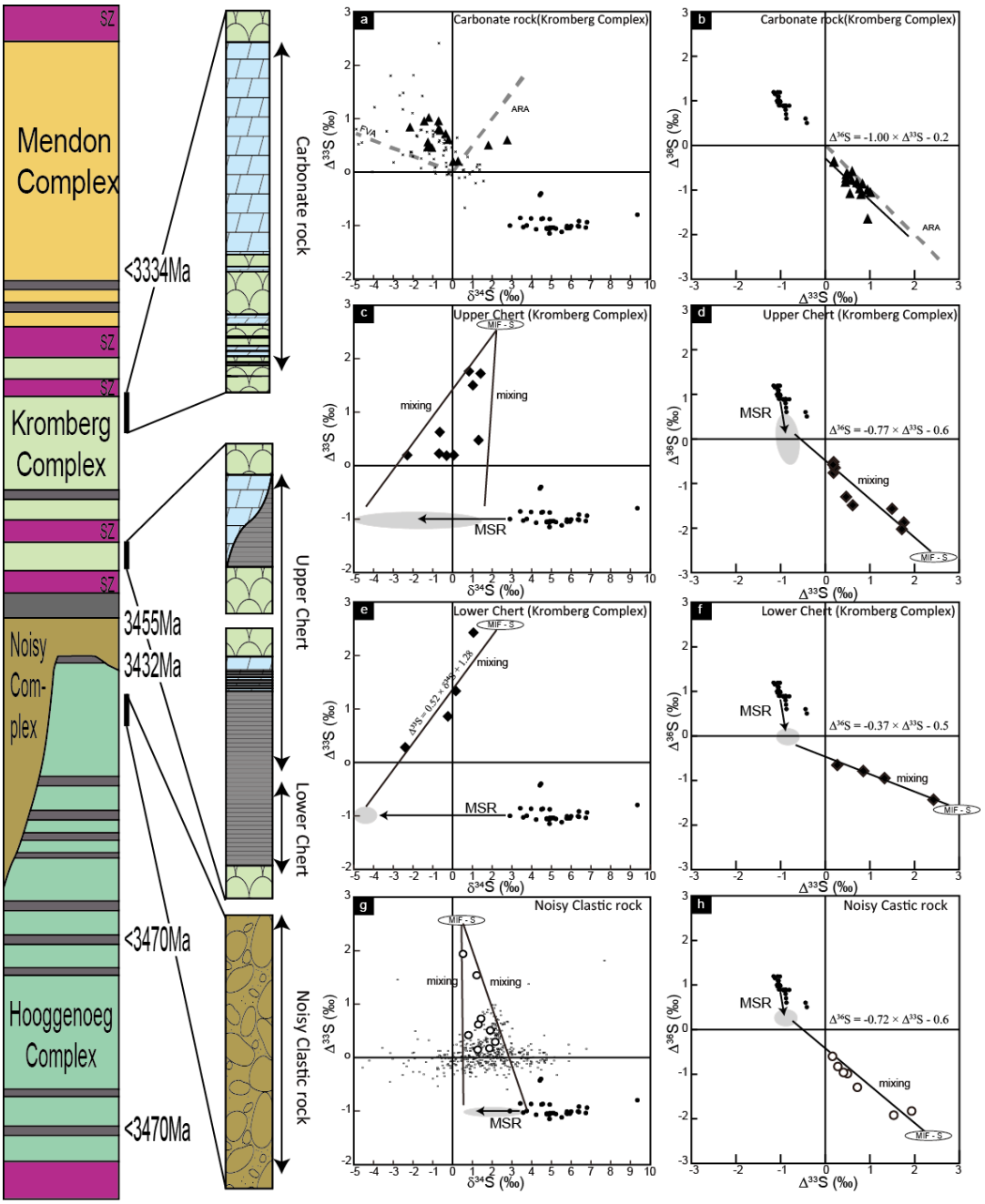

Fig. 5-5 Plots of $\delta^{34}S$, $\Delta^{33}S$ and $\Delta^{36}S$ for each formation in the BGB. (a)(b) carbonate rocks in Kromberg Complext, (c)(d) upper chert in Kromberg Complex, (e)(f) lower chert in Kromberg Complex, (g)(h) Noisy Complex. Solid lines show the mixing line of two different sulfur sources. Grey areas represent the predictable biogenic sulfide (Ono et al., 2003; Ueno et al., 2008). Solid arrows indicate microbial sulfate reduction (MSR). Dashed grey line represent the Achean Reference Array (ARA; e.g. Ono et al., 2003; Ueno et al., 2008) and Felsic volcanic Array (FVA; Philippot et al., 2012).

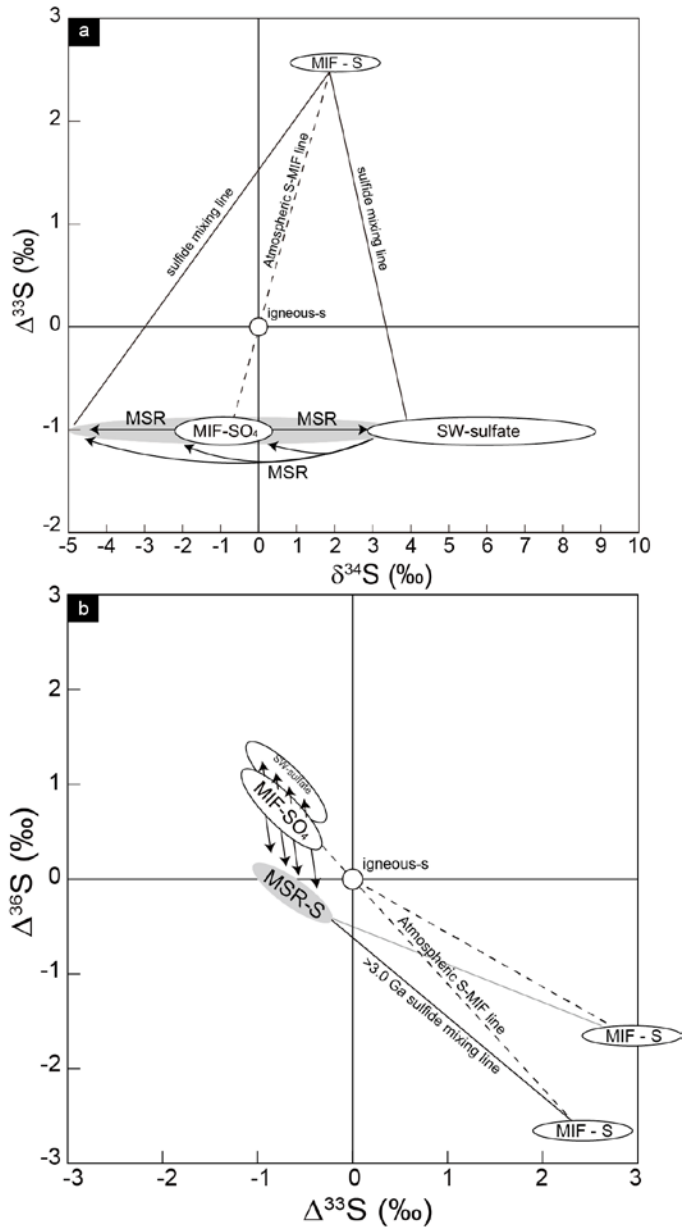

Fig. 5-6 Multiple sulfur isotope systematics for the Palearchean sediments in the Onverwacht Suite. (a) $\delta^{34}S$ vs. $\Delta^{33}S$ and (b) $\Delta^{33}S$ vs. $\Delta^{36}S$. Gray cells represent isotopic composition of microbial sulfate reduction sulfide (MSR-S). Mixing between atmospheric sulfide (MIF-S) and MSR-S is shown in dashed and solid line, respectively.

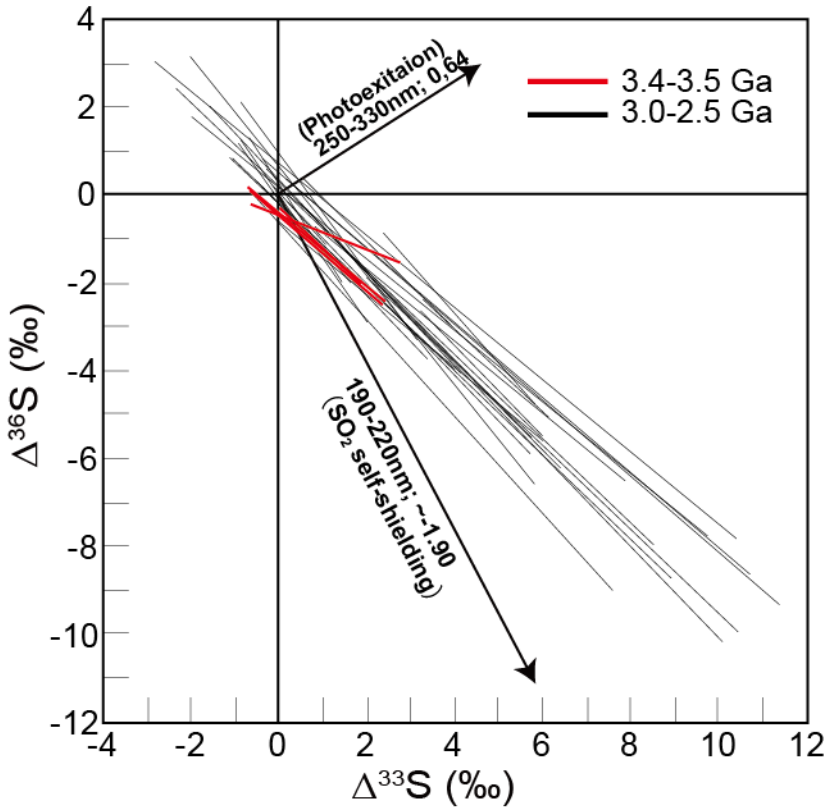

Fig. 5-7 Relationship between $\Delta^{36}S$ and $\Delta^{33}S$ values of the Archean sulfides. The black line indicates the Neoarchean line with $\Delta^{36}S/\Delta^{33}S = -0.9$ to -1.5 (derived from Ono et al., 2006, 2009, Kaufman et al., 2007, Farquhar et al., 2007, Thomazo et al., 2009, Guy et al., 2012, Kurzweil et al., 2013, Zerkle et al., 2012, Thomazot et al., 2013, 2015; Zhelezinskaia et al., 2014; Mishima et al., in review). The red line indicates the Paleoarchean line with $\Delta^{36}S/\Delta^{33}S = -0.4$ to -1.0 (This study). The positive arrow indicates the photoexcitation line ($\Delta^{36}S/\Delta^{33}S$ ratio of $+0.64 \pm 0.03$) and the negative arrow indicates the SO_2 self-shielding lines ($\Delta^{36}S/\Delta^{33}S$ ratio of -1.90) (Whitehill and Ono, 2012; Endo et al., 2016). Sulfur isotope variation of $\Delta^{36}S/\Delta^{33}S$ plot can be explained by these two experimental slopes.

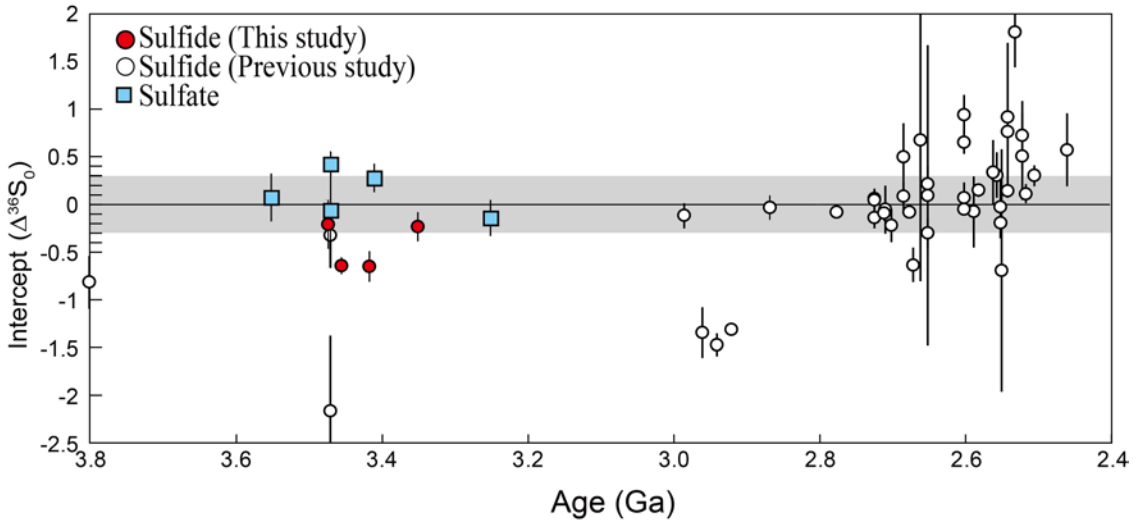

Fig. 5-8 Evolution of the intercept of $\Delta^{36}S/\Delta^{33}S$ values. The data of this study is illustrated by red circle. Literature data (derived from Ono et al., 2006, 2009, Kaufman et al., 2007, Farquhar et al., 2007, Ueno et al., 2008, Shen et al., 2009, Thomazo et al., 2009, Guy et al., 2012, Roerdink et al., 2012, Kurzweil et al., 2013, Zerkle et al., 2012, Thomazot et al., 2013, 2015; Zhelezinskaia et al., 2014; Wacey et al., 2015 and Mishima et al., in review.) is presented as white circles (sulfide) and blue square (sulfate). Shaded areas show from −0.3 to +0.3 of the intercept, which are interpreted as atmospheric MIF lines.

Table 1.
Results of Isotope analysis in the Dharwar Supergroup

Sample	Rock name	Unit	$\delta^{34}S$ (‰)	$\Delta^{33}S$ (‰)	$\Delta^{36}S$ (‰)
KD1 19-1	Carbonated Chert	Kromberg Fm.	-0.20	0.60	-0.58
KD1 19-6	Carbonated Chert	Kromberg Fm.	-1.20	1.01	-1.06
KD1 19-7	Carbonated Chert	Kromberg Fm.	-0.70	0.95	-1.65
KD1 19-9	Carbonated Chert	Kromberg Fm.	2.77	0.59	-0.78
KD1 20-1	Carbonated Chert	Kromberg Fm.	1.81	0.50	-0.64
KD1 20-8	Carbonated Chert	Kromberg Fm.	-1.25	0.47	-0.65
KD1 20-10	Carbonated Chert	Kromberg Fm.	-0.35	0.71	-0.83
KD1 20-14	Carbonated Chert	Kromberg Fm.	-1.43	0.95	-1.00
KD1 20-15	Carbonated Chert	Kromberg Fm.	-0.70	0.80	-1.10
KD1 20-16	Carbonated Chert	Kromberg Fm.	-2.15	0.84	-0.87
KD1 21-3	Carbonated Chert	Kromberg Fm.	-0.63	0.77	-0.97
KD1 21-8	Carbonated Chert	Kromberg Fm.	-1.25	0.55	-1.08
KD1 21-9	Carbonated Chert	Kromberg Fm.	-1.14	0.46	-0.73
KD1 21-11	Carbonated Chert	Kromberg Fm.	-1.05	0.45	-0.82
KD1 21-13	Carbonated Chert	Kromberg Fm.	0.27	0.20	-0.37
KD1 22-10	Carbonated Chert	Kromberg Fm.	0.03	0.19	-0.37
OW69	Metabasalt	Kromberg Fm.	0.48	0.18	-0.11
OW70	Chert	Kromberg Fm.	1.31	0.48	-1.30
OW71	Chert	Kromberg Fm.	-0.68	0.23	-0.65
OW74	Chert	Kromberg Fm.	0.06	0.20	-0.77
OW74(2)	Chert	Kromberg Fm.	-0.31	0.19	-0.59
OW75	Chert	Kromberg Fm.	-2.29	0.20	-0.53
OW94	Metabasalt	Kromberg Fm.	-0.17	0.29	-0.55
OW88	Black Chert	Kromberg Fm.	-0.64	0.63	-1.49
OW87	Black Chert	Kromberg Fm.	1.03	1.50	-1.57
OW85a	Black Chert	Kromberg Fm.	0.83	1.76	-1.88
OW85b	Black Chert	Kromberg Fm.	1.42	1.72	-2.03
OW84	Black Chert	Kromberg Fm.	1.06	2.43	-1.44
OW83	Black Chert	Kromberg Fm.	-2.39	0.28	-0.66
OW79	Black Chert	Kromberg Fm.	0.17	1.33	-0.95
OW78	Black Chert	Kromberg Fm.	-0.23	0.86	-0.79
OW11	Sandstone	Noisy Fm.	1.30	0.62	n.d.
OW10	Mudstone	Noisy Fm.	1.87	0.17	-0.61
OW9	Mudstone	Noisy Fm.	2.16	0.29	-0.84
OW8	Sandstone	Noisy Fm.	0.53	1.94	-1.83
OW6	Sandstone	Noisy Fm.	1.91	0.51	-0.99
OW5	Mudstone	Noisy Fm.	1.45	0.73	-1.30
OW3	Sandstone	Noisy Fm.	1.27	0.15	n.d.
KD2 7-4	Mudstone	Noisy Fm.	1.22	1.54	-1.92
KD2 16-3	Mudstone	Noisy Fm.	0.80	0.42	-0.97
OW57	Black Chert	Hoogenoeg Fm.	0.14	0.27	-0.49
OW56	Black Chert	Hoogenoeg Fm.	1.24	0.46	-0.90
OW54	Black Chert	Hoogenoeg Fm.	0.80	0.25	-0.70
OW51	Black Chert	Hoogenoeg Fm.	0.00	0.25	-0.47

n.d. shows no data

Table 2.
Published slopes in Δ33S versus Δ36S

Stratigraphic position	number	$\Delta^{36}S/\Delta^{33}S$[a]	error	R^2	$\Delta^{36}S/\Delta^{33}S_0$[d]	error	Age (Ma)	Reference
Sedimentary sulfide								
Upper Mt.McRae Formation, Western Australia	24	-1.06	0.06	0.93	0.30	0.11	2504	Kaufman et al., 2007
Under Mt.McRae Formation, Western Australia	19	-0.81	0.02	0.99	0.14	0.07	2541	Kaufman et al., 2007
Kuruman Iron Formation, South Africa	15	-1.52	0.17	0.86	0.57	0.38	2460	Kaufman et al., 2007
Gamohaan Formation, South Africa	8	-0.86	0.08	0.95	0.50	0.45	2521	Kaufman et al., 2007
Upper Nauga Formation, South Africa	15	-1.07	0.26	0.57	-0.70	1.27	2549	Zerkle et al., 2012
Lower Nauga Formation, South Africa	21	-0.96	0.08	0.88	-0.08	0.37	2588	Zerkle et al., 2012
Monteville Formation, South Africa	23	-1.24	0.05	0.97	0.65	0.12	2600	Zerkle et al., 2012
Lokammona Formation, South Africa	10	-1.00	0.04	0.99	0.23	0.18	2650	Zerkle et al., 2012
Babatal Formation, Brasil	68	-1.03	0.05	0.85	0.15	0.07	2580	Zhelezinskaia et al., 2014
Gamohaan Formation, South Africa	3	-0.94	0.07	0.99	0.72	0.36	2521	Izon et al., 2015
Kogelbeen Formation, South Africa	3	-1.14	0.09	0.99	1.81	0.37	2530	Izon et al., 2015
Papkuil Formation, South Africa	5	2.14	2.87	0.16	-2.00	4.30	2535	Izon et al., 2015[b]
Klipfontein Heuwel Formation, South Africa	4	-0.99	0.33	0.81	0.91	0.78	2540	Izon et al., 2015
Fairfield Formation, South Africa	2	-1.61	0.00	1.00	2.19	0.00	2545	Izon et al., 2015[c]
Reivilo Formation, South Africa	25	-0.95	0.05	0.94	-0.03	0.33	2550	Izon et al., 2015
Monteville Formation, South Africa	27	-1.04	0.05	0.94	0.30	0.24	2555	Izon et al., 2015
Lokammona Formation, South Africa	3	-0.93	0.32	0.90	0.09	1.58	2650	Izon et al., 2015
Boomplaas Formation, South Africa	3	-1.03	0.32	0.91	0.67	1.48	2660	Izon et al., 2015
Vryburg Formation, South Africa	21	-0.84	0.06	0.91	-0.64	0.18	2670	Izon et al., 2015
Wittenoom Formation, Western Austraria	15	-1.05	0.13	0.84	0.34	0.34	2561	Izon et al., 2015
MMIF, Western Austraria	8	-1.04	0.04	0.99	0.07	0.16	2600	Izon et al., 2015
Jeerinah Formation, Western Austraria	25	-0.81	0.05	0.92	0.09	0.15	2684	Izon et al., 2015
Tumbiana Formation, Western Australia	8	-1.11	0.16	0.89	0.05	0.11	2724	Izon et al., 2015
Carawine Dolomite, Western Austraria	11	-1.35	0.11	0.94	0.94	0.21	2630	Izon et al., 2015
Nauga/Klein Naute Formation, South Africa	29	-0.96	0.04	0.96	0.21	0.10	2516	Ono et al., 2009
Kidd Creek, Ontario, Canada	62	-0.93	0.06	0.81	0.11	0.08	2710	Kurzweil et al., 2013
Tumbiana Formation, Western Australia	30	-1.57	0.14	0.82	0.26	0.08	2724	Thomazo et al., 2009
Manjeri Formation, Zimbabwe	6	-1.39	0.37	0.78	0.34	0.17	2700	Thomazo et al., 2013
Cheshire Formation, Zimbabwe	22	-1.66	0.24	0.71	0.26	0.15	2650	Thomazo et al., 2013
Duitschland/Rooihoogte Formation, South Africa	22	-0.96		0.98			2300-2600	Guo et al., 2009
Jeerinah Formation, Western Austraria	19	-0.86	0.04	0.97	0.49	0.36	2684	Williford et al., 2016
Carawine Dolomite, Western Austraria	15	-1.06	1.10	0.07	-0.05	5.81	2600	Williford et al., 2016[b]
Mt.McRae Formation, Western Australia	24	-0.85	0.04	0.96	0.76	0.18	2541	Williford et al., 2016
Ventersdorp Formation, South Africa	3	-1.40	0.72	0.79	-0.06	0.25	2709	Farquhar et al., 2007
Tumbiana Formation, Western Australia	8	-1.65	0.17	0.98	-0.14	0.12	2724	Farquhar et al., 2007
Witwatersrand Supergroup, South Africa	19	-0.87	0.52	0.14	-0.49	0.13	2849-2985	Farquhar et al., 2007[b]
Mozaan Group, South Africa	8	-1.11	0.07	0.83	-0.50	0.21	2960-2840	Ono et al., 2006a
Jeppestown Subgroup, South Africa	6	-0.39	0.11	0.89	-1.02	0.05	2914	Guy et al., 2012
Government Subgroup, South Africa	26	-0.94	0.26	0.76	-1.18	0.12	2940	Guy et al., 2012
Hospital Hill Subgroup, South Africa	8	-0.74	0.63	0.57	-1.05	0.27	<2985	Guy et al., 2012
Nsuzu Group	13	-1.72	0.63	0.45	-0.12	0.13	2885	Tsuruoka, MSc thesis
Hiriyur Formation, Southern India	11	-0.93	0.06	0.97	-0.19	0.05	2550	Mishima et al., in prep
Ingaldhal Formation, Southern India	4	-1.07	0.13	0.93	-0.18	0.34	2670	Mishima et al., in prep
Vanivilas Formation, Southern India	7	-1.20	0.13	0.94	-0.08	0.08	2800	Mishima et al., in prep
Bababudan Formation, Southern India	15	-1.48	0.21	0.83	-0.03	0.13	2900	Mishima et al., in prep
Dresser Formation, Western Australia	14	-0.81	0.10	0.86	-0.23	0.17	3470	Ueno et al., 2008
Dresser Formation, Western Australia	23	-1.99	0.49	0.44	-2.17	0.80	3470	Wacey et al., 2015
Nuvvuagittuq Greenstone Belt, Quebec, Canada	13	-0.85	0.18	0.67	-0.62	0.28	3800	Thomassot et al., 2015
Kromberg Complex, South Africa	16	-1.00	0.20	0.64	-0.21	0.14	3416	This study
Kromberg Complex, South Africa	9	-0.77	0.13	0.84	-0.61	0.13	3430	This study
Kromberg Complex, South Africa	4	-0.37	0.04	0.98	-0.51	0.05	3430	This study
Noisy Complex, South Africa	7	-0.72	0.09	0.92	-0.64	0.09	3455	This study
Barite								
Figtree Group, South Africa	16	-1.16	0.35	0.43	-0.14	0.19	3250	Roerdink et al., 2012
Kromberg Formation, South Africa	8	-0.59	0.19	0.62	0.28	0.15	3410	Roerdink et al., 2012
Londozi, South Africa	23	-0.91	0.25	0.40	0.08	0.25	3550	Roerdink et al., 2012
Dresser Formation, Western Australia	9	-0.61	0.11	0.81	0.53	0.14	3470	Ueno et al., 2008
Dresser Formation, Western Australia	7	-0.91	0.51	0.82	0.14	0.61	3470	Shen et al., 2009

a. $\delta^{34}S = 1000 \times ({}^{34}R_{sample}/{}^{34}R_{standard} - 1)$

$\Delta^{33}S = 1000 \times \ln(\delta^{33}S/1000 + 1) - 0.515 \times 1000 \times \ln(\delta^{34}S/1000 + 1)$

$\Delta^{36}S = 1000 \times \ln(\delta^{36}S/1000 + 1) - 1.90 \times 1000 \times \ln(\delta^{34}S/1000 + 1)$

b. The trend show scattered $\Delta^{36}S$, indicating later mass-dependent isotope effects.

c. Too few samples

d. intercept of $\Delta^{36}S/\Delta^{33}S$ trend

References

Aoyama, S., Nishizawa, M., Takai, K., & Ueno, Y., 2014, Microbial sulfate reduction within the Iheya North subseafloor hydrothermal system constrained by quadruple sulfur isotopes. Earth and Planetary Science Letters, 398, 113-126.

Brocks, J. J., Buick, R., Summons, R. E., & Logan, G. A., 2003, A reconstruction of Archean biological diversity based on molecular fossils from the 2.78 to 2.45 billion-year-old Mount Bruce Supergroup, Hamersley Basin, Western Australia. Geochimica et Cosmochimica Acta, 67 (22), 4321-4335.

Brocks, J. J., Love, G. D., Summons, R. E., Knoll, A. H., Logan, G. A., & Bowden, S. A., 2005, Biomarker evidence for green and purple sulphur bacteria in a stratified Palaeoproterozoic sea. Nature, 437 (7060), 866-870.

Canfield, D. E., Raiswell, R., Westrich, J. T., Reaves, C. M., Berner, R. A., 1986, The use of chromium reduction in the analysis of reduced inorganic sulfur in sediments and shales. Chemical Geology, 54, 149–155.

Canfield D. E., Habicht, K. S., Thamdrup, B., 2000, The Archean sulfur cycle and the early history of atmospheric oxygen. Science, 288, 658-661.

Canfield, D. E., 2005, The early history of atmospheric oxygen: homage to Robert M. Garrels. Annu. Rev. Earth Planet. Sci., 33, 1-36.

de Wit, M.J., Armstrong, R.A., Hart, R.J., Wilson, A.H., 1987, Felsic igneous rocks within the 3.3–3.5 Ga Barberton Greenstone Belt: high crustal level equivalents of the surrounding Tonalite-Trondhjemite terrain, emplaced during thrusting. Tectonics 6, 529–549.

de Wit, M. J., Furnes, H., & Robins, B. 2011, Geology and tectonostratigraphy of the Onverwacht Suite, Barberton greenstone belt, South Africa. Precambrian Research, 186(1), 1-27.

de Wit, M. J., & Furnes, H., 2016. 3.5-Ga hydrothermal fields and diamictites in the Barberton Greenstone Belt—Paleoarchean crust in cold environments. Science advances, 2 (2), e1500368.

Ding, T., Valkiers, S., Kipphardt, H., De Bievre, P., Taylor, P. D. P., Gonfiantini, R., Krouse, R., 2001. Calibrated sulfur isotope abundance ratios of three IAEA sulfur isotope reference materials and V-CDT with a reassessment of the atomic weight of

sulfur. Geochimica et Cosmochimica Acta, 65, 2433-2437.

Domagal-Goldman, S. D., Kasting, J. F., Johnston, D. T., Farquhar, J., 2008, Organic haze, glaciations and multiple sulfur isotope in the Mid-Archean Era. Earth and Planetary Science Letters, 269, 29-40.

Endo, Y., Ueno, Y., Aoyama, S., & Danielache, S. O., 2016, Sulfur isotope fractionation by broadband UV radiation to optically thin SO2 under reducing atmosphere. Earth and Planetary Science Letters, 453, 9-22.

Farquhar, J., Bao, H., Thiemens, M. 2000, Atmospheric influence of earth's earliest sulfur cycle, Science, 289, 756-758.

Farquhar, J., Savarino, J., Airieau, S., Thiemens, M. H., 2001, Observation of wavelength-sensitive mass-independent sulfur isotope effects during SO2 photolysis: Implications for the early atmosphere. Journal of Geophysical Research, 106, 32829-32839.

Farquhar, J., Peters, M., Johnston, D.T., Strauss, H., Masterson, A., Wiechert, U., Kaufman, A.J., 2007, Isotopic evidence for Mesoarchaean anoxia and changing atmospheric sulphur chemistry. Nature 449 (7163), 706–709.

Furnes, H., de Wit, M. J., Robins, B., & Sandstå, N. R., 2011, Volcanic evolution of the upper Onverwacht Suite, Barberton greenstone belt, South Africa. Precambrian Research, 186 (1), 28-50.

Furnes, H., Robins, B., & de Wit, M. J., 2012, Geochemistry and petrology of lavas in the upper Onverwacht Suite, Barberton Mountain Land, South Africa. South African Journal of Geology, 115 (2), 171-210.

Grosch, E. G., McLoughlin, N., De Wit, M. J., & Furnes, H., 2009, Drilling for the Archean roots of life and tectonic Earth in the Barberton Mountains. Scientific Drilling, 8, 24-28.

Grosch, E. G., Kosler, J., McLoughlin, N., Drost, K., Slama, J., & Pedersen, R. B., 2011, Paleoarchean detrital zircon ages from the earliest tectonic basin in the Barberton Greenstone Belt, Kaapvaal craton, South Africa. Precambrian Research, 191 (1), 85-99.

Grosch, E. G., & McLoughlin, N., 2013, Paleoarchean sulfur cycle and biogeochemical surface conditions on the early Earth, Barberton, South Africa. Earth and Planetary Science Letters, 377, 142-154.

Guy, B. M., Ono, S., Gutzmer, J., Kaufman, A. J., Lin, Y., Fogel, M. L., & Beukes, N. J. 2012. A multiple sulfur and organic carbon isotope record from non-conglomeratic sedimentary rocks of the Mesoarchean Witwatersrand Supergroup, South Africa. Precambrian Research.

Habicht, K. S., Gade, M., Thamdrup, B., Berg, P., & Canfield, D. E., 2002, Calibration of sulfate levels in the Archean ocean. Science, 298 (5602), 2372-2374.

Hsieh, Y. P., Shieh, Y. N., 1997, Analysis of reduced inorganic sulfur by diffusion methods: improved apparatus and evaluation for sulfur isotopic studies. Chemical Geology, 137, 255–261.

Johnston, D. T., Farquhar, J., Wing, B. A., Kaufman, A. J., Canfield, D. E., & Habicht, K. S., 2005, Multiple sulfur isotope fractionations in biological systems: a case study with sulfate reducers and sulfur disproportionators. American Journal of Science, 305 (6-8), 645-660.

Johnston, D. T., Farquhar, J., & Canfield, D. E., 2007, Sulfur isotope insights into microbial sulfate reduction: when microbes meet models. Geochimica et Cosmochimica Acta, 71 (16), 3929-3947.

Kaufman, A. J., Johnston, D. T., Farquhar, J., Masterson, A. L., Lyons, T. W., Bates, S., Anbar, A. D., Arnold, G. L., Garvin, J., Buick, R., 2007, Late Archean biospheric oxygenation andatmospheric evolution. Science, 317, 1900–1903.

Kröner, A., Byerly, G.R., Lowe, D.R., 1991, Chronology of early Archaean granite greenstone evolution in the Barberton Mountain Land, South Africa, based on precise dating by single zircon evaporation. Earth and Planetary Science Letters, 103, 41–54.

Kröner, A., Hegner, E., Wendt, J.L., Byerly, G.R., 1996, The oldest part of the Barberton granitoid-greenstone terrain, South Africa: evidence for crust formation between 3.5 and 3.7 Ga. Precambrian Research, 78, 105–124.

Kurzweil, F., Claire, M., Thomazo, C., Peters, M., Hannington, M., & Strauss, H., 2013. Atmospheric sulfur rearrangement 2.7 billion years ago: Evidence for oxygenic photosynthesis. Earth and Planetary Science Letters, 366, 17-26.

Lowe, D.R., Byerly, G.R., 1999. Stratigraphy of the west-central part of the Barberton Greenstone Belt, South Africa. In: Lowe, D.R., Byerly, G.R. (Eds.). Geologic Evolution of the Barberton Greenstone Belt, South Africa. Boulder, Colorado, Geol.

Soc. Am. Spec. Pap. 329, 1–36.

Lowe, D. R., & Knauth, L. P., 1977, Sedimentology of the Onverwacht Group (3.4 billion years), Transvaal, South Africa, and its bearing on the characteristics and evolution of the early earth. The Journal of Geology, 699-723.

Ono, S., Eigenbrode, J. L., Pavlov, A. A., Kharecha, P., Rumble, D., Kasting, J. F., Freeman, K. H., 2003, New insights into Archean sulfur cycle from mass-independent sulfur isotope records from the Hamersley Basin, Australia. Earth and Planetary Science Letters, 213, 15-30.

Ono, S., Beukes, N.J., Rumble, D., Fogel,M.L., 2006a. Early evolution of atmospheric oxygen from multiple-sulfur and carbon isotope records of the 2.9 Ga Mozaan Group of the Pongola Supergroup, Southern Africa. South African Journal of Geology 109 (1–2), 97–108.

Ono, S., Wing, B., Johnston, D., Farquhar, J., Rumble, D., 2006b. Mass-dependent fractionation of quadruple stable sulfur isotope system as a new tracer of sulfur biogeochemical cycles. Geochimica Et Cosmochimica Acta 70 (9), 2238–2252."

Ono, S., Shanks, W. C., Rouxel, O. J., Rumble, D., 2007, S-33 constraints on the sea water sulfur contribution in modern seafloor hydrothermal vent sulfides. Geochimica et Cosmochimica Acta, 71, 1170-1182.

Ono, S., Beukes, N. J., Rumble, D., 2009a, Origin of two distinct multiple-sulfur isotope compositions of pyrite in the 2.5Ga Klein Naute Formation, Griqualand West Basin, South Africa. Precombrian Research, 169, 48-57.

Ono, S., Kaufman, A. J., Farquhar, J., Sumner, D. Y., Beukes, N. J., 2009b, Lithofacies control on multiple-sulfur isotope records and Neoarchean sulfur cycles. Precombrian Research, 169, 48-57.

Ono, S., Whitehill, A. R., & Lyons, J. R., 2013. Contribution of isotopologue self‐shielding to sulfur mass‐independent fractionation during sulfur dioxide photolysis. Journal of Geophysical Research: Atmospheres.

Pavlov, A. A., Kasting, J. F., 2002, Mass-independent fractionation of sulfur isotopes in Archean sediments: Strong evidence for an anoxic Archean atmosphere. Astrobiology, 2, 27-41.

Philippot, P., Van Zuilen, M., Lepot, K., Thomazo, C., Farquhar, J., & Van Kranendonk,

M. J., 2007 Early Archaean microorganisms preferred elemental sulfur, not sulfate. Science, 317 (5844), 1534-1537. ISO 690

Philippot, P., van Zuilen, M., & Rollion-Bard, C., 2012, Variations in atmospheric sulphur chemistry on early Earth linked to volcanic activity. Nature Geoscience, 5 (9), 668-674.

Ransom, B., Byerly, G. R., & Lowe, D. R., 1999. Subaqueous to subaerial Archean ultramafic phreatomagmatic volcanism, Kromberg Formation, Barberton greenstone belt, South Africa. SPECIAL PAPERS-GEOLOGICAL SOCIETY OF AMERICA, 151-166.

Rasmussen, B., Fletcher, I. R., Brocks, J. J., & Kilburn, M. R., 2008, Reassessing the first appearance of eukaryotes and cyanobacteria. Nature, 455 (7216), 1101-1104.

Roerdink, D. L., Mason, P. R., Farquhar, J., & Reimer, T., 2012. Multiple sulfur isotopes in Paleoarchean barites identify an important role for microbial sulfate reduction in the early marine environment. Earth and Planetary Science Letters,331, 177-186.

Roerdink, D. L., Mason, P. R., Whitehouse, M. J., & Reimer, T., 2013, High-resolution quadruple sulfur isotope analyses of 3.2 Ga pyrite from the Barberton greenstone belt in South Africa reveal distinct environmental controls on sulfide isotopic arrays. Geochimica et Cosmochimica Acta, 117, 203-215.

Roerdink, D. L., Mason, P. R., Whitehouse, M. J., & Brouwer, F. M., 2016, Reworking of atmospheric sulfur in a Paleoarchean hydrothermal system at Londozi, Barberton Greenstone Belt, Swaziland. Precambrian Research, 280, 195-204.

Shen, Y.A., Buick, R., Canfield, D.E., 2001. Isotopic evidence for microbial sulphate reduction in the early Archaean era. Nature 410 (6824), 77–81.

Shen, Y.N., Farquhar, J., Masterson, A., Kaufman, A.J., Buick, R., 2009. Evaluating the role of microbial sulfate reduction in the early Archean using quadruple isotope systematics. Earth and Planetary Science Letters 279 (3–4), 383–391.

Hsieh, Y. P., Shieh, Y. N., 1997, Analysis of reduced inorganic sulfur by diffusion methods: improved apparatus and evaluation for sulfur isotopic studies. Chemical Geology, 137, 255–261.

Sumner, D.Y., Bowring, S.A., 1996. U–Pb geochronologic conCompstraints on deposition of the Campbellrand Subgroup Transvaal Supergroup, South Africa.

Precambrian Research 79, 25–35.

Swaminath, J., Ramakrshnan, M., 1981, Early Precambrian supracrustals of southern Karnataka. Report of Geological Survey of India, 112, 350pp.

Taylor, P. N., Chadwick, B., Moorbath, S., Ramakrishnan, M., Viswanatha., M. N., 1984, Petrography, chemistry and isotopic ages of Peninsular Gneiss, Dharwar acid volcanic rocks and the Chitradurga granite with special reference to the late Archaean evolution of the Karnataka craton, Precambrian Research, 23, 349-375.

Thomazo, C., Ader, M., Farquhar, J., Philippot, P., 2009. Methanotrophs regulated atmospheric sulfur isotope anomalies during the Mesoarchean (Tumbiana Formation,

Thorpe, R. I., Hickman, A. H., Davis, D. W., Mortensen, J. K., & Trendall, A. (1992). Constraints to models for Archaean lead evolution from precise zircon U–Pb geochronology for the Marble Bar region, Pilbara Craton, Western Australia. The Archaean: Terrains, Processes and Metallogeny, 395-407.

Trendall, A. F., Compston, W., Nelson, D. R., De Laeter, J. R., & Bennett, V. C. 2004. SHRIMP zircon ages constraining the depositional chronology of the Hamersley Group, Western Australia*. Australian Journal of Earth Sciences, 51(5), 621-644.

Ueno, Y., Ono, S., Rumble, D., Maruyama, S., 2008, Quadruple sulfur isotope analysis of ca. 3.5 Ga Desser Formation: New evidence for microbial; sulfate reduction in the early Archean. Geochimica et Cosmochimica Acta, 72, 5675-5691.

Ueno, Y., Jhonston, M. S., Danielache, S. O., Eskebjerg, C., Pandey, A., Yoshida, N., 2009, Geological sulfur isotopes indicate elevated OCS in the Archean atmosphere, solving faint young sun paradox. Proceedings of the National Academy of Sciences of the United States of America, 106, 14784-14789.

Ueno, Y., Endo, Y., Mishima, K., Danielache, S. O., 2014, Decoding the evolution of early atmosphere: Experimental reconstruction of the Δ36S/Δ33S chemostratigraphy. Proceedings of the Japan Goscience Union Meeting 2014 (Jpn Geosci Union, Tokyo, Japan).

Viljoen, M.J. and Viljoen, R.P., 1969. An introduction the geology of the Barberton Granite-Greenstone Terrain. In Spacial Pablication, Geological Society of South Africa, 2: 9-28.

Walraven, F., Smith, C.B., Kruger, F.J., 1991. Age determinations of the Zoetlief Group–

Ventersdorp Supergroup correlatives. South African Journal of Geology 94, 220–227.

Whitehill A. R., and S. Ono, 2012, Excitation band dependence of sulfur isotope mass-independent fractionation during photochemistry of sulfur dioxide using broadband light sources, Geochim. Cosmochim. Acta, 94, 238–253.

Williford, K. H., Ushikubo, T., Lepot, K., Kitajima, K., Hallmann, C., Spicuzza, M. J., ... & Valley, J. W., 2016, Carbon and sulfur isotopic signatures of ancient life and environment at the microbial scale: Neoarchean shales and carbonates. Geobiology, 14(2), 105-128.

Zahnle, K., Claire, M., Catling, D., 2006, The loss of mass-independent fractionation in sulfur due to a Palaeoproterozoic collapse of atmospheric methane. Geobiology, 4, 271–283.

Zerkle, A. L., M. W. Claire, S. D. Domagal-Goldman, J. Farquhar, and S. W. Poulton 2012, A bistable organic-rich atmosphere on the Neoarchaean Earth, Nat. Geosci., 5(4), 1–5.

Chapter 6

Synthesis

6-1. Previous studies on the Archean atmospheric evolution

The Archean reducing atmospheric condition has been envisaged mainly from geological evidences such as absence of red bed (Chandler, 1980; Melezhik et al., 2005), abundant well-rounded pebbles of the minerals uraninite (UO_2), pyrite (FeS_2) and siderite ($FeCO_3$), which are unstable in modern oxidized fluvial environment, before 2.3 Ga (Holland, 1984; Rasmussen and Buick, 1999; Roscoe, 1996; England et al., 2002; Hofmann et al., 2009). In addition, sulfur mass-independent fractionation (S-MIF) is found only in the Archean sedimentary rocks (e.g. Farquhar et al., 2000). The origin of the sulfur isotope anomaly is believed to have resulted from SO_2 photolysis by UV radiation in a low oxygen atmosphere, as supported by photochemical experiments in the laboratory (Farquhar et al., 2001; Pavlov and Kasting, 2002; Ono et al., 2003). Thus, the existence of the S-MIF in the Archean sedimentary rock is strong evidence of the Archean oxygen free atmosphere.

While the presence of large Archean S-MIF is widely accepted as indicating a reducing atmosphere (Farquhar et al., 2007; Johnston, 2011), it is still debated what occupied in place of oxygen in the Archean atmosphere. Kasting (1987) suggested a dense CO_2 atmosphere ($pCO_2 > 0.1$ bar) could have provided sufficient warming to keep Earth unfrozen in the face of lower solar luminosity in early Earth. However, constraints derived from Archean/Paleoproterozoic paleosols suggest that actual atmospheric CO_2 levels were not that high (Rye et al., 1995; Sheldon, 2006). Thus, one or more reducing gases other than CO_2 could have been present at relatively high concentrations and may have provided additional greenhouse warming (Sagan and Mullen, 1972; Domagal-Goldman et al., 2008; Haqq-Misra et al., 2008). Formation of an organic haze at high CH_4:CO_2 concentrations was also shown to decrease SO_2 photolysis rates in a 1-D photochemical model (Domagal-Goldman et al., 2008), suggesting that shielding by organichaze might have caused the diminution of $\Delta^{33}S$ magnitudes in the Mesoarchean.

The Archean $\Delta^{33}S$ record exhibits clear changes in the magnitude of MIF over time: minimum $\Delta^{33}S$ at around 2.9 Ga, subsequent large $\Delta^{33}S$ variations culminating at 2.5 Ga, followed by its sudden drop in the Paleoproterozoic. The change in $\Delta^{33}S$ signature may possibly reflect a fluctuation in oxygen levels (Ono et al., 2006a), the presence of large volcanic eruptions (Ohmoto et al., 2006), speciation of volcanic gasses (SO_2/H_2S ratio;

Halevy et al., 2010) and/or other changes in atmospheric chemistry (Farquhar et al., 2007; Domagal-Goldman et al., 2008; Thomazo et al., 2009; Zerkle et al., 2012; Claire et al., 2014). In addition, the atmospheric $\Delta^{33}S$ value can be diluted by mixing it with mass-dependent sulfur compounds (Ono et al., 2003, Penniston-Dorland et al., 2008, Guy et al., 2012). So far, it has been difficult to decouple the $\Delta^{33}S$ variations caused by atmospheric processes from other reactions in subsequent processes (biology, photolysis, mixing, open system, etc.) before sedimentation (Halevy et al., 2013).

Recently, the quadruple sulfur isotope (^{32}S, ^{33}S, ^{34}S, ^{36}S) records provide evidence for a striking change in the terrestrial sulfur cycle related to the oxidation of Earth's surface environments (Kaufman et al., 2007; Zerkle et al., 2012; Kurzweil et al., 2013). The inclusion of $\Delta^{36}S$ measurements provides an important additional constraint on the mass-dependent character of the observed fractionation, and taken with the $\Delta^{33}S$ compositions, requires more than mixing to produce the small scale $\Delta^{33}S$ and $\Delta^{36}S$ effects and larger $\delta^{34}S$. For example, mass independent processes that occurred during the Archean show a different $\Delta^{36}S/\Delta^{33}S$ ratio from –1 to –1.5 (e.g. Kaufman et al., 2007; Zerkle et al., 2012). The mechanism to change the $\Delta^{36}S/\Delta^{33}S$ ratio is still uncertain, though it could potentially reflect the change in atmospheric chemistry before the GOE (Kaufman et al., 2007; Farquhar et al., 2007).

Geographically, most of the Archean S-MIF records measured so far are mainly derived from Pilbara Craton, Western Australia and Kaapvaal Craton, South Africa. However, several paleomagnetic and lithostratigraphic studies suggested that Pilbara and Kaapvaal Cratons might have been part of the same continent Vaalbara (Fig. 6-1; e.g., Bleeker et al., 2003, Cheney et al., 1996). A few previous works of quadruple sulfur isotope are reported from Zimbabwe, Canada and Brazil (Thomazo et al., 2013; Kurzwil et al., 2013; Zhelezinskaia et al., 2014). However, there studies lack the stratigraphic observation through the late Archean. Therefore, it is possible that the S-MIF signals in previous works may reflect local changes such as non-atmospheric reactions may be implicated in some sulfur MIF (e.g., Watanabe et al., 2009) and may not necessarily catch global events. In order to distinguish the local and global signatures, it is necessary to study other late Archean sections around the world.

Fig. 6-1 shows a cladogram which represents break-up and amalgamation, typically

associated with significant orogenies. Archean supercratons, break-up of which spawned the independent Archean cratons, are shown at the bottom (Superia, Sclavia, Vaalbara, and possibly a fourth supercraton). Composite cratons that resulted from collisional amalgamation of the Archean cratons during the Paleoproterozoic are shown at the top. While Williams et al. (1991) argued that all the Archean cratons originated from break-up of a single late Archean supercontinent (Kenorland), alternatively, Bleeker et al. (2003) argued that the cratons may have originated from break-up of several distinct supercratons. Considering the lithological differences between some of the better-known cratons such as the Slave, Superior, and Kaapvaal, it seems likely that these cratons originated from independent supercratons (Sclavia, Superia, Vaalbara) with distinct amalgamation and break-up histories (Bleeker et al., 2003). In contrast to the Superior and Kaapvaal cratons, which are radically different from the Slave craton and each other, the Dharwar craton of peninsular India, the Zimbabwe craton of southern Africa, and the Wyoming craton of North America all show significant similarities to the Slave craton. It thus seems likely that at least some of these were nearest neighbors to the Sclavia supercraton. Thus, according to Fig. 6-1, Dharwar is possibly separated from Vaalbara in the Archean period.

6-2. Summary of this study

The result of this research provided several new lines of paleo environmental evidence for the Archean as follows:

1. We provide new late Archean stratigraphy of the Chitradusrga Schist Belt, Western Dharwar Craton, Southern India apart from better-known cratons such as the Slave, Superior, Kaapvaal and Pilbara Cratons. The volcano-sedimentary sequences of 3.0-2.5 Ga Dharwar Supergroup should be divided into two units by an unconformity. The lower unit consists of basal conglomerate, stromatolitic carbonate, silici-clastics with diamictite (Talya conglomerate), chert/BIFs and thick pillowed basalt in ascending order, indicating that rift margin environment predominated at this time. The upper unit unconformably overlies the pillow lava, and consists of conglomerate/sandstone, mafic lava, BIFs and silici-clastic sequence. Especially, the age distribution in the upper unit (Hiriyur Formation) shows a peak age at around 2.54 Ga, suggesting the hinterland from the young granite intrusive. In the Chitradurga Schist Belt, tectonic

processes appear to have operated similar to those within modern plate boundaries.

2. The 2.8-2.7 Ga Sadarahalli diamictite in the Dharwar Supergroup are interpreted as a glaciomarine unit deposited on a marine shelf (or possibly on the slope) by rainout of iceberg-rafted coarse detritus and suspension settling of fine sediment. This evidence of new 2.8-2.7 Ga glaciation, together with the 2.9-2.8 Ga Pongola glaciation (Young et al., 1998) and 2.8 Ga Nuywane Formation, Botswana (Modie, 2002), envisage the climate cooling era at 2.9-2.7 Ga.
3. All the samples in the Dharwar Supergroup exhibit a clear MIF signature ($\Delta^{33}S$ = –1.2 to +3.9‰) with $\Delta^{36}S/\Delta^{33}S$ slope from –0.9 to –1.5, suggesting that the mixing of atmospheric sulfur and MDF components was responsible for the observed isotopic variation. Comparing the $\Delta^{36}S/\Delta^{33}S$ arrays reported from the Kaapvaal Craton (South Africa), Pilbara Craton (Western Australia), Babatal Formation (Brazil), Zimbabwe and Kidd Creek (Canada) with our new data from Dharwar Supergroup, the $\Delta^{36}S/\Delta^{33}S$ slopes seem to change globally from –1.5 to –0.9 through the late Archean (Fig. 6-4). The global nature of the trend contradicts the local S-MIF signal such as abiotic sulfate reduction (Watanabe et al., 2009) and supports the theory that the $\Delta^{36}S/\Delta^{33}S$ slope reflects the change in atmospheric chemistry through the late Archean. These results strengthen the use of S-MIF signal to trace the change of atmospheric chemistry before the Great Oxidation Event. The change in $\Delta^{36}S/\Delta^{33}S$ ratio may have another clue to monitor volcanic activity and amount of reducing gas in the atmosphere. The period characterized by the $\Delta^{36}S/\Delta^{33}S$ slope of ~ -1.5 seems to correspond to mid-Archean glaciation (2.9~2.8 Ga Pongora glaciation: Young et al., 1998). This correlation may suggest a potential link between atmospheric chemistry changes and climate during the late Archean era.
4. Quadruple sulfur isotope data from a sedimentary sulfide within the ~3.5 Ga Onverwacht Suite of the Barberton Greenstone Belt, South Africa, reveal previously undocumented high-resolution stratigraphic changes in middle Archean sulfur isotopes of $\Delta^{33}S/\delta^{34}S$ and $\Delta^{36}S/\Delta^{33}S$ ratio. First, two distinctive $\Delta^{33}S/\delta^{34}S$ trends in shallow-subaerial clastic rocks of the Noisy Complex and laminated deep water chert in Kromberg Complex are documented in Chapter 5. These variations are interpreted to reflect the microbial sulfate reduction activity in the different depositional setting.

Moreover, none of the regression lines of $\Delta^{36}S/\Delta^{33}S$ plots intersect the origin ($\Delta^{36}S = \Delta^{33}S = 0$) and these intersects are lower than barite intercepts. Since the SO_2 photochemical reactions originate from igneous sulfur ($\Delta^{36}S = \Delta^{33}S = 0$), the observed negative intercept strongly support the microbial sulfate reduction. Secondly, we detect the paleo Archean $\Delta^{36}S/\Delta^{33}S$ slope change for the first time. We deduce an atmospheric origin for the large variation in $\Delta^{33}S$ and $\Delta^{36}S$ in the Onverwacht sulfide. The observed slope of −1.0 to −0.4 are shallower than reported slopes from the late Archean (2.5-3.0 Ga). Based on the recently photochemical experiment (Whithill and Ono, 2012; Endo et al., 2016), the paleo Archean atmosphere possibly more reductive than the late Archean.

6-3. **New insights into the Archean microbial sulfur cycling**

Minor sulfur isotopic compositions of pyrite minerals associated with Paleoarchean barite deposits have been used as evidence for microbial sulfate reduction as early as 3.5 Ga (Roerdink et al., 2013; Shen et al., 2009; Ueno et al., 2008). In pre-2.4 Ga old rocks, these mass-dependent isotopic fractionation effects will overprint the mass-independently fractionated sulfur, because the potential sulfur sources, i.e. seawater sulfate and elemental sulfur have a photolytic origin. Thus, a combination of negative $\delta^{34}S$ values and either negative or positive $\Delta^{33}S$ values would be indicative for microbial sulfur cycling in the pre-2.4 Ga world (e.g., Johnston (2011) and references therein). However, the evolution of microbial sulfur cycling through the Archean is still unknow, because of minimal fractionation between sulfate and sulfide. Moreover, it is difficult to distinguish between initial mass-independent and later mass-dependent effect.

In this study, we newly propose that the intercept of $\Delta^{36}S$ axes ($\Delta^{36}S_0$) in the $\Delta^{33}S$-$\Delta^{36}S$ plot should be useful as an indicator of microbial activity (Fig. 6-2). Our understanding of the Archean sulfur cycle is the assumption of a magmatic sulfur source that does not carry a mass-independently fractionated sulfur isotope signature ($\Delta^{33}S = \Delta^{36}S = 0‰$; Ueno et al., 2008). The Archean sulfur cycle was dominated by volcanic input into the early atmosphere and its subsequent photochemical processing. Thus, the $\Delta^{33}S$-$\Delta^{36}S$ intercept which doesn't through the origin likely reflect the later mass-dependent processes (Fig. 6-2b). Prior to ca. 3.2 Ga, all sulfide intercepts are lower than $\Delta^{36}S_0 = 0$,

and intercepts of sulfate (barite deposit) are higher than $\Delta^{36}S_0 = 0$. This could be explained by fractionation during sulfate reduction, which is necessary to increase $\Delta^{33}S$ and decrease $\Delta^{36}S$ of the pyrites relative to a host sulfate (as discussed in Chapters 4 and 5). On the other hand, sulfide intercepts appear to shift from a negative to a positive value ($\Delta^{36}S_0$= ~+0.5) after ~2.7 Ga. To explain the positive intercept, we consider the 2 components mixing model which produce ^{36}S enrichments.

The magnitude of the effect on $\delta^{34}S$, $\Delta^{33}S$ and $\Delta^{36}S$ during a mixing of two sulfur pools (A and B), producing a new sulfur pool C is given as

$$\ln(\delta^{34}S_c/1000 + 1) = f' \times \ln(\delta^{34}S_A/1000 + 1) + (1 - f') \times \ln(\delta^{34}S_B/1000 + 1),$$

$$\Delta^{33}S_C = 1000 \times \ln\{f'(^{33}\alpha - 1) + 1\} - 0.515 \times 1000 \times \ln\{f'(^{34}\alpha - 1) + 1\} + \Delta^{33}S_B,$$

$$\Delta^{36}S_C = 1000 \times \ln\{f'(^{36}\alpha - 1) + 1\} - 1.9 \times 1000 \times \ln\{f'(^{34}\alpha - 1) + 1\} + \Delta^{36}S_B,$$

where f' is the ^{32}S normalized mixing ratio of the two initial sulfur reservoirs (Ono et al., 2006b).

Figure 6-3 shows the deviation from the reference mass-independent fractionation array ($\Delta^{36}S+\Delta^{33}S = 0$) versus the isotopic fractionation of $^{34}S/^{32}S$ between sulfate and sulfide ($\delta^{34}S_{sulfate}-\delta^{34}S_{sulfide}$). While the sulfate reduction (blue square) produces the negative deviation from $\Delta^{36}S+\Delta^{33}S = 0$, the two component mixings produce positive deviations. Thus, both can most easily explain the Archean $\Delta^{36}S_0$ variations through two component mixing. Before 2.7 Ga, an atmospheric source of positive $\Delta^{33}S$ and $\Delta^{36}S$ can mix back toward a biogenic sulfide, much like that of the well documented at 3.5 Ga. On the other hand, an atmospheric source can mix back toward 2 components mixing sulfide which produce positive deviation from original $\Delta^{33}S/\Delta^{36}S$ ratio after 2.7 Ga. Moreover, this 2component mixing model is supported by evolution of $\delta^{34}S$ values in the Archean sedimentary sulfide, indicating that the large $\delta^{34}S$ variation (>50‰) appeared after 2.7 Ga (Fig. 6-5c).

One interpretation of the positive shift of intercept $\Delta^{36}S_0$ and large variation of $\delta^{34}S$ in the late Archean sedimentary sulfide is that they reflect a sulfate concentration in the Archean seawater. After the evolution of oxygenic photosynthesis at ~2.7 Ga (Brocks et al., 2003, 2005; Canfield, 2005; Rasmussen et al., 2008), the oxygen which produced by photosynthesizer must have been consumed by the iron and sulfur oxidation in the water (Fig. 6-7). Indeed, the BIF depositions were increased after 2.7 Ga (Fig. 6-8; from Bekker

et al., 2010). However, the seawater sulfate concentration in the Archean period is still highly debated (Habicht et al., 2002; Crowe et al., 2014).

As such, reworking of atmospheric sulfur isotope record may have been more important for variations in $\Delta^{33}S$ and $\Delta^{36}S$ in Archean sedimentary sulfide than previously considered, possibly complicating the interpretation of ancient $\Delta^{36}S/\Delta^{33}S$ slope due to mixing of multiple atmospheric and microbial minor isotopic arrays. In this study, to discuss the Archean atmospheric chemistry in below section, we use the previous data of $\Delta^{36}S/\Delta^{33}S$ slope which through the origin of $\Delta^{33}S$-$\Delta^{36}S$ plot as reflecting the "Atmospheric S-MIF array".

6-3. New insights into the Archean atmospheric compositions

The new quadruple sulfur isotope evidences provide several new insights into the Archean atmospheric composition and its evolution. In order to compare our results with the previous data from Pilbara and Kaapvaal Craton, we have recalculated the published $\Delta^{33}S$ and $\Delta^{36}S$ values according to the logarithmic definition and obtained a $\Delta^{36}S/\Delta^{33}S$ ratio for each stratigraphic unit. Especially, we excluded later mass dependent processes using the $\Delta^{36}S_0$ to evaluate the original atmospheric $\Delta^{36}S/\Delta^{33}S$ ratio discussed above. The Archean atmospheric compositions which one of the major subject for the middle to late Archean environmental evolution are discussed and reconsidered.

Firstly, the discoveries of $\Delta^{36}S/\Delta^{33}S$ slope changes from −1.5 to −1.0 through the 3.0-2.5 Ga Dharwar Supergroup, Southern India indicate that the late Archean $\Delta^{36}S/\Delta^{33}S$ slopes changed globally: steep slopes (~−1.5) during 3.0-2.7 Ga, followed by its gradually shallow (~−1.0) before 2.7 Ga. This reconfirm that the $\Delta^{36}S/\Delta^{33}S$ slopes reflect the atmospheric composition before the Great Oxidation Event. On the other hand, recent studies by Kurzweil et al. (2013) have documented the variation of slope within sedimentary successions as old as 2.71 Ga Kidd Creek area, Ontario, Canada. Zerkle et al, (2012) also reported the several slope changes from −1.5 to −0.9 at late Archean. Thus, considering the secular $\Delta^{36}S/\Delta^{33}S$ slope changes in more detail, the late Archean period can be subdivided into three stages; 3.0-2.7 Ga, 2.7-2.6 Ga and 2.6-2.5Ga (Fig. 6-4). The $\Delta^{36}S/\Delta^{33}S$ slopes between 3.0 and ~2.7 Ga are steeper than other Archean slopes, which related to mid Archean glaciations (Fig. 6-7). On the other hand, the slopes between 2.7

and 2.6 Ga have a range of −2.0 to −1.0. This period is consistent with the geological record suggesting a major increase in subaerial volcanic activities around ~2.7 Ga (Kump and Barley, 2007; Condie et al., 2009; Bradley, 2011). After 2.6 Ga, the $\Delta^{36}S/\Delta^{33}S$ slopes became shallow ($\Delta^{36}S/\Delta^{33}S$ = ~−1.0) and stable. This stable state with shallow slopes implies a balance in the atmospheric composition.

Not only $\Delta^{36}S/\Delta^{33}S$ trend, but also magnitude and variation of $\Delta^{33}S$ values changed through time (Fig. 6-8). The MIF sulfide is dominant in the 2.7-2.5 Ga Archean sedimentary rocks, in contrast to the dominance of MDF or small MIF sulfide during 3.0-2.7 Ga. This change might have been caused by high SO_2 conditions implying enhanced subaerial volcanism at that time, which is consistent with the geological record suggesting a major increase in volcanic activities and subaerial Large Igneous Provinces from 2.7 to 2.5 Ga (Fig. 6-8; Condie et al., 2009; Kump and Barley, 2007; Bradley, 2011). In ambient atmosphere, optical thickness of SO_2 is unlikely to be high enough to cause the isotopic self-shielding, instead, the large S-MIF can be produced after subaerial extensive volcanism when pSO_2 is high enough to cause considerable S-MIF by isotopic self-shielding in volcanic plumes.

While the appearance of subaerial volcanic activity can explain the large $\Delta^{33}S$ values after 2.7 Ga, considering the S-MIF yielding mechanism by photochemical experiments, only the subaerial volcanism can't explain the $\Delta^{36}S/\Delta^{33}S$ trend. Recent photochemical experiment results of Whitehill and Ono (2012) indicate that light of 250-330 nm wavelength produces elemental sulfur with a positive $\Delta^{36}S/\Delta^{33}S$ ratio (0.64 ± 0.03) by photoexcitation, and the 190-220 nm band and the 250-330 nm region produces negative $\Delta^{36}S/\Delta^{33}S$ values (–1.90) by SO_2 self-shielding. Moreover, these magnitudes probably reflect both the intensity of volcanic SO_2 emissions (enhance the SO_2 self-shielding) and the concentration of reducing gasses (enhance the photoexcitation) under the O_2-free atmosphere (Endo et al., 2016). On the other hand, the subaerial volcanoes are more oxidative than submarine volcanoes (Hollamd, 2002; Gaillard et al., 2011), so a shift from predominantly submarine to a subaerial volcano at 2.7 Ga made $\Delta^{36}S/\Delta^{33}S$ slopes steeper. Thus, to explain the shallow $\Delta^{36}S/\Delta^{33}S$ slopes of ~–1.0 after 2.7 Ga, additional reducing gas such as CH_4 which functions as a greenhouse gas is needed. Indeed, multiple recent studies confirm the correlation between $\Delta^{36}S/\Delta^{33}S$ slopes and

negative $\delta^{13}C_{org}$ (Fig. 6-6), indicating a change in S-MIF forming reactions in association with enhanced methane production (Zerkle et al., 2012; Izon et al., 2015).

Fig. 6-7 represents the possible environmental changes at 2.7 Ga. During 3.0 to 2.7 Ga, both sulfur isotopic characteristic of small $\Delta^{33}S$ values and $\Delta^{36}S/\Delta^{33}S$ slopes suggest low pSO_2 and the low reducing gas atmosphere. On the other hand, during 2.7 to 2.5 Ga, both sulfur isotopic characteristic of large $\Delta^{33}S$ values and $\Delta^{36}S/\Delta^{33}S$ slopes suggest high pSO_2 and high reducing gas atmosphere. A dense reducing gas such as CH_4 could have provided sufficient warming to keep Earth unfrozen as greenhouse effects during 2.7-2.5 Ga. At some point during this era, methanogens evolved, and atmospheric CH_4 increased (Fig. 6-7). The early evolution of methanogens reported by geochemical evidence (Ueno et al., 2006; Battistuzzi et al., 2004). Also, in the absence or near absence of oxygen and sulfate, a greater amount of fragile organic matter is available for microbial methane production. The organic matter was produced by oxygen photosynthesis ($CO_2 + H_2O \rightarrow O_2 + CH_2O$), which are possibly link to the evolution of ~2.7 Ga oxygenic photosynthesis and stabilization of supercontinent (Brocks et al., 2003, 2005; Canfield, 2005; Rasmussen et al., 2008). Imagine a pre-GOE world, then, with mostly vanishingly small amounts of O_2 in the ocean and atmosphere; the ocean was dominated instead by high dissolved iron concentrations. The oxygen which produced by photosynthesizer must have been consumed by the iron and sulfur oxidation in the water. Indeed, the BIF depositions were increased after 2.7 Ga (Fig. 6-7; from Bekker et al., 2010). Our interpretation of S-MIF provides the solution of the causing 200 million years' gap between the appearance of oxygenic photosynthesis and Great Oxidation Even.

Together with the change in the $\Delta^{36}S/\Delta^{33}S$ slopes, the atmosphere may have been reducing with higher volcanic SO_2 input after 2.7 Ga (Fig. 6-7). The sudden change of $\Delta^{36}S/\Delta^{33}S$ slopes and magnitude of $\Delta^{33}S$ values at ~2.7 Ga contemporaneous with appearance of BIF and juvenile continental crust formation (Condie et al., 2009), suggesting slope changes as a consequence of major mantle activity and rapid crustal growth. Several recent geochemical and geological studies have reported anomalous thermal events at 2.7 Ga (e.g. Condie, 1998, 2001; Abbott & Isley, 1999, 2002). The distribution of large igneous provinces (LIPs) in almost every craton around 2.7 Ga shows the plume activity occurred worldwide. Their high proportion and worldwide distribution

indicate that the great magmatism occurred globally, and leads us to deduce hypothesis of mantle overturn.

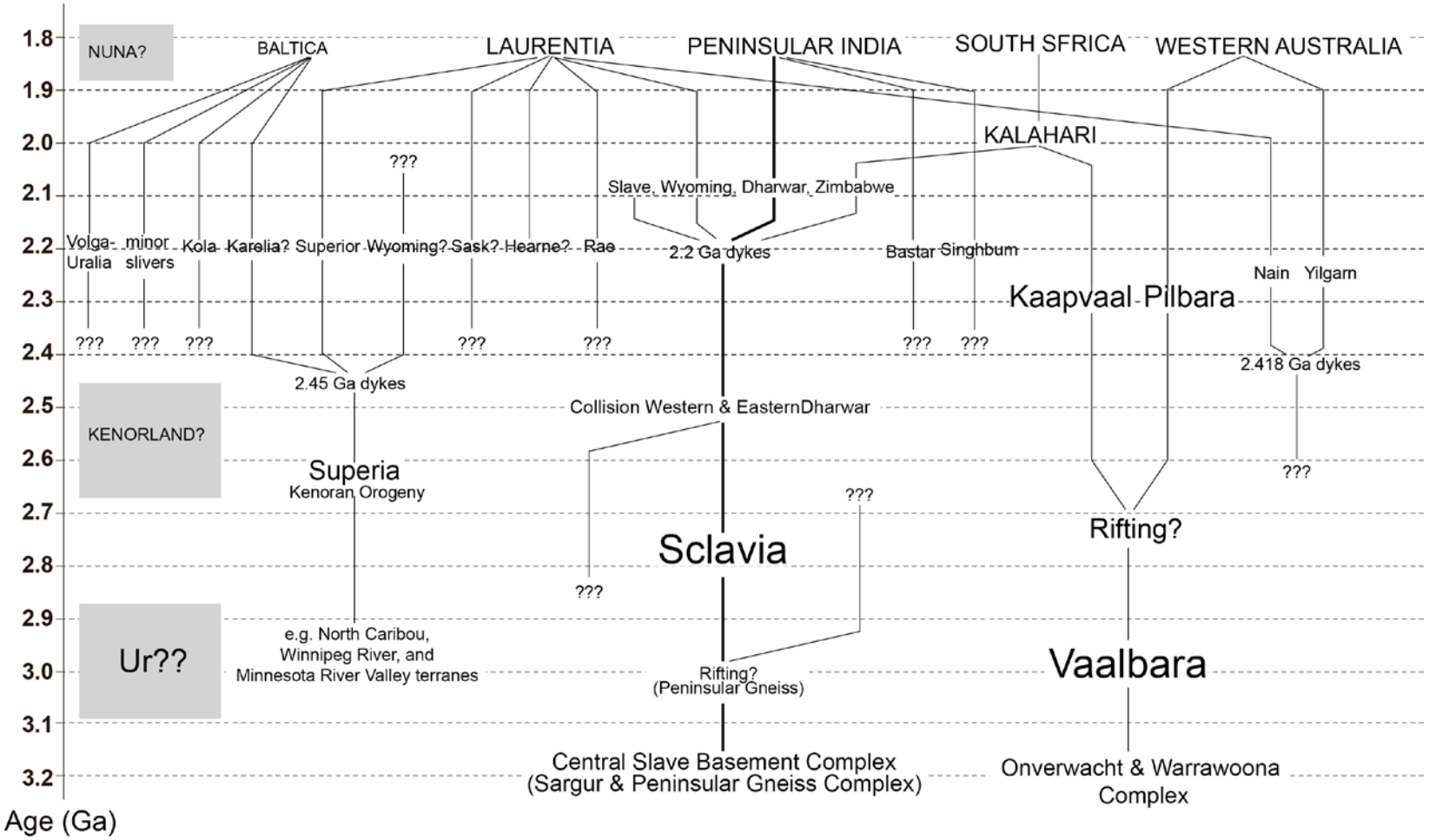

Fig. 6-1 Cladogram showing possible relationships between Archean cratons. In this cladogram, divergence represents break-up, whereas convergence represents amalgamation, typically associated with significant orogenies; question marks represent significant uncertainties or unknowns. Modified from Bleeker et al. (2003).

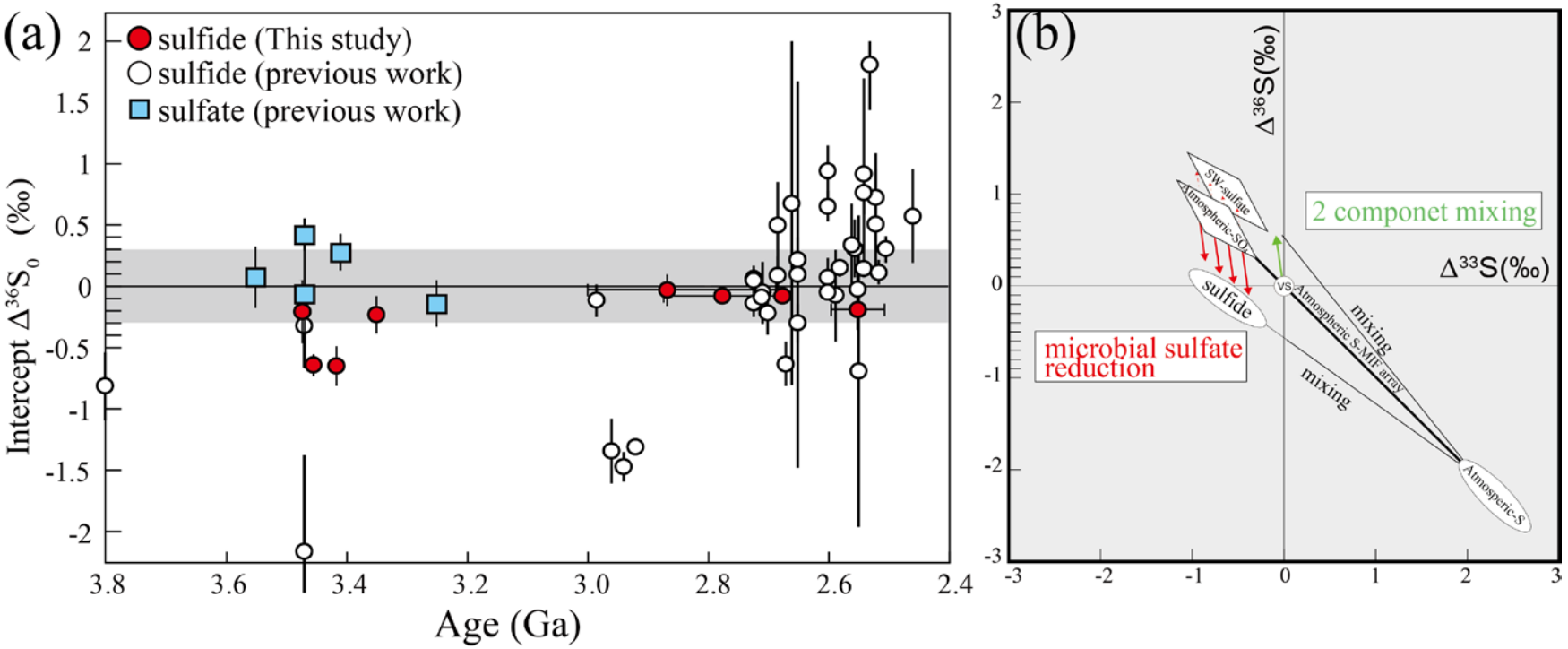

Fig. 6-2 (a) Evolution of the intercept of $\Delta^{36}S/\Delta^{33}S$ values. The data of this study is illustrated by red circle. Literature data (derived from Ono et al., 2006, 2009, Kaufman et al., 2007, Farquhar et al., 2007, Ueno et al., 2008, Shen et al., 2009, Thomazo et al., 2009, Guy et al., 2012, Roerdink et al., 2012, Kurzweil et al., 2013, Zerkle et al., 2012, Thomazot et al., 2013, 2015; Zhelezinskaia et al., 2014; Wacey et al., 2015) is presented as white circles (sulfide) and blue square (sulfate). Shaded areas show from −0.3 to +0.3 of the intercept, which are interpreted as atmospheric MIF lines. (b) Multiple sulfur isotope systematics for the Archean sediments.

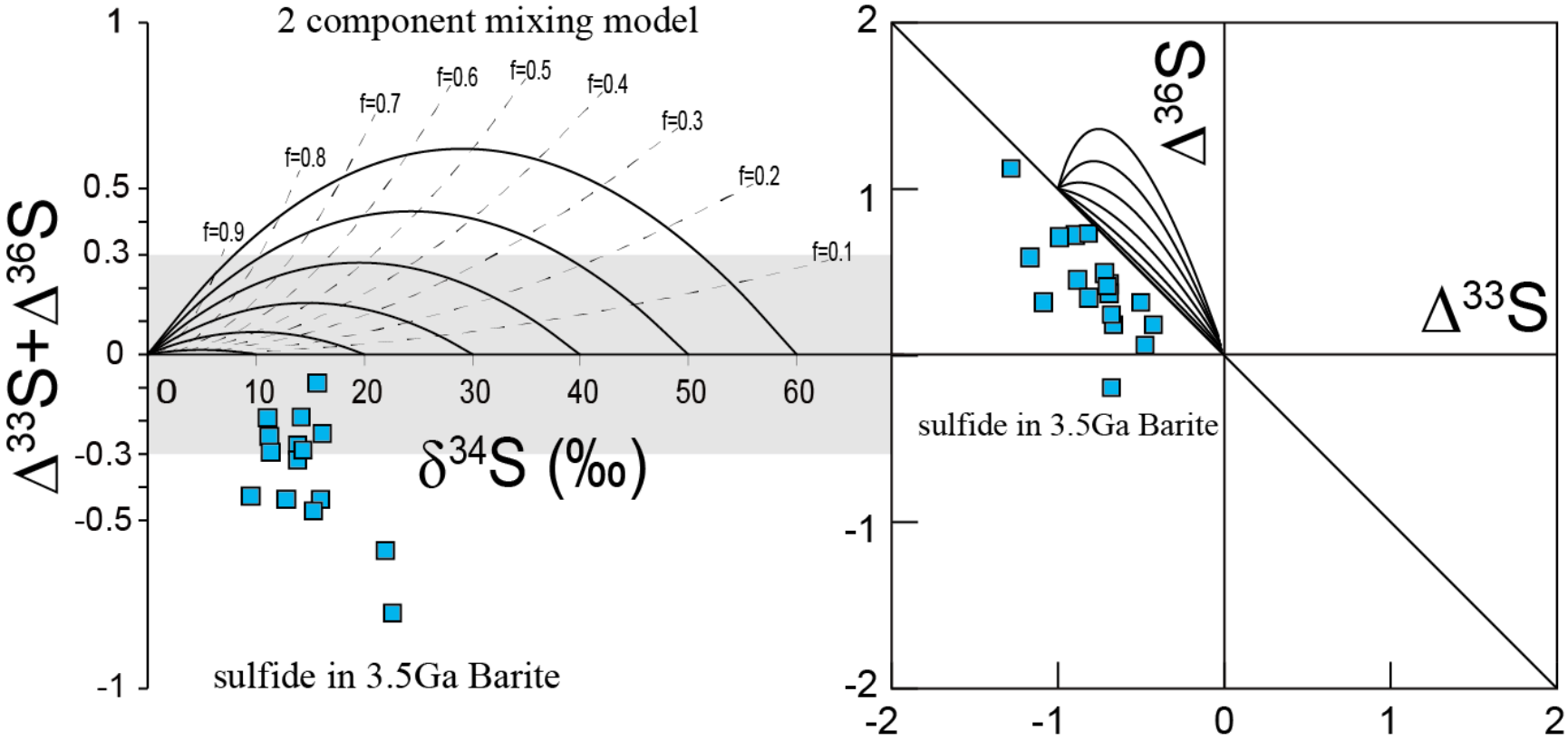

Fig. 6-3 Plot of the deviation from the reference mass-independent fractionation array ($\Delta^{36}S+\Delta^{33}S = 0$) versus the isotopic fractionation of $^{34}S/^{32}S$ between sulfate and sulfide ($\delta^{34}S_{sulfate}-\delta^{34}S_{sulfide}$). Black curves indicate two sulfur components mixing. Blue squears indicate the sulfide in 3.5 Ga barite (from Ueno et al., 2008 and Shen et al., 2009).

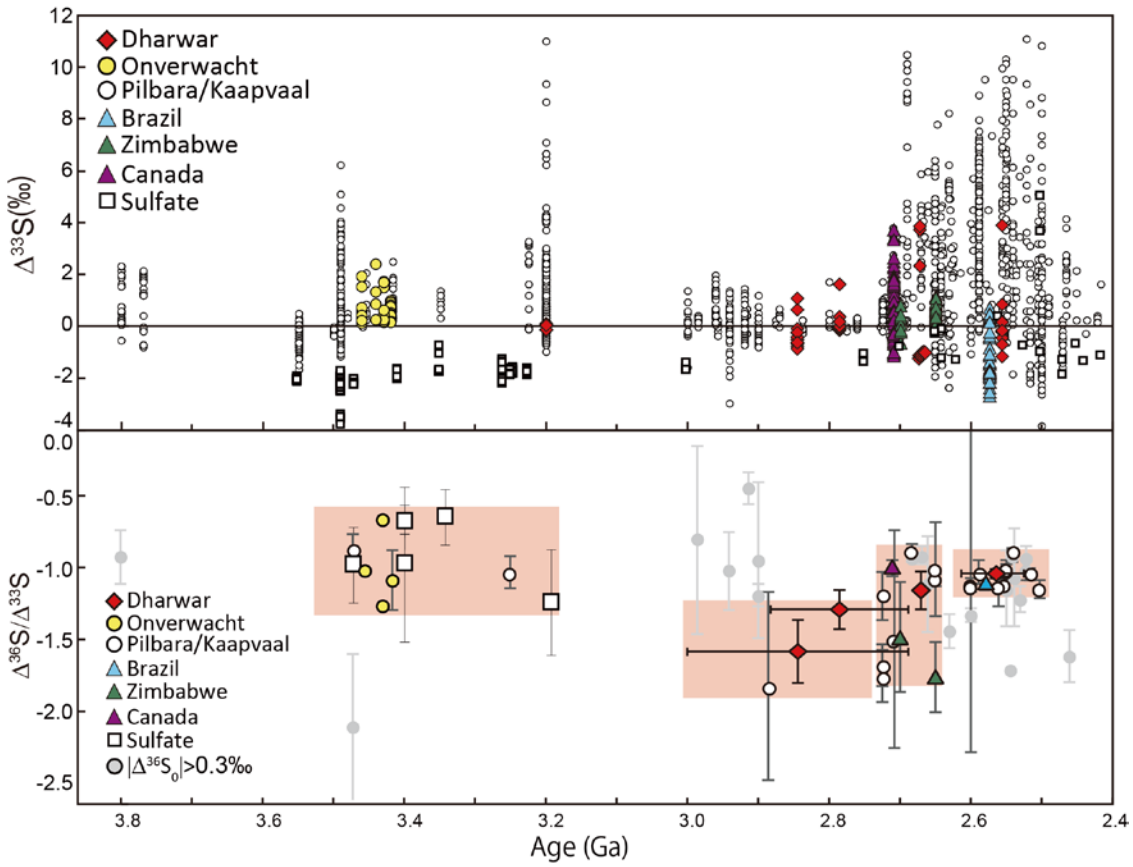

Fig. 6-4 Secular variation of $\Delta^{33}S$ and $\Delta^{36}S$ /$\Delta^{33}S$ values. Grey circles likely reflect later mass dependent process.

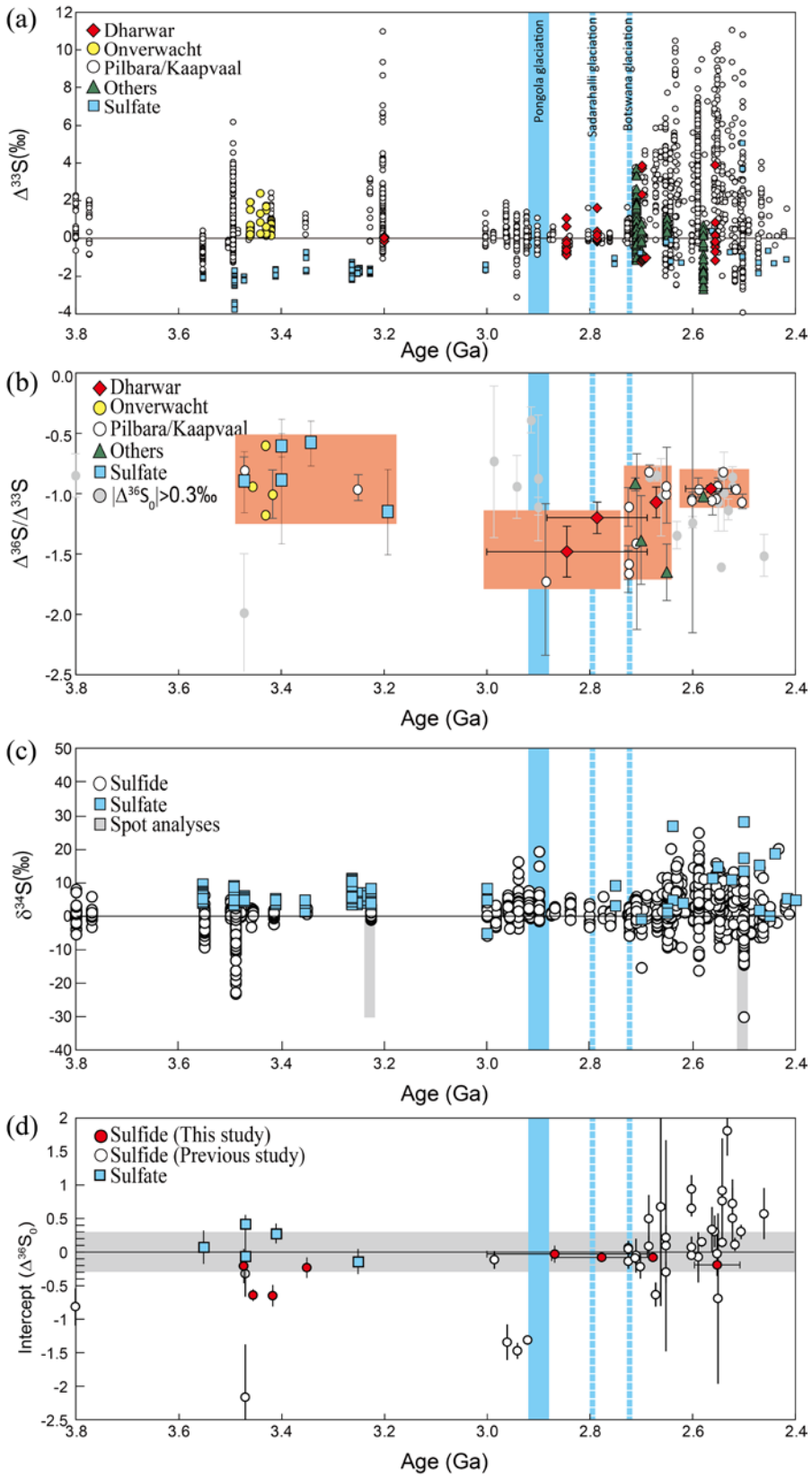

Fig. 6-5 Secular variation of $\Delta^{33}S$, $\delta^{34}S$, $\Delta^{36}S/\Delta^{33}S$ and $\Delta^{36}S/\Delta^{33}S_0$ values.

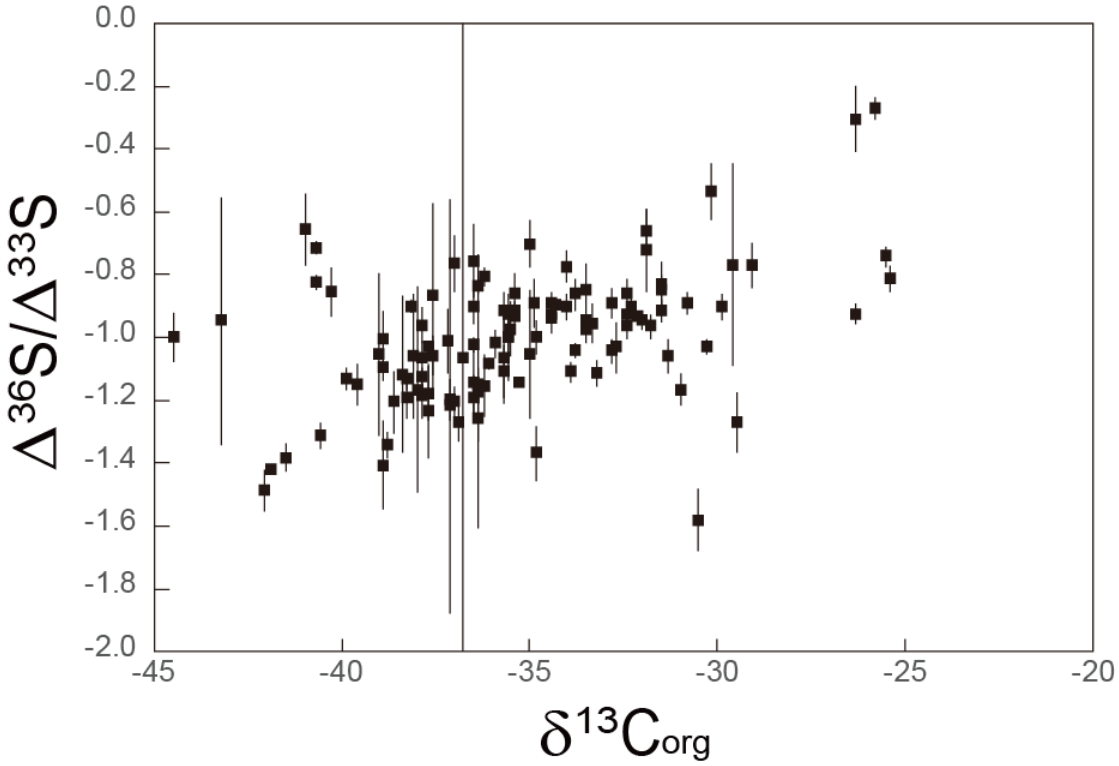

Fig. 6-6 Deviations in the slope of $\Delta^{36}S/\Delta^{33}S$ versus $\delta^{13}C_{org}$ for samples analyzed in Zerkle et al. (2012) and Izon et al. (2015).

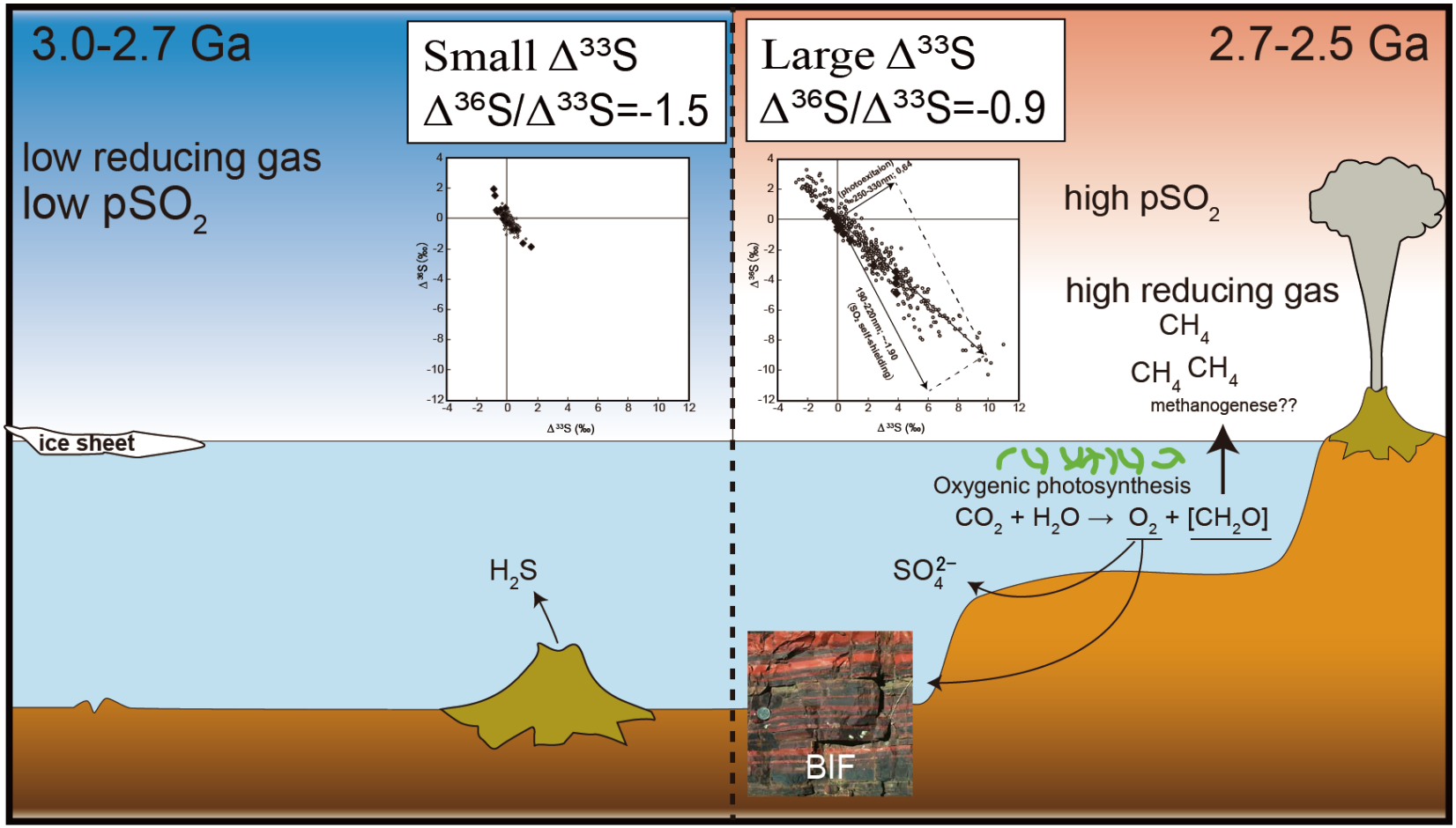

Fig. 6-7 The earth's surface environment during 3.0-2.7 Ga and 2.7-2.4 Ga. This studies in this issue aim to determine the evolution of Archean atmospheric composition. A key factor in this process is the mass-independent fractionation of ^{33}S, which is indicative of photochemical reactions in the ancient atmosphere.

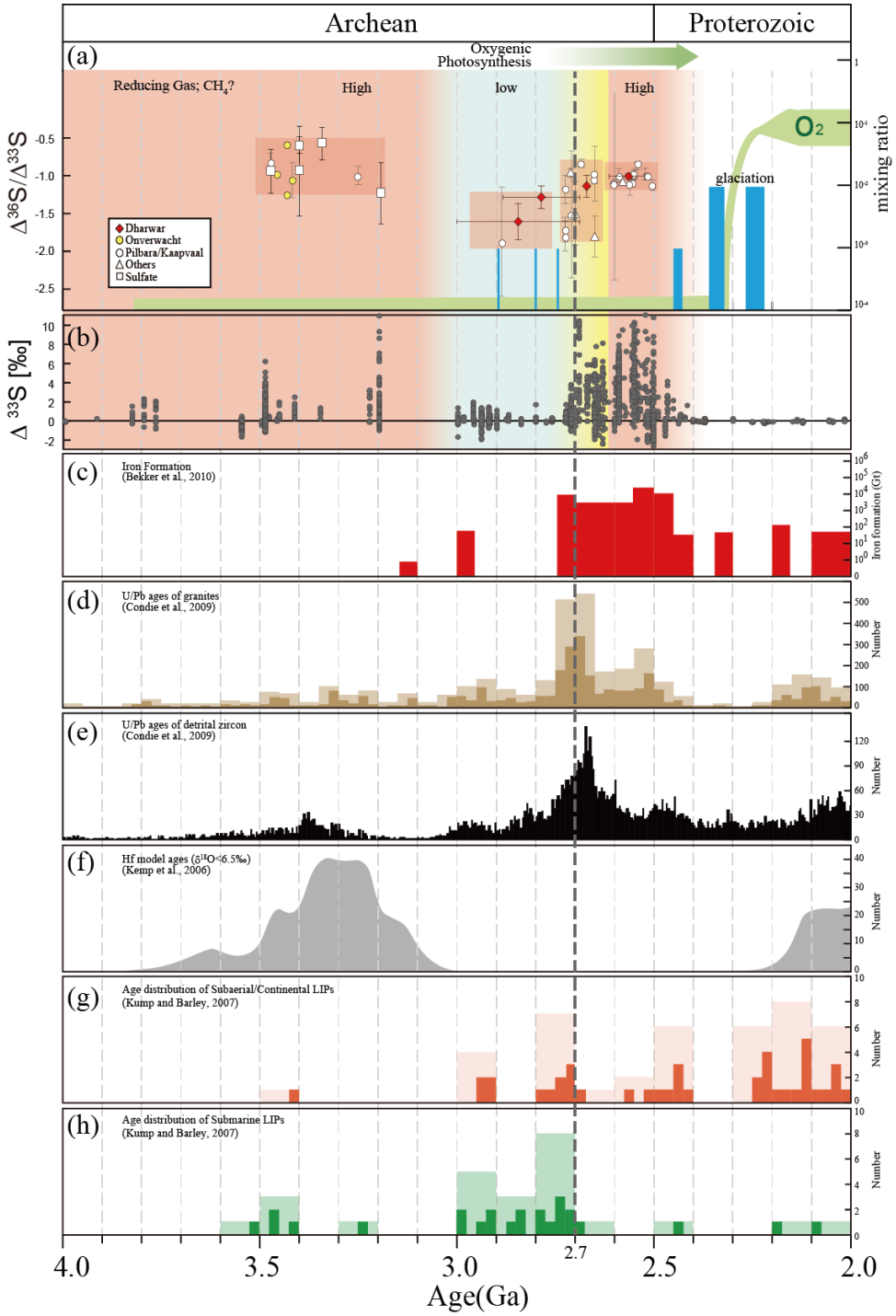

Fig. 6-8 Summary of the Earth' evolution (a) Summary of the earth's atmospheric oxygen content and reducing gas through time compared with glaciation (modified Hoffman et al., 2009). (b) $\Delta^{33}S$ secular variation. (c) Secular trend in the distribution of iron formations (after Bekker et al., 2010). (d) Distribution of U–Pb zircon ages for juvenile crust (after Condie et al., 2009). (e) Distribution of U–Pb detrital zircon ages (after Condie et al., 2009) (f) Gaussian probability distribution of Hf model ages for zircons with low $\delta^{18}O$ values (after Kemp et al., 2006). (g) Age distribution of subaerial or continental large igneous provinces (LIPs). (h) Age distribution of submarine LIPs (from Kump and Barley, 2007).

References

Battistuzzi, F. U., Feijao, A., & Hedges, S. B., 2004. A genomic timescale of prokaryote evolution: insights into the origin of methanogenesis, phototrophy, and the colonization of land. BMC evolutionary biology, 4 (1), 1.

Bekker, A., Slack, J. F., Planavsky, N., Krapež, B., Hofmann, A., Konhauser, K. O., & Rouxel, O. J., 2010. Iron formation: the sedimentary product of a complex interplay among mantle, tectonic, oceanic, and biospheric processes. Economic Geology, 105 (3), 467-508.

Brocks, J. J., Buick, R., Summons, R. E., & Logan, G. A., 2003. A reconstruction of Archean biological diversity based on molecular fossils from the 2.78 to 2.45 billion-year-old Mount Bruce Supergroup, Hamersley Basin, Western Australia. Geochimica et Cosmochimica Acta, 67 (22), 4321-4335.

Brocks, J. J., Love, G. D., Summons, R. E., Knoll, A. H., Logan, G. A., & Bowden, S. A., 2005. Biomarker evidence for green and purple sulphur bacteria in a stratified Palaeoproterozoic sea. Nature, 437 (7060), 866-870.

Canfield, D. E., 2005. The early history of atmospheric oxygen: homage to Robert M. Garrels. Annu. Rev. Earth Planet. Sci., 33, 1-36.

Chandler, F. W., 1980. Proterozoic redbed sequences of Canada. Energy, Mines and Resources Canada, Geological Survey of Canada.

Cheney, E. S., 1996. Sequence stratigraphy and plate tectonic significance of the Transvaal succession of southern Africa and its equivalent in Western Australia. Precambrian Research, 79 (1), 3-24.

Domagal-Goldman, S. D., Kasting, J. F., Johnston, D. T., & Farquhar, J., 2008. Organic haze, glaciations and multiple sulfur isotopes in the Mid-Archean Era. Earth and Planetary Science Letters, 269 (1), 29-40.

Endo, Y., Ueno, Y., Aoyama, S., & Danielache, S. O., 2016. Sulfur isotope fractionation by broadband UV radiation to optically thin SO 2 under reducing atmosphere. Earth and Planetary Science Letters, 453, 9-22.

Farquhar, J., Bao, H., Thiemens, M., 2000. Atmospheric influence of earth's earliest sulfur cycle, Science, 289, 756-758.

England, G. L., Rasmussen, B., Krapez, B., & Groves, D. I., 2002. Palaeoenvironmental significance of rounded pyrite in siliciclastic sequences of the Late Archaean

Witwatersrand Basin: oxygen‐deficient atmosphere or hydrothermal alteration?. Sedimentology, 49 (6), 1133-1156.

Farquhar, J., Savarino, J., Airieau, S., & Thiemens, M. H., 2001. Observation of wavelength‐sensitive mass‐independent sulfur isotope effects during SO2 photolysis: Implications for the early atmosphere. Journal of Geophysical Research: Planets, 106 (E12), 32829-32839.

Farquhar, J., Peters, M., Johnston, D. T., Strauss, H., Masterson, A., Wiechert, U., & Kaufman, A. J., 2007. Isotopic evidence for Mesoarchaean anoxia and changing atmospheric sulphur chemistry. Nature, 449 (7163), 706-709.

Gaillard, F., Scaillet, B., & Arndt, N. T., 2011. Atmospheric oxygenation caused by a change in volcanic degassing pressure. Nature, 478(7368), 229-232.

Haqq-Misra, J. D., Domagal-Goldman, S. D., Kasting, P. J., & Kasting, J. F., 2008. A revised, hazy methane greenhouse for the Archean Earth. Astrobiology, 8 (6), 1127-1137.

Hofmann, A., Bekker, A., Rouxel, O., Rumble, D., & Master, S., 2009. Multiple sulphur and iron isotope composition of detrital pyrite in Archaean sedimentary rocks: a new tool for provenance analysis. Earth and Planetary Science Letters, 286 (3), 436-445.

Holland, H., & Schopf, J. W., 1984. Earth's Earliest Biosphere: Its Origin and Evolution.

Holland, H. D., 2002. Volcanic gases, black smokers, and the Great Oxidation Event. Geochimica et Cosmochimica Acta, 66 (21), 3811-3826.

Johnston, D. T., Wing, B. A., Farquhar, J., Kaufman, A. J., Strauss, H., Lyons, T. W., ... & Canfield, D. E., 2005. Active microbial sulfur disproportionation in the Mesoproterozoic. Science, 310 (5753), 1477-1479.

Johnston, D. T., Farquhar, J., & Canfield, D. E., 2007. Sulfur isotope insights into microbial sulfate reduction: when microbes meet models. Geochimica et Cosmochimica Acta, 71 (16), 3929-3947.

Johnston, D. T., 2011. Multiple sulfur isotopes and the evolution of Earth's surface sulfur cycle. Earth-Science Reviews, 106 (1), 161-183.

Kasting, J. F., 1987. Theoretical constraints on oxygen and carbon dioxide concentrations in the Precambrian atmosphere. Precambrian research, 34 (3), 205-229.

Kaufman, A. J., Corsetti, F. A., & Varni, M. A., 2007. The effect of rising atmospheric

oxygen on carbon and sulfur isotope anomalies in the Neoproterozoic Johnnie Formation, Death Valley, USA. Chemical Geology, 237 (1), 47-63.

Kurzweil, F., Claire, M., Thomazo, C., Peters, M., Hannington, M., & Strauss, H., 2013. Atmospheric sulfur rearrangement 2.7 billion years ago: Evidence for oxygenic photosynthesis. Earth and Planetary Science Letters, 366, 17-26.

Melezhik, V. A., Fallick, A., Hanski, E. J., Kump, L. R., Lepland, A., Prave, A. R., & Strauss, H., 2005. Emergence of the aerobic biosphere during the Archean-Proterozoic transition: challenges of future research. GSA Today, 15 (11), 4-11.

Ono, S., Eigenbrode, J. L., Pavlov, A. A., Kharecha, P., Rumble, D., Kasting, J. F., & Freeman, K. H., 2003. New insights into Archean sulfur cycle from mass-independent sulfur isotope records from the Hamersley Basin, Australia. Earth and Planetary Science Letters, 213 (1), 15-30.

Ono, S., Whitehill, A. R., & Lyons, J. R., 2013. Contribution of isotopologue self‐shielding to sulfur mass‐independent fractionation during sulfur dioxide photolysis. Journal of Geophysical Research: Atmospheres, 118 (5), 2444-2454.

Pavlov, A. A., & Kasting, J. F., 2002. Mass-independent fractionation of sulfur isotopes in Archean sediments: strong evidence for an anoxic Archean atmosphere. Astrobiology, 2 (1), 27-41.

Rasmussen, B., & Buick, R., 1999. Redox state of the Archean atmosphere: evidence from detrital heavy minerals in ca. 3250–2750 Ma sandstones from the Pilbara Craton, Australia. Geology, 27 (2), 115-118.

Rasmussen, B., Fletcher, I. R., Brocks, J. J., & Kilburn, M. R., 2008. Reassessing the first appearance of eukaryotes and cyanobacteria. Nature, 455 (7216), 1101-1104.

Roscoe, S. M., 1996. Paleoplacer uranium, gold. Geology of Canada, 8, 10-23.

Rye, R., Kuo, P. H., & Holland, H. D., 1995. Atmospheric carbon dioxide concentrations before 2.2 billion years ago. Nature, 378 (6557), 603-605.

Sagan, C., & Mullen, G., 1972. Earth and Mars: Evolution of atmospheres and surface temperatures. Science, 177 (4043), 52-56.

Sheldon, N. D., 2006. Precambrian paleosols and atmospheric CO_2 levels. Precambrian Research, 147 (1), 148-155.

Shen, Y., Farquhar, J., Masterson, A., Kaufman, A. J., & Buick, R., 2009. Evaluating the

role of microbial sulfate reduction in the early Archean using quadruple isotope systematics. Earth and Planetary Science Letters, 279 (3), 383-391.

Ueno, Y., Yamada, K., Yoshida, N., Maruyama, S., & Isozaki, Y., 2006. Evidence from fluid inclusions for microbial methanogenesis in the early Archaean era. Nature, 440 (7083), 516-519.

Watanabe, Y., Farquhar, J., & Ohmoto, H., 2009. Anomalous fractionations of sulfur isotopes during thermochemical sulfate reduction. Science, 324 (5925), 370-373.

Whitehill A. R., Ono, S., 2012. Excitation band dependence of sulfur isotope mass-independent fractionation during photochemistry of sulfur dioxide using broadband light sources. Geochim. Cosmochim. Acta, 94, 238–253.

Williams, H., Hoffman, P. F., Lewry, J. F., Monger, J. W., & Rivers, T., 1991. Anatomy of North America: thematic geologic portrayals of the continent. Tectonophysics, 187 (1-3), 117-134.

Young, G. M., Brunn, V. V., Gold, D. J., & Minter, W. E. L., 1998. Earth's oldest reported glaciation: physical and chemical evidence from the Archean Mozaan Group (~ 2.9 Ga) of South Africa. The Journal of geology, 106 (5), 523-538.

Zerkle, A. L., Claire, M. W., Domagal-Goldman, S. D., Farquhar, J., & Poulton, S. W., 2012. A bistable organic-rich atmosphere on the Neoarchaean Earth. Nature Geoscience, 5 (5), 359-363.

Acknowledgements

I would like to express my sincere gratitude to my supervisor Prof. Yuichiro Ueno at Tokyo Institute of Technology, who gave me the best advice through the project, great editorial suggestions for this work. I also thank to Prof. M. Satish-Kumar at Niigata University for organizing my opportunity to join the field research in Dharwar in five field seasons during the period of 2011-2015. I would have never studied freely without his great efforts.

I also thank Prof. Tsuyoshi Toyoshima at Niigata University for introducing me to intricasies of structural geology of Dharwar and geological investigation. Next, a special word of thanks to Prof. Tomokazu Hokada at National Institute of Polar Research who kindly introduce me to the zircon U/Pb analysis by SHRIMP. I also thank him for really geological discussions for this work.

I wish to thank Prof. Maarten J. de Wit at Nelson Mandela University for suppoting my field research in South Africa, critical reading of this manuscript and geological investigations.

A special word of thanks to Miss. Rie Yamazaki and Mr. Yoshihiro Enya at Niigata University for giving me the gratefull data. I greatly thank to Drs. Kenji Horie at National Institute of Polar Research, Prof. Takafumi Hirata at Kyoto University, Drs. Shinji Yamamoto at Tokyo University for analyzing zircon U-Pb geochronology.

I would like to thank assistant Prof. Yusuke Sawaki and Prof. Shigenori Maruyama for enthusiastic support and geological investigation.

Working in Dharwar, I wish to thank Prof. Atsushi Kamei of Shimane University, Prof. Kyoko Kataoka of Niigata University, Drs. Sajeev Krishnan, Drs. Ishwar-Kumar, Drs. Ratheesh Kumar, Drs. George Paul Mathews, Drs. Vinod Oommen Samuel, Drs. Abdulla nasheeth of Indian Institue od Science, Mr. Shinnosuke Aoyama, Mr. Fumiya Tomiyasu, Mr. Kentaro Koinuma, Mr. Itsuki Muramatsu, Miss. Chie Kato, for supporting field work in Dharwar.

Working in South Africa, I wish to thank Drs. Takuya Saito for supporting field work at 2012.

I greatly appreciate Drs. Masashi Ushioda and Mr. Tatsuyuki Arai for assisting electron probe analyses.

I also sincere thank the members of Maruyama-Hirose-Ueno laboratory; Prof. Kei Hirose, Drs. Kenji Ohta, Prof. Kenji Kawai, Prof. Soichi Omori, Drs. Kazumi Yoshiya, Masafumi Saito, Takahiro Aze, Tomohiko Sato, Yoshihiko Okada, Motoko Yoshizaki, Miyuki Tahata, Fumihiro Matsuura, Kazue Suzuki, Konomi Suda, Mr. Yoshiaki Endo, Wataru Fujisaki, Ryohei Suzuki, Hisashi Asanuma, Fumiya Tomiyasu, Tetsuya Kawamura, Hikaru Sawada, Tsubasa Hirai, Yuki Murakami, Sho Suehiro, Rei Morishita, Sho Tagawa, Tomokazu Murai and Mss. Waka Kawade for encouraging discussions and secretaries for helping dairy college life and research in various aspects.

I grateful thank to Miss. Shio Watanabe, Kei Kudo, Satsuki Sekiguchi and Mayumi Ohno for their kindness.

Finally, I would like to thank my parents, Naoto Mishima and Noriko Mishima for financial support. I thank my girl friend, Chika Hayashi for affectionate support.